Biological functions of Sphingomyelin synthase related protein and Ceramide synthase 4 investigated with transgenic mouse mutants

Dissertation

Zur

Erlangung des Doktorgrades (Dr. rer. nat.)

der

Mathematisch-Naturwissenschaftlichen Fakultät

der

Rheinischen Friedrich-Wilhelms-Universität Bonn

vorgelegt von

Andreas Bickert

aus

Neuwied

Bonn, 2016

Angefertigt mit Genehmigung der Mathematisch-Naturwissenschaftlichen Fakultät
der Rheinischen Friedrich-Wilhelms-Universität Bonn

Erstgutachter: Prof. Dr. Klaus Willecke
Zweitgutachter: Prof. Dr. Michael Hoch

Tag der Promotion: 25.10.2016

Erscheinungsjahr: 2017

Table of Contents

1 Introduction

1.1 Biological lipids

As one of the four main classes of biological molecules, lipids besides carbohydrates, proteins and nucleic acids are of crucial importance for cellular integrity and survival. Among a plethora of biological functions, they are essential constituents of cellular membranes, serve energy storage and are involved in multiple signaling pathways regulating cellular functions. Lipids can be defined as hydrophobic or amphiphatic molecules originating from carbanion-based condensations of thioesters and/or carbocation-based condensation of isoprene units (Fahy *et al.*, 2009). Based on this definition lipids can be subdivided into eight categories i.e. fatty acyls, glycerolipids, glycerophospholipids, sphingolipids, sterol lipids, prenol lipids, saccharolipids and polyketides (Fahy *et al.*, 2005, 2009).

The most fundamental lipid category is represented by fatty acyls. The category includes several subclasses e.g. eicosanoids, which comprise a huge number of lipid hormones (Marion-Letellier *et al.*, 2015) or fatty acids. Fatty acids, besides being a major source of energy, which can be released in a degradation process termed ß-oxidation, are important building blocks for a large number of biological lipids. Fatty acids are synthesized through successive attachment of malonyl-CoA to an acetyl-CoA primer (propionyl-CoA for odd-numbered fatty acids) and differ in chain length and degree of saturation.

Glycerolipids are based on the trihydric sugar alcohol glycerol. Step-wise esterification of the hydroxy groups at C1 and C2 (per definition depicted as *sn1* and *sn2*) with fatty acyl-CoAs produces monoacylglycerol and diacylglycerol (DAG), a universal intermediate of glycerolipid synthesis. Further esterification with a fatty acyl-CoA at C3 (*sn3*) produces triacylglycerol (TAG). While TAGs primarily serve storage of metabolic energy, DAGs can also act as membrane bound second messengers.

Glycerophospholipids are directly derived from glycerolipids, with DAG being the backbone of most glycerophospholipids. The most common representatives, phosphatidylcholine (PC), phosphatidylethanolamine (PE), phosphatidylserine (PS) and phosphatidylinositol (PI) are presented in Figure 1.1 A. The synthesis of PC is mainly accomplished through the Kennedy pathway in which CDP-choline originating from sequential conversion of choline in the cytoplasm, reacts with DAG in the endoplasmic reticulum (ER)(Gibellini & Smith, 2010). The synthesis of PE is analogous to this. While PC and PE can be converted to PS in a base-exchange reaction in the ER, PE can also be produced by decarboxylation of PS in mitochondria (Vance & Tasseva, 2013). In an alternative pathway of glycerophospholipid synthesis, phosphatidic acid, a phosphorylated derivative of

DAG, is activated with CTP. The resulting CDP-diacylglycerol can be converted to PI. PI is the basic structure of a specific class of membrane-bound second messengers, summed up as phosphoinositides. They regulate a wide array of biological processes including lipid distribution and metabolism, or vesicular trafficking (Balla, 2013). PC, PE, PS and PI represent the vast majority of phospholipids in eukaryotic cell membranes.

Another category of lipids are the sphingolipids. The backbone of all higher order sphingolipids is ceramide, the central intermediate of the sphingolipid metabolic pathway. Sphingolipids and especially ceramides are of central importance in the course of this thesis and a more detailed introduction is given in chapter 1.3. The most abundant sphingolipid is sphingomyelin (SM). SM structurally resembles glycerophospholipids, sharing a similar backbone of two hydrophobic acyl tails and a phosphate containing hydrophilic head group (Figure 1.1 B). Together these lipids can be referred to as phospholipids. Phospholipids, together with glycosphingolipids and cholesterol, represent the main constituents of eucaryotic membranes. While only PC and PE account for more than 50 % of all phospholipids in eucaryotic cell membranes, sphingolipids account for 10-20 % (Holthuis *et al.*, 2001).

A very prominent lipid is the sterol cholesterol (Figure 1.1 C). Together with higher sterols e.g. ergosterol, it represents 20-40 mol % of lipids in eukaryotic membranes and is an essential regulator of membrane fluidity (Mouritsen & Zuckermann, 2004). Due to its biophysical properties it increases lipid order and establishes low permeability barriers by specifically interacting with certain phospholipids in cellular lipid-bilayers (Ohvo-Rekilä *et al.*, 2002; Mouritsen & Zuckermann, 2004).

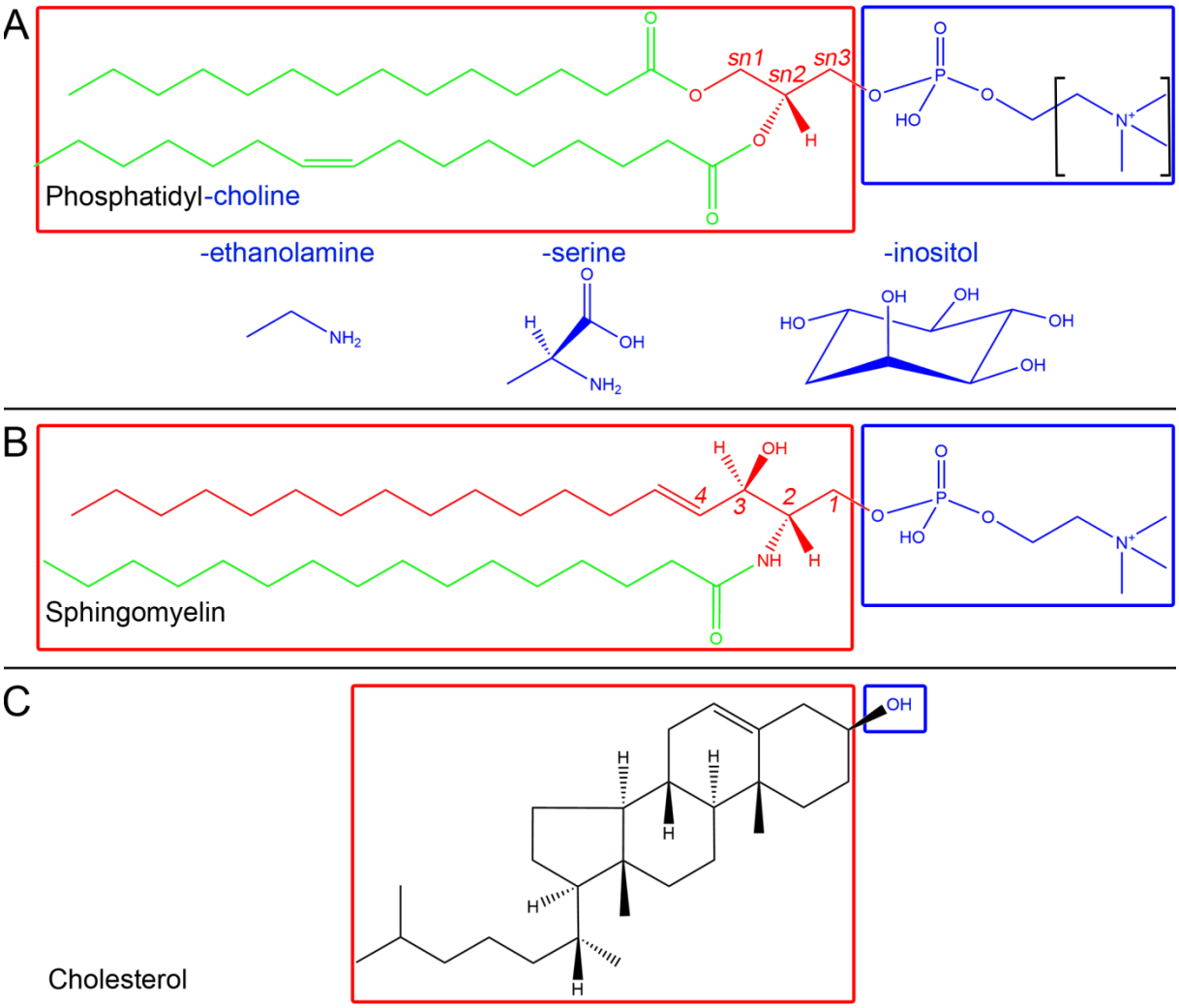

Figure 1.1 - Representative structures for the most common glycerophospholipids, sphingolipids and sterols. (A) Structural formula of the glycerophospholipid phosphatidylcholine with myristic acid at *sn1* and palmitoleic acid at *sn2* (C14:0/C16:1 cis-9). Substitution of the choline head group (in brackets) with the below depicted head groups leads to representative structural formulas of phosphatidylethanolamine, phosphatidylserine and phosphatidylinositol. Substitution of the phosphocholine group at *sn3* with a hydroxy group leads to the structural formula of diacylglycerol, the precursor of the most abundant glycerophospholipids. The glycerol backbone is depicted in red. The acyl chains at *sn1* and *sn2* can differ in chain length and degree of saturation. (B) Structural formula of the sphingolipid sphingomyelin with *N*-acylated palmitic acid (d18:1/C16:0). The sphingoid backbone (sphingosine) is depicted in red. Substitution of the phosphocholine group at C3 with a hydroxy group leads to the structural formula of ceramide, the precursor of all higher order sphingolipids. The *N*-acyl chain can differ in chain length and degree of saturation. (C) Structural formula of the steroid cholesterol. Red boxes highlight hydrophobic backbones, blue boxes highlight hydrophilic head groups. Fatty acyl chains are depicted in green, hydrophilic head groups in blue. Molecule structures were created and modified according to the LIPID MAPS Lipidomics Gateway (http://www.lipidmaps.org/) using ChemDraw Prime 15 software (Perkin Elmer).

1.2 Eucaryotic membranes

Eukaryotic membranes are characterized by a number of functions that are vital for cellular survival and integrity. Besides the surrounding cell membrane, which provides mechanical stability and represents a protective barrier between the interior

and the outside of the cell, each cell contains specialized membranes that surround organelles to establish separated reaction spaces. For instance, mitochondrial membranes that provide the basis for oxidative phosphorylation or membranes of the ER that facilitate lipid synthesis. Despite different function, all of these membranes share a similar structure consisting of a selectively-permeable lipid bilayer with associated proteins (Figure 1.2). The basic architecture of cellular lipid bilayers is established by amphipathic phospholipids (Figure 1.1 A, B). In an aqueous environment these lipids tend to organize in a thermodynamically favorable arrangement. While the non-polar acyl chains establish a hydrophobic core, the phosphate containing hydrophilic head groups build up the inner and outer surface of the bilayer. The protein portion comprises a large subset of structurally and functionally diverse proteins that for instance mediate cell to cell communication and transport of metabolites, or confer mechanical stability by connecting the cell membrane to the cytoskeleton.

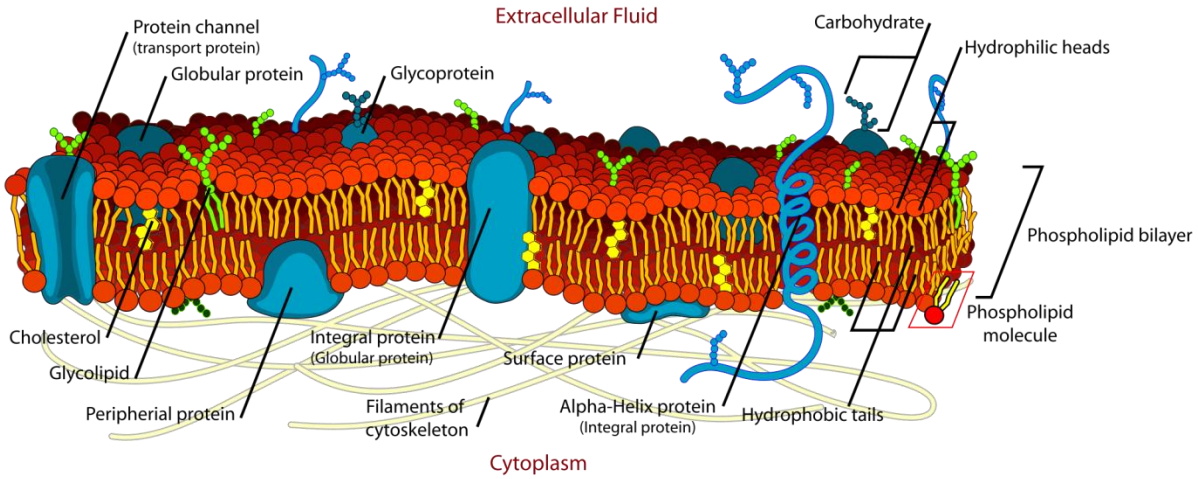

Figure 1.2 - Schematic drawing of the eukaryotic cell membrane. The picture illustrates the typical organization with the semi-permeable phospholipid bilayer and inserted cholesterol as an essential regulator of membrane fluidity. Carbohydrate moieties of glycolipids and glycosylated proteins are exclusively directed to the extracellular space. Proteins are subdivided in peripheral proteins on the surface of the bilayer and integral proteins inserted into the bilayer. (Modified and adopted from https://upload.wikimedia.org/wikipedia/en/9/9c/Cell_membrane_detailed_diagram_edit2.svg)

According to the fluid mosaic model, lipid bilayers represent a fluid continuum, allowing lateral diffusion and free rotation of lipids and proteins around an axis perpendicular to the membrane (Singer & Nicolson, 1972). In contrast, transbilayer movement (also known as flip-flop) is thermodynamically unfavorable and rather rare. This leads to asymmetric distribution of phospholipids in cellular lipid bilayers by specialized transbilayer transporters, which is of fundamental importance for cellular function and integrity (Daleke, 2007). The outer monolayer of the cell membrane mainly consists of PC, SM and glycosylated sphingolipids, whereas PE, PI and PS mainly occur in the inner monolayer. PS is almost exclusively found in the inner

monolayer, its exposure in the outer monolayer due to increased transbilayer movement during early stages of apoptosis represents a signal for phagocytosis (Vance & Tasseva, 2013).

According to function and needs of different cell types, the lipid (and protein) composition of cell and organelle membranes can strongly differ from each other, especially with respect to incorporated fatty acids. Nevertheless, the vast majority of the glycerophospholipids in eukaryotic lipid bilayers are composed of a saturated fatty acid at position *sn1* and an unsaturated fatty acid at *sn2* (Zarringhalam *et al.*, 2012). The cis-configured double bonds of unsaturated fatty acyl chains prevent tight packing of individual lipid molecules, which is mainly responsible for the fluidity of eukaryotic membranes. In contrast, the structure of sphingolipids allows tighter packing. As a consequence they preferentially assemble with each other and with cholesterol, and establish highly ordered membrane domains (Pike, 2009). Several studies indicated that such lipid microdomains, originally termed lipid rafts, compartmentalize cellular processes by facilitating local clustering of proteins involved in the execution and control of cellular signaling (Pike, 2009; van Meer & Hoetzl, 2010). The existence of lipid microdomains *in vivo* is subject of a controversial debate, for instance, because detection in living cells is restricted by the resolution limit of optical microscopy (Fan *et al.*, 2010). Stimulated emission depletion (STED) far-field fluorescence nanoscopy allows to detect single diffusing (lipid) molecules in nanosized membrane areas (Eggeling *et al.*, 2009). Using this technique it was demonstrated that cholesterol-mediated molecular complexes (<20 nm in diameter) of sphingolipids and glycosylphosphatidylinositol (GPI)-anchored proteins transiently exist (~10–20 ms) in plasma membranes of living mammalian cells (Eggeling *et al.*, 2009). According to the general consensus lipid microdomains are rather small (10-200 nm), heterogeneous, highly dynamic and can be stabilized to larger platforms (Pike, 2009). Several of the studies focusing on lipid microdomain function in the control of cellular signaling made use of detergent-resistant membranes (DRMs), but it is questionable whether these actually resemble lipid microdomains that exist *in vivo* or are artifacts resulting from the isolation procedure (Brown & London, 1997; Rodgers *et al.*, 2005).

1.3 Sphingolipids

Emerging evidence in the last decades highlighted the importance of sphingolipids in several cellular processes. As major constituents of eukaryotic membranes they provide mechanical stability and mediate molecular sorting, cell recognition or signal transduction (Holthuis *et al.*, 2001; Lopez & Schnaar, 2009; Breslow & Weissman, 2010). In their function as signaling molecules they cover a wide array of cellular processes including cell growth, death, senescence, adhesion, migration,

inflammation, angiogenesis or intracellular trafficking (Hannun & Obeid, 2008; Lingwood & Simons, 2010).

1.3.1 Sphingolipid metabolic pathway

The central intermediate of the sphingolipid metabolic pathway (Figure 1.3) is ceramide (Figure 1.3 E). Ceramides were shown to be potent mediators of cellular stress responses, cell cycle arrest and apoptosis (Merrill, 2002; Hannun & Obeid, 2008; Morad & Cabot, 2013) and are the precursors for all higher order sphingolipids. Ceramide originates either from a '*de novo* pathway' or from a recycling pathway, referred to as 'salvage pathway'. The backbones of ceramides are sphingoid long chain bases (LCBs). The basic LCB of the *de novo* synthesis is sphinganine (Figure 1.3 C). The most common LCB, sphingosine (Figure 1.3 F), is a sphinganine analog containing a 4, 5-trans double bond. The less common sphingadiene contains an additional double bond of varying position (Zhang *et al.*, 2015). Another less common LCB in mammals is phytosphingosine, which harbors an additional hydroxy group at C4. It is the predominant LCB in plants and yeast (Mizutani *et al.*, 2004).

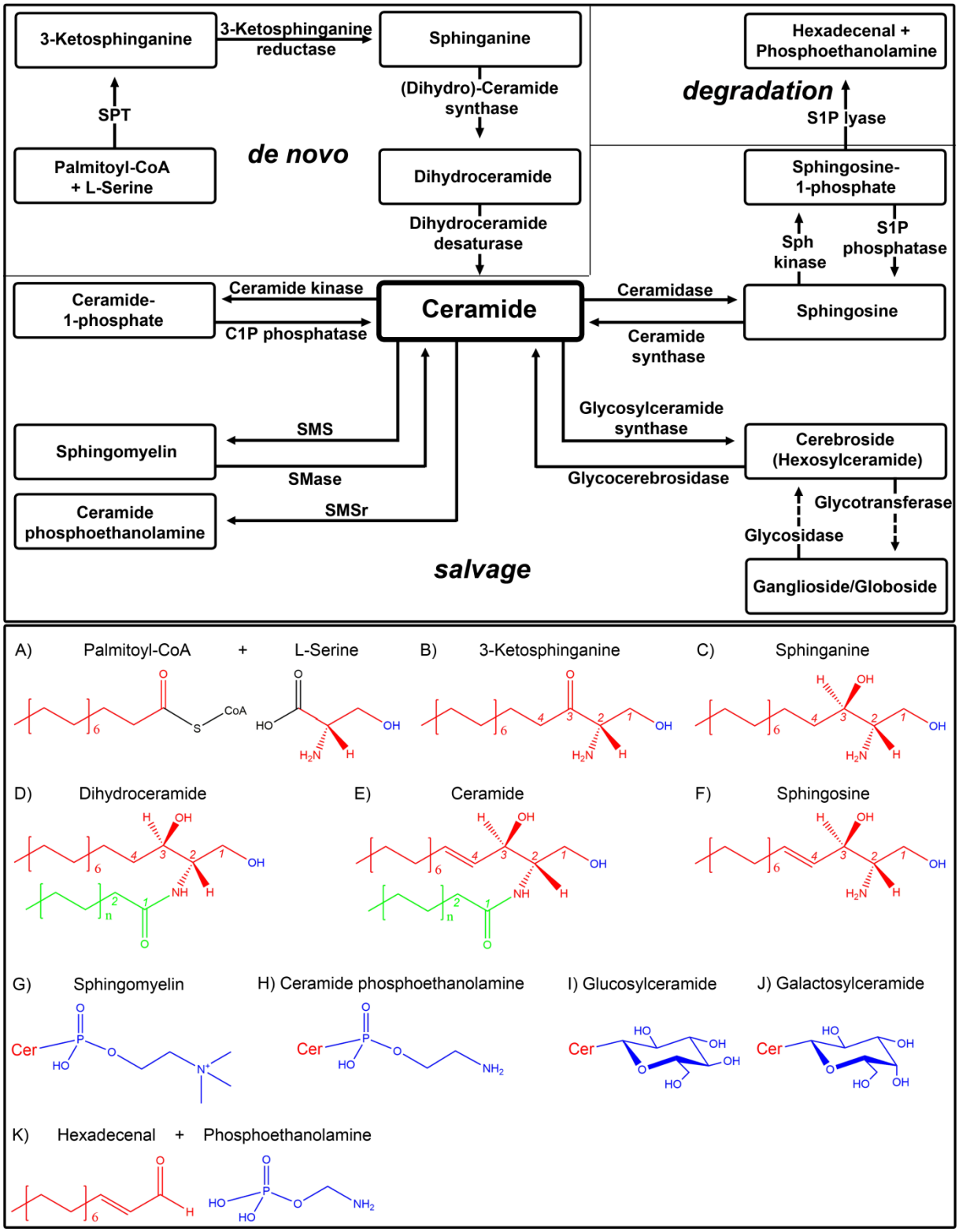

Figure 1.3 - Schematic drawing of the sphingolipid metabolic pathway. The central intermediate of the sphingolipid biosynthetic pathway is ceramide. It can either be produced through *de novo* synthesis starting with the condensation of palmitoyl-CoA and L-serine or through recycling of sphingolipids in the salvage pathway. The only exit point from the sphingolipid metabolic pathway is the degradation of sphingosine-1-phosphate to hexadecenal and phosphoethanolamine. The upper part depicts common intermediates and corresponding enzyme families of the sphingolipid metabolism (dashed lines refer to synthesis pathways involving multiple enzymes). The lower part depicts representative structures occurring during the *de novo* synthesis (A-D), the salvage pathway (E-J), or the

degradation pathway (K). Red structures depict sphingoid backbones including precursor (A) and degradation products (K), green structures depict *N*-acyl chains with n referring to any fatty acid (usually ranging from C14 to C36) and blue structures depict hydrophilic head groups. Abbreviations: Cer, ceramide; C1P, ceramide-1-phosphate; Sph, sphingosine; S1P, sphingosine-1-phosphate; SMase, sphingomyelinase; SMS, sphingomyelin synthase; SMSr, sphingomyelin synthase related protein. Molecule structures were created and modified according to the LIPID MAPS Lipidomics Gateway (http://www.lipidmaps.org/) using ChemDraw Prime 15 software (Perkin Elmer).

1.3.1.1 *De novo* sphingolipid biosynthesis

The *de novo synthesis* of ceramide (Figure 1.3, upper left part) exclusively takes place in the cytoplasmic leaflet of the ER (Tidhar & Futerman, 2013). The first and rate limiting step is the condensation of palmitoyl-CoA and L-serine (Figure 1.3 A) catalyzed by the enzyme serine palmitoyltransferase (SPT), resulting in the formation of 3-ketosphinganine (3-ketodihydrosphingosine; Figure 1.3 B) (Hanada, 2003). Alternatively, SPT can metabolize non-canonical substrates including acyl-CoAs ranging from C12 to C18, as well as L-alanine or glycine (Wei *et al.*, 2014). Moreover, alternative use of L-alanine or glycine leads to the generation of neurotoxic 1-deoxyspingolipids, which can neither be metabolized to higher order sphingolipids nor being degraded by the canonical catabolic pathway (Wei *et al.*, 2014). In the second step of the *de novo* ceramide synthesis 3-ketosphinganine is reduced to sphinganine (Figure 1.3 C) catalyzed by 3-ketosphinganine reductase (Kihara & Igarashi, 2004). By the action of (dihydro)-ceramide synthases (CerS), the primary amino group of sphinganine can be *N*-acylated with different fatty acids leading to the formation of dihydroceramide (Figure 1.3 D)(Levy & Futerman, 2010). Mammals express six different CerS isoforms (CerS1-6; see chapter 1.3.2), which are characterized by different specificities towards fatty acyl-CoAs of varying chain length (ranging from C14 to C36). The fatty acyl chains can also differ in the degree of saturation (usually saturated and less often monounsaturated) or hydroxylation. In the last step, dihydroceramide is converted to ceramide (Figure 1.3 E) by the action of dihydroceramide reductase (Fabrias *et al.*, 2012). The insertion of the 4, 5-trans-double bond is also the initial step in the production of sphingosine, which can be liberated by deacylation of ceramide as part of the salvage pathway.

1.3.1.2 The ceramide transfer protein

Synthesis of higher order sphingolipids mainly occurs at the Golgi. Therefore, newly synthesized ceramide is constantly removed from the cytosolic leaflet of the ER and transported to the Golgi. While part of the ceramide is moved by vesicular transport to the cis-medial-Golgi for glycosphingolipid synthesis (van Meer & Holthuis, 2000), most of the ceramide is specifically transported to the site of SM synthesis at the trans-Golgi by the cytosolic ceramide transfer protein (CERT)(Hanada *et al.*, 2003). CERT contains a FFAT (two phenylalanines in an acidic tract) domain, which can interact with ER resident VAP (vesicle-associated membrane protein (VAMP)-

associated protein) proteins (Loewen *et al.*, 2003) and an *N*-terminal PH (pleckstrin homology) domain, which allows the binding of phosphatidylinositol-4-phosphate (PI4P) at trans-Golgi acceptor membranes (Levine & Munro, 2002). Ceramide binding is facilitated by the *C*-terminal START (steroidogenic acute regulatory protein-related lipid transfer) domain (Hanada *et al.*, 2003). The domain preferentially binds ceramide species with acyl chain length ranging from C14 to C20, whereas the transfer of C22 and C24 species is less efficient (Kumagai *et al.*, 2005).

1.3.1.3 Biosynthesis of complex sphingolipids

The biosynthesis of higher order sphingolipids is depicted in Figure 1.3. Synthesis of the most abundant sphingolipid in mammalian cells, SM (Figure 1.3 G), is mediated by a family of phosphatidylcholine: ceramide choline phosphotransferases or SM synthases (SMS; see chapter 1.3.4), which catalyze head group transfer from PC to ceramide to produce SM and DAG at the Golgi and the plasma membrane (Villani *et al.*, 2008; Ternes *et al.*, 2009). Another member of the SMS family is the sphingomyelin synthase related protein (SMSr), which catalyzes synthesis of the SM analog ceramide phosphoethanolamine (CPE; Figure 1.3 H) in the luminal leaflet of the ER. SMSr is of central importance in the course of this thesis and will be discussed in detail in chapter 1.3.4.2.

Cerebrosides are monohexosylceramides in which either glucose or galactose is attached to ceramide via a β-glycosidic bond. Glucosylceramide (Figure 1.3 I) is synthesized by the enzyme glucosylceramide synthase (GCS) at the cytosolic surface of the cis-Golgi. Galactosylceramide (Figure 1.3 J) is produced by ceramide galactosyltransferase (CGT) in the luminal leaflet of the ER (Gault *et al.*, 2010). Glucosylceramide is the obligatory precursor for the synthesis of complex glycosphingolipids (GSLs) and its synthesis is essential for mouse development, as GCS deficient mice show embryonic lethality already on embryonic day 6.5 to 7.5. The vast majority of newly synthesized glucosylceramide at the cytoplasmic surface of cis- and medial-Golgi compartments is constantly extracted and transported to the trans-Golgi for GSL synthesis by the cytosolic lipid transfer protein FAPP2 (four phosphate adaptor protein)(D'Angelo *et al.*, 2007).

The precursor for the synthesis of complex GSLs is lactosylceramide, which is generated by attachment of a galactose residue to the glucose moiety of glucosylceramide catalyzed by β4-galactosyltransferases (Kumagai *et al.*, 2010). Complex GSLs are synthesized by a diverse set of glycotransferases that transfer a specific carbohydrate to the glycan structure of lactosylceramide (D'Angelo *et al.*, 2013). At least 12 different carbohydrate moieties can be used to produce more than 400 different glycan structures in vertebrates (Sud *et al.*, 2007). The glycan structures can contain up to 20 highly-branched sugar residues (D'Angelo *et al.*,

2013). Common residues, besides glucose and galactose, are *N*-acteylgalactosamine (GalNAc) or sialic acids e.g. *N*-acetylneuraminic acid (NANA). Globosides are characterized by GalNAc residues and like cerebrosides are neutral GSLs. Gangliosides due to integration of sialic acid moieties are acidic GSLs. GSLs together with other sphingolipids and cholesterol contribute to the establishment of membrane lipid microdomains (Simons & Sampaio, 2011).

An important intermediate in the sphingolipid metabolic pathway is sphingosine-1-phosphate (S1P). S1P is a second messenger with essential functions in cellular proliferation and growth and acts as a suppressor of ceramide induced apoptosis (Cuvillier *et al.*, 1996). The counteracting functions and the interconvertibility of ceramide and S1P with the intermediate sphingosine are commonly referred to as the 'sphingolipid rheostat', a concept of fundamental importance in cancer development (Cuvillier *et al.*, 1996; Newton *et al.*, 2015). Mammalian cells consist of two sphingosine kinases, namely SK1 and SK2, which phosphorylate the hydroxy group at C1 of free sphingosine or sphinganine. Both are cytosolic proteins, which localize to the nucleus and the plasma membrane (Wattenberg, 2010). SK function depends on peripheral membrane association in response to stimulation by various agonists e.g. growth factors (Gault *et al.*, 2010). Such stimuli can induce SK1 translocation to the plasma membrane through a PKC (protein kinase C)-dependent mechanism, leading to extracellular release of S1P (Johnson *et al.*, 2002).

Another signaling molecule that can be produced by phosphorylation of ceramide is ceramide-1-phosphate (C1P). C1P is produced by the action of ceramide kinase (CERK) in the trans-Golgi, where it enhances release of arachidonic acid, an important mediator of immune responses (Lamour *et al.*, 2007).

1.3.1.4 Sphingolipid degradation and the salvage pathway

The sphingolipid salvage pathway (Figure 1.3) represents an independent source for the generation of ceramide and is essential to prevent toxic accumulation of particular sphingolipid species. Mammalian cells have evolved counteracting catabolizing enzymes for all sphingolipid generating enzymes. Usually, most of the ceramides used for synthesis of higher order sphingolipids originate from the salvage pathway (Kitatani *et al.*, 2008). Degradation of complex sphingolipids mainly occurs in lysosomes and is strongly dependent on sphingolipid activator proteins (SAPs) at the luminal surface of intralysosomal vesicles (Schulze & Sandhoff, 2014). Several lysosomal storage diseases result from genetic defects of SAPs or sphingolipid-degrading enzymes and are known as sphingolipidoses.

GSLs are degraded by stepwise removal of monosaccharide units from the non-reducing end. According to the high complexity, a large variety of lysosomal enzymes

(glycosidases) are involved in this process. The degradation of GSLs is of special interest, as inherited defects of several enzymes are linked to sphingolipidoses (Schulze & Sandhoff, 2014). The most common sphingolipidosis is Gaucher disease, which originates from a defect in the gene for glucocerebrosidase 1 (GBA1) and is characterized by accumulation of glucosylceramide and glucosylsphingosine (Nilsson & Svennerholm, 1982). The most severe variant, Gaucher Type II is characterized by hepatosplenomegaly, neurological and skeletal disorders and premature death (Schulze & Sandhoff, 2014).

The major source for rapid ceramide generation is SM. Hydrolysis of the phosphocholine head group of SM is catalyzed by a family of sphingomyelinases (SMases). Based on their pH optimum these enzymes are subdivided into acid-, alkaline- and neutral SMases. Alkaline SMase has an exclusive function in digesting dietary SM in intestine and liver (Gault *et al.*, 2010). In contrast, acid SMase (aSMase) and neutral SMase (nSMase) are ubiquitously expressed. aSMase is predominantly localized to lysosomes, where it metabolizes SM from endosomal membranes (Gault *et al.*, 2010). Alternatively, aSMase can be secreted into the extracellular space, where it mediates the hydrolysis of SM in lipoproteins (Schissel *et al.*, 1996). Complete absence of functional aSMase causes the sphingolipidosis Niemann Pick Disease, which is characterized by neurodegeneration, hepatosplenomegaly, impaired lung function and premature death (Brady *et al.*, 1966).

Another catabolic reaction that leads to the generation of ceramide is the degradation of C1P mediated by C1P phosphatases at the plasma membrane (Gault *et al.*, 2010). Deacylation of ceramide to sphingosine is mediated by ceramidases, which are classified according to their pH optimum. Acid ceramidase (AC) is localized to lysosomes and catabolizes ceramide species originating from degradation of plasma membrane sphingolipids (Gault *et al.*, 2010). AC dysfunction leads to the sphingolipidosis Farber disease, which is characterized by early onset arthritis, swollen lymph nodes, psychomotor difficulties and vocal cord pathology (Park & Schuchman, 2006). Alkaline ceramidases (ACER1-3) localize to the ER and the Golgi (Gault *et al.*, 2010). Neutral ceramidase (NC) is a plasma membrane-associated protein that contributes to degradation of dietary ceramides in intestinal epithelial cells (Gault *et al.*, 2010).

Degradation of cytosolic S1P is mediated by ER-resident S1P phosphatases (SPPs). SPP1 was suggested to regulate the re-introduction of LCBs into ceramide at the ER (Le Stunff *et al.*, 2002). An alternative pathway of S1P degradation and at the same time the final step in sphingolipid degradation is the conversion to hexadecenal and phosphoethanolamine (Figure 1.3 K) catalyzed by S1P lyase in the cytosolic leaflet of

the ER (Ikeda *et al.*, 2004). The enzyme is also capable of catabolizing the other mammalian LCB-phosphates.

1.3.2 Ceramide synthases

The first ceramide synthase homologs were found in yeast, where it was shown that Lag1 and Lac1 are required for ceramide synthesis (Guillas *et al.*, 2001). Meanwhile, it was shown that ceramide synthase homologs exist throughout the whole animal kingdom including mammals and the model organisms *Caenorhabditis elegans*, *Drosophila melanogaster* and *Danio rerio* (Voelzmann & Bauer, 2010). The first mammalian ceramide synthase (CerS1) was identified based on its homology to the yeast Lag1 (Venkataraman *et al.*, 2002), further research revealed additional paralogs in mammals (Riebeling *et al.*, 2003). Since Lag1 (longevity assurance gene 1) was identified in a screen for longevity-related genes (D'mello *et al.*, 1994), the mammalian paralogs were originally termed longevity assurance homolog of yeast lag1 (Lass), but according to their biochemical function were renamed ceramide synthases (CerS).

The single CerS in *Drosophila* is called schlank. Schlank mutants show delayed growth, remain slim and die during larval stages (Bauer *et al.*, 2009). This is accompanied by a reduction of TAG storage in the fat body. It was shown that schlank negatively regulates expression of lipases and hence lipolysis, whereas it promotes lipogenesis through activation of SREBP (sterol-responsive element binding protein), indicating a role of CerS in the regulation of body fat metabolism.

The mammalian CerS family consists of six different members (CerS1-6). All members are ER-resident, multi-pass transmembrane proteins, most likely with six predicted transmembrane domains and both termini facing the ER lumen (Figure 1.4)(Tidhar *et al.*, 2012). CerS were also found in mitochondria and mitochondria-associated membranes (Bionda *et al.*, 2004; Siskind, 2005).

All members of the CerS family share a TLC (TRAM-Lag-CLN8) domain of approximately 200 amino acid residues, named according to its similarity to TRAM1 (translocating chain associating membrane protein) and CLN8 (ceroid-lipofuscinosis neuronal 8) proteins (Winter & Ponting, 2002). The main distinctive feature is the highly conserved 52 amino acid residues long LAG1p motif, which is essential for ceramide synthase activity (Spassieva *et al.*, 2006). Especially important are two conserved histidine residues at the cytosolic face of transmembrane domain 4.

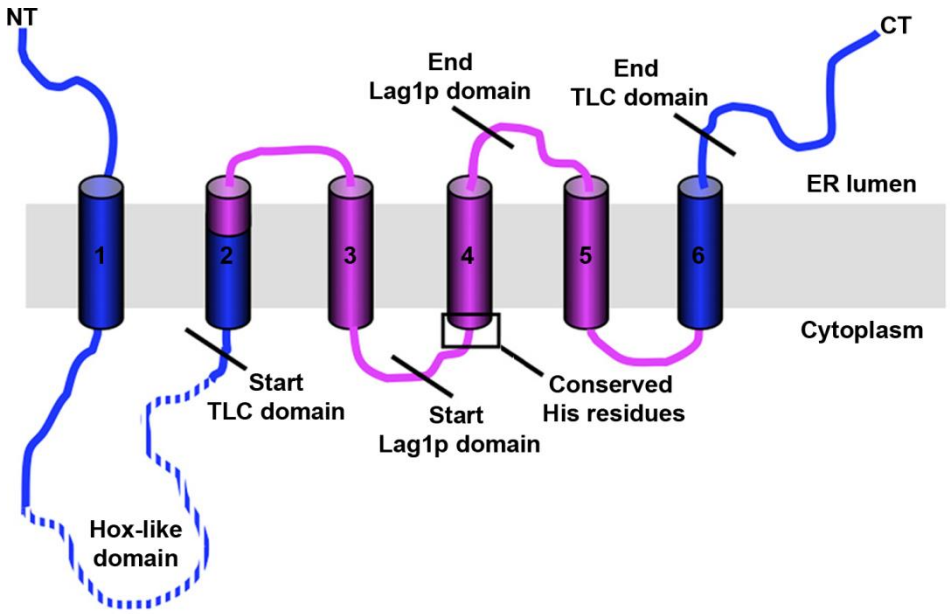

Figure 1.4 - Schematic drawing of the putative topology of CerS. Mammalian CerS most likely consist of six transmembrane domains with both termini facing the ER lumen. The Hox-like domain, present in CerS2-6, is located in the cytoplasm and followed by the TLC domain, which comprises five transmembrane domains. The Lag1p domain is located in transmembrane domain 4 with the two conserved active site histidine residues (area in the box) facing the cytoplasm. The violet part of the TLC domain refers to the 150 amino acid residues that are essential for CerS specificity. (Adopted and modified from Tidhar et al., 2012)

All CerS, except for CerS1, contain a homeobox (Hox)-like domain in the first cytoplasmic loop (Venkataraman & Futerman, 2002). Classical Hox-domains are composed of 60 amino acid residues and share a typical helix-turn-helix motif of three alpha-helices that is capable of binding specific DNA sequences. Hox-domain containing proteins act as transcription factors with essential regulatory functions in the development of bilaterian animals (Gehring *et al.*, 1994). The term Hox-like domain refers to the fact that the first 15 amino acid residues of classical Hox-domains, including a key asparagine residue that is involved in DNA binding, are missing. Therefore, it is controversly discussed whether Hox-like domains in CerS *de facto* have DNA binding capacity. However, a more recent study reported that the *Drosophila* CerS, Schlank, gets imported into the nucleus, depending on two nuclear localization signals in the Hox-like domain (Voelzmann *et al.*, 2016). Moreover, expression of catalytically inactive Schlank rescued the fat metabolism phenotype of Schlank mutant larvae. Although this points to a role of the Hox-like domain in lipid metabolism, it remains to be established whether Hox-like domains in mammalian CerS exhibit comparable functions. Furthermore, it was shown that a highly conserved region of 12 amino acid residues located *C*-terminally of the Hox-like domain, right before the TLC domain is essential for the catalytic activity of CerS5 and CerS6 (Mesika *et al.*, 2007).

1.3.2.1 Ceramide synthase expression pattern and substrate specificity

The first studies focusing on CerS expression in mice (Mizutani *et al.*, 2005, 2006; Laviad *et al.*, 2008) and humans (Levy & Futerman, 2010) were based on the analyses of mRNA levels. An overview of CerS mRNA expression in mice is presented in Figure 1.5. CerS2 shows the strongest expression of all CerS and is ubiquitously expressed with high levels in liver and kidney. CerS1 is virtually absent from most tissues, but shows strong expression in brain and skeletal muscle. CerS3 is exclusively expressed in skin and testis. CerS4-6 are ubiquitously expressed. CerS4 is strongly expressed in skin, heart, leucocytes and liver. The lowest expression levels were observed for CerS5 and CerS6. CerS5 shows the strongest expression in skeletal muscle and testis and CerS6 is strongly expressed in intestine and kidney. By the help of reporter proteins, expressed in CerS deficient mice and specific antibodies raised against most CerS proteins, the mRNA analyses were complemented. The corresponding studies revealed only minor deviations to the existing expression data and provided additional information concerning tissue specific expression (Ginkel *et al.*, 2012; Ebel *et al.*, 2013, 2014; Kremser *et al.*, 2013; Gosejacob *et al.*, 2016). For instance, CerS2 was shown to be highly expressed in lung and CerS4 besides skin, was highly expressed in spleen and lung.

All mammalian CerS have a similar K_M (Michaelis constant), and hence binding affinity, towards sphinganine (Lahiri *et al.*, 2007). In contrast, they show distinct, specificity for the acyl-CoAs used for the *N*-acylation of LCBs. According to the incorporated fatty acids, ceramides are subdivided into long chain- (C14-C20), very long chain- (C22/C24) and ultra long chain (≥C26) ceramides. CerS5 and CerS6 exhibit a specificity towards the use of C14 and C16 acyl-CoAs, additionally CerS5 was suggested to be capable of using C18 acyl-CoAs (Mizutani *et al.*, 2005; Ebel *et al.*, 2013; Gosejacob *et al.*, 2016). CerS1 exclusively uses C18 acyl-CoAs (Mizutani *et al.*, 2005; Ginkel *et al.*, 2012). The specificity of CerS4 ranges from C18-C22 acyl-CoAs (Mizutani *et al.*, 2005; Ebel *et al.*, 2014). CerS2 has a specificity towards C20-C26 acyl-CoAs (Mizutani *et al.*, 2005; Kremser *et al.*, 2013). CerS3 is capable of using very long chain and ultra long chain fatty acyl-CoAs ranging from C22-C36 (Mizutani *et al.*, 2006; Jennemann *et al.*, 2012).

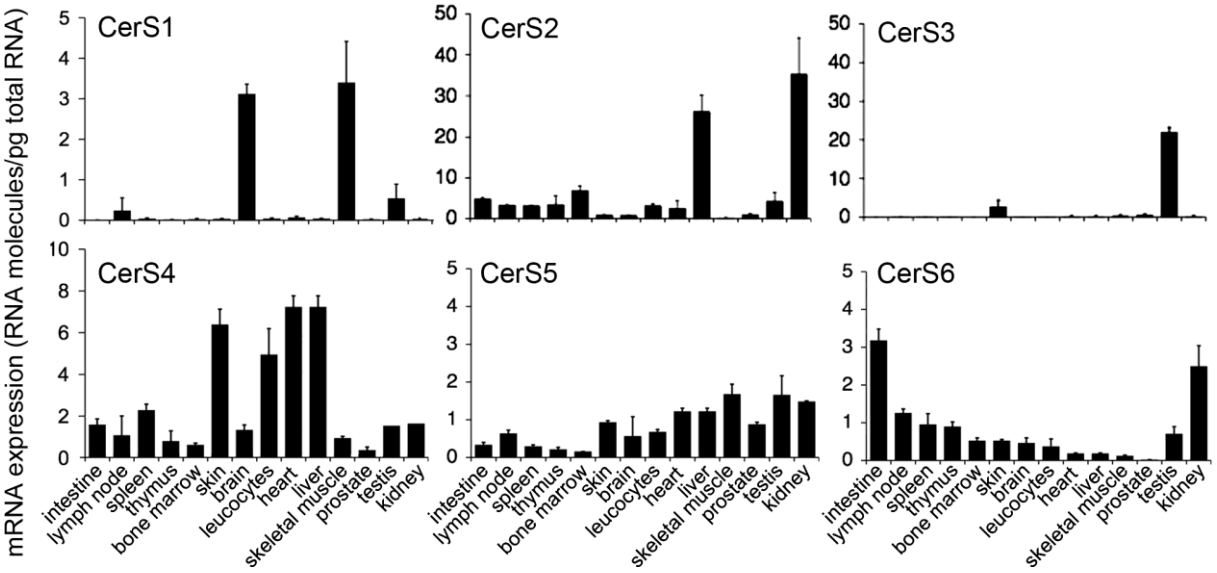

Figure 1.5 - Quantitative Real Time-PCR analysis of CerS mRNA expression in mouse tissues. CerS1 shows high expression levels in brain and skeletal muscle and is virtually absent in other tissues. CerS3 is strongly expressed in skin and testis. CerS2, 4, 5 and 6 are ubiquitously expressed. CerS2 shows the strongest expression in liver and kidney. CerS4 is predominantly expressed in skin, leucocytes, heart and liver. The highest levels of CerS5 are detected in skeletal muscle and testis. CerS6 is strongly expressed in intestine and kidney. (adopted and modified from Laviad et al., 2008)

1.3.2.2 Chain length-specific functions of ceramides

Several studies in the past have shown that ceramides with different acyl-chain length are implicated in different cellular processes, often with opposing functions (Grösch *et al.*, 2012). An overview of chain length-specific actions of ceramides in cellular processes and diseases is presented in Figure 1.6. Studies of cultured cell lines led to the general consensus that elevated levels of C16 ceramide play a decisive role in the induction of apoptosis (Eto *et al.*, 2003; Osawa *et al.*, 2005; White-Gilbertson *et al.*, 2009). However, in human head and neck squamous cell carcinomas (HNSCCs) the levels of CerS6 mRNA and C16 ceramides are increased (Karahatay *et al.*, 2007) and the CerS6-mediated production of C16 ceramide in cultured HNSCC cells prevented ER-stress induced apoptosis (Senkal *et al.*, 2010). In addition to an increase in C16 ceramide, some studies reported an increase in C24 ceramide following induction of apoptosis (Siskind *et al.*, 2002, 2010; Seumois *et al.*, 2007; Mesicek *et al.*, 2010). Nevertheless, overexpression of CerS2 in HeLa cells reduced radiation-induced apoptosis by approximately 50 % and overexpression of CerS5 promoted apoptosis (Mesicek *et al.*, 2010). Similar to that, overexpression of CerS4 and CerS6 induced apoptosis in human breast and colon cancer cell lines, which was attenuated by overexpression of CerS2 (Hartmann *et al.*, 2013). It appears that with minor exceptions long chain ceramides have anti-survival function, whereas very long chain ceramides have pro-survival function.

Attributing cellular functions to specific ceramide species is complicated, since it is often not clear whether changes in the ceramide composition are the cause or the consequence of an observed effect. This is further complicated by the fact that ceramides can be metabolized to complex sphingolipids or sphingosine.

Figure 1.6 - Overview of cellular processes, (dys)functions and diseases associated with altered levels of ceramides of differing acyl-chain length. Several diseases have been shown to be associated with changes in the ceramide composition (red). For example, disease progression in patients with Alzheimer's disease is associated with elevated C18 and C24 ceramide levels in the brain and C16 and C18 ceramide species are increased in the airway epithelium of patients suffering from cystic fibrosis. Several cancers are associated with elevation of C16 and very long chain ceramides, while C18 ceramides are decreased in HNSCC. In addition, several cellular dysfunctions have been shown to be associated with altered ceramide levels (brown). Data from CerS2 deficient mice propose a role for C22 and C24 in myelin sheath formation and motorneuron activity. Very long chain ceramides are also decreased during autophagy, while C14 and C16 ceramides and several dihydroceramide (dh) species are elevated. Experiments with cultured cells suggest pro-apoptotic and anti-proliferative roles of C16 and C18 ceramide, while C24 ceramides were shown to be rather pro-proliferative (green). It was shown that elevated levels of C16 ceramide increase membrane fluidity, while very long chain ceramides have opposing effects. C16 and C18 ceramides may specifically regulate the function of protein phosphates and kinases (blue). (adopted and modified from Grösch et al., 2012).

1.3.2.3 Ceramide synthase deficient mice

To investigate the *in vivo* function of CerS, different mouse mutants for all members of the CerS family were generated and characterized in the last years. CerS1 deficient mice suffer from cerebellar ataxia and foliation defects, as well as from Purkinje cell degeneration (Zhao *et al.*, 2011; Ginkel *et al.*, 2012). The effects are associated with decreased levels of gangliosides and myelin-associated glycoprotein (MAG) in the brain. Studies on CerS2 deficient mice reported several severe phenotypes including reduced body size, myelin sheath defects, age-related hepatocarcinomas or hepatic insulin resistance associated with depletion of very long chain ceramides and increases in C16 ceramides (Imgrund *et al.*, 2009; Pewzner-Jung *et al.*, 2010a; b; Park *et al.*, 2013a). CerS3 deficient mice show defects in the transepidermal water barrier of the skin, resulting from the loss of ultra long chain ceramides, and die shortly after birth (Jennemann *et al.*, 2012). CerS5 deficient mice are viable and fertile and show no obvious phenotypic alterations under non-challenging conditions (Gosejacob *et al.*, 2016). Analyses of steady state sphingolipid levels and ceramide synthase activity revealed decreases in C16 ceramide production in lung, spleen, muscle, liver and white adipose tissue. Also for CerS6 deficient mice, no severe phenotypic alterations were observed (Ebel *et al.*, 2013). The mice exhibited a clasping phenotype of the hind limbs and behavioral analyses revealed a habituation deficit. It was shown that CerS6 significantly contributes to the generation of C16-containing sphingolipids in kidney and small intestine. CerS2, CerS5 and CerS6 deficient mice were also investigated in the context of diet-induced obesity, the results of these studies are discussed in chapter 1.3.3.5.

1.3.2.4 Ceramide synthase 4

The mouse *cers4* gene is encoded on chromosome 8 and comprises 11 exons with the first harboring the 5’ untranslated region. The CerS4 protein consists of 393 amino acid residues and has a molecular mass of 39.3 kDa. The enzyme exhibits a specificity towards the use of acyl-CoAs ranging from C18-C22 and shows a broad tissue distribution with the highest mRNA and protein levels in skin (Mizutani *et al.*, 2005; Ebel *et al.*, 2014).

First insights for a specific function of CerS4 came from the analysis of a pancreatic β-cell line. It was suggested that CerS4-dependent increases in C18 and C22 ceramides contribute to glucolipotoxicity-induced apoptosis (Véret *et al.*, 2011). Similar to that, a study focusing on light stress-induced photoreceptor apoptosis in rats, reported increased levels of C14-C26 ceramides that were associated by an increase in CerS4, but not CerS2 mRNA levels (Chen *et al.*, 2013a). In contrast, a more recent study reported an increase in CerS4 mRNA levels in human breast cancer tissue, which was accompanied by estrogen-dependent proliferation (Wegner *et al.*, 2014). In the same line CerS4 mRNA levels were shown to be increased in

endometrial and colon cancer cells and induction of apoptosis decreased these levels (Mojakgomo *et al.*, 2015).

To investigate the *in vivo* functions of CerS4 and corresponding ceramide species, Dr. Silke Imgrund in our group generated CerS4 deficient mice. These mice were characterized by Dr. Philipp Ebel. In line with the high expression level of CerS4 in the skin, the mice displayed an age-related, progressive hair loss, altered sebum composition (including decreased levels of wax diesters) and a general decrease in C18 and C20-containing sphingolipids in the skin (Ebel *et al.*, 2014). Using newly generated, specific antibodies against CerS4, it was shown that the protein is strongly expressed in suprabasal layers of the epidermis and sebum producing sebaceous glands, which are part of the hair follicle (HF). It was shown that the sebum of CerS4 deficient mice has a significantly higher melting temperature, which might at least partially be explained by a strong decrease in the levels of 1, 2-alkane diols and wax diesters. The sebum usually supports hair growth by greasing the hair canals. Therefore, it was suggested that the solidification of the sebum leads to physical blocking of hair canals and consequently to the observed hair loss.

Later on, Peters et al. generated a mouse line for the conditional depletion of CerS4. Consistent with the previous findings, ubiquitous-, as well as epidermis-specific depletion of CerS4 led to age-related, progressive hair loss (Peters *et al.*, 2015). While HFs are characterized by constant renewal through continuous phases of growth (anagen), regression (catagen) and resting (telogen), CerS4 deficient HFs persisted in an anagen-like state at postnatal day 51 (P51) due to precocious entry of HF stem cells into growth phase. Entry into telogen and quiescence of stem cells is depending on bone morphogenetic protein (BMP), which was strongly decreased in CerS4 deficient HFs at P47. Moreover, Wnt signaling, which promotes entry into anagen was increased. The precocious activation of growth phase in HF stem cells resulted in exhaustion over time, which is probably responsible for hair loss in older mice. The study provided another example for a presumably anti-proliferative function of CerS4 and corresponding ceramide species.

Although CerS4 was shown to be broadly expressed with high levels in spleen, liver, pancreas, heart, lung and brain (Ebel *et al.*, 2014), deficient mice are fertile, show no obvious phenotypic alterations, aside from the observed skin phenotype, and have a normal life-expectancy (Ebel *et al.*, 2014; Peters *et al.*, 2015). Whether CerS4 and the corresponding ceramide species exhibit other specific functions in mice remains to be established.

1.3.2.5 Regulation of ceramide synthase activity

The mRNA expression of CerS in several tissues does not always correlate with the ceramide acyl-chain composition (Laviad *et al.*, 2008). While the ceramide composition certainly depends on substrate availability and metabolizing enzymes, it is likely that posttranscriptional mechanisms regulate protein levels or activity of CerS. A possible mechanism for the regulation of CerS activity could include dimerization of CerS. In human embryonic kidney (HEK) cells homo- and heterodimer formation of overexpressed, flag-tagged CerS was observed after cross-linking and under non-denaturing conditions (Laviad *et al.*, 2012). A more recent study showed co-immunoprecipitation of endogenous CerS1, CerS2 and CerS6 in isolated brain mitochondria (Novgorodov *et al.*, 2015). It was suggested that such interactions modulate CerS activity, e.g. co-expression of CerS2 and CerS5 increased the CerS2mediated production of C24 ceramides in HEK cells (Laviad *et al.*, 2012). In a similar fashion, C24 ceramide production was increased in a human colon carcinoma cell line after co-expression of CerS2 with CerS4 or CerS6, whereas the CerS4dependent production of C20 ceramide was slightly decreased upon co-expression with CerS6 (Hartmann *et al.*, 2013). Whether dimerization of CerS is relevant under physiological conditions is largely unexplored. Nevertheless, data from CerS deficient mice argue against dimer-dependent regulation of CerS activity *in vivo*. For instance, steady state levels and activity towards production of C24 ceramides are unaltered in the lung of CerS5- or the kidney of CerS6 deficient mice, respectively (Ebel *et al.*, 2013; Gosejacob *et al.*, 2016). Moreover, using antibodies against different CerS it was not possible to detect putative dimers according to their expected molecular size under non-denaturing conditions in cultured mouse embryonic fibroblasts (MEFs) and human embryonic kidney (HEK) cells (personal communication with Christiane Kremser).

Another mechanism could include acetylation of CerS. Studies with cerebral mitochondria revealed that CerS1, CerS2 and CerS6, but not CerS4 are acetylated and that deacetylation mediated by SIRT3 (sirtuin 3) activates ceramide synthesis (Novgorodov *et al.*, 2015). This regulatory mechanism seems to be specific to mitochondria and the physiological relevance remains to be investigated. A more recent study reported several phosphorylation sites in the *C*-terminal regions of CerS2-6 (Sassa *et al.*, 2016). *In vitro* activity assays using either membrane fractions from HEK cells overexpressing HA-tagged CerS or from mouse brain revealed that phosphorylation of these sites is casein kinase 2 (CK2) dependent and increases activity of the respective CerS, whereas phosphatase treatment reduces activity. Additionally, CerS2, CerS4, CerS5 and CerS6 have been shown to be *N*-terminally glycosylated (Mizutani *et al.*, 2005; Sassa *et al.*, 2016). The function of this glycosylation is not yet understood, but it was shown that at least the glycosylation of CerS6 is dispensable for its activity (Mizutani *et al.*, 2005).

1.3.3 Ceramides in metabolic disease

Detailed analyses of obese humans revealed that obese tissues including liver, skeletal muscle and adipose tissue are characterized by increased sphingolipid contents (Adams *et al.*, 2004; Kotronen *et al.*, 2010). Several studies investigated the correlation between sphingolipids and obesity and especially highlighted the implication of ceramides in obesity-associated metabolic diseases such as type 2 diabetes, cardiomyopathy or atherosclerosis (Hla & Dannenberg, 2012; Russo *et al.*, 2013; Choi & Snider, 2015).

1.3.3.1 Ceramides in the development of obesity and insulin resistance

Free fatty acids (FFAs) originating from dietary intake are stored in adipose tissue and can be released in the fasting state (Hajer *et al.*, 2008). Diet-induced obesity in humans and mice is characterized by an excess in FFAs, resulting from an overload of adipocytes (Russo *et al.*, 2013). This leads to increased lipolysis and release of further FFAs, which consequently accumulate in peripheral tissues including liver, skeletal muscle or pancreas. As FFAs provide additional acyl-CoAs for ceramide synthesis, the obese state is characterized by a strong increase in sphingolipid levels. Accumulation of lipids in peripheral tissues is associated with several detrimental effects, referred to as lipotoxicity (Turpin *et al.*, 2009). A direct cause is insulin resistance, a preliminary state in the development of type 2 diabetes and metabolic syndrome (Chavez & Summers, 2012). In skeletal muscle and adipose tissue, insulin stimulates uptake and storage of glucose, whereas in liver it inhibits glucose release and gluconeogenesis. Notably, ceramides antagonize insulin-stimulated glucose uptake and anabolism and a block in synthesis is insulin sensitizing and prevents several pathologies associated with insulin resistance e.g. diabetes, atherosclerosis, hepatic steatosis or cardiomyopathy (Chavez & Summers, 2012).

Insulin signaling is initiated by extracellular binding of insulin to insulin receptors (IRs), receptor tyrosine kinases that subsequently phosphorylate intracellular insulin receptor substrates (IRSs), which in turn recruit and activate several effector enzymes (White, 1998). One of the most important effector kinases is PI3K (phosphoinositide 3 kinase) (Shepherd *et al.*, 1998), which after activation mediates phosphorylation of specific phosphoinositides, as a prerequisite for the recruitment of Akt/PKB (protein kinase B) to the plasma membrane. Akt/PKB, the central mediator of anabolism is subsequently activated by PKD-mediated phosphorylation at two regulatory residues (T308 and S473) (Alessi & Cohen, 1998).

It was shown that ceramide blocks Akt/PKB activation probably by activating PKCζ, leading to phosphorylation of Akt/PKB on a regulatory site (S34) in the enzymes PH domain (Bourbon *et al.*, 2000), which prevents interaction with phosphoinositides and

hence translocation to the plasma membrane (Hajduch *et al.*, 2001; Powell *et al.*, 2003). Additional studies suggested that ceramide might stabilize interactions between Akt/PKB and PKCζ by recruiting them to membrane lipid microdomains (Fox *et al.*, 2007; Hajduch *et al.*, 2008). Moreover, an alternative mechanism was proposed in which ceramide inhibits Akt/PKB activation by mediating dephosphorylation of the regulatory residues T308 and S473 through protein phosphatase 2A (PP2A) (Zinda *et al.*, 2001; Chavez *et al.*, 2003).

Insulin resistance is often associated with mitochondrial dysfunction. Some studies suggested negative effects of ceramides or DAGs that might originate from impaired β-oxidation of fatty acids (Bruce *et al.*, 2009), others suggested that mitochondrial overload leads to incomplete β-oxidation and subsequent impairments in glucose utilization (Koves *et al.*, 2008). Interestingly, studies focusing on insulin resistance and mitochondrial dysfunction in high fat diet (HFD)-fed mice reported improved mitochondrial performance after depletion of ceramides by the SPT inhibitor myriocin (Schmitz-Peiffer, 2010; Ussher *et al.*, 2010).

1.3.3.2 Obesity-associated ceramide function in peripheral tissues

It was shown that nutrient oversupply in the liver of mice and humans leads to a strong decrease in *de novo* ceramide production, but also to secretion of ceramides and transport to peripheral tissues, which might contribute to global development of insulin resistance (Watt *et al.*, 2012). In line with that notion, a study focusing on HFD-induced obesity in mice suggested that hepatic ceramides may mediate brain insulin resistance and neurodegeneration in patients suffering from type 2 diabetes and steatohepatitis (Lyn-Cook *et al.*, 2009). The sustained uptake of FFAs together with continuous synthesis of TAGs in the obese liver at some point leads to steatohepatosis (and perhaps steatohepatitis), which contributes to hepatic insulin resistance (Deevska *et al.*, 2009). This is characterized by constitutive gluconeogenesis and consequently hyperglycemia (Bijl *et al.*, 2009). Interestingly, TAG accumulation, hyperglycemia and insulin resistance were prevented in aSMase deficient mice, in which ceramide generation from SM is impaired (Deevska *et al.*, 2009), pointing to a role of ceramide in the development these pathologies. Hyperglycemia also results from skeletal muscle insulin resistance, under these conditions translocation of glucose transporter 4 (GluT4) to the plasma membrane and hence glucose uptake is impaired (Górski *et al.*, 2002). Hyperglycemia consequently leads to hyperinsulinemia due to increased insulin production in pancreatic β-cells, which try to compensate increasing plasma glucose levels (Cavaghan *et al.*, 2000; Bijl *et al.*, 2009). At some point the pancreas loses its ability to produce insulin due to aberrant signaling and β-cell apoptosis (Hirose *et al.*, 1996; Pick *et al.*, 1998), leading to the development of type 2 diabetes. Interestingly,

palmitate-induced apoptosis in cultured β-cells can be prevented by a fumonisin B1-mediated block in *de novo* ceramide synthesis (Maedler *et al.*, 2003).

Besides liver, the most important tissue in the development of obesity and associated pathologies is adipose tissue. Aside from a decisive role in energy storage, it exhibits endocrine functions and thereby contributes to regulation of metabolic homeostasis. These regulatory functions are exerted through production and release of proinflammatory cytokines and chemokines collectively referred to as adipokines (Samad *et al.*, 2011; Freitas Lima *et al.*, 2015). One of the obesity-associated pathologies is adipose tissue inflammation, which is characterized by secretion of chemokines that mediate macrophage infiltration (Nishimura *et al.*, 2009; Ouchi *et al.*, 2011). In a similar fashion adipokines seem to be involved in the development of atherosclerosis, which is also characterized by inflammation (Zhang *et al.*, 2010). In the obese state exhausted capacity of adipocytes directly contributes to development of insulin resistance in peripheral tissues and it was suggested that adipokines are implicated in this process (Samad *et al.*, 2011; Freitas Lima *et al.*, 2015). Under normal conditions adipocytes secrete adiponectin, which is suggested to have insulin-sensitizing and cardioprotective functions, in contrast enlarged adipocytes secrete high levels of leptin and TNFα, which are associated with insulin resistance (Chavez & Summers, 2012). Leptin is usually secreted in response to dietary intake and regulates satiety. It has been shown that leptin treatment reduces ceramide levels in the hypothalamic arcuate nucleus of rats and that the decrease is important for leptins anorectic functions (Gao *et al.*, 2011). TNFα was shown to mediate accumulation of the ganglioside GM3 in membrane lipid microdomains, thereby inhibiting IR clustering (Inokuchi, 2006; Kabayama *et al.*, 2007). One of the effects of adiponectin includes activation of ceramidase activity, leading to depletion of ceramide and generation of the pro-survival factor S1P (Holland *et al.*, 2011).

1.3.3.3 Adipose tissue

Adipose tissue can be divided into white adipose tissue (WAT) and brown adipose tissue (BAT). WAT is primarily responsible for energy storage in the form of TAGs in response to dietary intake and releases fatty acids for skeletal and cardiac muscles in the fasting state. In contrast, BAT is responsible for non-shivering thermogenesis and is abundant in small mammals and especially new borns to counteract heat loss due to small body volume to surface ratio (Saely *et al.*, 2012). BAT is characterized by high expression levels of uncoupling protein 1 (UCP1), which is directly responsible for its thermogenic function. During oxidative phosphorylation a proton gradient across the inner mitochondrial membrane is established and the resulting intrinsic energy can be used to produce ATP as a universal carrier of free energy. In metabolically active BAT, UCP1 uncouples the proton gradient from ATP production,

dissipating the energy as heat, which goes along with higher oxygen consumption and an overall increase in energy expenditure (Saely *et al.*, 2012).

Originally, it was thought that white and brown adipocytes originate from a common precursor, but more recent studies suggested that brown adipocytes, similar to muscle cells, originate from Myf5 (Myogenic factor 5)-positive precursor cells (Warner & Mittag, 2015). White adipocytes are spherical, have low numbers of mitochondria and usually a single size determining lipid droplet filled with TAGs. In contrast, brown adipocytes are polygonal and similar to muscle cells characterized by a huge number of mitochondria. They rather catabolize lipids than storing them and display several small TAG containing vacuoles (Warner & Mittag, 2015).

WAT can be found in several depots throughout the whole mammalian body including subcutaneous and visceral depots (Cinti, 2012). Subcutaneous adipose tissue underneath the skin provides minor insulation and includes anterior depots at the level of the scapulae and posterior depots in the lower ventral part of the body, e.g. inguinal WAT (igWAT). Visceral adipose tissue surrounds inner organs and is closely associated to the aorta and connected vessels, it can be found in the mediastinum and especially the abdomen. The main abdominal depot is gonadal WAT (gWAT). Different WAT depots are not homogenous, especially subcutaneous and visceral depots strongly differ in their biochemical profiles (Sackmann-Sala *et al.*, 2012) and it was shown that visceral adipose tissue is significantly stronger correlated with obesity comorbidities (Booth *et al.*, 2014; Walker *et al.*, 2014).

BAT is mainly located in regions around neck and shoulders and in low amounts around kidneys, with the biggest depot being the interscapular BAT (iBAT) (Sidossis & Kajimura, 2015). While WAT continuously increases after birth, BAT already develops in midgestation, reaching its maximum size relative to body weight at birth (Gesta *et al.*, 2007). It was originally discussed that in contrast to adult rodents, no functional BAT is anymore present in adult humans (Saely *et al.*, 2012). However, meanwhile several studies reported generally high levels of functional BAT in adult humans (Nedergaard *et al.*, 2007; Virtanen *et al.*, 2009). BAT activity was shown to be induced by acute cold exposure, stimulated by the sympathetic nervous system and it negatively correlates with increased body weight (Nedergaard *et al.*, 2007; van Marken Lichtenbelt *et al.*, 2009; Virtanen *et al.*, 2009).

Intriguingly, a lot of studies reported the occurrence of brown adipocytes aside from the typical BAT depots, interspersed in WAT depots, and notably, it was shown that these cells did not originate from Myf5-positive precursor cells (Seale *et al.*, 2008). These brown-like adipocytes, referred to as beige (or brite) adipocytes could derive

from dormant precursor cells or from white to brown adipocyte transdifferentiation in a process commonly referred to as browning (Cinti, 2009; Warner & Mittag, 2015).

Adipose tissue metabolism is tightly regulated by β-adrenoceptors (β-ARs) and strongly depends on catecholamines e.g. norepinephrine or epinephrine. Activation of β-ARs usually leads to a strong increase in intracellular cAMP levels and subsequently to activation of PKA, which finally results in the activation of transcriptional regulators of metabolism or development (Kajimura & Saito, 2014). Catecholamines can be released from the sympathetic nervous system in response to stress, cold exposure or diet and for example stimulate lipolysis and release of FFAs in WAT (Collins *et al.*, 2014). They are also important mediators of BAT activation, they stimulate expression of UCP1 and oxidation of glucose and FFAs for thermogenesis and play a decisive role in browning of WAT (Warner & Mittag, 2015).

Mechanisms leading to development and activation of brown and beige adipocytes to increase whole body energy expenditure have gained particular interest as a treatment for obesity (Kim & Plutzky, 2016). Several genes implicated in browning and a large number of 'browning agents', including pharmacological substances and nutritional components, have already been identified (Bonet *et al.*, 2013; Kim & Plutzky, 2016). Understanding the mechanisms by which browning agents act and further identification of genes and possible regulators would be valuable for the development of new strategies for obesity treatment.

1.3.3.4 Ceramide in the development of diet-induced obesity in mice

Most of the studies on ceramide dependent insulin resistance focused on manipulation of cultured skeletal muscle cells, isolated myotubes or hepatocytes with exogenous palmitate or ceramide (Chavez & Summers, 2012). Meanwhile, several studies addressed the question how ceramides affect obesity-associated pathologies in rodents and collectively reported increased ceramide levels in all investigated tissues including liver, skeletal and cardiac muscle, pancreas or adipose tissue (Chavez & Summers, 2012; Choi & Snider, 2015).

Several of these studies used administration of the SPT inhibitor myriocin to block *de novo* ceramide synthesis and reported prevention of insulin resistance and diabetes (Frangioudakis *et al.*, 2010; Ussher *et al.*, 2010), atherosclerosis (Glaros *et al.*, 2008; Park *et al.*, 2008) and cardiomyopathy (Park *et al.*, 2008). Interestingly, several studies reported increased levels of complex gangliosides in adipose tissue following HFD feeding (Chavez & Summers, 2012), and it was shown that depletion of GM3, the major ganglioside precursor, protects mice from diet-induced insulin resistance (Yamashita *et al.*, 2003). Moreover, the use of glucosylceramide synthase inhibitors

in different mouse models for obesity improved insulin sensitivity and prevented from steatosis and adipose inflammation (Bijl *et al.*, 2009; van Eijk *et al.*, 2009).

1.3.3.5 Diet-induced obesity in ceramide synthase deficient mice

While the previously mentioned studies clearly indicated that ceramides and corresponding sphingolipids are involved in the pathogenesis of obesity, it remains unclear whether distinct pathologies result from a general increase or an increase in specific ceramide species. To shed more light on chain length-specific ceramide function in the development of obesity, different groups investigated diet-induced obesity in CerS deficient mice.

The first study was published by Turpin et al., and focused on CerS6 deficient mice (Turpin *et al.*, 2014). As a basis for their investigations, they reported increased levels of CerS6 mRNA and C16:0 ceramide in the adipose tissue of obese humans, in correlation with insulin resistance. CerS6 deficient mice displayed reduced levels of C16:0 ceramides in WAT, BAT and liver and were protected from HFD-induced obesity with higher insulin sensitivity and glucose tolerance. Reductions in body weight, fat content and adipocyte size correlated with increased energy expenditure and decreased leptin levels. CerS6 deficiency also prevented macrophage infiltration in WAT, but despite reduction in C16:0 ceramide levels in macrophages none of the beneficial effects upon HFD feeding were observed after conditional depletion of CerS6 in myeloid cells. Similar to ubiquitous depletion, conditional depletion of CerS6 in BAT improved overall glucose tolerance and increased energy expenditure after HFD feeding, although weight gain and body fat reduction was only minor compared to wild type littermates. Moreover, isolated brown adipocytes exhibited reduced lipid accumulation and increased β-oxidative capacity. In the liver, HFD feeding led to a general increase in ceramide levels, but the levels of C14:0 and C16:0 ceramides were strongly decreased in CerS6 deficient mice. After HFD feeding, the liver of CerS6 deficient mice displayed reduced levels of the transcription factor peroxisome proliferator-activated receptor γ (PPARγ) and transcriptional targets, which control lipid uptake and storage. Isolated hepatocytes from these mice exhibited increased palmitate oxidation. Conditional depletion of CerS6 in liver significantly improved glucose tolerance, but not insulin sensitivity and weight gain was only slightly decreased compared to wild type mice upon HFD feeding. This study demonstrated that CerS6 in iBAT and liver contributes to diet-induced obesity and glucose intolerance in mice, at least partially by affecting β-oxidation.

In line with the comparable substrate specificity, a more recent study published by Gosejacob et al., also reported protection from HFD-induced obesity in CerS5 deficient mice (Gosejacob *et al.*, 2016), including protection from glucose intolerance and insulin resistance. The study reported generally low levels of C16:0 ceramide in

liver and skeletal muscle. These levels were further decreased in CerS5 deficient mice, but not influenced by the HFD. A particular increase in C18:0 ceramide in skeletal muscle after HFD feeding was prevented in CerS5 deficient mice. In gonadal WAT (gWAT), HFD feeding led to a particular increase in C16:0 and C18:0 ceramide, which was prevented in CerS5 deficient mice. Changes in ceramide levels usually mirrored changes in SM levels, with the exception of gWAT, where no HFD-mediated increases in SM were detectable. HFD feeding revealed a strong reduction in weight gain, gWAT and adipocyte size, and circulating leptin levels of CerS5 deficient compared to wild type mice. The levels of TAGs and FFAs in the liver were decreased and signs of steatosis were only found in wild type mice fed a HFD. In line with that, several genes involved in fatty acid uptake were downregulated, whereas genes responsible for lipogenesis or oxidation were not affected. Morphological analyses of gWAT revealed crown-like structures in wild type, but not in CerS5 deficient mice after HFD feeding, indicating protection from obesity-associated gWAT inflammation, which usually contributes to the development of insulin resistance. This was confirmed by reduced expression of the pro-inflammatory cytokines TNFα (tumor necrosis factor α) and IL1β (interleukin 1β). Further analyses revealed increased expression of genes responsible for lipogenesis, but also for lipolysis, in gWAT of CerS5 deficient mice after HFD feeding. Genes responsible for β-oxidation and acylcarnitine levels were largely unaffected. This study demonstrated that CerS5 in gWAT contributes to diet-induced obesity, glucose intolerance and insulin resistance in mice, probably by promoting lipid accumulation without affecting β-oxidation.

Another study, published by Raichur at al., reported that haploinsufficiency in heterozygous CerS2gt mice increases susceptibility to HFD-induced obesity (Raichur *et al.*, 2014). Heterozygous deficiency of CerS2 (CerS2gt/+) does not lead to obvious phenotypic alterations under normal conditions. However, HFD feeding did not alter weight gain, but did severely impair liver integrity in CerS2gt/+ compared to wild type mice. This was characterized by increased weight, elevated TAG levels, and increased macrophage infiltration. Morphological analyses and increased serum levels of ALT, AST and cholesterol clearly demonstrated liver damage in HFD-fed CerS2gt/+ mice. These mice displayed glucose intolerance and insulin resistance and the ratio of body fat to lean body mass was increased. No alteration of energy expenditure was detectable, but locomotor activity was decreased. Analyses of liver sphingolipid content after HFD feeding revealed only minor decreases in very long chain (C22-C24) ceramides, glucosylceramides and SMs, but a substantial compensatory increase in the corresponding C16:0 species in CerS2gt/+ compared to wild type mice. In line with that, total sphingolipid levels were not altered, but mRNA levels of CerS5 and CerS6 were increased. Pretreatment with the SPT inhibitor myriocin protected CerS2gt/+ mice from diet-induced phenotypes, indicating that the elevation in C16 ceramides, rather than decreases in very long chain

ceramides, is responsible for the detrimental effects observed in these mice after HFD feeding. Increased levels of certain acylcarnitine species indicated incomplete lipid oxidation and isolated hepatocytes from CerS2gt/+ mice exhibited impaired β-oxidation, as well as impaired activity of the respiratory chain complexes II and IV, which was associated with reduced ATP levels. Strikingly, overexpression of CerS6 in wild type hepatocytes strongly increased C16 ceramide levels and was accompanied by TAG accumulation and disturbed insulin signaling and complex II activity. This indicated that lipid accumulation, impaired β-oxidation and steatosis in haploinsufficient CerS2gt/+ mice after HFD feeding is mediated by C16 ceramide.

All of these studies consistently indicate an important role of C16 ceramide in the development of diet-induced obesity and highlight it as a potential therapeutical target for obesity treatment. It appears that depending on the tissue, C16 ceramide can contribute to different pathologies. It remains to be investigated how C16 ceramide and possibly other ceramide species affect obesity-associated pathologies in different peripheral tissues. The involvement of three different CerS with distinct substrate specificity indicates that also other CerS could be involved in the development of diet-induced obesity. CerS3 is presumably not involved due to its specific expression in skin and testis, but according to its high expression in skeletal muscle, CerS1 could be involved. However, C18 ceramides in skeletal muscles were increased following HFD feeding, but the increase was probably mediated by CerS5 (Gosejacob *et al.*, 2016). This leaves CerS4, with its ubiquitous expression and broad substrate specificity (C18-C22), ranging between those of CerS5/6 and CerS2, as an interesting target.

1.3.4 Sphingomyelin synthase family

Biosynthesis of SM is catalyzed by a family of phosphatidylcholine: ceramide choline phosphotransferases or SM synthases (SMSs), which occurs throughout the whole animal kingdom (Tafesse *et al.*, 2006). Mammalian cells express two isoforms of SMS, the first member SMS1 resides in the Golgi, whereas the second member SMS2 resides primarily in the plasma membrane, but also in the Golgi (Villani *et al.*, 2008; Ternes *et al.*, 2009). A third member of this family is the ER-resident sphingomyelin synthase related protein (SMSr). All members share a similar membrane topology with the lipid phosphate phosphatase (LPP) superfamily including six transmembrane domains, exoplasmic *N*- and *C*-terminus and an active site facing the exoplasmic space (Figure 1.7) (Holthuis & Luberto, 2010). Responsible for the catalytic activity is a conserved domain build up by two histidine and one aspartate residues (Tafesse *et al.*, 2006; Yeang *et al.*, 2008). The conventional SMSs catalyze the transfer of a phosphocholine head group from PC to ceramide, generating SM (Figure 1.3 G) and DAG (Huitema *et al.*, 2004). In contrast, SMSr catalyzes transfer of a phosphoethanolamine head group from PE to ceramide,

generating trace amounts of the SM analog ceramide phosphoethanolamine (CPE; Figure 1.3 H) and DAG (Vacaru *et al.*, 2009). SMS2 shows a dual activity and is also capable of synthesizing CPE (Ternes *et al.*, 2009).

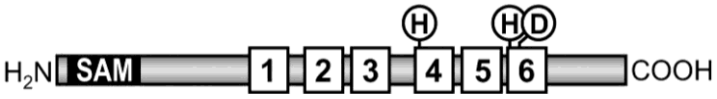

Figure 1.7 - Domain structure of the mammalian SMS family. SMS share a similar domain structure with six transmembrane domains, *N*-terminal SAM-domain and both termini and active side residues in transmembrane domains 4 and 6 directed to the exoplasmic space. (adopted and modified from Vacaru et al., 2009)

An interesting feature shared by SMSr and SMS1 is the *N*-terminal sterile α motif (SAM)-domain. SAM-domains were found in a diverse set of proteins including scaffolding proteins, regulators of transcription/translation or in Tyr- and Ser/Thr-kinases (Kim & Bowie, 2003). The SAM-domain of the *Drosophila* Smaug protein for example mediates RNA binding and is involved in post-transcriptional regulation of development (Aviv *et al.*, 2003; Green *et al.*, 2003). A broad analysis of human SAM-domains predicted a role for the SMSr SAM-domain in oligomerization (Knight *et al.*, 2011). The SAM-domain of SMSr was shown to be essential for ER retention of the protein (Vacaru *et al.*, 2009). In contrast, removal of the SAM-domain from SMS1 did not alter subcellular localization (Yeang *et al.*, 2008).

1.3.4.1 Sphingomyelin synthase 1 and 2

SMS1 and SMS2 support cell growth in certain types of cultured cancer cells (Yamaoka *et al.*, 2004; Tafesse *et al.*, 2007). It was shown that SMS1-mediated ceramide generation at the plasma membrane is critical for Fas-clustering and Fas-mediated-apoptosis (Miyaji *et al.*, 2005) and depletion of SMS1 enhanced ceramide production and apoptosis after light-induced stress (Separovic *et al.*, 2008). SMS1 deficiency in mice causes moderate neonatal lethality, reduction of body weight and fat tissue mass, and affects WAT function associated with impaired insulin secretion (Yano *et al.*, 2011, 2013). Depletion of SMS1 led to decreased SM and elevated glycosphingolipid levels in plasma, liver and macrophages, attenuated macrophage activation by NFκB (nuclear factor κ B) and MAPK (mitogen-activated protein kinase) in response to inflammatory stimuli, and transplantation of deficient macrophages to LDL (low density lipoprotein)-receptor deficient mice reduced atherosclerosis (Li *et al.*, 2012). SMS2 deficient mice display decreased SM and increased apolipoprotein E (ApoE) levels in plasma, which was reversed in mice liver-specifically overexpressing SMS2 (Liu *et al.*, 2009b). Interestingly, atherosclerotic lesions were also significantly reduced when transplanting SMS2 deficient macrophages to LDL-receptor deficient mice (Liu *et al.*, 2009a). Moreover, SMS2 deficiency increased insulin sensitivity and ameliorated HFD-induced obesity and liver steatosis (Li *et al.*, 2011; Mitsutake *et al.*, 2011), as well as lipopolysaccharide-induced lung injury

(Gowda *et al.*, 2011). Another study reported decreased expression and altered function of drug transporters in the brain of SMS2 deficient mice (Zhang *et al.*, 2011).

1.3.4.2 Sphingomyelin synthase related protein

SMSr shares a similar reaction mechanism with conventional SMSs, but uses PE instead of PC for head group transfer to ceramide, and produces trace amounts of the SM analog CPE in the ER (Vacaru *et al.*, 2009). SMSr is the best-conserved member of the SMS family and found in several organisms, e.g. *Drosophila*, which lacks SM and instead produces CPE as the major sphingolipid (Tafesse *et al.*, 2014). Although SMSr is capable of synthesizing CPE in *Drosophila*, bulk production is mediated by a Golgi-resident CPE synthase that belongs to the CDP-alcohol phosphotransferase superfamily (Vacaru *et al.*, 2013). In contrast, the levels of CPE in mammalian cells are rather low and approximately 300-fold lower than those of SM (Malgat *et al.*, 1986, 1987; Vacaru *et al.*, 2009).

The mouse *smsr* gene, also known as *samd8* (sterile alpha motif domain-containing protein 8) is located on chromosome 14 and consists of six exons. The encoded protein (mSMSr) includes 415 amino acid residues and consists of six transmembrane domains, with both termini facing the ER lumen. The *N*-terminal SAM-domain ranges from amino acid residues 12 to 78 and is located in the ER lumen, and the catalytically active amino acid residues are located in the transmembrane domains 4 (H301) and 6 (H344 and D348) at the luminal surface of the ER (Huitema *et al.*, 2004; Tafesse *et al.*, 2006).

Remarkably, siRNA-mediated downregulation of SMSr in cultured HeLa- and *Drosophila* S2-cells caused a significant increase in ER ceramide levels and led to a structural collapse of ER exit sites and fragmentation of the Golgi (Vacaru *et al.*, 2009). Since SMSr is only capable of converting trace amounts of ceramide to CPE, the ceramide accumulation cannot be explained by missing conversion. In contrast to the endogenous SMSr, catalytically inactive SMSr was not able to rescue the observed phenotypes, pointing to an essential role of SMSr catalytic activity. Based on their observations, Vacaru et al., proposed a model for a possible ceramide sensor function of SMSr (Figure 1.8)(Vacaru *et al.*, 2009). In a later study it was shown that the ceramide accumulation following acute disruption of SMSr triggers a mitochondrial pathway of apoptosis in various human carcinoma cell lines, including HeLa (Tafesse *et al.*, 2014). This was characterized by proteolytic activation of caspase-3, PARP (Poly ADP ribose polymerase) cleavage, release of cytochrome c from mitochondria to the cytosol and subsequent activation of caspase-9, an initiator caspase of mitochondrial apoptosis. Interestingly, acute disruption of SMS1 or SMS2 in HeLa cells, despite similar increases in ceramide levels did not lead to caspase and PARP cleavage, indicating that the site of ceramide accumulation is the

determining factor (Tafesse *et al.*, 2007; Vacaru *et al.*, 2009). In line with that, reduction of ER ceramide levels e.g. by targeting SMS1 to the ER or by inhibition of ceramide *de novo* synthesis prevented activation of the apoptotic machinery (Tafesse *et al.*, 2014). Suppression of ceramide accumulation and apoptosis did not solely depend on SMSr catalytic activity, but also on its SAM-domain. Overexpression of a catalytically active SMSr variant lacking the SAM-domain was not able to rescue the phenotype, even when targeted to the ER using an alternative retention signal (Tafesse *et al.*, 2014). Based on these results it was postulated that SMSr is essential in monitoring ER ceramide levels to prevent inappropriate cell death during sphingolipid synthesis (Vacaru *et al.*, 2009; Tafesse *et al.*, 2014).

While it was shown that SMSr catalytic activity is essential to prevent ceramide accumulation and apoptosis in cultured HeLa cells, not much is known about the biological function of the product CPE. In *Drosophila* it is the major sphingolipid and an essential constituent of cellular membranes (Vacaru *et al.*, 2013). It is known that at least two different enzymes are capable of producing CPE in mammals, but it remains to be established whether and how CPE influences cellular functions.

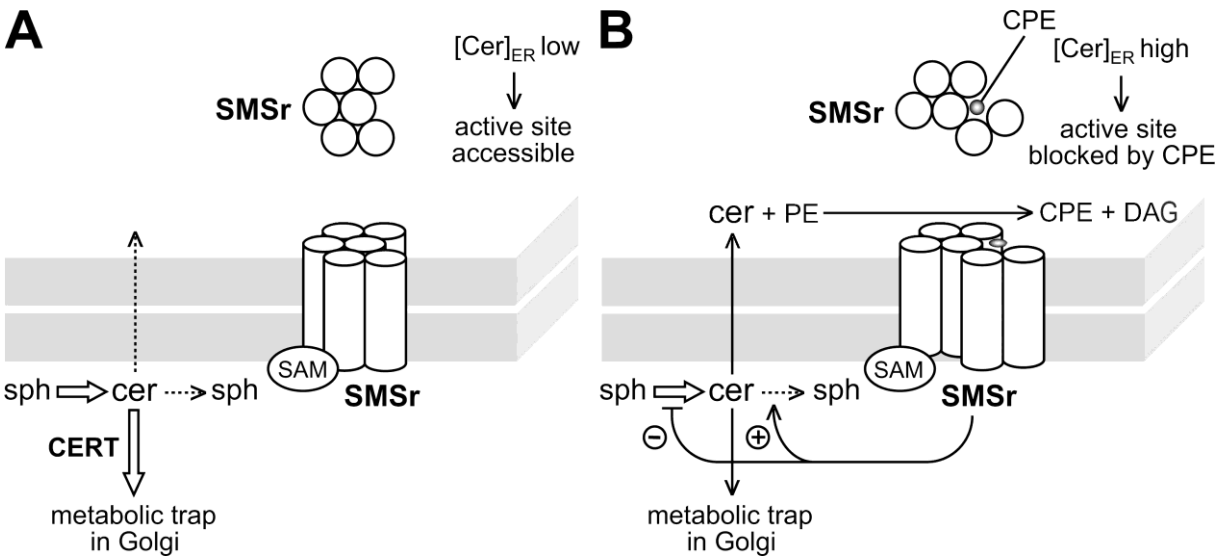

Figure 1.8 - Hypothetical model for SMSr-mediated regulation of ceramide homeostasis in the ER. (A) In the normal situation newly synthesized ceramide is constantly extracted from the cytoplasmic leaflet of the ER and transported to the Golgi by CERT. (B) At some point CERT may not be able to cope with increasing ceramide levels and ceramides reaches the luminal leaflet of the ER by transbilayer movement. This allows binding to the active site of SMSr and conversion to CPE. Due to the high affinity of CPE to the active site it remains bound, leading to a conformational change of the protein. This might initiate signaling cascades that inhibit ceramide synthesis or stimulate degradation to restore ceramide homeostasis. cer, ceramide; sph, sphingosine. (adopted from Vacaru et al., 2009)

1.4 The mouse as model organism

While cultured cells and cell free systems allow rapid manipulation and investigation of gene, protein or lipid function, it is absolutely essential to test hypotheses resulting

from such investigations *in vivo*. A valuable tool for the analyses of physiological processes in mammals is the house mouse *mus musculus*. Mice facilitate understanding of complex biological processes in mammals and according to high similarities in structure, physiology and genetics allow comparative studies with humans. Despite complex physiology mice are easy to breed, display short generation times, high number of offspring and require less effort in housing.

1.4.1 Transgenic mice

The targeted manipulation of genes is an effective means for the investigation of gene function in mice. An effective method for genetic manipulation is blastocyst injection (Bradley *et al.*, 1984). This method allows depletion of existing genes ('knock out') or introduction of modified genes ('knock in'). Specific sequences of the target gene can be manipulated by molecular cloning strategies to produce a specialized DNA plasmid that can be used as an exchange vector. The vector backbone harbors different antibiotic resistance genes for selection of bacteria and eucaryotic cells. The manipulated sequence is flanked by homology regions that allow exchange of the targeted genomic region by homologous recombination, following transfection of embryonic stem (ES) cells with the targeting vector. The manipulated region can also contain a reporter gene like eGFP (enhanced green fluorescent protein) or LacZ (β-galactosidase) to investigate expression of the target gene (Hadjantonakis *et al.*, 1999; Serebriiskii & Golemis, 2000). The reporter gene can either completely exchange the target gene, be introduced in frame with the mutated gene to produce a fusion protein or be expressed from a bicistronic transcript under control of an IRES (internal ribosomal entry site)(Attal *et al.*, 1999). Successful homologous recombination in ES cells is confirmed by PCR and Southern blot analyses. Positive ES cells are injected into isolated blastocysts at postnatal day 3.5 (P3.5) and these are implanted into pseudopregnant surrogate mothers. As the ES cells are derived from agouti-colored SV/129 mice and the blastocysts from black C57BL/6 mice, successful blastocyst injection results in chimeric offspring with mixed fur color. Germ-line transmission of the transgenic allele is confirmed by subsequent backcrossing of chimeric mice with C57BL/6 mice and PCR analyses of agouti-colored offspring. Resulting heterozygous carriers of the transgenic allele can then be used to generate homozygous animals for investigation.

1.4.2 Conditional and non-conditional systems to manipulate gene function

The easiest way to manipulate gene function is the non-conditional and hence ubiquitous depletion of a gene. However, depending on the function of the corresponding gene product this can lead to embryonic lethality or interfere with the investigation of tissue specific functions. To circumvent such problems, conditional approaches were established that allow development and cell type specific, as well as inducible modification of gene function (Rodríguez *et al.*, 2000; Feil *et al.*, 2009).

One possibility is the Cre/loxP system derived from the bacteriophage P1 (Plück, 1996; Cvetkovic & Sigmund, 2000). The basis of this system are so-called loxP (locus of crossing over in P1) sites, specific recognition sites that consist of an asymmetric 8 bp long core element that determines direction and two terminal 13 bp long palindromic sequences. LoxP sites are specifically recognized by the Cre (Causes recombination) recombinase, which mediates site-specific recombination (Figure 1.9). If a DNA sequence is surrounded by two loxP sites in identical direction, recombination leads to deletion of this region and one loxP site remains. In contrast, opposite direction of loxP sites lead to inversion of the flanked region. An alternative is the Flp/frt system from the yeast *Saccharomyces cerevisiae*, which is based on the Flp (flippase) recombinase and frt (flippase recognition target) sites in a recombination mechanism analogous to the Cre/loxP system (Rodríguez *et al.*, 2000). To manipulate gene function in mice, target sequences on the exchange vector can be flanked by recognition sites and the respective recombinases can be expressed under control of specific promoters, which allows development or cell type-specific depletion of the target sequence.

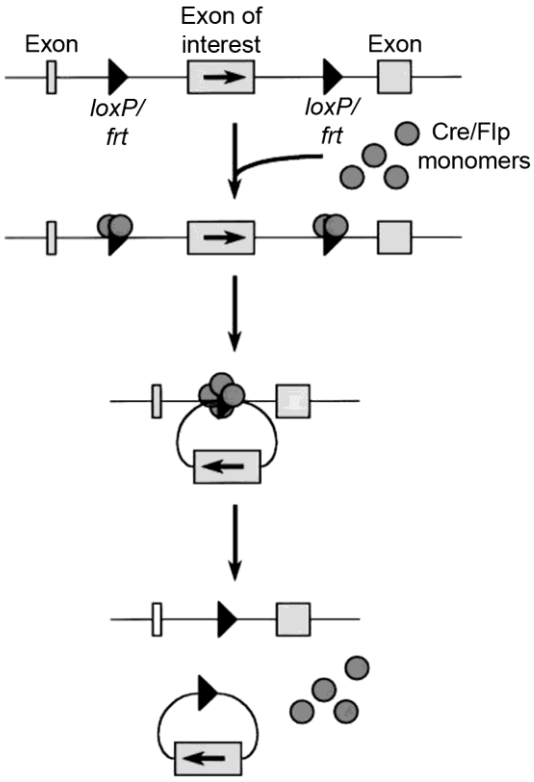

Figure 1.9 - Schematic illustration of the recombination mechanism mediated by Cre and Flp recombinase. Sequence deletion requires flanking of the targeted sequence by two loxP/frt sites in the same direction. Direction is determined by the 8 bp asymmetric core element and the terminal 13 bp palindromic sequences mediate binding of Cre/Flp recombinase monomers. The initial step requires dimerization at each loxP/frt site, before recombination is mediated by tetramer formation. The flanked sequence is irreversibly excised and released as a covalent ring structure and one loxP/frt site remains in the excision locus. (adopted and modified from Cvetkovic & Sigmund, 2000)

1.5 Aim of the study

It was shown that acute depletion of SMSr function in cultured HeLa cells leads to ceramide accumulation in the ER and disruption of ER exit sites and Golgi stack morphology (Vacaru *et al.*, 2009). Based on these results it was postulated that SMSr is an essential regulator of ceramide homeostasis (Vacaru *et al.*, 2009). To test this hypothesis it was aimed to deplete SMSr catalytic activity in mice, as in contrast to functional SMSr, the catalytically inactive SMSrD348E failed to rescue the phenotype in HeLa cells (Vacaru *et al.*, 2009). In the initial mouse line this was accomplished by introducing the SMSrD348E point mutation (Ginkel, 2013). In expectance of potential embryonic lethality a conditional mouse line was established for specific depletion of SMSr exon 6, encoding two catalytically essential amino acids (Bickert, 2011). As SMSrD348E mice were born in a Mendelian ratio, exon 6 was ubiquitously depleted. The SMSrdelEx6 mice express an $SMSr^{NT}$-eGFP fusion protein and were used to verify the specificity of newly generated antibodies targeting the SMSr *C*-terminus. The antibodies were used to determine the tissue specific expression pattern of SMSr in mice. SMSrD348E mice were bred with SMS2gt mice (Liu *et al.*, 2009b) and together with wild type and single mutant mice were subjected to mass spectrometric analyses to investigate the impact of SMSr and SMS2 on distribution and abundance of CPE (and SM) in ten different tissues. The analyses also included determination of ceramide and hexosylceramide contents to see whether depletion of SMSr catalytic activity affects ceramide metabolism. Moreover, integrity of brain, liver and kidney cells in SMSrD348E mice was investigated by electron microscopy.

The implication of ceramides in the development of diet-induced obesity has long been proposed (Chavez & Summers, 2012). However, data from *in vivo* systems are scarce. Prior to starting this project, high fat diet-induced obesity was investigated in heterozygous CerS2gt and CerS6 deficient mice (Raichur *et al.*, 2014; Turpin *et al.*, 2014), followed recently by CerS5 deficient mice (Gosejacob *et al.*, 2016). Depletion of CerS5 and CerS6 protected from diet-induced obesity associated by increased β-oxidation in liver and iBAT, or by decreased lipid accumulation in WAT, respectively. In contrast, heterozygous depletion of CerS2 increased susceptibility, associated by disturbed β-oxidation in liver. The data suggest that C16 ceramide is responsible for the observed phenotypes, as it was decreased in the respective tissues of CerS5 and CerS6 deficient mice and increased in heterozygous CerS2gt mice. To investigate the function of CerS4 and the corresponding ceramide species, CerS4 deficient mice were fed a high fat diet for 16 weeks. Food intake and weight gain were measured once a week and glucose and insulin tolerance was determined before and after the experiment. After the experiment, the sphingolipid contents were quantified by mass spectrometry and CerS and insulin receptor expression was investigated in liver, pancreas and iBAT. In addition, energy expenditure and adipose tissue development were investigated in 5 week old CerS4 deficient mice.

2 Material

Materials used for this thesis, including chemicals, buffers, media, accessories, supplies and devices, unless explicitly mentioned in this section were already described before (Bickert, 2011; Ginkel, 2013; Ebel, 2014).

2.1 Antibodies

Primary antibodies

Antibodies	Host	Dilution	Company/Reference
anti-calnexin	rabbit	1:200	Abcam
anti-CerS2	rabbit	1:750	(Kremser *et al.*, 2013)
anti-CerS4	rabbit	1:300	(Ebel *et al.*, 2014)
anti-CerS5	sheep	1:2000	(Gosejacob *et al.*, 2016)
anti-CerS6	mouse	1:500	Santa Cruz Biotechnology
anti-GAPDH	mouse	1:10000	Millipore
anti-IRβ	mouse	1:500	Thermo scientific
anti-SMSr	rabbit	1:1000	(Ginkel, 2013; Bickert *et al.*, 2015; this study)
anti-V5	mouse	1:1000	Invitrogen

Secondary antibodies

Antibodies	Host	Dilution	Company/Reference
anti-mouse (HRP conjugated)	goat	1:10000	Dianova
anti-rabbit (HRP conjugated)	goat	1:10000	Dianova
anti-sheep (HRP conjugated)	goat	1:20000	Dianova

All antibodies were used in immunoblot analyses. HRP - horseradish peroxidase

2.2 Primer

All oligonucleotides were ordered from MWG Eurofins and diluted to 100 pmol/µl.

Primer	Sequence 5'→3'	Binding region	Application
SMSr_1 (forward)	GAA ACT ACG ACG GGC ATT	SMSr; exon 5	SMSrD348E PCR
SMSr_2b (forward)	GGC TAA CTG AAA CAC GGA AGG	SMSr; neomycin cassette in intron 5	
SMSr_3b (reverse)	TTC AGC TCT GTC TCA TGT GGC	SMSr; intron 5, downstream of neomycin cassette	

SMSr_loxP_for (forward)	AGC TCT GGT AAT TCT CTG GGC	SMSr; intron 4, upstream of 5' loxP site	SMSrdelEx6 PCR
SMSr_loxP_rev (reverse)	TCT CAC TTC CTC CCT AGT TCC	SMSr; intron 5	
SMSr_eGFP_rev (reverse)	AAG TCG TGC TGC TTC ATG TGG	SMSr; eGFP	
SMS2_WT_FP (forward)	GTG GCG GAC AAT GGA TAT CA	SMS2; exon 2, upstream of gene trap insertion site	SMS2gt PCR
SMS2_KO_FP (forward)	GGT GGA TGT GGA ATG TGT GC	SMS2; neomycin cassette in exon 2	
SMS2_WT&KO_RP (reverse)	TAC GGA CAA AAG GTG GTG AG	SMS2; exon 2, downstream of gene trap insertion site	
CerS4_E11_for (forward)	CCA CAG CTG AAG AAT GGG ATG G	CerS4; exon 11	$CerS4^{-/-}$ PCR
CerS4_LacZ_ 3'HR_for (forward)	TCA GTA TCG GCG GAA TTC CAG C	Cers4; LacZ upstream of 3' homology region	
CerS4_ 3'HR_rev (reverse)	CTC TGG CGC AGA GAA TTC ATC G	CerS4; 3'homology region	
Pgk1_for (forward)	GCT GTT CTC CTC TTC CTC ATC TCC	Pgk promoter	PGK-Cre PCR
Int-Cre_rev (reverse)	TCC ATG AGT GAA CGA ACC TGG TCG	Cre-recombinase coding region	
USP_Flp (forward)	TAA GGT CCT GGT TCG TCA GTT TGT GG	Flp-recombinase coding region	Flp PCR
DSP_Flp (reverse)	GTG ATA TTA TCC CAT TCC ATG CGG GG	Flp-recombinase coding region	
5' probe_for (forward)	AGA GGT GAT GCA TTC CTT GG	SMSr; upstream of 5' homology region	External SMSrdelEx6 5' probe
5' probe_rev (reverse)	TGA ACT TCA CTA CGA CCT CG	SMSr; upstream of 5' homology region	

2.2.1 Primer Real Time-PCR

Primer	Sequence 5'→3'	Target gene
aP2 forward	TGA AAG AAG TGG GAG TGG GCT TTG C	aP2
aP2 reverse	CAC CAC CAG CTT GTC ACC ATC TCG T	
Cidea forward	ATT TAA GAG ACG CGG CTT TGG GAC A	CIDEA
Cidea reverse	TTT GGT TGC TTG CAG ACT GGG ACA T	
HPRT forward	ACA TTG TGG CCC TCT GTG TGC TCA	HPRT
HPRT reverse	CTG GCA ACA TCA ACA GGA CTC CTC GT	
PGC1α forward	GCA CAC ACC GCA ATT CTC CCT TGT A	PGC1α
PGC1α reverse	ACG CTG TCC CAT GAG GTA TTG ACC A	
PPARγ2 forward	TCC GTA GAA GCC GTG CAA GAG ATC A	PPARγ
PPARγ2 reverse	CAG CAG GTT GTC TTG GAT GTC CTC G	
UCP1 forward	GGT GAA CCC GAC AAC TTC CGA AGT G	UCP1
UCP1 reverse	GGG TCG TCC CTT TCC AAA GTG TTG A	

2.3 Southern blot probes

Probe	Description/Binding region
External SMSrdelEx6 5' probe	513 bp PCR fragment amplified from BAC-DNA (see 2.4)/binds upstream of 5' homology region
Internal SMSrdelEx6 probe	969 bp *Hinc*II/*Xba*I fragment from pDTA+Ex5+3'HR (Bickert, 2011)/binds in 3' homology region

2.4 Bacterial artificial chromosomes

BAC	Library	Description	Source
BMQ-369P9	129S7Ab2.2	comprises the genomic sequence of SMSr	Sanger institute

2.5 Plasmids

Plasmid	Description	Company
pYES2.1/V5-His-TOPO	yeast expression vector	Invitrogen
pADTrack-CMV	shuttle vector for adenovirus generation	Addgene
pADEasy-1	adenoviral vector	Addgene

2.6 Adeno- and lentiviruses

Virus	Description	Reference
Ad. GFP	adenovirus expressing GFP	Dr. Rene Jacobs (Edmonton)
Ad. PEMT	adenovirus expressing phosphatidylethanolamine *N*-methyltransferase and GFP	Dr. Rene Jacobs (Edmonton)
rrl156-PGK-Tag	lentivirus expressing the SV40 T large antigen for cell immortalization	Prof. Alexander Pfeifer (Bonn)

2.7 Primary and immortalized cells

Cells	Description	Reference
HM1 ES cells (wild type)	mouse embryonic stem cells derived from mouse strain Sv129P2/OlaHsd	(Magin *et al.*, 1992)
HM1 ES cells (SMSrD348E)	HM1 cells heterozygous for SMSrD348E allele	(Ginkel, 2013)
BMDM (wild type)	bone marrow derived macrophages from C57BL/6 mice	this thesis
BMDM (SMSrdelEx6)	bone marrow derived macrophages from SMSrdelEx6 mice	this thesis
MEF (wild type)	mouse embryonic fibroblasts derived from embryos (ED 10.5) of C57BL/6 mice	this thesis
MEF (SMSrD348E)	mouse embryonic fibroblasts derived from embryos (ED 10.5) of SMSrD348E mice	this thesis
MEF (SMSrdelEx6)	mouse embryonic fibroblasts derived from embryos (ED 10.5) of SMSrdelEx6 mice	this thesis
IAY11 yeast cells	*S. cerevisiae* yeast strain	(Huitema *et al.*, 2004)
IAY11 yeast cells (empty vector)	IAY11 cells transfected with pYES2.1/V5-His-TOPO expression vector	(Vacaru *et al.*, 2009)
IAY11 yeast cells (mSMSr-V5)	IAY11 cells transfected with pYES2.1/V5-His-TOPO expression vector harboring cDNA of murine SMSr	Prof. Joost Holthuis (Osnabrück)
IAY11 yeast cells (hSMSr-V5)	IAY11 cells transfected with pYES2.1/V5-His-TOPO expression vector harboring cDNA of human SMSr	(Vacaru *et al.*, 2009)

4Δ.Lass5 yeast cells	*S. cerevisiae* yeast strain expressing murine CerS5 cDNA instead of endogenous ceramide synthases	(Cerantola *et al.*, 2007)
4Δ.Lass5 yeast cells (mSMSr-V5)	4Δ.Lass5 yeast cells transfected with pYES2.1/V5-His-TOPO expression vector harboring cDNA of murine SMSr	Prof. Joost Holthuis (Osnabrück)
Brown adipocytes (wild type)	immortalized mature brown adipocytes differentiated from iBAT preadipocytes of new born C57BL/6 mice	this thesis
Brown adipocytes (CerS4$^{-/-}$)	immortalized mature brown adipocytes differentiated from iBAT preadipocytes of new born CerS4$^{-/-}$ mice	this thesis
White adipocytes (wild type)	mature white adipocytes differentiated from igWAT preadipocytes of 5 week old C57BL/6 mice	this thesis
White adipocytes (CerS4$^{-/-}$)	mature white adipocytes differentiated from igWAT preadipocytes of 5 week old CerS4$^{-/-}$ mice	this thesis

2.8 Transgenic mouse lines

Mouse line	Description	Reference
SMSrD348E	Insertion of point mutation D348E and NLS-lacZ reporter cDNA	(Ginkel, 2013; Bickert *et al.*, 2015; this study)
SMSrflox	Insertion of loxP sites flanking exon 5 and 6 for conditional exchange by an exon 5-eGFP fusion sequence	(Bickert, 2011; Bickert *et al.*, 2015; this study)
SMSrdelEx6	Exchange of exon 5 and 6 by an exon 5-eGFP fusion sequence	(Bickert, 2011; Bickert *et al.*, 2015; this study)
SMS2gt	Exchange of exon 2 (including translation initiation codon) by neomycin cassette	(Liu *et al.*, 2009b)
PEMT$^{-/-}$	Exchange of exon 2 (including translation initiation codon) by neomycin cassette	(Walkey *et al.*, 1997)
Deleter-Flp	Ubiquitous expression of Flp-recombinase under control of the human β-actin promoter	(Rodríguez *et al.*, 2000)
Pgk-Cre	Ubiquitous expression of Cre-recombinase under control of the pgk promoter	(Lallemand *et al.*, 1998)
CerS4$^{-/-}$	Exchange of the whole coding region of the *cers*4 gene by NLS-lacZ cDNA	(Imgrund, 2011; Ebel, 2014; Ebel *et al.*, 2014)

All mouse lines were in a C57BL/6 background (at least 87.5 %).

2.9 Lipid standards

All lipid standards were ordered from Avanti polar lipids, except for NBD-GlcCer (Matreya) and NBD-CPE (generous gift of P. Devaux from Institut de Biologie Physico-Chimique, Paris).

Lipid standard	Chain length	Application
Ceramide (Cer)	d18:1-12:0	MS (Dörmann)
	d18:1-h12:0	MS (Dörmann)
	d18:1-17:0	MS (Dörmann/Somerharju)
Ceramide phosphoethanolamine (CPE)	d18:1-17:0	MS (Somerharju)
Sphingomyelin (SM)	d18:1-12:0	MS (Dörmann)
	d18:1-17:0	MS (Dörmann)
	d18:1-15:0	MS (Somerharju)
Hexosylceramide (HexCer)	Glc-d18:1-12:0	MS (Dörmann)
	Gal-d18:1-24:1	MS (Dörmann)
	Gal-d18:1-15:0	MS (Somerharju)
Long chain bases (LCBs)	d17:1	MS (Dörmann)
	d16:0	MS (Dörmann)
	d20:0	MS (Dörmann)
Phosphatidylcholine (PC)	di20:1	MS (Somerharju)
Phosphatidylethanolamine (PE)	di22:1	MS (Somerharju)
Phosphatidylinositol (PI)	di16:0	MS (Somerharju)
Phosphatidylserine (PS)	di14:1	MS (Somerharju)
NBD-Ceramide	d18:1-6:0	TLC
NBD-CPE	d18:1-6:0	TLC
NBD-GlcCer	d18:1-6:0	TLC
NBD-SM	d18:1-6:0	TLC
Cholesterol (Chol)		TLC
Diacylglycerol (DAG)		TLC
Triacylglycerol (TAG)		TLC

d refers to two hydroxy groups in the sphingoid backbone; h refers to a hydroxylated fatty acyl chain; Gal - galactose; Glc - glucose

2.10 Buffers

Buffer R	20 mM	HEPES-KOH (pH 7.2)
	15 mM	KCl
	5 mM	NaCl
	250 mM	Sucrose
	1 mM	PMSF
	0.1 % (v/v)	PIC

PMSF (phenylmethanesulfonylfluoride; 200 x stock 34,8 mg/ml in isopropanol) and PIC (protease inhibitor cocktail; 1000 x stock in DMSO containing 1 mg/ml aprotinin, 1 mg/ml leupeptin, 1 mg/ml pepstatin, 5 mg/ml antipain, 157 mg/ml benzamidine) were added right before use.

Modified RIPA buffer	150 mM	NaCl
(pH 7.4)	50 mM	Tris-HCl
	1 mM	EDTA
	1 mM	NaF
	1 % (v/v)	NP-40
	0.25 % (w/v)	Na-deoxycholate
	1 mM	PMSF
	1 tablet/ml	Complete® (Roche)

Buffer was autoclaved and PMSF and Complete® protease inhibitor cocktail were added right before use.

2.11 Cell culture media

All media and supplements were cell culture grade or stock solutions were autoclaved/sterile filtered before use.

DMEM(+)		DMEM (Dulbecco's Modified Eagle Medium)-GlutaMAX; 4500 mg/L glucose; Gibco)
	10 %	Fetal calf serum (FCS)
	1 %	Penicillin/Streptomycin (P/S)

For brown adipocytes (B) DMEM with pyruvate and for white adipocytes (W) DMEM without pyruvate was used.

Collagenase digestion buffer-B	123 mM	NaCl
(pH 7.4)	5 mM	KCl
	1.3 mM	CaCl
	100 mM	HEPES
	5 mM	Glucose
	1.5 % (w/v)	BSA (Bovine serum albumin)
	0.2 % (w/v)	Collagenase type II (Worthington)
Culture medium-B		DMEM(+)
	10 nM	HEPES
	4 nM	Insulin (Sigma)
	4 nM	Triiodothyronine (T3; Sigma)
	25 µg/ml	L-Ascorbat (Sigma)
Differentiation medium-B		DMEM(+)
	20 nM	Insulin
	1 nM	T3
Induction medium-B		Differentiation medium-B
	500 µM	Isobutylmethylxanthine (Sigma)
	1 µM	Dexamethasone (Sigma)
Collagenase digestion buffer-W		DMEM
	0.5 % (w/v)	BSA
	0.15 % (w/v)	Collagenase type II

Maintenance medium-W		DMEM
	5 %	FCS
	1 %	P/S
	1 µg/ml	Insulin
	1 nM	T3
	0.1 %	ABP

ABP: 50 mg/ml L-ascorbate, 1 mM d-biotin and 17 mM pantothenate (all Sigma)

Induction medium-W		Maintenance medium-W
	500 µM	Isobutylmethylxanthine
	0.25 µM	Dexamethasone

3 Methods

Applied methods that are not explicitly mentioned in this section were conducted as described before (Bickert, 2011; Ginkel, 2013; Ebel, 2014).

3.1 Nucleic acid analysis

3.1.1 Mouse genotyping

Genotyping of transgenic mice was performed by PCR. Reaction mixtures and programs are listed in tables below. Concentrations were as follows: $MgCl_2$ (25 mM), primer (0.1 mM), dNTPs (10 mM each), GoTaq-Polymerase (5 U/µl; Promega). Expected fragment sizes for the respective alleles are indicated below the corresponding tables.

SMSrD348E genotyping PCR:

Components	Volume
Go-Taq buffer (5x)	5 µl
$MgCl_2$	1 µl
dNTPs	0.5 µl
Primer: SMSr_1	0.2 µl
Primer: SMSr_2b	0.2 µl
Primer: SMSr_3b	0.2 µl
H_20	16.7 µl
Go-Taq polymerase	0.2 µl
DNA	1 µl

Temperature	Time	Cycles
95°C	5 min	1
95°C	45 s	35
65°C	45 s	
72°C	45 s	
72°C	10 min	1

Fragment sizes: SMSr wild type allele, 393 bp; SMSrD348E allele, 580 bp, SMSrD348ENeo allele, 493 bp.

SMSrflox genotyping PCR:

Components	Volume
Go-Taq buffer (5x)	5 µl
$MgCl_2$	1 µl
DMSO	0.5 µl
dNTPs	0.5 µl
Primer: SMSr_loxP_for	0.2 µl
Primer: SMSr_loxP_rev	0.2 µl
Primer: SMSr_eGFP_rev	0.2 µl
H_20	16.2 µl
Go-Taq polymerase	0.2 µl
DNA	1 µl

Temperature	Time	Cycles
95°C	5 min	1
95°C	45 s	35
56°C	45 s	
72°C	60 s	
72°C	10 min	1

Fragment sizes: SMSr wild type allele, 386 bp; SMSrflox allele, 451 bp; SMSrdelEx6 allele, 707 bp.

SMS2gt genotyping PCR:

Components	Volume
Go-Taq buffer (5x)	5 µl
$MgCl_2$	1.5 µl
dNTPs	0.5 µl
Primer: SMSr_loxP_for	0.2 µl
Primer: SMSr_loxP_rev	0.2 µl
Primer: SMSr_eGFP_rev	0.2 µl
H_20	16.2 µl
Go-Taq polymerase	0.2 µl
DNA	1 µl

Temperature	Time	Cycles
94°C	5 min	1
94°C	60 s	30
58°C	60 s	
72°C	60 s	
72°C	7 min	1

Fragment sizes: SMS2 wild type allele, 252 bp; SMSgt allele, 354 bp.

CerS4 genotyping PCR:

Components	Volume
Go-Taq buffer (5x)	5 µl
$MgCl_2$	1 µl
dNTPs	0.2 µl
Primer: CerS4_E11_for	0.2 µl
Primer: CerS4_LacZ_3'HR_for	0.2 µl
Primer: CerS4_3'HR_rev	0.4 µl
H_20	16.8 µl
Go-Taq polymerase	0.2 µl
DNA	1 µl

Temperature	Time	Cycles
95°C	5 min	1
95°C	60 s	35
65°C	60 s	
72°C	60 s	
72°C	10 min	1

Fragment sizes: CerS4 wild type allele, 400 bp; $CerS4^{-/-}$ allele, 539 bp.

Flp genotyping PCR:

Components	Volume
Go-Taq buffer (5x)	5 µl
$MgCl_2$	2 µl
dNTPs	1 µl
Primer: USP_Flp	0.2 µl
Primer: DSP_Flp	0.2 µl
H_20	15.25 µl
Go-Taq polymerase	0.25 µl
DNA	1 µl

Temperature	Time	Cycles
96°C	5 min	1
95°C	60 s	34
58°C	60 s	
72°C	90 s	
72°C	10 min	1

Fragment size: Flp recombinase allele, 1200 bp.

Pgk-Cre genotyping PCR:

Components	Volume
Go-Taq buffer (5x)	5 µl
$MgCl_2$	2 µl
dNTPs	0.2 µl
Primer: Pgk1_for	0.2 µl
Primer: Int-Cre_rev	0.2 µl
H_20	16.3 µl
Go-Taq polymerase	0.1 µl
DNA	1 µl

Temperature	Time	Cycles
94°C	5 min	1
94°C	30 s	35
60°C	50 s	
72°C	90 s	
72°C	10 min	1

Fragment size: Pgk-Cre recombinase allele, 500 bp.

3.1.2 Southern blot analysis

Southern blot analysis was performed as already described previously (Bickert, 2011). For analysis of SMSrdelEx6 mice, genomic DNA from livers of homozygous, heterozygous and wild type mice was extracted and digested with *Xmn*I. After electrophoretic separation DNA was transferred to Hybond-N^+-membranes (Amersham Biosciences) and cross-linked by UV light exposure. External and internal probe (see chapter 2.3) were radioactively labeled with α-^{32}P-dCTP (Hartmann Analytik) and incubated with the membrane in QuickHyb solution (Stratagene) at 68°C for 2 h.

3.1.3 Real Time-PCR analysis

For quantitative Real Time (RT)-PCR analysis, total RNA from cultured adipocytes was isolated using Trizol® (Invitrogen) according to the manufacturer's instructions. For reverse transcription of RNA to complementary DNA (cDNA) the Transcriptor First Strand Synthesis Kit (Roche) was used according to the manufacturer's instructions. PCR was done with SYBR-Green (Roche) using a HT7900 FAST Real Time-PCR system (Applied Biosystems). Fold changes were calculated using relative quantification methods (ΔΔCt algorithm). HPRT (hypoxanthine guanine phosphoribosyl transferase) served as internal control. Primer sequences are listed in chapter 2.2.1.

3.2 Protein analysis

3.2.1 Affinity chromatography of antisera

For the generation of polyclonal antibodies targeting the SMSr protein, rabbits were immunized with an internal peptide (CWPFSKPAIMKRLIG) and a *C*-terminal peptide (CDGPIPDLSSDQYQY) of the mouse SMSr protein. Peptides were synthesized by Prof. Marten Egmond (Utrecht) and Pineda Antibody Service (Berlin) was responsible for immunization. For affinity chromatography of rabbit antisera two *N*-hydroxysuccinimide columns were loaded with the internal or the *C*-terminal

peptide, respectively (Ginkel, 2013). Antibody purification was essentially done as previously described (Ginkel, 2013), using either the column with the internal peptide or the column with the *C*-terminal peptide. Antibodies were eluted with 0.2 M glycine (pH 3) and collected in tubes with 0.5 ml 1 M Tris (pH 7.25) per 2 ml eluate.

3.2.2 Immunoblot analysis

For immunoblot analyses mouse tissues were homogenized in 1 ml/g wet weight of modified RIPA buffer using a Precellys® homogenizer (Peqlab Biotechnology). Cell debris was removed by centrifugation at 13,000g for 10-20 min at 4°C. For adipose tissue, supernatant centrifugation was repeated to avoid transferring excess lipids. For cell lysates, MEFs or BMDMs were grown on 10 cm plates and at 80-100 % confluence medium was removed and cells were washed with PBS. Subsequently, cells were scraped, diluted in 200 µl modified RIPA buffer and passed 10 times through a 27G needle. Protein concentration of tissue and cell lysates was determined using a BCA assay kit (Sigma-Aldrich). Depending on tissue or cell type 25-50 µg of protein were mixed with urea buffer (40 mM Tris-HCl, 9 M urea, 1 mM EDTA, 5 % SDS, 5 % (v/v) ß-mercaptoethanol, 0.01 % (w/v) bromophenol blue, pH 6–8) heated for 15 min at 65°C and separated by SDS-PAGE (12 %). Blotting onto nitrocellulose membranes (Hybond-ECL, GE Healthcare) was performed in transfer buffer (20 mM TrisBase, 150 mM glycine, 20 % methanol) for 1 h at 100 V. Transfer was checked by Ponceau S staining before membranes were incubated with blocking solution (5 % milk powder in TBS-T) for 1 h at RT to prevent unspecific binding. All antibodies were diluted to the appropriate concentrations (see chapter 2.1) in blocking solution. Incubation with primary antibody solution was done overnight at 4°C, following three consecutive washing steps with TBS-T. Subsequently, membranes were incubated with secondary antibody solution for 1 h at RT. After repeated washing with TBS-T membranes were incubated with Amersham ECL Prime Western Blotting Detection Reagent (GE Healthcare) and developed using VersaDoc Imaging System (Bio-Rad).

3.2.3 CPE/SM synthase activity assay

Brain (0.4 g) and liver (0.6 g) tissue samples from 10 week old mice were homogenized in 800 µl ice cold buffer R using a Precellys® homogenizer (Peqlab Biotechnology). Cell debris was removed by centrifugation at 960 g for 10 min at 4°C and microsomal fractions were obtained by centrifugation of the supernatant at 100,000 g for 1 h at 4°C. The microsomal pellet was resuspended in 0.5-1 ml buffer R and passed 20 times through a 27G needle, aliquots were frozen in liquid nitrogen and stored at -80°C. Protein concentration was determined using the BCA assay kit (Sigma-Aldrich). To ensure that microsomal fractions contained comparable amounts of ER membranes, protein expression of the ER marker calnexin was determined by immunoblot analysis as described in chapter 3.2.2.

Microsomes were diluted in a total volume of 400 µl ice cold buffer R including 0.1 % v/v of 1000x PIC (final protein concentration: 2 mg/ml and 3.7 mg/ml for brain and liver microsomes, respectively) and kept on ice in 15 ml pyrex screw cap glass tubes (VWR). To this suspension N-ethylmaleimide (NEM) was added to a final concentration of 0.5 mM (100 mM stock solution in ethanol), to inhibit endogenous SMase activity. After this, C6-NBD-ceramide (NBD-Cer; (6-((*N*-(7-Nitrobenz-2-Oxa-1,3-Diazol-4-yl)amino)hexanoyl) sphingosine; Molecular Probes); 2 mM stock in ethanol) was added to a final concentration of 2.5 µM. Samples were kept on ice for 10 min, allowing incorporation of NBD-Cer into microsomal membranes. The reaction was started by shifting the samples to 37°C for 2 h under continuous shaking. Following incubation the reaction was stopped by addition of 1 ml methanol and 0.5 ml chloroform, and vigorous vortexing. Lipids were extracted by further addition of 0.5 ml chloroform and 0.5 ml 0.45 % NaCl, and vigorous vortexing. Following centrifugation at 3,000 g for 5 min at RT the lower organic phase was transferred to a fresh tube. The upper phase was re-extracted with 1 ml chloroform and after vortexing and another centrifugation step the lower phases were pooled. The combined organic phase was washed with 2 ml methanol/0.45 % NaCl (1:1 v/v) and following centrifugation the lower organic phase was transferred to a fresh tube and evaporated under a stream of nitrogen.

For TLC (thin layer chromatography) analysis, lipids were redissolved in a suitable volume of chloroform/methanol (2:1 v/v). Samples together with NBD-Cer, NBD-CPE, NBD-GlcCer and NBD-SM lipid standards were applied to a TLC plate (NANO-ADAMANT #821150; Macherey & Nagel) using the Linomat 5 (022.7808; CAMAG), operated at a dosage speed of 120 nl/s from a 100 µl syringe (Hamilton). The TLC plate was developed using an ADC2 TLC developer (CAMAG). The procedure comprised two consecutive 1D-runs. In the first run acetone was used to elute the excess NBD-Cer. In the second run chloroform/methanol/25 % ammonia (50:25:6 v/v/v) was used in the same dimension to separate the reaction products NBD-SM and NBD-CPE.

After drying the TLC plate, NBD-lipid species were visualized by scanning on a Typhoon FLA 9500 imager (laser 473 nm, filter setting BPB1, PMT 290 V; GE Healthcare) at a resolution of 50 µm pixel size. Using Imagequant software (GE Healthcare), images were contrast-adjusted and exported to TIFF format.

3.3 Analysis of PEMT-mediated conversion of CPE in mouse liver

For the construction of a recombinant adenovirus expressing phosphatidylethanolamine *N*-methyltransferase (PEMT) a cDNA encoding human PEMT was subcloned into a pADTrack-CMV shuttle vector. The vector was linearized with *Pme*I and inserted into an adenovirus using pADEasy-1 system for homologous

recombination in *E. coli*. The Ad.PEMT adenovirus expressed PEMT and GFP. An Ad.GFP adenovirus expressing only GFP was used as a control.

Prior to infection, male wild type and PEMT deficient mice were given a standard diet *ad libitum* (#5001, LabDiet)(Jacobs *et al.*, 2010). In 8 week old mice a single dose of Ad.GFP or Ad.PEMT (1.0×10^9 plaque-forming units) was injected into the tail vein. Seven days after injection mice were fasted and anesthetized with metofane (Pitmann-Moore Inc.) for tissue dissection. All procedures were approved by the University of Alberta's Institutional Animal Care Committee in accordance with guidelines of the Canadian Council on Animal Care.

The influence of the adenoviral infection on liver CPE content was investigated by mass spectrometry as described in chapter 3.4.1. PEMT activity in the liver was determined as previously described (Ridgway & Vance, 1992).

3.4 Lipid analysis

3.4.1 Mass spectrometric analyses (Somerharju group)

Tissues were homogenized in a small volume of water using a Precellys® homogenizer (Peqlab Biotechnology). Lipids were extracted according to Folch et al. (Folch *et al.*, 1957) and lipid standards (see chapter 2.9) were added at the one-phase stage of extraction. After evaporation of the solvents, the lipids were dissolved in methanol/chloroform (2:1 v/v) and for normalization the phosphate contents of the extracts were determined as described before (Bartlett & Lewis, 1970), samples were stored at -20°C. Glycerophospholipids, ceramides and hexosylceramides were quantified using direct infusion of the samples into the electrospray source of a Quattro Premier triple-quadrupole mass spectrometer (Waters Inc.) operated in the MS/MS mode. Analytes and internal standards were detected based on class-specific precursor ion (PC, PI, ceramide, hexosylceramide) or neutral loss (PE, PS) scanning as described previously (Kainu *et al.*, 2010). Data were analyzed with Microsoft Excel using the LIMSA add-on (Haimi *et al.*, 2006).

For quantification of CPE and SM, a volume of the lipid extract corresponding to 100 nmol of lipid phosphate was taken to dryness and dissolved in 1.5 ml methanol. Then 0.5 ml chloroform/methanol (9:1 v/v) containing C15:0-SM (1 nmol) and C17:0-CPE (0.25 nmol) standards (see chapter 2.9) and 0.5 ml NaOH (0.3 M) were added and samples were incubated overnight at RT. The solution was neutralized by addition of 0.3 ml HCl (0.3 M). Subsequently 3.5 ml chloroform and 1.2 ml water were added followed by vigorous vortexing. After centrifugation for 10 min at 3,000 rpm the upper phase was removed and the lower organic phase was washed twice with 3.5 ml of theoretical Folch upper phase (Folch *et al.*, 1957). After evaporating the

solvents under a stream of nitrogen, lipids from the lower phase were dissolved in 0.2 ml methanol, transferred to conical MS vials, dried and dissolved in 40 µl LC-MS quality methanol and stored at -20°C.

CPE and SM species were quantified using LC-MS. Chromatographic separation was carried out in the gradient mode using an Acquity Ultra Performance LC system equipped with an Acquity BEH-C_{18} 1.0 × 150 mm column (Waters Inc.). The column temperature was 60°C and the flow rate 0.13 ml/min. Solvent A was acetonitrile/water (60:40 v/v) containing 10 mM ammonium formate and 1 % NH_4OH, solvent B consisted of isopropanol/acetonitrile (90:10 v/v) containing 10 mM ammonium formate and 1 % NH_4OH. The gradient started from 40 % B, changed linearly to 70 % B in 10 min and then to 100 % B in 4 min. After 2 min at 100 %, B changed to 40 % in 3 min and was kept there for 3 min prior to the next injection. For CPE and SM detection, the column eluent was infused to the ESI source of the Quattro Premier mass spectrometer operated in the positive ion mode using selective reaction monitoring (SRM). CPE species were detected based on neutral loss of m/z 141 and SM species based on precursor ion scan/EIC of m/z 184. Peak areas of SM and CPE species and standards were obtained from the SRM chromatograms using QuanLynx software (Waters Inc.) and concentrations of molecular species and classes were determined with Microsoft Excel.

3.4.2 Mass spectrometric analyses (Dörmann group)

Tissues were homogenized in a small volume of water using a Precellys® homogenizer (Peqlab Biotechnology). Homogenates were transferred to Pyrex screw cap tubes and filled up with water to a final volume of 2 ml. The protein concentration for normalization was determined using BCA assay kit (Sigma-Aldrich). For lipid extraction 5 ml chloroform and 2.5 ml methanol, together with 50 µl lipid standard mixture (see chapter 2.9) were added and samples were vigorously vortexed. Samples were incubated overnight at 37°C under continuous shaking. Following incubation, samples were centrifuged at 5,300 rpm for 20-30 min at RT. Supernatants were transferred to fresh tubes and evaporated under a stream of nitrogen. For the second extraction step 5 ml chloroform/methanol 1:1 (v/v) were added to the remaining tissue pellet and samples were incubated as described above. For the third extraction step 5 ml chloroform/methanol 1:2 (v/v) were used. The supernatants resulting from each extraction step were pooled with the extracted lipids from the first step and solvents were evaporated under nitrogen.

For alkaline hydrolysis, lipid extracts were dissolved in 2 ml chloroform/methanol 1:1 (v/v) and mixed with 150 µl 1 M KOH in methanol. Following incubation for 2 h at 40°C samples were neutralized with 6 µl acetic acid. Desalting of lipid extracts was performed essentially as described before (Brodesser, 2007).

Neutral sphingolipids were quantified by quantitative Time of Flight mass spectrometry (Q-TOF-MS). Lipid extracts were dissolved in Q-TOF solvent (methanol/chloroform/300 mM ammonium acetate (665:300:35, v/v/v)(Welti *et al.*, 2002)) and measured via direct infusion using an Agilent HPLC-Chip Cube MS interface coupled to an Agilent 6530 Accurate-Mass Q-TOF LC/MS instrument as previously described (Wewer *et al.*, 2011; Ginkel *et al.*, 2012). Sphingolipids were ionized in the positive mode and quantified after collision-induced dissociation by scanning for characteristic fragment ions (Ginkel *et al.*, 2012).

3.4.3 Thin layer chromatographic analysis of mouse feces

Collected mouse feces were stored at –80°C. Prior to sample preparation feces and diet samples (control) were thawed and dried for 1 h at 37°C. Dried samples were grounded using mortar and pestle. Lipid extraction was performed according to the method of Bligh and Dyer (Bligh & Dyer, 1959). For that 100 mg of the grounded samples were suspended in 0.4 ml water in Pyrex screw cap tubes. To the suspension 1.5 ml chloroform/methanol 1:2 (v/v) were added, followed by vigorous vortexing. In the next step 0.5 ml chloroform were added and the mixture was vigorously vortexed. Then 0.5 ml water were added, followed by vigorous vortexing. Following extraction samples were centrifuged at 2,500 rpm for 10 min at RT. The lower organic phase was transferred to a fresh tube and solvents were evaporated under a stream of nitrogen.

For TLC analysis lipid extracts were dissolved in 100 µl chloroform/methanol 1:1 (v/v) and 5 µl together with lipid standards for cholesterol, DAG and TAG (see chapter 2.9) were applied to a TLC plate (HPTLC Silica gel 60; Merck). TLC plates were developed in *n*-hexane/diethylether/acetic acid 70:30:1 (v/v/v) as previously described (Bauer *et al.*, 2009). After thoroughly drying, TLC plates were incubated in a solution of 10 % $CuSO_4$ and 8 % H_2PO_4 and heated to 180°C for 15 min to visualize lipids (Yao & Rastetter, 1985).

3.5 Histological analysis

3.5.1 β-galactosidase staining

Cryostat sectioning of mouse tissues and β-galactosidase staining of tissue sections and cultured cells was essentially done as previously described (Degen, 2003).

3.5.2 H&E staining

Adipose tissue samples were fixed in 4 % paraformaldehyde in PBS for 24 h at 4°C and then embedded in paraffin. Paraffin embedding, microtome sectioning and H&E staining was essentially done as previously described (Schütz, 2011).

3.5.3 Electron microscopy

Wild type and SMSrD348E mice were anesthetized with Florene® (AbbVie) and fixed by transcardial perfusion via the left ventricle with 2.5 % glutaraldehyde in 0.1 M cacodylate buffer. After fixation small pieces of liver, brain and kidney were incubated in 1 % (w/v) osmium tetroxide. After washing in cacodylate buffer samples were treated with 30 % and 50 % ethanol and subsequently incubated in 1 % uranyl acetate in 70 % ethanol for 6 min in the dark. Following incubation samples were dehydrated in a graded series of ethanol and propylenoxide and embedded in EPON® (Polysciences) according to the manufacturer's protocol. Ultrathin sections were obtained with an UltracutE® ultramicrotome (Reichert-Jung) and mounted on copper grids. Grids were incubated with 1 % uranyl acetate for 20 min and with 0.4 % lead citrate for 3 min. Samples were investigated using a transmission electron microscope (EM 902A; Zeiss). Digital image acquisition was performed using a MegaViewII slow-scan-CCD camera and ITEM® 5.0 software (Soft-imaging-systems). Images were stored as uncompressed TIFF files in 16 bits of gray and were processed with Photoshop® CS5 (Adobe).

3.6 Isolation and culture of primary cells

Isolation and culture of primary cells was performed as previously described: bone marrow derived macrophages (Ebel, 2014), mouse embryonic fibroblasts (ED 10.5) (Klahre, 2012), culture of embryonic stem (ES) cells (Bickert, 2011) and culture of yeast cells (Vacaru *et al.*, 2009).

3.6.1 Isolation and differentiation of brown preadipocytes

For *in vitro* differentiation of brown preadipocytes, the stromal vascular fraction (SVF) containing preadipocytes was isolated from interscapular brown adipose tissue (iBAT) of newborn wild type and CerS4 deficient littermates (iBAT samples from 2-3 animals per genotype were pooled). All steps were conducted under sterile conditions in a laminar flow hood. Adipose tissue samples were transferred into collagenase digestion buffer-B and cut into small pieces. The suspension was incubated for 30 min at 37°C and vortexed every 5 min. The suspension was filtered through a 100 µm nylon mesh to remove undigested tissue remnants, and incubated on ice for 30 min. The infranatant containing the SVF was filtered through a 30 µm nylon mesh, and SVF cells were pelleted by centrifugation at 700 g for 10 min at RT. Cells were resuspended in culture medium-B, seeded on 6-well plates (5.7×10^5 cells per well) and incubated at 37°C and 5 % CO_2.

One day following isolation (passage 0), brown preadipocytes were immortalized by infection with a lentivirus containing the SV40 T large antigen (rrl156-PGK-Tag), which elicits cellular transformation. For this purpose, medium was exchanged with DMEM(+) containing 0.25 ng/µl virus (800 µl per well). Cells were incubated

overnight and the next day, 3 ml DMEM(+) were added. Medium was replenished every second day and at 90 % confluence cells were splitted.

For differentiation to mature brown adipocytes, 1.8 x 10^5 cells per well were seeded on 6-well plates. Two days after seeding, medium was exchanged with differentiation medium-B. Adipogenesis was induced by treating confluent cultures four days after seeding with induction medium-B for 48 hours. After this, cells were cultured in differentiation medium, which was replenished every second day until day 7 or 8 past induction. For stimulation, mature cells were incubated for 8 h in DMEM(+) containing 200 µM cGMP (pCPT-cGMP; Biolog).

3.6.2 Isolation and differentiation of white preadipocytes

For *in vitro* differentiation of white preadipocytes, the SVF was isolated from inguinal white adipose tissue (igWAT) of 5 week old wild type and CerS4 deficient littermates (igWAT samples from 3 animals per genotype were pooled). After igWAT dissection, all steps were conducted under sterile conditions in a laminar flow hood. After removal of lymph nodes, igWAT samples were minced and suspended in collagenase digestion buffer-W (7 ml/g wet weight). The suspension was incubated for 30 min at 37°C and vortexed every 5 min. After this, DMEM(+) was added to a total volume of 14 ml. After 10 min at RT the infranatant was transferred to a fresh tube and SVF cells were pelleted by centrifugation at 700 g for 10 min at RT. The pellet was resuspended in DMEM(+) (2 ml/g adipose tissue) and the suspension was filtered through a 100 µm nylon mesh. Cells were seeded in T175 flasks and incubated at 37°C and 5 % CO_2. At 70-80 % confluence, cells were splitted for differentiation.

For differentiation to mature white adipocytes, cells were grown to confluence and after two days medium was exchanged by induction medium-W for seven days. Following this, cells were grown in maintenance medium-W for 5 days. Media were replenished every second day. For experiments, cells were splitted to 6-well plates (0.2 x 10^3 cells per well) and incubated for one day. For stimulation, mature cells were incubated for 8 h in DMEM(+) containing 200 µM cGMP or 1µM noradrenaline (Sigma), respectively.

3.7 Physiological activation of energy expenditure in mice

5 week old wild type or CerS4 deficient mice were fasted for 2 h and then put into Phenomaster cages (TSE Systems) at 4°C. Oxygen consumption was measured for 100 s every 5 min for 1 h. Oxygen consumption, motility and food intake of wild type and CerS4 deficient animals was measured for 120 s every 18 min for 24 h at 23°C and 5 h at 30°C, respectively.

3.8 Feeding experiments

Wild type (WT) and CerS4 deficient (KO) mice originated from homozygous WT and KO breedings, respectively. To retain comparability, littermates from heterozygous breedings were cross-bred (i.e. WT litter 1 *X* WT litter 2 and KO litter 1 *X* KO litter 2 etc.) to obtain experimental animals.

Experimental animals were exclusively male, started at the age of 7-8 weeks and were fed either a high fat diet (HFD; 60 % kcal from fat; C1090-60; Altromin) or a low fat diet (LFD; 10 % kcal from fat; C1090-10, Altromin) for 16 weeks. Each group (WT HFD, KO HFD, WT LFD and KO LFD) consisted of 20-25 mice. Mice were given access to food and water *ad libitum* and animal and food weight was determined once a week. Before and after the 16 week feeding period animals were subjected to glucose and insulin tolerance tests. After 5 weeks feces were collected for TLC analysis of excreted lipids. At the end of the experiment animals were anesthetized with Florene® (AbbVie) and transcardially perfused with PBS. Tissues were dissected, frozen on dry ice and stored at -80°C.

3.8.1 Glucose tolerance test (GTT)

Prior to starting GTTs mice were transferred to fresh cages and fasted for 6 h with free access to water during the whole procedure. After fasting, animals were weighed and the appropriate volume of 10 % glucose solution (Braun) for injection of 1 g glucose per kg mouse weight was determined. To measure basal glucose levels the tail vein was punctured 1-2 cm proximal of the tail tip with a sterile 20G Sterican® needle (0.9 x 60 mm; Braun), the first blood was wiped away and the next drop was measured using an Accu-Chek® Aviva glucometer (Roche) according to the manufacturer's instructions. Immediately after this, mice were intraperitoneally injected with the appropriate volume of glucose solution using a sterile 1 ml Inject® F syringe (Braun) equipped with a sterile 24G Sterican® needle (0.55 x 25 mm; Braun). Glucose levels were determined 15, 30, 60, 90 and 120 min after injection. For each measurement clotted blood was rubbed away and blood was obtained by gently pressing it towards the punctured site, the first drop was discarded before measuring as described above. After the last measurement animals were supplied with food.

3.8.2 Insulin tolerance test (ITT)

For ITTs mice were transferred to fresh cages and were not fasted to avoid potential hypoglycemia. Food was removed only before starting the measurements and free access to water was given during the whole procedure. Animals were weighed and the appropriate volume for injection of 0.75 U/kg insulin (Insuman; Sanofi Aventis; 100 U/ml freshly diluted to 0.1 U/ml in sterile PBS before use) was determined. Glucose measurements and injections were conducted as described in the previous chapter. Glucose levels were determined 15, 30, 45 and 60 min after insulin injection.

In case of hypoglycemia mice were intraperitoneally injected with 150 µl 10 % glucose solution and were excluded from data analysis. After the last measurement animals were supplied with food.

3.9 Mouse handling

Animals were kept under standard conditions with a 12 h dark to light cycle with food and water *ad libitum*. Prior to dissection animals were anesthetized with Florene® (AbbVie) and transcardially perfused with PBS as previously described (Requardt *et al.*, 2009). For serum analyses blood was collected by cardiac puncture from mice anesthetized with Florene® (Parasuraman *et al.*, 2010), followed by immediate cervical dislocation. All housing and experimental conditions were in accordance to instructions of local and state authorities.

3.10 Statistical analyses and image processing

Data were processed using Microsoft Excel. For graphical presentation and statistical analyses Graph Pad Prism 5 software (Graph Pad Software) was used. Statistical significance for two group comparisons was determined by two-tailed *Student's t test.* If not mentioned otherwise, multiple group comparisons were done using two-way analysis of variance (ANOVA) with Bonferroni post-hoc tests. Differences were considered statistically significant when $p<0.05$. Images were processed using Photoshop® CS5 (Adobe) and densitometric analysis was done using Fiji software.

4 Results

4.1 Characterization of transgenic mice lacking SMSr catalytic activity

As SMSr catalytic activity proved to be essential for preventing ceramide accumulation and overall integrity in HeLa cells (Vacaru *et al.*, 2009), it was aimed to deplete SMSr catalytic activity in mice to study the *in vivo* function of SMSr.

The mouse *smsr* (or *samd*8) gene comprises six exons and is located on chromosome 14. The activity of the protein is depending on a catalytic triad of two histidine (H301 and H344) and one aspartate (D348) residues (Huitema *et al.*, 2004; Tafesse *et al.*, 2006), two of these residues are encoded by exon 6 (H344 and D348). In consequence of the results of (Vacaru *et al.*, 2009), a very severe phenotype was expected for mice lacking SMSr catalytic activity, therefore it was decided to generate two different mouse lines. In the beginning, Dr. Christina Ginkel from our group generated SMSrD348E mice, these mice ubiquitously express the D348E point mutation, that was shown to lead to catalytic inactivity of SMSr in cultured HeLa cells (Vacaru *et al.*, 2009). To circumvent possible embryonic lethality and to investigate SMSr function after tissue-specific depletion of SMSr catalytic activity, an additional mouse line for conditional deletion of exon 6 was generated during my diploma thesis (SMSrflox). For this Ph. D thesis these mice were crossbred with mice expressing Cre recombinase to generate SMSrdelEx6 mice. During this thesis, these mice were characterized and published (Bickert *et al.*, 2015), the corresponding text is not further denoted.

4.1.1 SMSrD348E mice

The non-conditional SMSrD348E mouse line was generated by Dr. Christina Ginkel during her Ph. D thesis (Ginkel, 2013). Aside from the D348E point mutation these mice express a *lacZ* reporter gene encoding for β-galactosidase under transcriptional control of the endogenous SMSr promoter (Figure 4.1).

The scheme for homologous recombination and generation of SMSrD348E mice is presented in Figure 4.1. Briefly, the SMSrD348E targeting vector included the genomic sequence of SMSr exons 4 and 5, a neomycin selection cassette (flanked by *frt*-sites) for selection of homologously recombined ES-cell clones in intron 5, and the mutated exon 6 encoding the D348E point mutation. After exon 6, NLS-lacZ reporter cDNA under control of an internal ribosomal entry site (IRES) was introduced followed by the SMSr 3’ untranslated region (for details see (Ginkel, 2013)).

For this thesis heterozygous animals (+/SMSrD348E) without neomycin selection cassette and backcrossed to 87.5 % C57BL/6 background were used to breed wild type and homozygous SMSrD348E littermates for investigation. Against our

expectations SMSrD348E mice were born according to the Mendelian ratio, indicating a non-essential role for SMSr during embryogenesis. Furthermore, adult animals showed normal morphology, behavior and fertility.

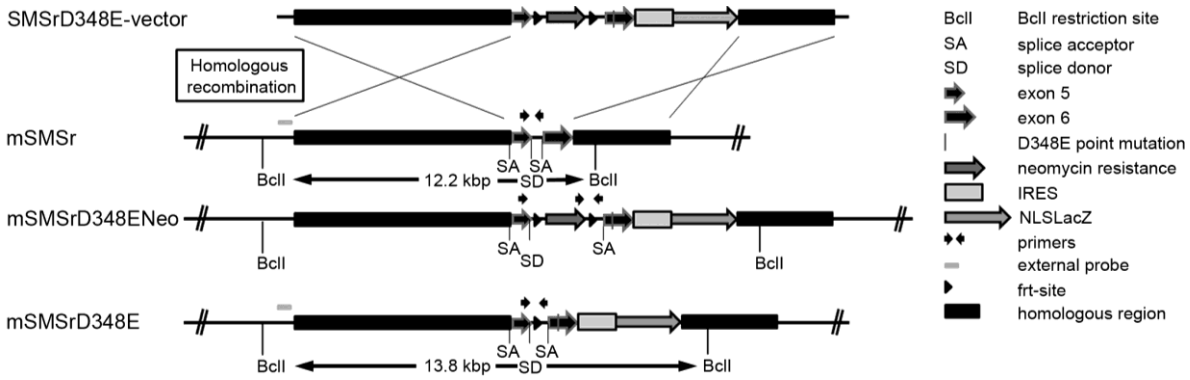

Figure 4.1 - Generation of SMSrD348E mice. (A) Scheme of homologous recombination for generation of SMSrD348E mice. (adopted and modified from Bickert et al., 2015)

4.1.2 SMSrdelEx6 mice

The SMSrflox mouse line for conditional deletion of exon 6 and expression of a catalytically inactive SMSr^{NT}-eGFP fusion protein was generated during my diploma thesis. Briefly, the approximately 19.5 kbp conditional SMSrflox targeting vector contained the genomic region of SMSr from exon 4 (5' homology region) to exon 6 and the 3' untranslated region followed by a neomycin resistance cassette flanked by *frt*-sites. To deplete SMSr catalytic activity, two *loxP*-sites were introduced in intron 4 and downstream of the neomycin selection cassette. Behind the 3' *loxP*-site a fusion sequence of exon 5 with an in-frame *egfp*, followed by the 3' homology region was introduced. In SMSrflox mice, Cre mediated recombination allowed the conditional deletion of exon 6 and the expression of an exon 5-*egfp* fusion sequence for translation of an SMSr^{NT}-eGFP fusion protein in the resulting SMSrdelEx6 mice (Figure 4.2 A; for details see (Bickert, 2011)).

For generation of SMSrflox mice, the targeting vector was transfected into HM1-ES cells. Transfected ES cell clones were analyzed for correct insertion of the targeting vector into the *smsr* locus by homologous recombination (Bickert, 2011). Positive clones were used for blastocyst injections (see chapter 1.4.1). Germ-line transmission chimeras resulting from blastocyst injections were available in the beginning of this Ph. D thesis, these mice were bred with C57BL/6 animals. Agouti-colored offspring were genotyped and heterozygous animals were mated with deleter-Flp mice to remove the neomycin selection cassette (see chapter 1.4.2). Since SMSrD348E mice were vital and fertile, the conditional SMSrflox mice were crossbred with mice expressing the Cre recombinase under control of the phosphoglycerate kinase (pgk)-promoter for ubiquitous deletion of exon 6, generating

SMSrdelEx6 mice. These mice express an $SMSr^{NT}$-eGFP fusion protein under control of the endogenous SMSr promoter.

To verify the SMSrflox/SMSrdelEx6 mouse line, genotypes were analyzed by PCR analyses (Figure 4.2 B) and Southern blot hybridization (Figure 4.2 C, D). For Southern blot analyses liver DNA of wild type (+/+), heterozygous (+/SMSrdelEx6) and SMSrdelEx6 (SMSrdelEx6) mice was digested with *Xmn*I. For hybridization an internal probe (969 bp part of the 3' homology region) was cut from the targeting vector by restriction digest with *Hinc*II and *Xba*I and a 5' external probe (513 bp sequence upstream of the 5' homology region), was amplified by PCR from a bacterial artificial chromosome (BAC) containing the genomic sequence of SMSr (see chapter 2.4). Southern blot hybridization using these probes confirmed correct insertion of the targeting vector by homologous recombination (Figure 4.2 C, D; for details see Bickert et al., 2015). The internal probe further confirmed that no multiple insertion of the targeting vector occurred.

Heterozygous animals (+/SMSrdelEx6) were backcrossed to 87.5 % C57BL/6 background and used to breed wild type and homozygous SMSrdelEx6 littermates for investigation. SMSrdelEx6 mice, like the SMSrD348E mice, were born in a Mendelian ratio and showed normal morphology, behavior and fertility. As a consequence, primarily SMSrD348E mice were used to investigate *in vivo* SMSr function in this thesis.

The $SMSr^{NT}$-eGFP fusion protein expressed in SMSrdelEx6 mice lacks the endogenous *C*-terminus of SMSr. Therefore, SMSrdelEx6 mice represented a valuable tool to verify the specificity of custom-made polyclonal antibodies targeting the *C*-terminus of SMSr and were used to investigate the tissue-specific expression pattern of SMSr.

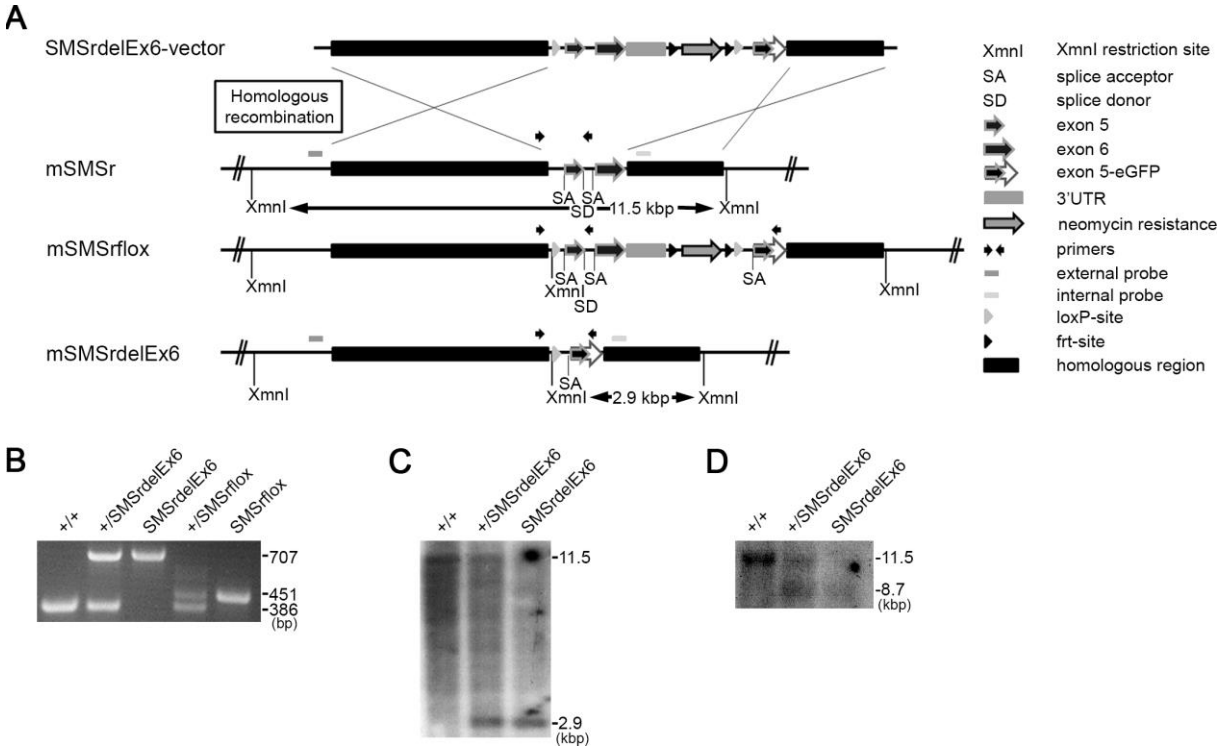

Figure 4.2 - Generation of SMSrdelEx6 mice. (A) Schematic drawing for the generation of SMSrdelEx6 mice by homologous recombination (B) Genotyping PCR for wild type (+/+), heterozygous (+/SMSrdelEx6) and homozygous (SMSrdelEx6) mice; characteristic DNA fragments 386 bp (wild type), 707 bp (delEx6), 451 bp (floxed) (C, D) Southern blot analysis of SMSrdelEx6 mice. Expected fragment sizes: *Xmn*I restriction: Internal probe (C): wild type 11.5 kbp, delEx6 2.9 kbp. 5' external probe (D): wild type 11.5 kbp, delEx6 8.7 kbp. (Panels A-C were adopted and modified from Bickert et al., 2015)

4.1.3 SMSr expression in mice

The ceramide accumulation after acute down regulation of SMSr in HeLa cells, led to the hypothesis that SMSr functions as a ceramide sensor in the ER (Vacaru *et al.*, 2009). A sensor function would imply that SMSr is ubiquitously expressed. To test this hypothesis and to provide a basis for the functional analysis of SMSr in mice, transcript and protein expression were investigated in several mouse tissues and primary cells.

4.1.3.1 ß-galactosidase staining in SMSrD348E mice

As discussed in chapter 4.1.1, SMSrD348E mice express a ß-galactosidase-reporter protein with a nuclear localization signal (NLS). As the reporter protein is expressed under the control of the endogenous SMSr promoter, SMSrD348E mice were used to investigate the cell type specific expression of the SMSr protein.

The first ß-galactosidase stainings were performed by Dr. Christina Ginkel during her Ph. D thesis. In these analyses cryo-sections from forebrain, cerebellum, kidney, heart and liver of SMSrD348E mice showed ß-galactosidase expression (Figure 4.3 A-E; (Ginkel, 2013)). In the present thesis these stainings were complemented with

cryo-sections from testis and pancreas (Figure 4.3 F, G) and the original stainings were verified by repeated stainings (Figure 4.4 A-G). All stainings were evaluated in collaboration with the histologists Dr. Holger Jastrow and Prof. Elke Winterhager (University Hospital/University of Essen).

In brain, neuronal areas like the forebrain cortex, the dentate gyrus and the hippocampal regions CA1, CA2, CA3 and CA4, as well as the cerebellar and the granular cell layer showed prominent ß-galactosidase staining (Figure 4.3/Figure 4.4 A, B) In kidney, *smsr* promoter activity was mainly detected in the cortex (Figure 4.3/Figure 4.4 C), whereas ß-galactosidase activity was not detectable in the medulla and papilla (data not shown; for details see Ginkel 2013). Moderate ß-galactosidase staining was detected in the AV-node of the heart, whereas cardiomyocytes in the myocard showed weaker staining (Figure 4.3/Figure 4.4 D). In liver, the whole tissue showed *smsr* promoter activity, but regions surrounding portal fields showed more prominent nuclear staining (Figure 4.3/Figure 4.4 E). In testis, ß-galactosidase signals were found adjacent to the basal epithelium of seminiferous tubules, probably resulting from nuclear staining of spermatogonia (Figure 4.3/Figure 4.4 F). In pancreas, ß-galactosidase staining was detected throughout the whole tissue, with strong staining of the exocrine portion and a somewhat weaker staining of the endocrine islets of Langerhans (Figure 4.3/Figure 4.4 G). For all investigated tissues, specificity of the ß-galactosidase staining was validated using cryo-sections of the corresponding wild type tissues (Figure 4.4 A-G). Importantly, no obvious alterations in cellular and tissue morphology were observed between wild type and SMSrD348E mice in any of the investigated tissues.

Taken together, the analyses of *smsr* promoter activity in SMSrD348E mice show that *smsr* transcripts are nearly ubiquitously expressed in mice. A comprehensive microarray analysis of different mouse tissues already suggested a relatively even distribution of *smsr* transcripts in mice, especially when compared to *sms1* and *sms2* transcripts (Figure 4.4 H).

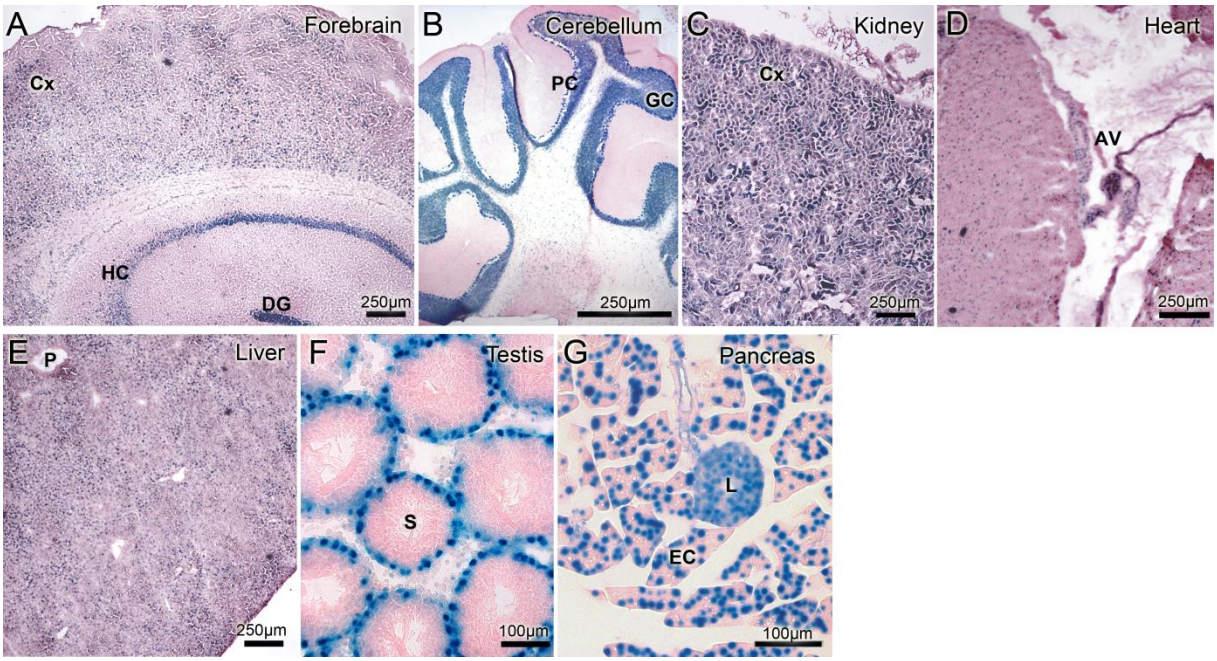

Figure 4.3 - Mouse *smsr* is a widely expressed gene. (A-G) Analysis of *smsr* promoter activity by ß-galactosidase staining of cryo-sections (12 µm) from various SMSrD348E mouse tissues. Neuronal regions of allo- and neocortical brain areas (A) and cerebellum (B) show prominent ß-galactosidase staining mainly of nuclei and perinuclear areas of neurons. In kidney, prominent ß-galactosidase staining is displayed in the tubular system of the cortex (C). In heart, nuclei of all cardiomyocytes are ß-galactosidase positive, especially those of the AV-node (D). In liver, the distribution of ß-galactosidase activity is diffuse with areas of more and others of less intensive staining that cannot be clearly associated to special regions of the hepatic lobules (E). In testis, spermatogonia in the basal epithelium of the seminiferous tubules show similar nuclear ß-galactosidase staining (F). In pancreas, ß-galactosidase expression is displayed throughout the whole tissue, with a prominent staining of the exocrine portion and a somewhat weaker staining of the endocrine ß-islets (G). AV, atrioventricular node; Cx, cortex; DG, dentate gyrus; EC, exocrine cells; GC, granular cell layer; HC, hippocampus; L, islets of Langerhans; P, portal field; PC, Purkinje cell layer; S, seminiferous tubule (adopted and modified from Bickert et al., 2015; Panels A-E were taken from the Ph. D thesis of Dr. Christina Ginkel and are presented here for immediate comparison (Ginkel, 2013)).

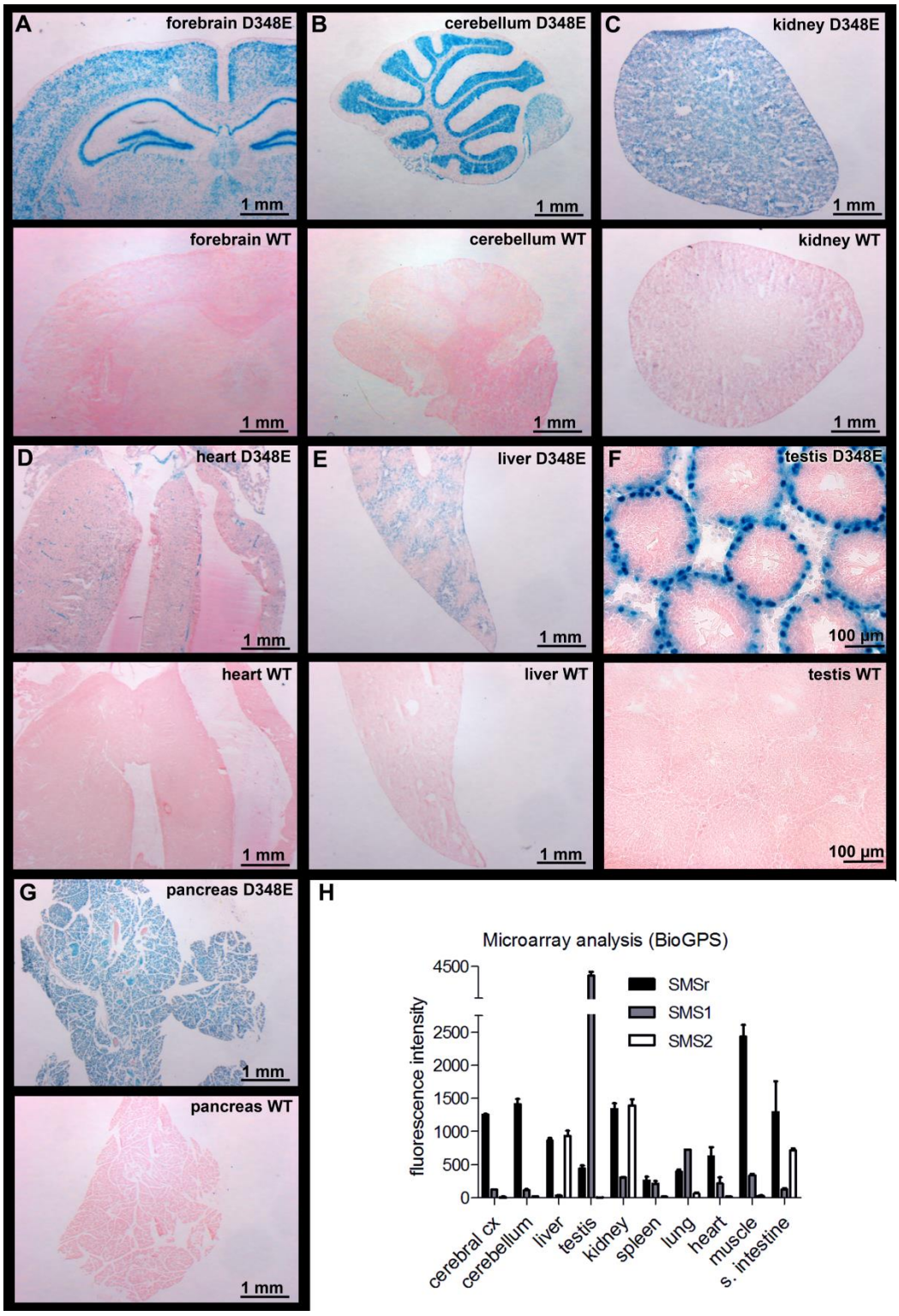

Figure 4.4 – Repeated analysis of ß-galactosidase expression in SMSrD348E and wild type control mice. ß-galactosidase staining of cryo sections from SMSrD348E (D348E) and wild type (WT) animals proved to be specific in forebrain (A), cerebellum (B), kidney (C), heart (D), liver (E), testis (F) and pancreas (G), no staining was observed in wild type tissues. Images represent overviews and supplement images in Figure 4.3. (H) Transcript expression profiles from microarray analysis of SMSr (Samd8), SMS2 (Sgms2) and SMS1 (Sgms1), modified according to http://BioGPS.org (Wu *et al.*, 2013), data set Mouse MOE430 Gene Atlas (Lattin *et al.*, 2008). Microarray data were generated using an Affymetrix Mouse Genome 430 2.0 Array (GEO platform accession number GPL1261). cx, cortex, s., small. (Panel H was adopted and modified from Bickert et al., 2015)

4.1.3.2 Affinity purification of polyclonal antibodies targeting SMSr

To analyze the tissue-specific expression pattern of SMSr in mice, new polyclonal antibodies targeting the mouse SMSr protein were generated. An internal peptide (CWPFSKPAIMKRLIG) between the SAM-domain and the first transmembrane domain and a *C*-terminal peptide (CDGPIPDLSSDQYQY) of the mouse SMSr protein (Figure 4.5 A) were synthesized by Prof. Marten Egmond (University of Utrecht). A mixture of these peptides was used to immunize different rabbits (Pineda Antibody Service, Berlin). For affinity chromatography of the rabbit sera two columns were loaded with the internal or the C-terminal peptide, respectively.

The first antibodies were affinity purified by Dr. Christina Ginkel, using both columns connected in series. In immunoblot analysis of yeast cells (lack endogenous SMSr) overexpressing V5-tagged SMSr, these antibodies recognized a protein corresponding to SMSr-V5 (Ginkel, 2013). However, in immunoblot analyses of mouse tissue lysates these antibodies proved to be unspecific (data not shown). To improve quality of immunoblot signals, I repeated purification of three different rabbit sera (#1, #2 and #4) using either the column with the internal peptide or the column with the *C*-terminal peptide.

The sequence of the peptides used for immunization is identical in the mouse (mSMSr) and the human (hSMSr) protein. For that reason, it was possible to use yeast cells overexpressing hSMSr-V5 to test the specificity of the newly generated antibodies in immunoblot analyses. The antibodies purified with the *C*-terminal peptide recognized a band at approximately 42-kDa, that was missing for lysates of yeast cells transfected with an empty vector (Figure 4.5 B, left panel). Incubation with an anti-V5 antibody revealed the same pattern (Figure 4.5 B, middle panel), demonstrating that the detected protein corresponds to hSMSr-V5. In contrast, antibodies purified with the internal peptide did not recognize hSMSr-V5 (data not shown), suggesting that the internal peptide had no immunogenic effect. Accordingly, only antibodies purified with the *C*-terminal peptide (derived from serum #4) were used for further analyses.

4.1.3.3 SMSr tissue-specific expression

Using total protein extracts of 19 different tissues of wild type mice, the tissue-specific distribution of SMSr was determined by immunoblot analyses using the newly generated anti-SMSr antibodies. The $SMSr^{NT}$-eGFP fusion protein produced in SMSrdelEx6 mice lacks the endogenous *C*-terminus of SMSr (Figure 4.5 A), hence the antibodies which target the *C*-terminus do not recognize the truncated protein. Therefore, protein extracts from SMSrdelEx6 mice served as controls to ensure the specificity of the antibodies in each tissue.

For wild type protein extracts a protein migrating at approximately 42-kDa was detected in all of the investigated tissues. In tissues of SMSrdelEx6 mice this protein was consistently absent (Figure 4.5 C, D). The mouse and the human *smsr* gene each encode a 415-residue protein with a predicted molecular weight close to that of the detected protein. As the protein migrated approximately to the same height as the hSMSr-V5 protein (Figure 4.5 B) it is hereafter referred to as SMSr.

The analyses confirmed a broad tissue distribution of the SMSr protein, in line with the ß-galactosidase expression and the microarray analyses discussed in chapter 4.1.3.1. The strongest expression of all tissues was observed in testis, brain, kidney and pancreas (Figure 4.5 C, D). In comparison to these tissues expression was rather low in spleen, lung, heart and eye and moderate in liver and other investigated tissues.

In several of the wild type tissues (forebrain, cerebellum, testis, stomach, small intestine, muscle, skin, eye, prostate and pancreas) the anti-SMSr antibodies recognized an additional protein migrating at approximately 48-kDa, which was absent in tissues of SMSrdelEx6 mice (Figure 4.5 C, D). Database analysis revealed two protein coding transcripts for the mouse SMSr, coding for a 415-residue protein and a 478-residue protein, respectively (http://www.ensembl.org; Gene ID: ENSMUSG00000021770). As already mentioned, the protein detected at 42-kDa corresponds to the 415-residue protein isoform (SMSr). Consequently, the protein detected at 48-kDa corresponds to the 478-residue protein isoform, hereafter referred to as SMSr-2. The protein is the predominant isoform only in testis (Figure 4.5 C). In a subset of tissues (large intestine, caecum, kidney, spleen, lung, heart and fat) unequivocal identification of SMSr-2 expression was not possible due to unspecific binding of the anti-SMSr antibodies at the corresponding height (Figure 4.5 C, D).

Notably, the anti-SMSr antibodies did not recognize SMSr in immunofluorescence analyses of wild type cryo-sections from liver and brain under different experimental conditions (data not shown).

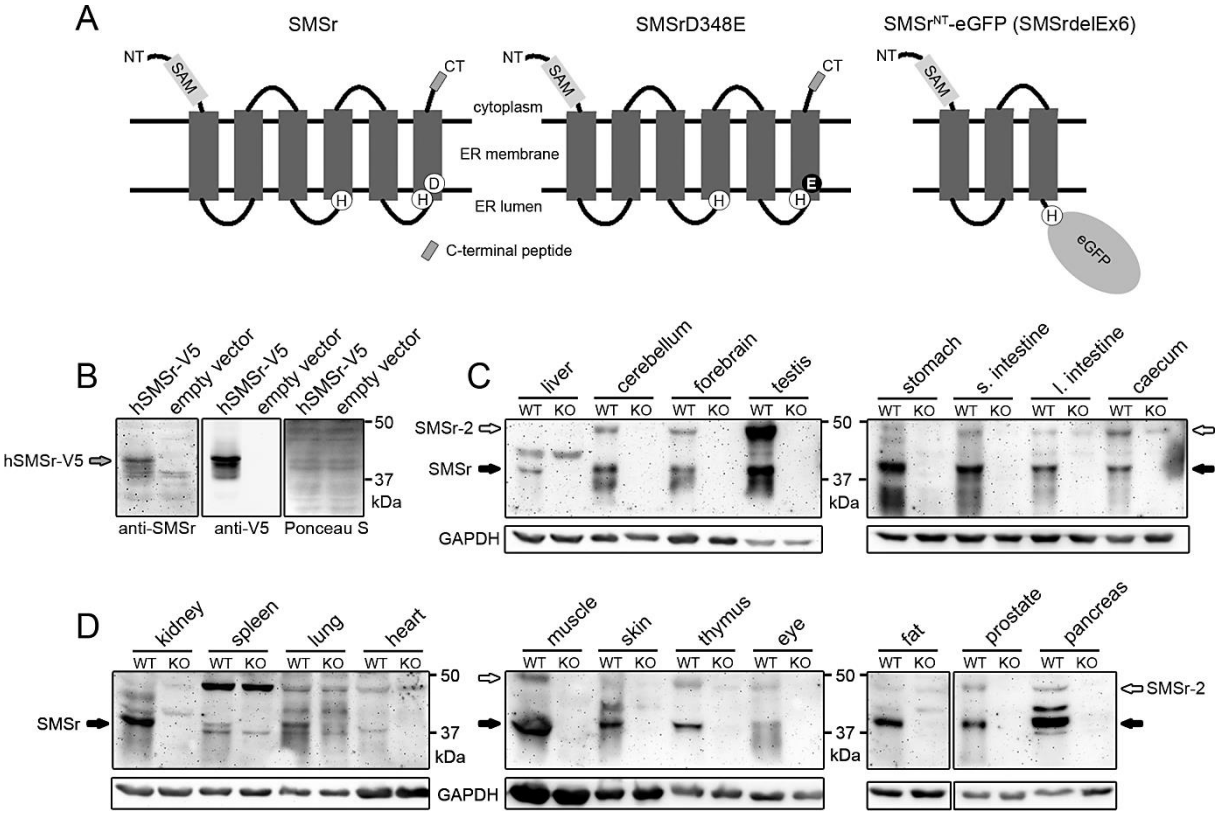

Figure 4.5 - Tissue-specific distribution of the SMSr protein in mice. (A) Putative membrane topology of native SMSr, SMSrD348E and SMSr^{NT}-eGFP fusion protein (SMSrdelEx6 mice) predicted by TMHMM (http://www.cbs.dtu.dk/services/TMHMM/). The endogenous *C*-terminus in the SMSr^{NT}-eGFP (SMSrdelEx6) fusion protein is replaced by an eGFP reporter which is predicted to be oriented towards the ER lumen. Lack of the *C*-terminus allowed verifying the specificity of the newly generated anti-SMSr antibodies in immunoblot analysis (B-D). Predicted molecular mass: wild type and SMSrD348E 48.2 kDa (415 aa), SMSr^{NT}-eGFP (SMSrdelEx6) 63.5 kDa (559 aa). (B) Immunoblot analysis with lysates from yeast cells overexpressing an hSMSr-V5 construct. The anti-SMSr antibodies specifically recognized the 49.6 kDa hSMSr-V5 fusion protein, as well as an antibody targeting the V5-tag. Ponceau S staining was used as loading control. (C, D) Immunoblot analyses of wild type (WT) tissue lysates, lysates from SMSrdelEx6 mice (KO) served as negative controls. The anti-SMSr antibodies specifically recognized the predicted 48.2 kDa (SMSr) and 54.7 kDa (SMSr-2) protein isoforms. Both isoforms did not migrate to positions expected for their theoretical mass. Different protein standards revealed, SMSr and the corresponding SMSr-V5 migrate at about 42 kDa, SMSr-2 migrates at about 48 kDa. GAPDH was used as loading control. 25 µg of protein were applied for forebrain, cerebellum and testis, 50 µg for liver and other tissues. (Data are representative of at least 3 independent experiments; s. - small; l. - large). (adopted and modified from Bickert et al., 2015).

4.1.3.4 SMSr expression in primary cells

The analyses of SMSr expression in mice were supplemented by the investigation of different primary cells. In contrast to previous data (Ginkel, 2013), no ß-galactosidase staining was observed in embryonic stem cells from SMSrD348E mice (Figure 4.6 A). Nuclear ß-galactosidase staining was found in embryonic fibroblasts from SMSrD348E mice (Figure 4.6 B). Immunoblot analyses of cell lysates from wild type embryonic fibroblasts confirmed the expression of SMSr (Figure 4.6 C; left panel).

Additionally SMSr was found to be expressed in bone marrow derived macrophages from wild type mice (Figure 4.6 C; right panel).

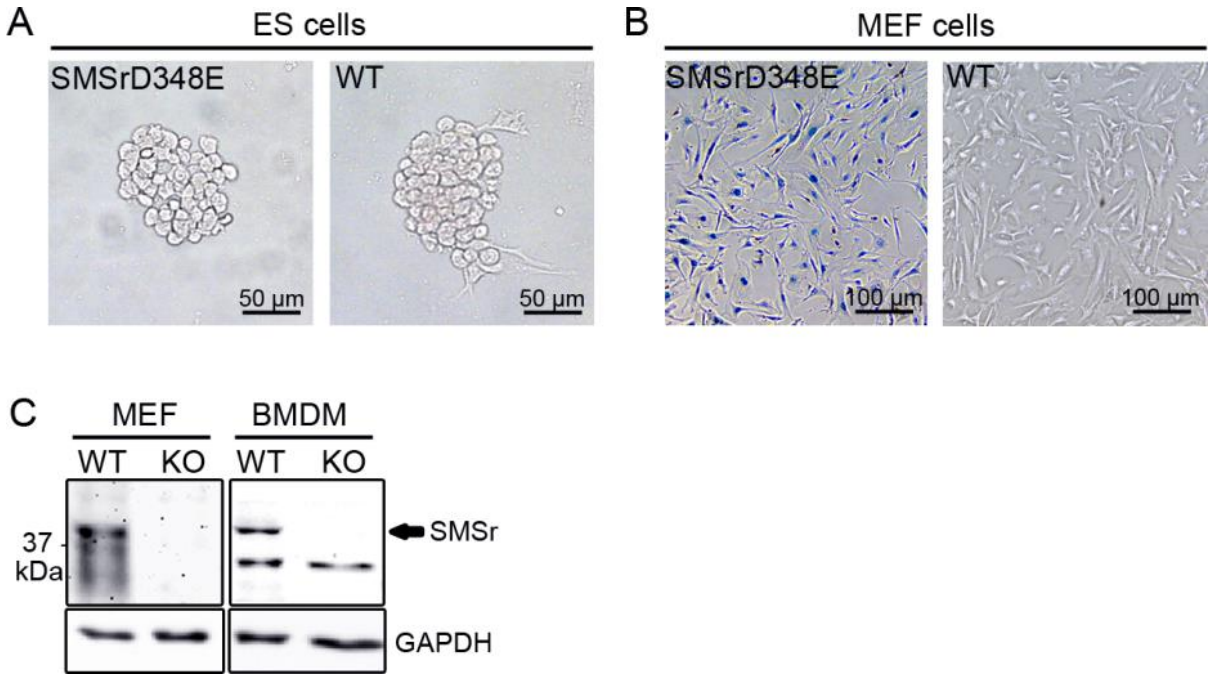

Figure 4.6 - Analyses of SMSr expression in primary cells (A) ß-galactosidase staining of embryonic stem (ES) cells from SMSrD348E mice revealed no nuclear staining. (B) ß-galactosidase staining of mouse embryonic fibroblasts (MEF; ED 10.5) revealed nuclear staining in SMSrD348E cells. Wild type (WT) cells served as negative controls. (C) SMSr was specifically detected by the anti-SMSr antibodies in cell lysates of MEF cells (left panel) and bone marrow derived macrophages (BMDM; right panel). MEFs and BMDMs from SMSrdelEx6 mice (KO) served as negative controls. GAPDH was used as loading control, 20 µg of protein were applied.

4.1.4 Activity and protein expression in SMSrD348E and SMSrdelEx6 mice

As a prerequisite for the phenotypic analyses, functionality of the transgenic mouse lines was verified. For this purpose enzyme activity and protein expression of the point-mutated SMSrD348E and the truncated $SMSr^{NT}$-eGFP protein were determined in CPE synthase activity assays and immunoblot analyses, respectively.

4.1.4.1 CPE synthase activity of mouse SMSr

Previously, it was shown that human SMSr (hSMSr) and *Drosophila* SMSr (dSMSr) exhibit CPE synthase activity (Vacaru *et al.*, 2009). In collaboration with the group of Prof. Joost Holthuis (University of Osnabrück) it was investigated whether mSMSr is also capable of catalyzing the synthesis of CPE. Therefore, a construct carrying a V5-tagged version of mSMSr (mSMSr-V5) was transfected to budding yeast, an organism which lacks endogenous CPE synthase activity. In a CPE synthase activity assay lysates of these yeast cells supported conversion of C6-NBD-ceramide (NBD-Cer) into NBD-CPE (Figure 4.7 A). In the next step, 4Δ.Lass5 yeast cells which express ceramide synthase 5 instead of the endogenous enzymes for ceramide

production (Cerantola *et al.*, 2007), were transfected with mSMSr-V5. LC-MS/MS analysis of these yeast cells in collaboration with Prof. Pentti Somerharju (University of Helsinki), revealed production of several species of CPE that were missing in mock-transfected cells (Figure 4.7 B). In addition, CPE synthase activity was determined in yeast cells transfected with hSMSr or hSMSr^{D348E} (Figure 4.7 C). While NBD-CPE production was observed in cells transfected with hSMSr, activity was abrogated in cells transfected with hSMSr^{D348E}.

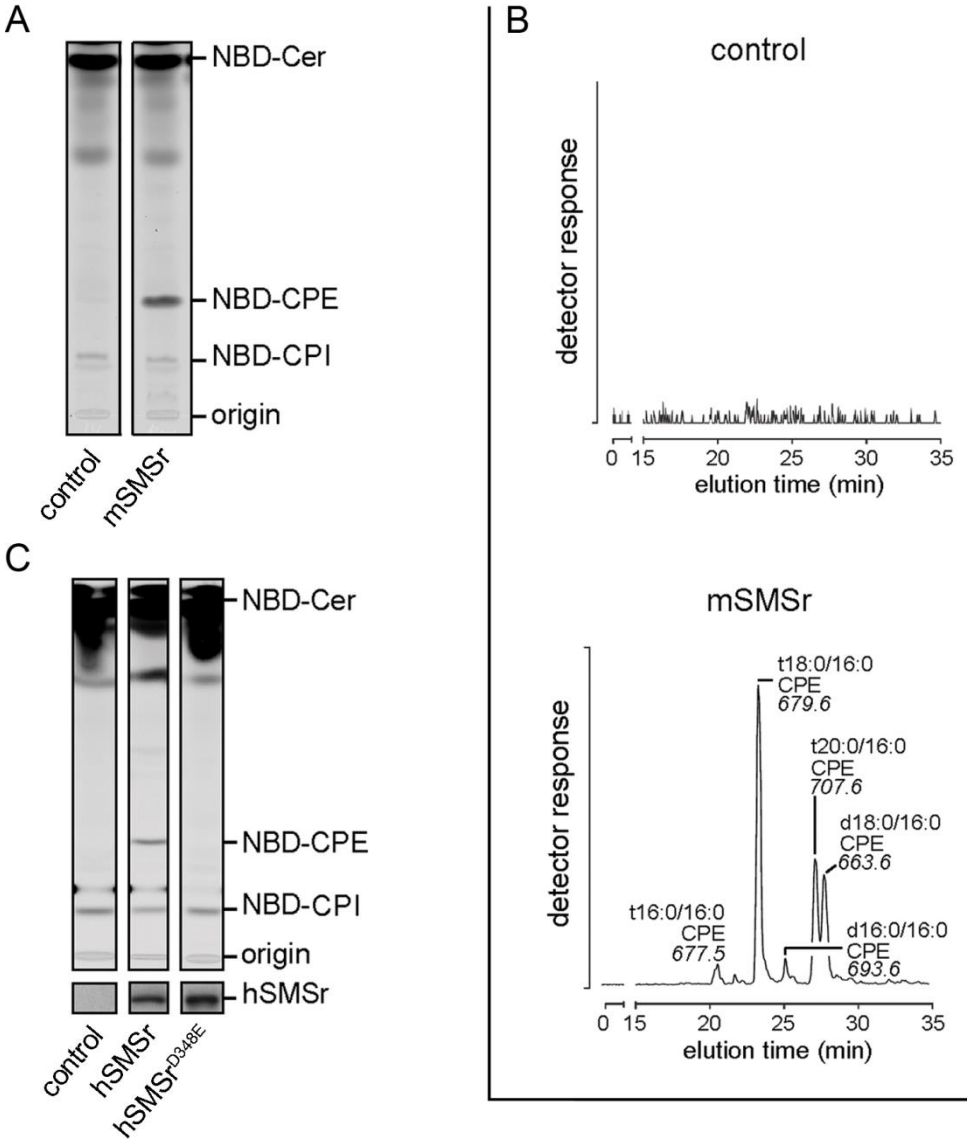

Figure 4.7 - Mouse SMSr catalyzes CPE production and point mutation D348E leads to catalytic inactivation of SMSr. (A) TLC (thin layer chromatography) analysis showing production of NBD-CPE and NBD-CPI after incubation of NBD-ceramide with lysates of yeast strains overexpressing hSMSr or mSMSr. CPI (ceramide phophoinositol) is a major constituent of cell membranes in yeast cells, which lack endogenous SM and CPE production (B) LC-MS/MS analysis (neutral loss m/z 141 scan) showing different molecular species of CPE after alkaline hydrolysis of glycerolipids in 4Δ.Lass5 yeast cells (express ceramide synthase 5 instead of the endogenous ceramide synthases) transfected with mSMSr. (C) TLC analysis after incubation of NBD-ceramide with lysates of yeast strains overexpressing hSMSr or hSMSr^{D348E}. In contrast to yeast cells transfected with hSMSr, conversion of NBD-ceramide to NBD-CPE was not supported by cells transfected with

hSMSr^{D348E}, indicating that catalytic activity of the point-mutated protein is lost. Immunoblot analysis (below TLC) confirms that comparable amounts of protein were used. (adopted and modified from Bickert et al., 2015).

4.1.4.2 CPE/SM synthase activity in SMSr and SMS2 mutant mice

CPE synthase activity was readily detectable in lysates of yeast cells overexpressing mSMSr-V5 or hSMSr-V5 (Figure 4.7 A). Detection of endogenous CPE synthase activity of SMSr in mouse tissues is complicated, since SMSr produces only trace amounts of CPE and since sphingomyelin synthase 2 (SMS2) is known to have a dual activity towards the production of SM and CPE (Ternes *et al.*, 2009). To prove that catalytic activity is indeed lost in SMSrD348E and SMSrdelEx6 mice, it was necessary to distinguish between CPE synthase activity exhibited by SMSr and SMS2. Therefore, double mutants of SMSr mutant and SMS2gt mice (Liu *et al.*, 2009b) were bred. SMS2gt mice were provided by Prof. Xian-Cheng Jiang (SUNY Downstate Medical Center, New York). CPE synthase activity was first described in microsomal preparations of rat brain and liver (Malgat *et al.*, 1986). Therefore, microsomal preparations of brain and liver from wild type, SMSrD348E, SMSrdelEx6, SMS2gt single mutant and SMS2gt *X* SMSrD348E and SMS2gt *X* SMSrdelEx6 double mutant mice were used for analyses of CPE (and SM) synthase activity. CPE/SM synthase activity measurements and subsequent TLC (thin layer chromatography) analyses were done in collaboration with Dr. Matthijs Kol from the group of Prof. Joost Holthuis (University of Osnabrück).

Incubation of brain and liver microsomal fractions with NBD-Cer led to the formation of NBD-SM, NBD-CPE and NBD-GluCer (Figure 4.8 A and B). In brain, NBD-GluCer formation was not altered in microsomal fractions of any of the investigated genotypes compared to wild type (Figure 4.8 A). NBD-SM production was reduced approximately by half for SMS2gt and double mutant animals compared to wild type (Figure 4.8 A). No changes were detectable in SMSr single mutants. For SMS2gt mice the signal for NBD-CPE was only slightly decreased compared to wild type, but completely missing for all SMSr single and double mutants (Figure 4.8 A).

As shown in Figure 4.8 B, in liver microsomal fractions no alterations in NBD-GluCer signals were observed between the investigated genotypes and the wild type control. In microsomal fractions from SMS2gt and double mutants, synthesis of NBD-SM was strongly decreased compared to wild type (Figure 4.8 B). Similar to brain, no change in NBD-SM production was observed for SMSr single mutants in the liver, showing that SMSr does not exhibit or influence SM synthase activity. NBD-CPE formation was only slightly decreased for all single mutants compared to wild type, but was completely missing for all double mutants (Figure 4.8 B).

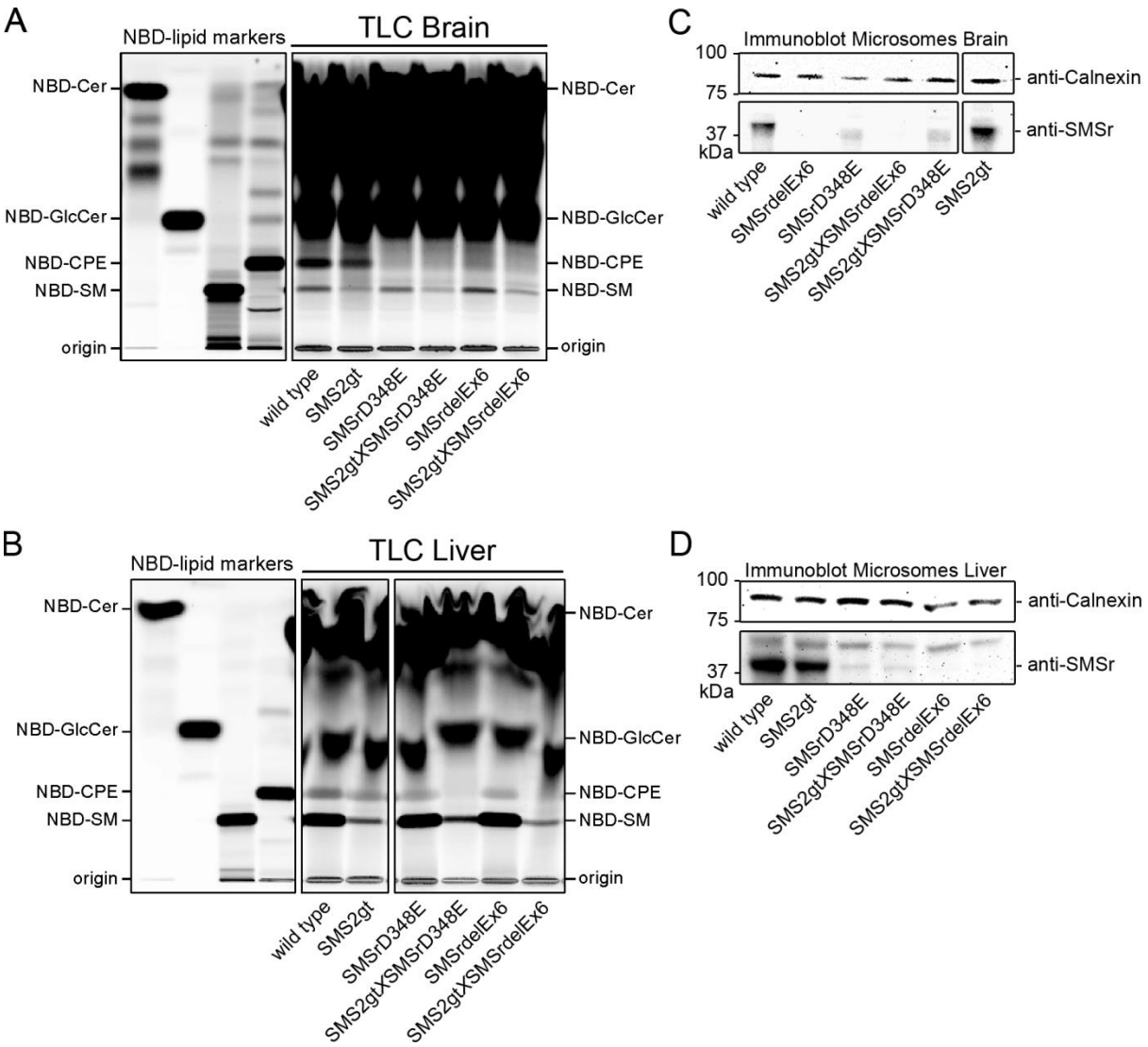

Figure 4.8 - CPE and SM synthase activity in brain and liver microsomes of SMSr, SMS2 and double mutant mice. (A, B) TLC (thin layer chromatography) separation of reaction products NBD-SM, NBD-CPE and NBD-GluCer after incubation of NBD-ceramide with brain or liver microsomal fractions of wild type, SMSrD348E, SMSrdelEx6, SMS2gt single mutant or SMS2gt X SMSrD348E and SMS2gt X SMSrdelEx6 double mutant mice. (A) In brain microsomal fractions production of NBD-SM was strongly reduced only in SMS2gt and double mutant animals. NBD-CPE production was essentially abolished in SMSr single and double mutant microsomes and only slightly decreased for SMS2gt mice. (B) In liver microsomal fractions production of NBD-SM was strongly decreased for SMS2 single and double mutant mice. NBD-CPE production was reduced by half in single mutant microsomes and completely abolished for all double mutants. (C, D) Immunoblot analyses of microsomal fractions used in A and B (note that in A sample arrangement differs between TLC and immunoblot). Antibodies against the ER marker calnexin confirmed that equal amounts of ER membranes were used in the assay. Antibodies against SMSr recognized a protein in wild type and SMS2gt samples. As expected, no signal was detected in SMSrdelEx6 and SMS2gt X SMSrdelEx6 samples, but the point-mutated SMSrD348E protein was strongly reduced for all corresponding genotypes in both tissues. 25 µg of protein were applied per lane. (Panels A and B adopted and modified from Bickert et al., 2015).

To ensure that equal amounts of ER membranes were used in the CPE/SM synthase assay, microsomal preparations were analyzed by immunoblot prior to the assay. An

antibody against the ER marker calnexin confirmed equal loading for both tissues (Figure 4.8 C, D). Moreover, anti-SMSr antibodies were used to determine expression of SMSr and SMSrD348E protein levels. In wild type and SMS2gt microsomal preparations of both tissues, the SMSr protein was readily detectable and as expected, no signal was detected for SMSrdelEx6 and SMS2gt *X* SMSrdelEx6 mice. Notably, compared to the wild type, the signal for the SMSrD348E protein was strongly reduced in both tissues (Figure 4.8 C, D).

4.1.4.3 SMSrD348E and SMSr^{NT}-eGFP protein expression

To further investigate the expression of the SMSrD348E protein, total tissue lysates from wild type and SMSrD348E mice were investigated by immunoblot analyses using the anti-SMSr antibodies. In tissue lysates from forebrain small amounts of SMSrD348E protein were detectable, but the protein was virtually absent in liver, kidney, lung, spleen and cerebellum (Figure 4.9).

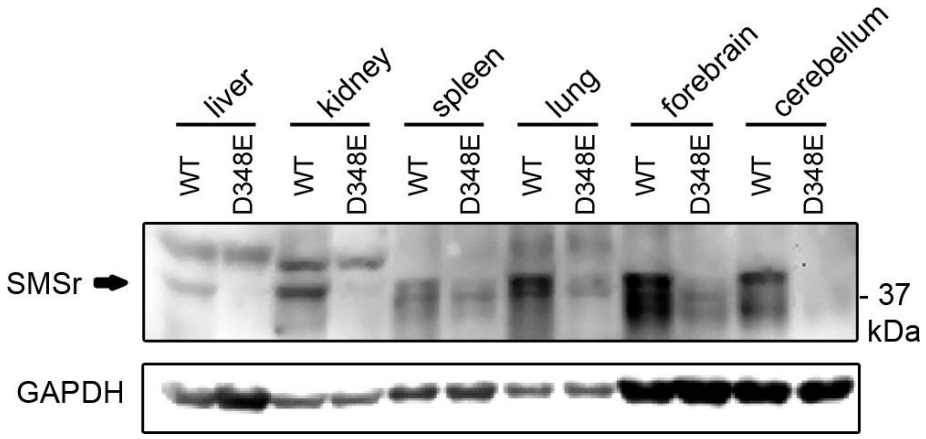

Figure 4.9 – Immunoblot analysis of protein expression in SMSrD348E mice. (D) Immunoblot analyses of total protein lysates from different tissues of wild type (WT) and SMSrD348E (D348E) mice using anti-SMSr antibodies. 75 µg protein were applied per lane; GAPDH served as loading control.

Similar to what was observed for the SMSrD348E mice, the SMSr^{NT}-eGFP fusion protein in SMSrdelEx6 mice might also be degraded. On cryo-sections from kidney and liver of SMSrdelEx6 mice the fusion protein was neither detectable by endogenous fluorescence of eGFP, nor in immunofluorescence analyses using different antibodies against GFP (data not shown). In the same line, these antibodies did not detect the fusion protein in immunoblot analyses of total protein lysates from liver of SMSrdelEx6 mice (data not shown).

4.1.5 Analysis of sphingolipid content in SMSr and SMS2 mutant mice

As a basis for the functional analysis of SMSr in mice, the sphingolipid content in a variety of tissues from wild type and SMSrD348E mice was determined by mass spectrometric analyses in collaboration with Prof. Pentti Somerharju (University of

Helsinki). To get a more comprehensive overview of CPE metabolizing enzymes in mice, the analysis was extended by including tissues from the SMS2gt and SMS2gt X SMSrD348E mice that were already discussed in chapter 4.1.4.2.

4.1.5.1 Distribution of CPE and SM in mouse tissues

The analysis started with the quantification of CPE and SM levels in forebrain, cerebellum, liver, testis, kidney, spleen, lung, heart, muscle and small intestine of wild type mice. Since CPE could not be detected by direct infusion MS/MS, CPE and SM levels were quantified by LC-MS analysis (Figure 4.10 A, B). In all investigated tissues the steady-state levels of CPE were exceedingly low, in comparison the levels of SM were 300 to 1,500 fold higher depending on the tissue. While CPE levels were relatively high in testis and brain (~0.020 mol % of total phospholipid), they were particularly low in heart and liver (~0.002-0.005 mol % of total phospholipid).

It was suggested that in liver low quantities of SM can be produced by the step-wise methylation of CPE (Muehlenberg *et al.*, 1972; Malgat *et al.*, 1986). This reaction is analogous to the S-adenosylmethionine-dependent conversion of PE to PC catalyzed by the liver-specific enzyme phosphatidylethanolamine *N*-methyltransferase (PEMT)(Ridgway & Vance, 1992; Jacobs *et al.*, 2010). As CPE levels were particularly low in the liver, the impact of PEMT removal on liver CPE levels was investigated in collaboration with Dr. René Jacobs, Prof. Dennis Vance (University of Alberta) and Prof. Pentti Somerharju (University of Helsinki). In the liver of PEMT KO mice CPE levels were 20 times higher compared to wild type controls (Figure 4.10 C). Moreover, CPE levels in PEMT KO mice were reduced by 50 % after adenovirus-mediated transduction with a functional PEMT construct (Figure 4.10 C), which restored PEMT activity (Figure 4.10 D).

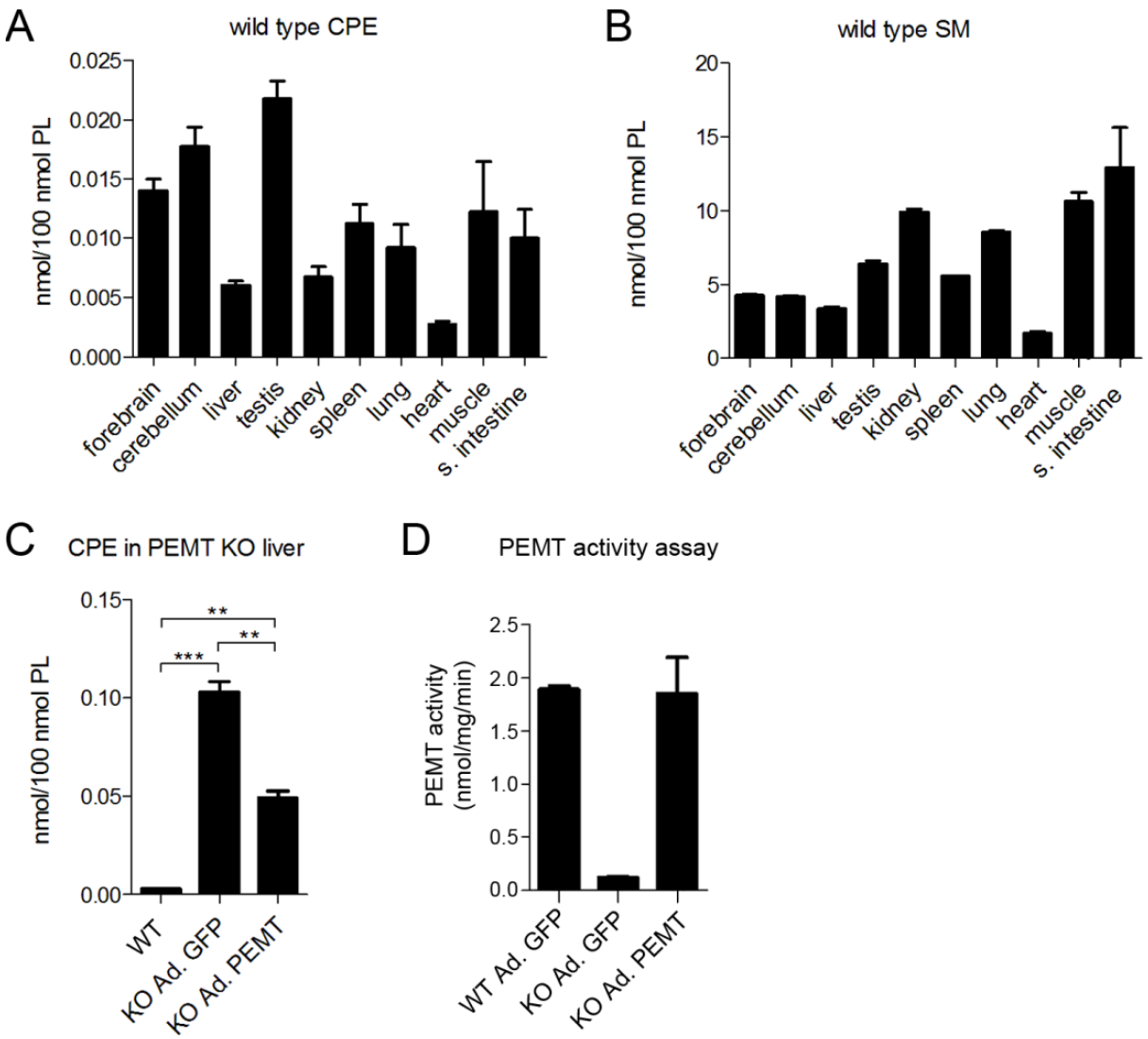

Figure 4.10 – Mass spectrometric quantification of CPE and SM levels in different mouse tissues. (A, B) LC-MS analysis of CPE and SM levels in forebrain, cerebellum, liver, testis, kidney, spleen, lung, heart, muscle and small intestine of wild type mice (n=4). (C) LC-MS analysis for comparison of liver CPE content of wild type (WT) mice, PEMT KO mice transduced with GFP (KO Ad. GFP) and PEMT KO mice transduced with functional PEMT (KO Ad. PEMT)(n=2-3). (D) PEMT activity assay from liver lysates of wild type mice transduced with GFP (WT Ad. GFP), PEMT KO mice transduced with GFP (KO Ad. GFP) and PEMT KO mice transduced with PEMT (KO Ad. PEMT) proved functionality of the PEMT construct (n=3). Data are means ± SEM; **, p<0.05; **, p<0.005; ***; p<0.001.* (adopted and modified from Bickert et al., 2015)

4.1.5.2 Impact of SMSr and SMS2 inactivation on tissue CPE and SM levels

The impact of disrupting SMSr and SMS2 catalytic activity on CPE and SM levels was investigated in a variety of tissues from wild type, SMSrD348E, SMS2gt and SMS2gt X SMSrD348E double mutant mice. The LC-MS analysis of forebrain and cerebellum revealed a 40-60 % reduction in short-chain CPE species (C18:0, C20:0) in SMSrD348E and double mutant mice relative to wild type mice (Figure 4.11 A, B). In contrast, inactivation of SMSr did not lead to significant changes in the levels of long-chain CPE species (C22:0, C24:0, C24:1). Depletion of SMSr decreased the total levels of CPE by about 30 % in forebrain and cerebellum (Figure 4.12 A, B). SM

levels in brain were not affected by depletion of SMSr (Figure 4.11 D, E). The depletion of SMS2 did not alter the levels of CPE in the brain, but caused a reduction in total SM levels by about 15 % (Figure 4.12 K, L). The loss of SMS2 affected all major species except for C16:0 SM in forebrain and C20:0 to C22:0 SM species in cerebellum (Figure 4.11 D, E). In liver, no significant differences in CPE levels between wild type and mutant mice were detectable (Figure 4.11 C and Figure 4.12 C). Inactivation of SMS2 led to a decrease (~20%) in total SM levels in liver (Figure 4.12 M), the decrease affected all major species (Figure 4.11 F), but was only significant for SMS2gt mice.

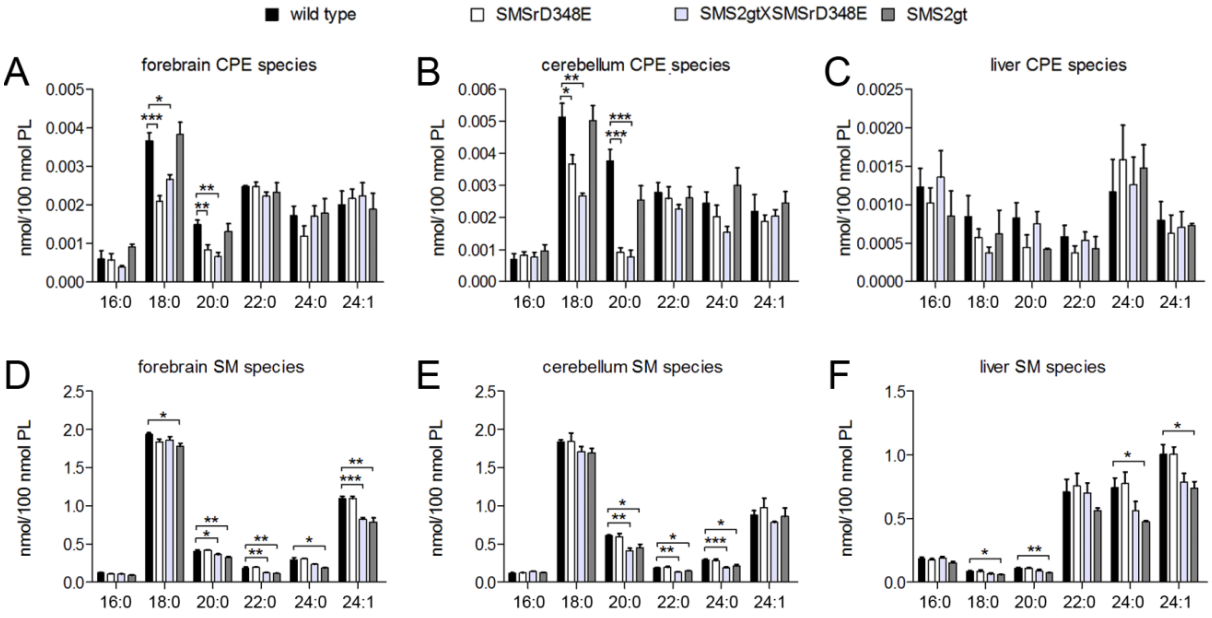

Figure 4.11 - LC-MS analyses of CPE, SM, ceramide and hexosylceramide species in forebrain, cerebellum and liver of wild type, SMSrD348E, SMS2gtXSMSrD348E and SMS2gt mice. (A-C) Analysis of main CPE species. (D-E) Analysis of main SM species. (F-H) Analysis of main ceramide species. (I-K) Analysis of main hexosylceramide (Hex-Cer) species. Data are means ± SEM; two-tailed *Student's t test:* *, p<0.05; **, p<0.005, ***, p<0.001; n=3-4. (adopted and modified from Bickert et al., 2015).

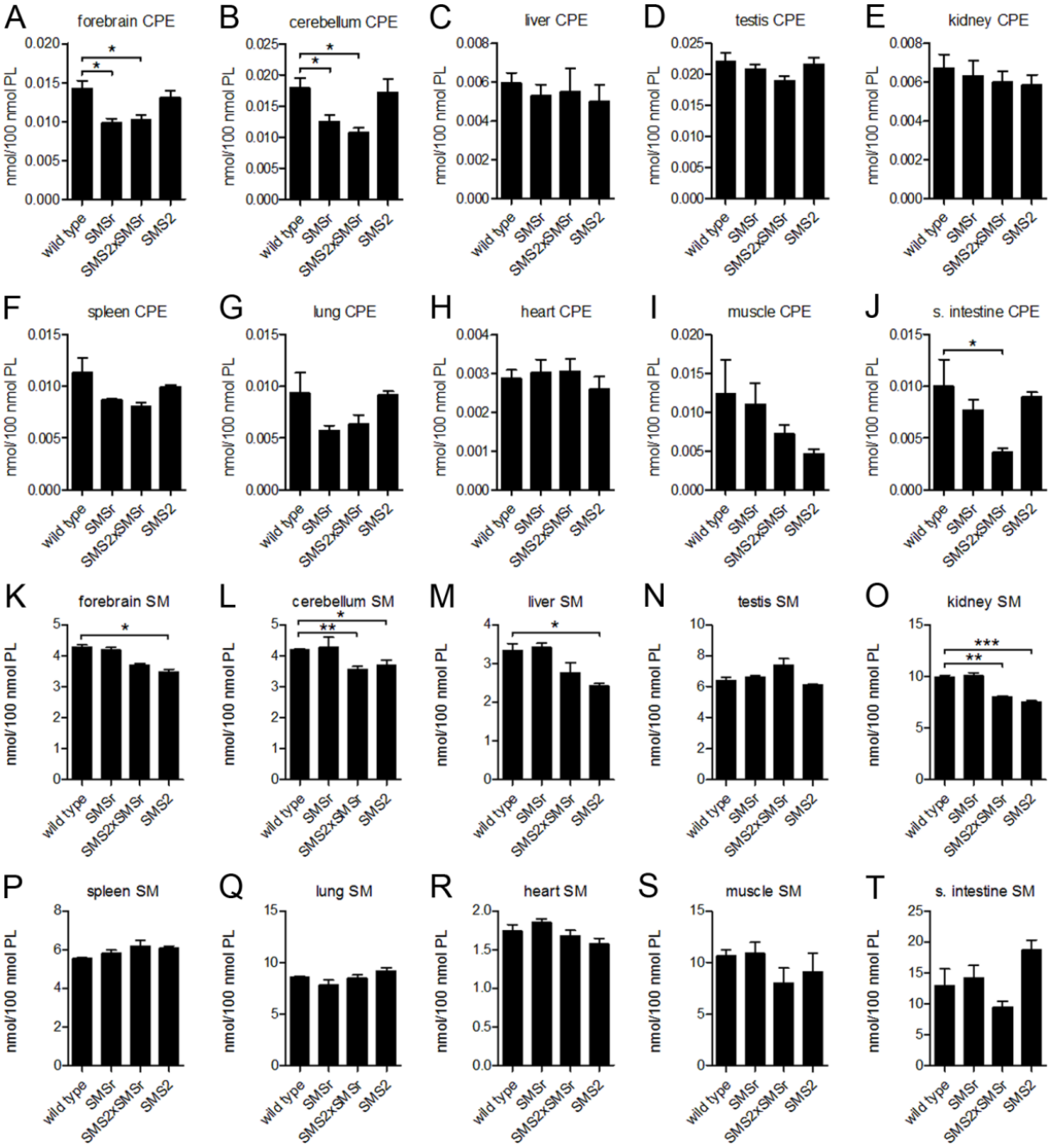

Figure 4.12 - LC-MS analysis of CPE and SM content in forebrain, cerebellum, liver, testis, kidney, spleen, lung, heart, muscle and small intestine of wild type, SMSrD348E, SMS2gtXSMSrD348E and SMS2gt mice. (A-J) Sum of main CPE species. (K-T) Sum of main SM species. Data are means ± SEM; two-tailed *Student's t test*: *, *p<0.05;* **, *p<0.005;* ***, *p<0.001; n=3-4.* (adopted and modified from Bickert et al., 2015)

In addition to brain and liver, the CPE (and SM) content was also determined in other tissues. In testis and kidney total CPE levels were largely unaffected in mutant mice (Figure 4.12 D, E). However, a minor decrease in C16:0 and a significant decrease in C18:0 CPE species were observed compared to wild type mice (~10-20%), depending on depletion of SMSr in testis and of both CPE synthases in kidney (Figure 4.13 A, B). In spleen total CPE levels were decreased by about 30 % and in lung by about 50 % compared to wild type mice, but the difference was not significant

(Figure 4.12 F, G). This was characterized by a decrease in C16:0 to C20:0 CPE species, which only reached statistical significance for C20:0 species (Figure 4.13 C, D). In small intestine, the sum of the main CPE species was decreased by about 70 % only in SMS2gt X SMSrD348E double mutant mice (Figure 4.12 J). This was characterized by a decrease C16:0 to C20:0 CPE species, which was only significant for C16:0 species (Figure 4.13 G). No significant differences in total CPE levels between wild type and mutant mice were observed in heart (Figure 4.12 H), but C16:0 CPE levels, although not significant, were decreased in SMS2 mutant mice (Figure 4.13 E). In muscle, total CPE levels were decreased by 40-50 % in SMS2 and double mutant compared to wild type mice, but the differences were not significant (Figure 4.12 I). The loss of SMS2 affected C16:0, as well as C18:0 CPE species (Figure 4.13 F). Total SM levels were significantly decreased in kidney (~25 %) of SMS2 and double mutant mice (Figure 4.12 O), depletion of SMS2 affected all major species except for C16:0 SM (Figure 4.14 B).

The data on steady-state CPE levels in wild type and SMSr mutant mice show that SMSr is a major determinant for CPE levels in the brain. Furthermore, SMSr contributes to a minor extent to the CPE content in testis, kidney, spleen and lung. In none of the investigated tissues, combined inactivation of both known CPE synthases (i.e. SMSr and SMS2) did completely eliminate CPE.

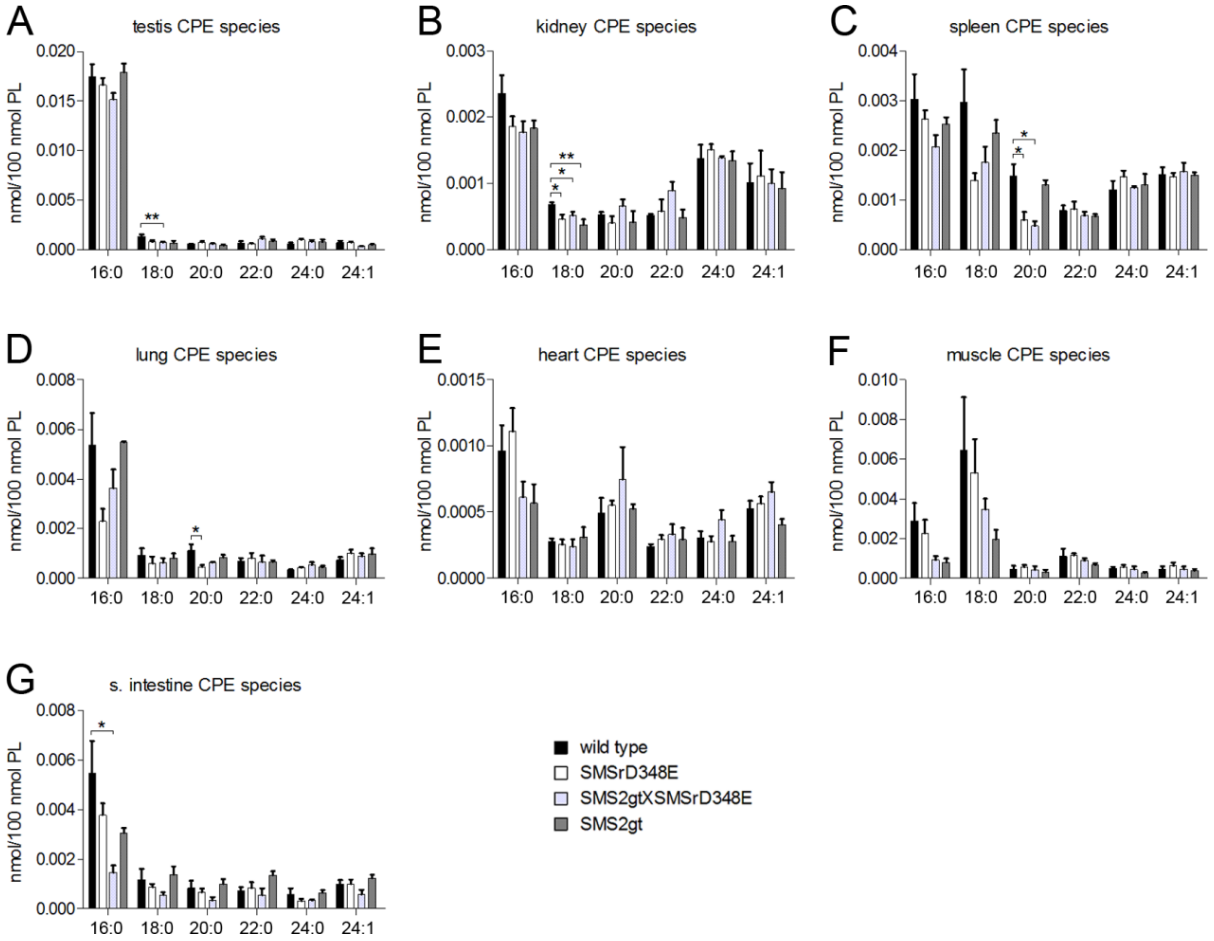

Figure 4.13 - LC-MS analysis of main CPE species in testis (A), kidney (B), spleen (C), lung (D), heart (E), muscle (F) and small intestine (G) of wild type, SMSrD348E, SMS2gtXSMSrD348E and SMS2gt mice. Data are means ± SEM; two-tailed *Student's t test*: *, *p<0.05; **, p<0.005; n=3-4.* (adopted and modified from Bickert et al., 2015)

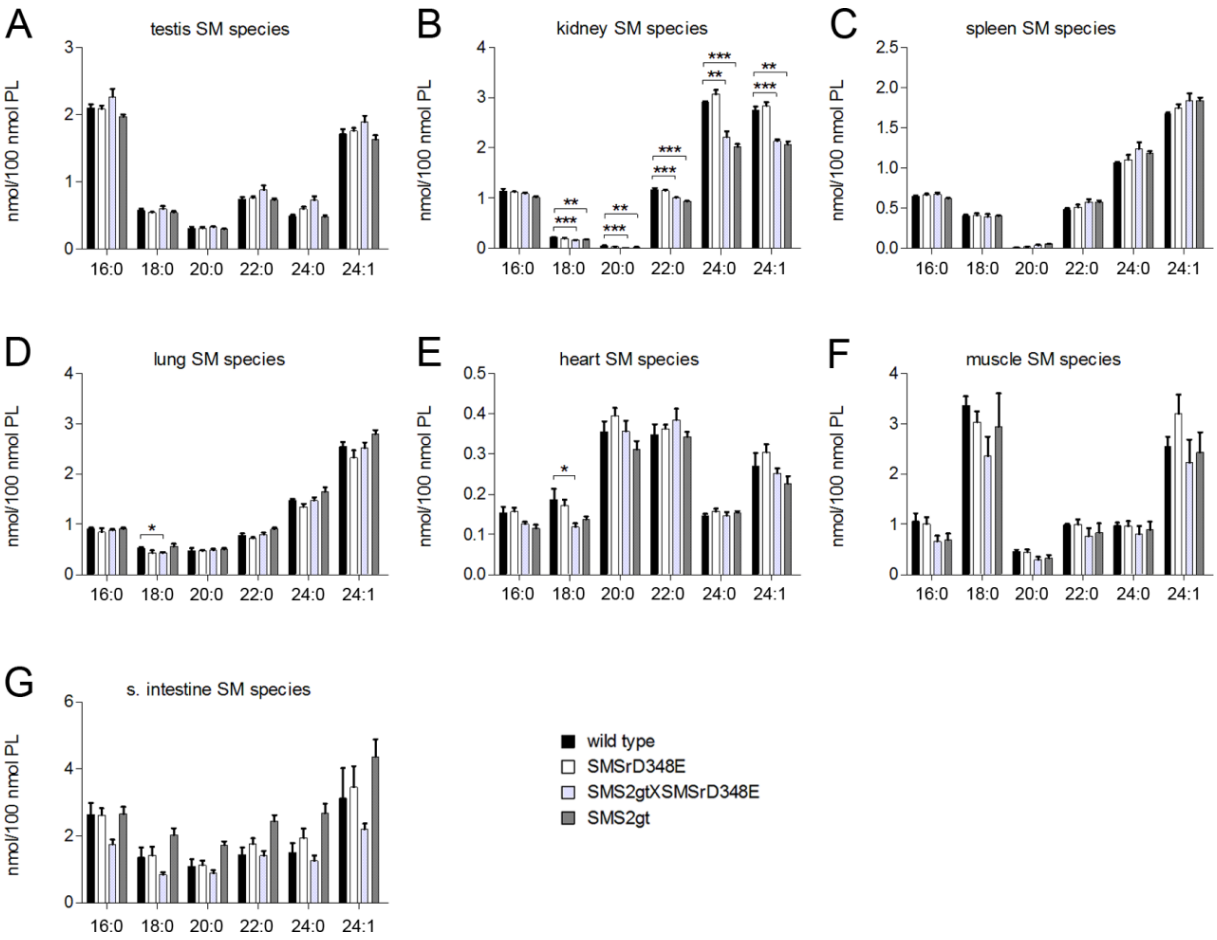

Figure 4.14 - LC-MS analysis of main SM species in testis (A), kidney (B), spleen (C), lung (D), heart (E), muscle (F) and small intestine (G) of wild type, SMSrD348E, SMS2gtXSMSrD348E and SMS2gt mice. Data are means ± SEM; two-tailed *Student's t test*: *, *p<0.05; **, p<0.005; ***, p<0.001; n=3-4.* (adopted and modified from Bickert et al., 2015)

4.1.5.3 Determination of ceramide levels in SMSr and SMS2 mutant mice

In human HeLa and *Drosophila* S2 cells, acute depletion or catalytic inactivation of SMSr led to a massive accumulation of ceramide and hexosylceramide in the ER (Vacaru *et al.*, 2009). To investigate if inactivation of SMSr leads to a similar effect in mice, the ceramide and hexosylceramide levels in different tissues from wild type and SMSrD348E mice were determined by quantitative MS/MS analysis. Additionally, the analysis included SMS2gt and SMS2gt X SMSrD348E mice.

In forebrain, cerebellum and liver of SMSrD348E mice none of the investigated main species of ceramide or hexosylceramide were increased compared to wild type mice (Figure 4.15). The same was true for ceramide species (Figure 4.16) and hexosylceramide species (Figure 4.17) in the other investigated tissues of SMSrD348E compared to wild type mice. Only in testis of SMSrD348E compared to wild type mice a slight increase in C24:0 ceramide (~50 %) was observed (Figure 4.16 A), but the levels of C24:0 ceramide in testis are rather low (~0.5 % relative to the total level of main ceramide species Figure 4.18 D). Consistent with these

findings, total levels of ceramide and hexosylceramide species were unaltered in SMSrD348E compared to wild type mice in all of the investigated tissues (Figure 4.18).

A minor increase in C24:1 ceramide was observed in forebrain of SMS2gt compared to wild type mice and a similar increase was observed for C24:1 hexosylceramide (Figure 4.15 A, D). Moreover, C18:0 to C24:1 hexosylceramide species were increased in liver of SMS2 mutant compared to wild type mice (Figure 4.15 F). Total ceramide levels were not affected by SMS2 depletion in brain and liver (Figure 4.18 A-C). Total hexosylceramide levels were increased by about 30 % in liver of SMS2gt compared to wild type mice, but the difference did not reach statistical significance (Figure 4.18 M). In kidney of SMS2gt and double mutant mice C16:0 and C24:0 ceramide species were increased compared to wild type mice (Figure 4.16 B) and also C16:0, C22:0 and C24:0 hexosylceramide species were increased in these mice Figure 4.17 B). Consistent with these findings, total ceramide levels in kidney were increased by about 15 % in SMS2 mutant compared to wild type mice, and total hexosylceramide species were increased by about 25 % (Figure 4.18 E, O). In spleen of SMS2gt and double mutant mice C22:0, C24:0 and C24:1 ceramide (Figure 4.16 C) and hexosylceramide (Figure 4.17 C) species were increased compared to wild type mice. Total ceramide and hexosylceramide levels in these mice were increased by about 15-20 % compared to wild type mice (Figure 4.18 F, P). Depletion of SMS2 increased C22:0 and C24:0 ceramide- (Figure 4.16 D, E) and hexosylceramide (Figure 4.17 D, E) species in lung and heart compared to mice expressing functional SMS2. The decrease significantly affected total ceramide levels in lung (~30 %; Figure 4.18 G) and total hexosylceramide levels in heart (~60 %; Figure 4.18 R) of SMS2 mutant mice.

These results indicate that ceramide and hexosylceramide levels are not affected by loss of SMSr catalytic activity. In contrast, loss of SMS2 increased ceramide and hexosylceramide levels in liver, kidney, spleen, lung and heart and to a minor extent in forebrain, but the increases were not especially pronounced.

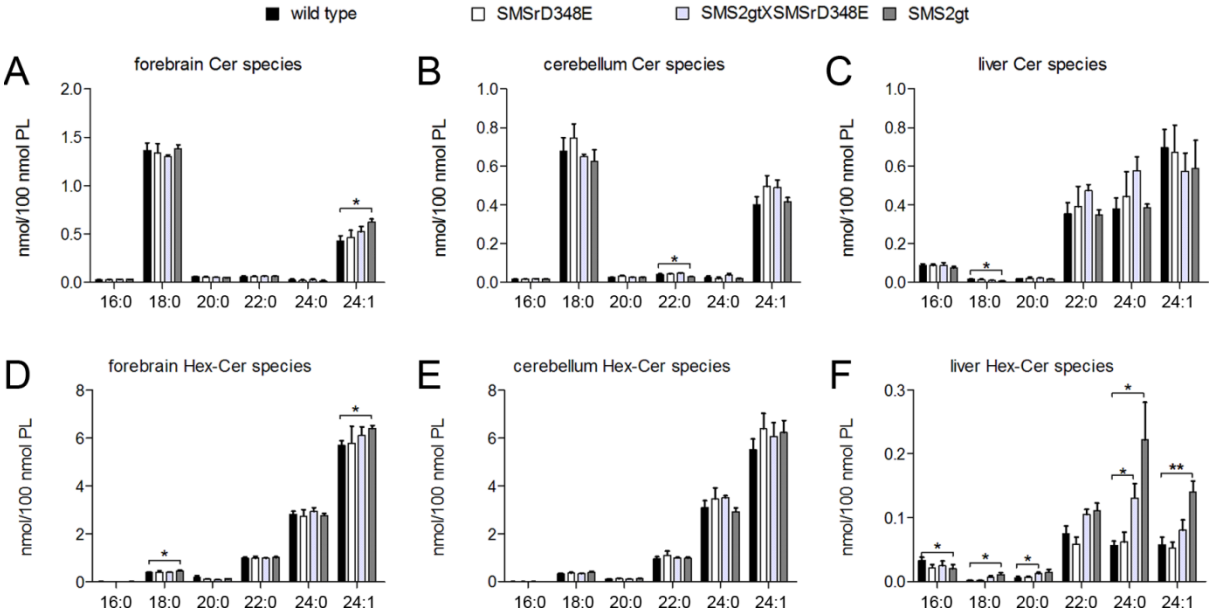

Figure 4.15 - MS analysis of ceramide and hexosylceramide species in forebrain, cerebellum and liver of wild type, SMSrD348E, SMS2gtXSMSrD348E and SMS2gt mice. (A-C) Analysis of main ceramide species. (D-E) Analysis of main hexosylceramide (Hex-Cer) species. Data are means ± SEM; two-tailed Student's t test: *, p<0.05; **, p<0.005; n=3-4. (adopted and modified from Bickert et al., 2015).

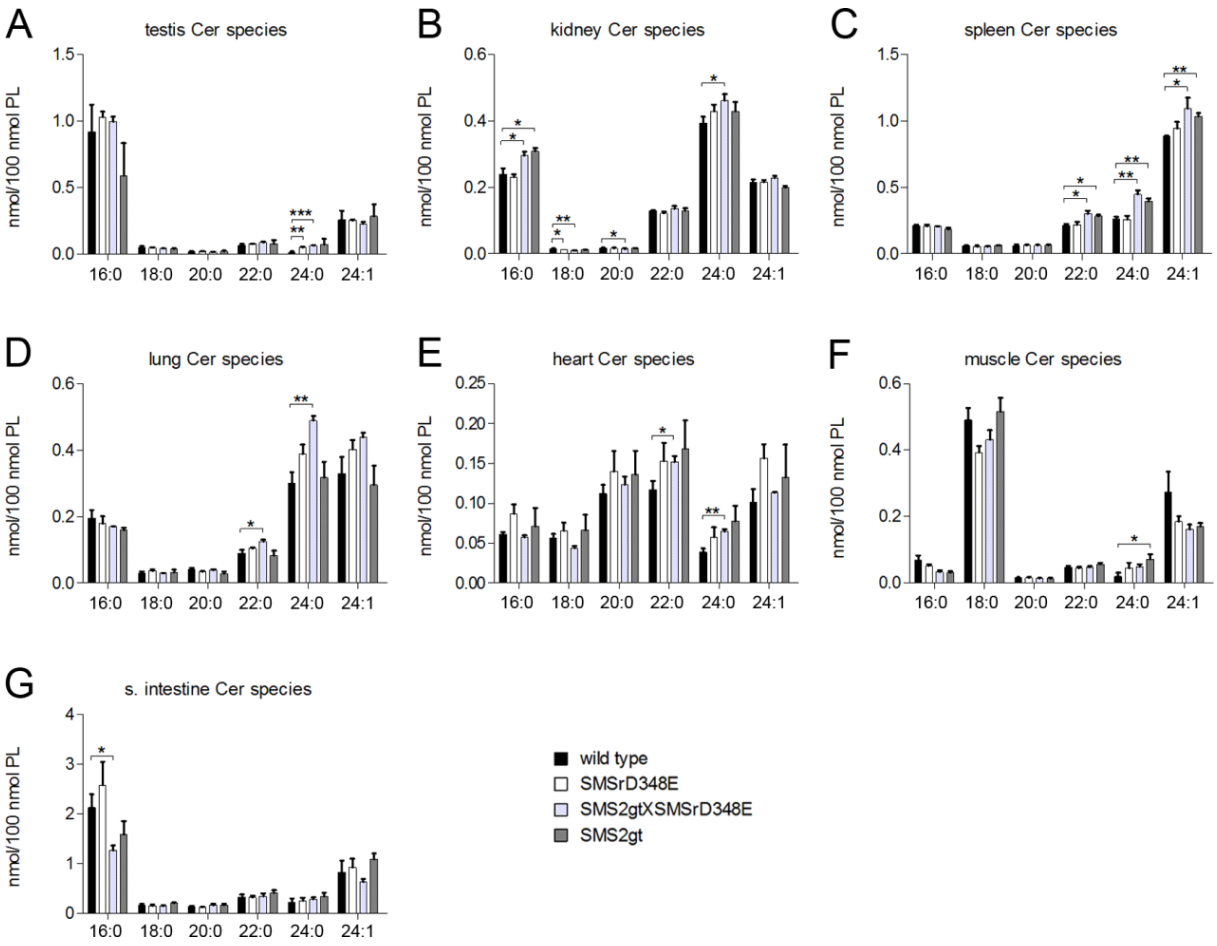

Figure 4.16 - MS analysis of main ceramide species in testis (A), kidney (B), spleen (C), lung (D), heart (E), muscle (F) and small intestine (G) of wild type, SMSrD348E, SMS2gtXSMSrD348E and SMS2gt mice. Data are means of two independent

measurements ± SEM; two-tailed *Student's t test*: *, *p<0.05; **, p<0.005; ***, p<0.001; n=3-4.* (adopted and modified from Bickert et al., 2015)

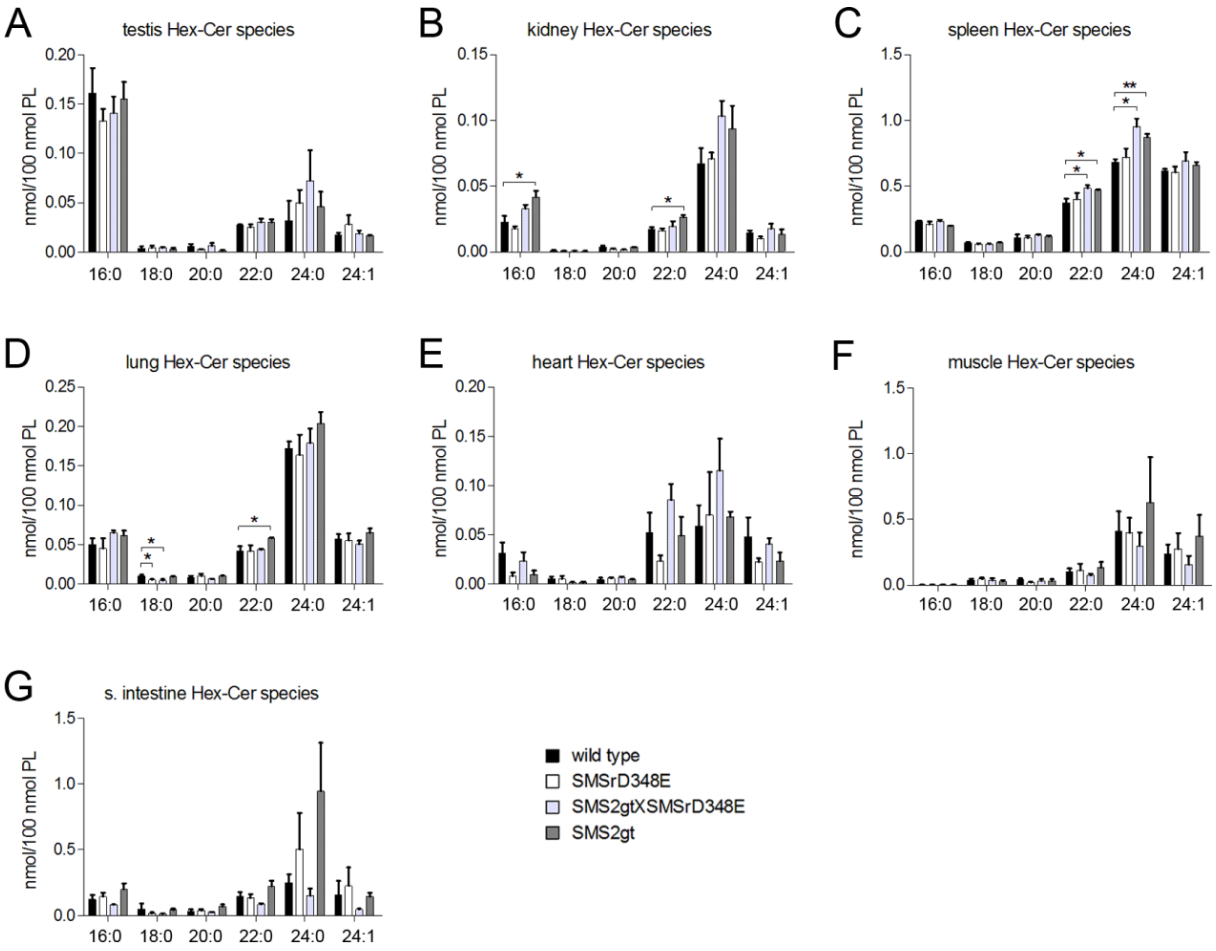

Figure 4.17 - MS analysis of main hexosylceramide species in testis (A), kidney (B), spleen (C), lung (D), heart (E), muscle (F) and small intestine (G) of wild type, SMSrD348E, SMS2gtXSMSrD348E and SMS2gt mice. Data are means of two independent measurements ± SEM; two-tailed *Student's t test*: *, p<0.05; **, p<0.005; n=3-4.* (adopted and modified from Bickert et al., 2015)

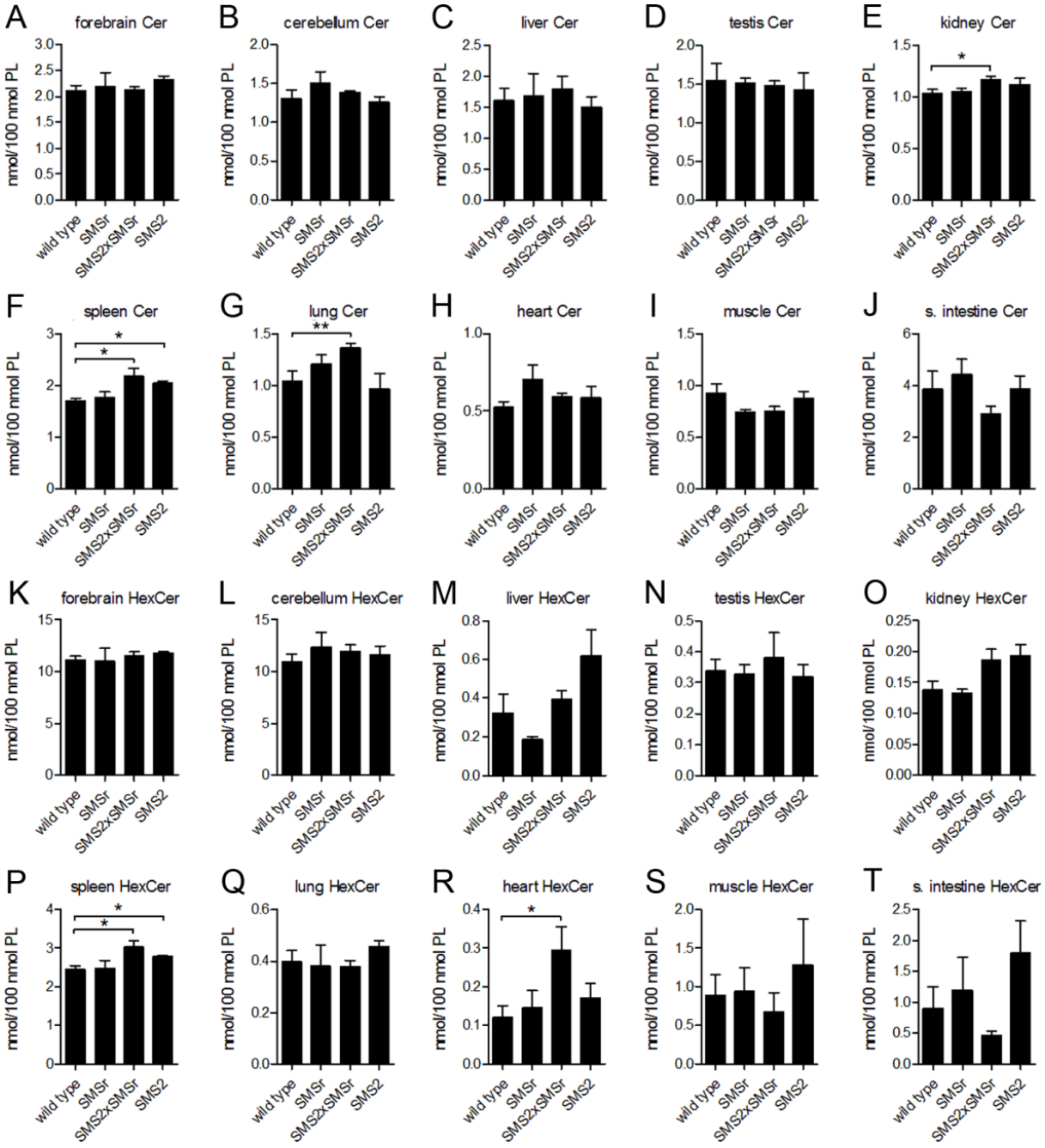

Figure 4.18 - MS analysis of ceramide and hexosylceramide content in forebrain, cerebellum, liver, testis, kidney, spleen, lung, heart, muscle and small intestine of wild type, SMSrD348E, SMS2gtXSMSrD348E and SMS2gt mice. (A-J) Sum of main ceramide species. (K-T) Sum of main hexosylceramide species. Data are means of two independent measurements ± SEM; two-tailed *Student's t test*: **, p<0.05; **, p<0.005; n=3-4.* (adopted and modified from Bickert et al., 2015)

Besides measuring the sphingolipid levels in wild type and SMSr and SMS2 mutant mice, various glycerophospholipid classes were analyzed by quantitative MS/MS analysis (Figure 4.19). The analysis revealed no remarkable changes for most of the investigated tissues. The total levels of phosphatidylethanolamine (PE) and phosphatidylserine (PS) were slightly increased in spleen and heart of the mutant mice (Figure 4.19 F, H).

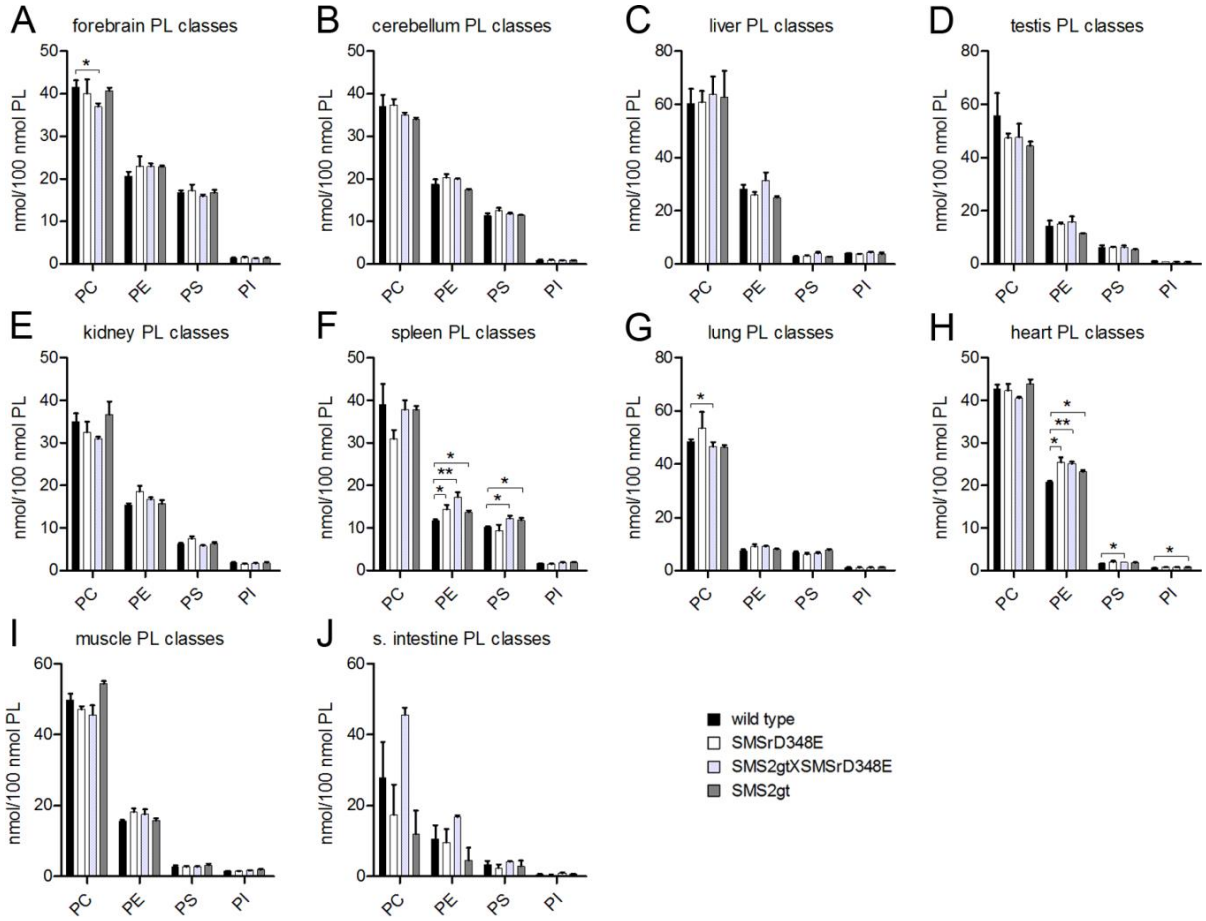

Figure 4.19 - MS analysis of glycerophospholipid content in forebrain (A), cerebellum (B), liver (C), testis (D), kidney (E), spleen (F), lung (G), heart (H), muscle (I) and small intestine (J) of wild type, SMSrD348E, SMS2gtXSMSrD348E and SMS2gt mice. Data are means of two independent measurements ± SEM; two-tailed *Student's t test*: **, p<0.05; **, p<0.005; n=3-4* (PC, phosphatidylcholine, PE, phosphatidylethanolamine, PS, phosphatidylserine, PI, phosphatidylinositol). (adopted and modified from Bickert et al., 2015)

Liver and brain samples from wild type and SMSrD348E mice were also investigated in independent MS analyses in collaboration with Dr. Katharina vom Dorp from the group of Prof. Peter Dörmann (University of Bonn). These quantitative-time of flight (Q-TOF)-MS analyses confirmed the data presented on SM, ceramide and hexosylceramide content and additionally, revealed no significant alterations in the levels of species with hydroxylated and odd-numbered fatty acyl-chains or in free LCBs (d18:0, d18:1, d18:2; data not shown).

4.1.6 Ultra-structural analysis of cellular integrity in SMSrD348E mice

Acute depletion of SMSr in cultured HeLa cells was accompanied by fragmentation of ER exit sites, a structural collapse of the early secretory pathway and induction of a mitochondrial pathway of apoptosis (Vacaru *et al.*, 2009; Tafesse *et al.*, 2014). Therefore, liver and brain ultra-thin sections from SMSrD348E mice were screened for ultra-structural aberrations in collaboration with Dr. Holger Jastrow and Prof. Elke Winterhager (University Hospital/University of Essen).

A systematic analysis of brain sections from SMSrD348E mice revealed that the integrity of neuronal cells from different brain regions of SMSrD348E mice was not significantly altered compared to wild type littermates (Figure 4.20 A, B). In hepatocytes of SMSrD348E mice no obvious alteration in ER or Golgi morphology was observed compared to wild type littermates (Figure 4.20 C, D). Moreover, neither integrity of mitochondria, nor the number or appearance of lipid droplets or glycogen granules was altered. In conjunction with these findings, analysis of kidney sections also revealed no differences in cellular integrity between wild type and SMSrD348E mice (data not shown).

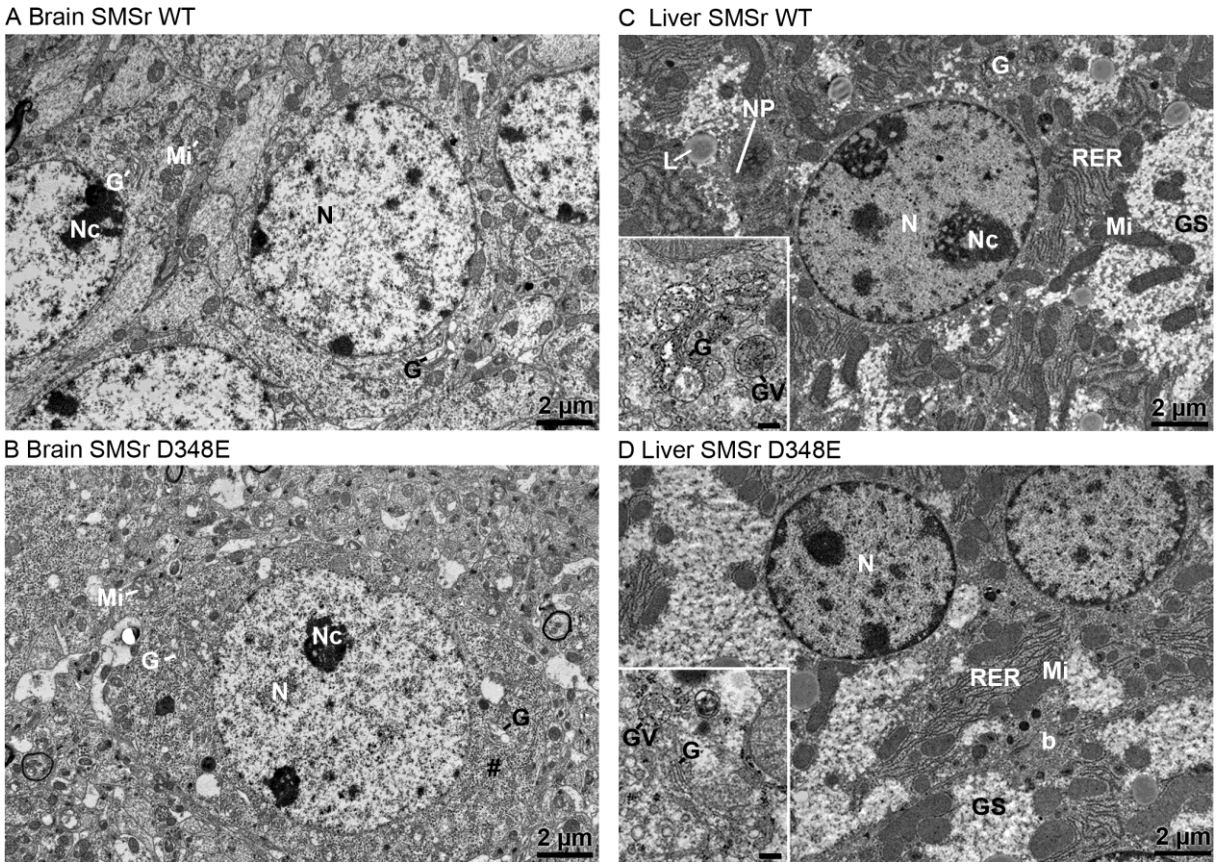

Figure 4.20 - Electron micrographs of hepatocytes and hippocampal neurons of wild type and SMSrD348E mice. (A) Hippocampal neurons of wild type mice revealed the typical morphology with abundant free ribosomes, mitochondria and some Golgi-complexes. (B) No obvious alterations in the morphology of cell organelles were observed in comparable SMSrD348E neurons. (C) Wild type mice reveal the typical cellular equipment of liver cells with abundant rough endoplasmic reticulum (RER), numerous mitochondria (Mi), lipid droplets (L) and large glycogen stores (Gs). Higher magnification of a small Golgi-apparatus which is typical for liver cells shows big vesicles containing lipoprotein complexes (insert). (D) No obvious morphological differences are detectable in cell organelles of a SMSrD348E hepatocyte. Higher magnification of a comparable Golgi-complex does show the same appearance with large vesicles containing lipoproteins (insert). For analysis littermates were used (*n=4*). b, bile canaliculus; G, Golgi-apparatus, Gs, glycogen stores; GV, Golgi vesicle; L, lipid droplet; Mi, mitochondria; #, Nissl substance; NP, nuclear pores; Nc, nucleolus; N, nucleus; scale bar insert, 200 nm. (adopted and modified from Bickert et al., 2015)

To further investigate liver integrity in SMSrD348E mice, serum activities of liver transaminases (ALT/AST) and creatine phosphokinase (CPK) were measured in collaboration with Prof. Gunther Hartmann (University Hospital Bonn). No significant differences were found between wild type and SMSrD348E mice (Figure 4.21).

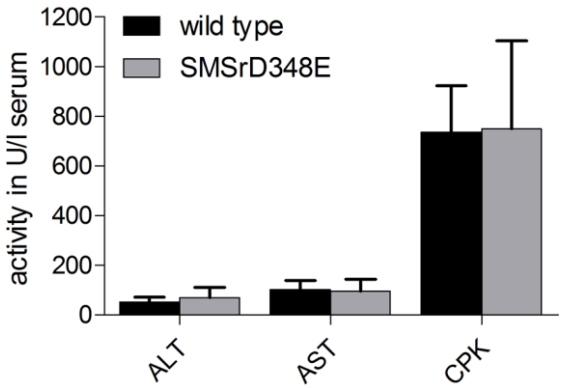

Figure 4.21 - Analysis of serum activities of alanine transaminase (ALT), aspartate transaminase (AST) and creatine phosphokinase (CPK) in wild type (n=6) and SMSrD348E (n=3) mice. Data are means ± SEM. (adopted and modified from Bickert et al., 2015)

Taken together, disruption of SMSr catalytic activity has no impact on the structural integrity of mouse brain, liver and kidney cells. Therefore, in contrast to human HeLa and *Drosophila* S2 cells after acute depletion of SMSr, cells in SMSrD348E mice appear to lack phenotypic abnormalities associated with a deregulation of ER ceramide levels.

4.2 Diet-induced obesity in ceramide synthase 4 deficient mice

As discussed in chapter 1.3.3.5 several CerS have been shown to be involved in diet-induced obesity in mice. These studies suggested an essential function of C16 ceramide in the development of obesity. Nevertheless, not much is known about the specific function of CerS4 and corresponding C18 to C22 ceramides in mice, except for an essential function in the skin (see chapter 1.3.2.4). To investigate possible implications of CerS4 and corresponding ceramide species in the development of obesity, CerS4 deficient mice were subjected to high fat diet feeding.

CerS4 deficient mice were generated in our group by Dr. Silke Imgrund and the basic characterization was performed by Dr. Philipp Ebel (see chapter 1.3.2.4). In these mice the whole coding region, ranging from exon 2 to exon 11 was exchanged by an NLS-LacZ reporter gene for investigation of CerS4 expression (Figure 4.22).

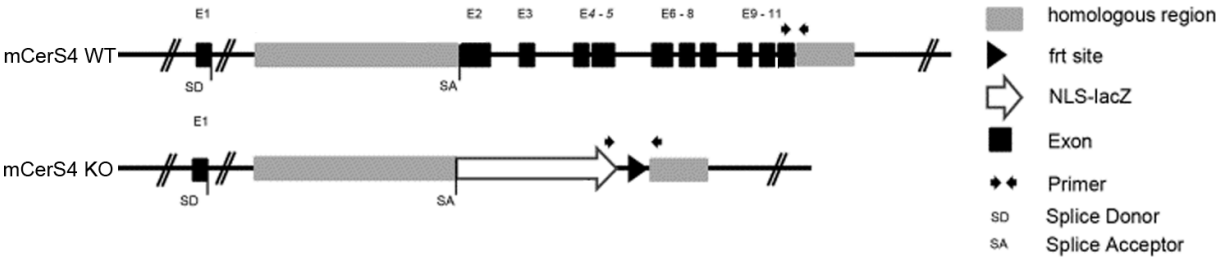

Figure 4.22 – Scheme of the CerS4 locus in wild type and CerS4 deficient mice. The CerS4 wild type (WT) locus is approximately 33 kb in size and consists of 11 exons of which the first encodes the 5' untranslated region. To generate CerS4 deficient (KO) mice, the whole coding region (exons 2-11) was exchanged by an NLS-LacZ reporter gene. Arrows indicate position of primers used for mouse genotyping. (adopted and modified from Ebel et al., 2014)

4.2.1 High fat diet feeding of CerS4 deficient mice

For analysis of CerS4 function in the development of obesity, male wild type (WT) and CerS4 deficient (KO) mice were either fed a high fat diet (HFD; 60 % kcal from fat) or a low fat diet (LFD; 10 % kcal from fat) for 16 weeks. Four different groups, each of approximately 20 mice were investigated, subsequently denoted as WT HFD, KO HFD, WT LFD and KO LFD. Prior to starting the experiment, animals were 7-8 weeks old and weight matched.

HFD feeding led to a strong, diet-dependent increase in weight gain within genotypes, the differences for WT mice were significant starting from week 4 (week 4: WT HFD +1.6 g; week 16: WT HFD +6.6 g), those for KO mice starting from week 6 (week 6: KO HFD +2.0 g; week 16: KO HFD +3.0 g) (Figure 4.23 A). Strikingly, KO mice fed HFD showed significantly reduced weight gain compared to WT mice starting from week 10 (week 10: WT HFD +1.9 g; week 16: WT HFD +3.7 g), while no difference was observed between WT and KO mice on LFD (week 16: WT LFD +0.1 g). Remarkably, weight gain after HFD consumption was

reduced, although food intake was significantly increased in KO compared to WT mice (~3.2 g per week; Figure 4.23 B). This was also the case for intake of LFD (~3.8 g per week), but weight gain was not altered between WT and KO mice.

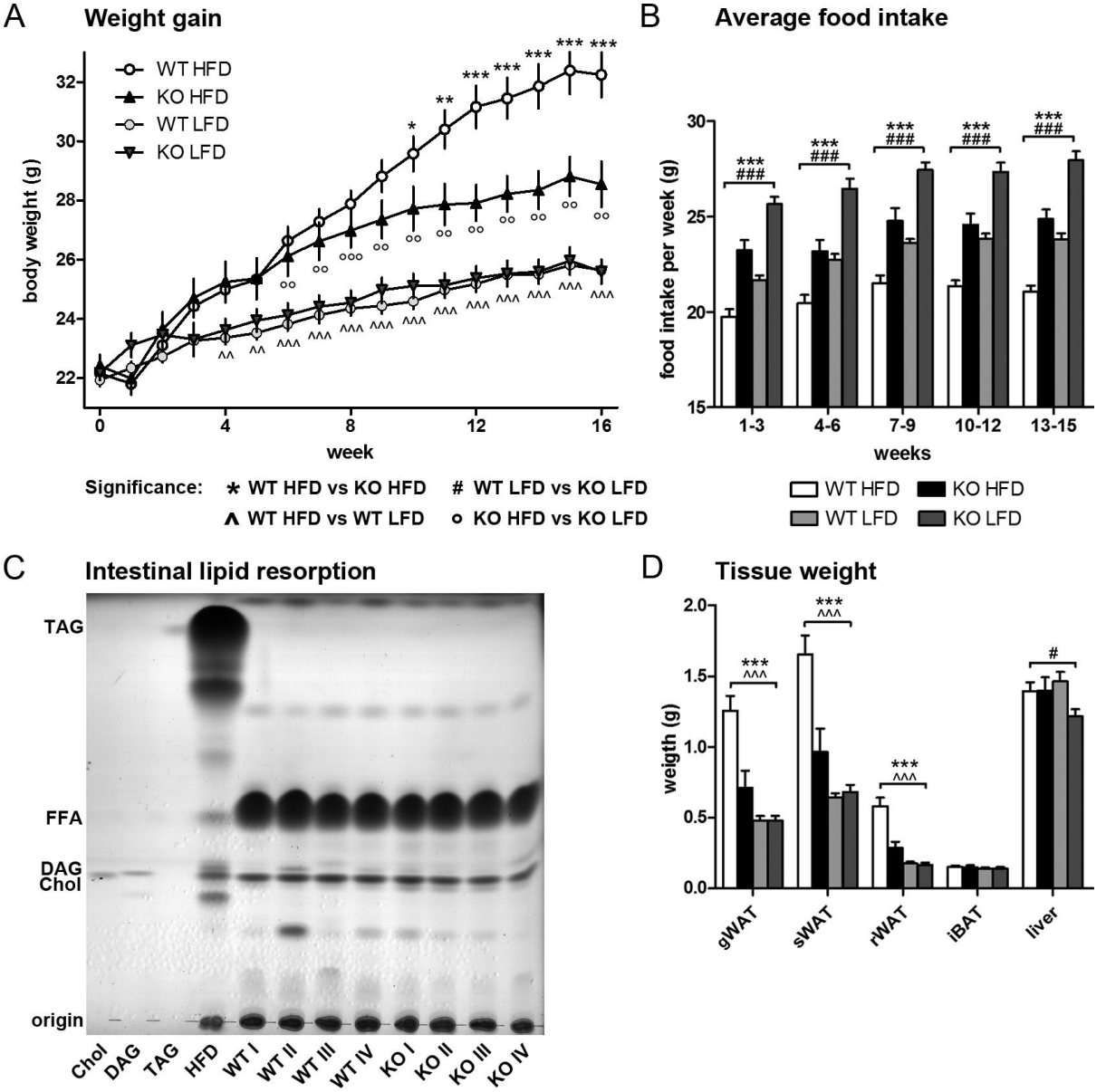

Figure 4.23 – Weight gain and food intake during high fat diet feeding. 7-8 week old wild type (WT) and Cers4 deficient mice (KO) were fed either high fat diet (HFD) or low fat diet (LFD) for 16 weeks. (A) Growth curve illustrating genotype and diet-dependent weight gain differences. (B) Average food intake per week, depicted are means of three consecutive weeks. Intake of HFD and LFD strongly differed within genotypes, but for reasons of clarity significance is not depicted (A and B n=22; 16; 22; 17 mice for WT HFD; KO HFD; WT LFD; KO LFD, respectively). (C) TLC analysis of lipid extracts from feces collected after 5 weeks of HFD feeding (n=4 mice). Chol, cholesterol; DAG, diacylglycerol; FFA, free fatty acids; TAG, triacylglycerol. (D) Tissue weight after 16 week exposure to HFD or LFD (n=19; 13; 19; 13 mice). g, gonadal; i, interscapular; r, renal; s, subcutaneous. Data are means ± SEM; significance indicators: *1x, p<0.05; 2x, p<0.01; 3x, p<0.001*.

TLC analysis of lipid extracts from feces collected after 5 weeks of HFD feeding revealed no alterations in the levels of triacylglycerols, diacylglycerols or free fatty acids between WT and KO mice (Figure 4.23 C). In line with the observed body weight gain, analysis of tissue weights revealed a substantial increase in gonadal- (~160 %), subcutaneous- (~160 %) and renal- (~230 %) WAT weight in WT mice fed HFD compared to WT mice fed LFD (Figure 4.23 D). In comparison, consistent with the reduction in body weight gain, KO mice showed strongly reduced weights of gonadal- (~40 %), subcutaneous- (~40 %) and renal- (~50 %) WAT compared to WT mice after HFD consumption. Adipose tissue weights from KO mice fed HFD were slightly but not significantly increased compared to those of WT and KO mice fed LFD, which did not differ from each other. HFD feeding did not alter weights of interscapular BAT (iBAT) and liver. Moreover, the genotype had no effect on iBAT weight, but liver weight was significantly decreased in KO compared to WT mice after 16 week exposure to LFD.

4.2.2 Glucose tolerance and insulin sensitivity in CerS4 deficient mice

Prior to starting the feeding experiment, animals were subjected to glucose tolerance tests (GTTs) and insulin tolerance tests (ITTs). Interestingly, at the age of 7-8 weeks KO mice displayed significantly increased glucose tolerance (Figure 4.24 A and E) and insulin sensitivity (Figure 4.24 B and G). Upon exposure to HFD, WT mice developed severe glucose intolerance (Figure 4.24 C and F) and moderate insulin insensitivity compared to WT mice fed LFD (Figure 4.24 D and H). Strikingly, KO mice were protected from diet-induced glucose intolerance and displayed an insulin sensitivity similar to that observed for KO mice after consumption of LFD. Moreover, comparable to the measurements from 7-8 week old animals, glucose tolerance and insulin sensitivity were still significantly increased in 23-24 week old KO compared to WT mice after consumption of LFD.

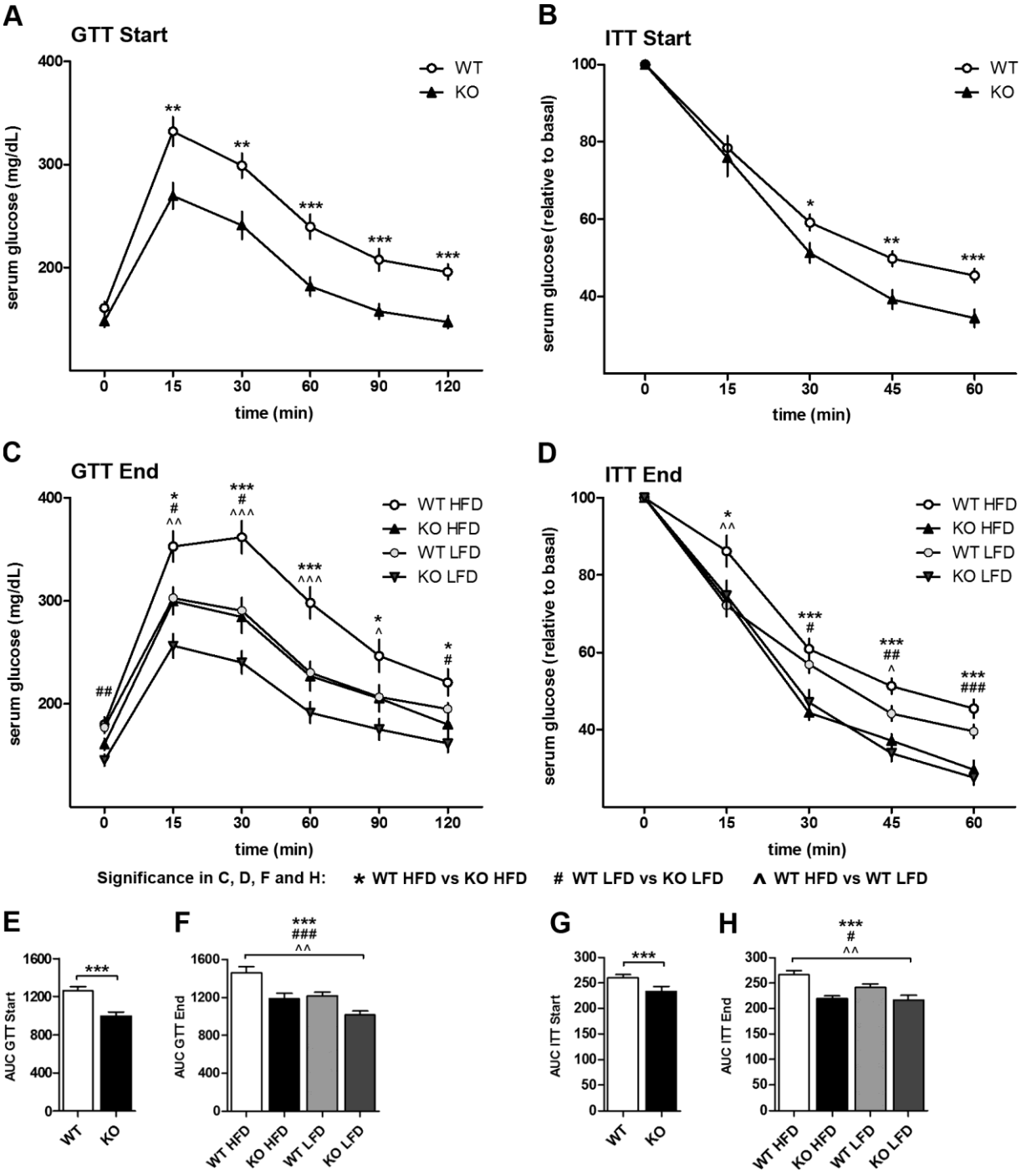

Figure 4.24 - Glucose and insulin tolerance in CerS4 deficient mice. (A and B) Glucose tolerance test (GTT) and insulin tolerance test (ITT) from 7-8 week old wild type (WT) and CerS4 deficient (KO) mice prior to starting feeding experiment (n=19 for WT, 18 for KO). (C and D) GTT and ITT from 23-24 week old WT and KO mice after 16 week exposure to HFD or LFD (n=22; 16; 22; 17 mice for WT HFD; KO HFD; WT LFD; KO LFD, respectively). (E-H) Area under the curve (AUC) of GTT and ITT prior and after feeding experiment. Data are means ± SEM; significance indicators: *1x, p<0.05; 2x, p<0.01; 3x, p<0.001*.

4.2.3 CerS expression after HFD feeding

To investigate how HFD and depletion of CerS4 affect expression of CerS in mice, tissue lysates of liver and pancreas were investigated by immunoblot analyses (Figure 4.25). Antibodies against CerS4 revealed low expression in WT livers and

suggested an increase following HFD feeding, however due to unspecific binding of the antibodies protein expression was not quantifiable in the liver (Figure 4.25 A and C). Analysis of CerS2 expression revealed no diet-dependent alterations between WT groups, but a moderate increase in KO compared to WT mice on both diets (HFD ~15 %; LFD ~30 %). Expression of CerS6 was not altered between WT and KO mice on both diets. Since insulin receptor (IR)-dependent signaling in the liver was shown to be impaired in CerS2 deficient mice (Park *et al.*, 2013a), expression of the IRβ subchain was investigated in the liver. Diet did not influence IRβ subchain expression in WT mice. However, expression was increased in KO compared to WT mice fed LFD (~30 %) and the difference was even stronger following exposure to HFD (~40 %).

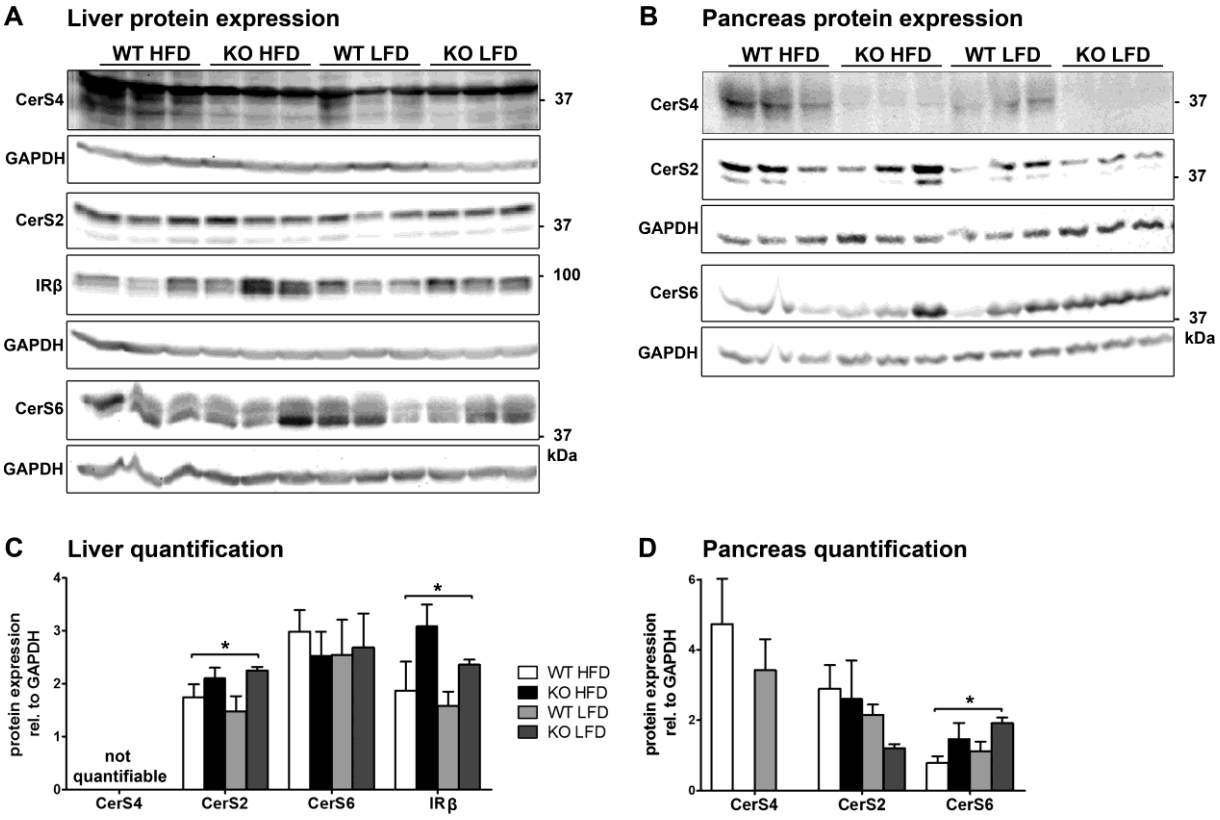

Figure 4.25 – Immunoblot analyses of CerS and insulin receptor expression in liver and pancreas. (A) Protein expression of CerS4, CerS2, CerS6 and insulin receptor β chain (IRβ) in the liver of wild type (WT) and CerS4 deficient mice (KO) after consumption of HFD or LFD. (B) Protein expression of CerS4, CerS2, CerS6 in the pancreas of WT and KO mice KO after consumption of HFD or LFD. (C and D) Densitometric quantification of protein expression relative to GAPDH in liver and pancreas. Due to background signals CerS4 expression was not quantifiable in the liver. Values for pancreas CerS4 expression represent means after background subtraction. 50 µg protein were applied per lane. Data are means ± SEM; n=3-5. Significance indicators refer to genotype-dependent differences based on two-way ANOVA (*, $p<0.05$), Bonferroni post hoc group comparisons revealed no significances.

In pancreas, CerS4 expression was readily detectable and similar to liver, expression seemed to be increased after consumption of HFD (~25 %), but the difference did not reach statistical significance (Figure 4.25 B and D). While CerS2 expression was not

altered between WT and KO mice after HFD consumption, the expression was decreased in KO compared to WT mice following LFD feeding (~40 %), but the difference was not significant. Analysis of CerS6 expression revealed increases in KO compared to WT mice after consumption of both diets (~30-40 %).

4.2.4 Analysis of sphingolipid content in CerS4 deficient mice

To investigate the influence of CerS4 depletion and HFD on the sphingolipid content, lipids extracted from liver, iBAT and pancreas of WT and KO mice after 16 week exposure to HFD or LFD were analyzed. Following extraction the sphingolipid content was determined by quantitative-time of flight (Q-TOF) mass spectrometry in collaboration with Dr. Katharina vom Dorp from the group of Prof. Peter Dörmann (University of Bonn).

In liver, the levels of C18:0, C20:0 and also C22:0 ceramide were decreased in KO compared to WT mice (~50-60 %), but the differences were not significant (Figure 4.26 A). These species were slightly increased (~40-50 %) in HFD compared to LFD fed WT mice. The situation was similar for hexosylceramide species, but C22:0 hexosylceramide was not altered between WT mice after HFD and LFD consumption (Figure 4.26 B). Analysis of liver SM content revealed significant increases in C18:0, C20:0 and C22:0 (~40-50 %) SM levels in HFD compared to LFD fed WT mice (Figure 4.26 C). Moreover, these species were decreased in KO compared to WT mice after exposure to HFD (C18:0 ~50 %; C20:0 ~40 %; C22:0 ~30 %), but the difference was not significant for C22:0 SM species. These data show that CerS4 contributes to the levels of C18:0 and C20:0 sphingolipid species in liver and that C22:0 sphingolipid levels at least partially depend on CerS4.

In iBAT, C16:0 and C24:1 ceramide species were significantly increased in HFD compared to LFD fed WT mice (~50 %; Figure 4.26 D). C18:0 and C20:0 ceramide species were decreased in KO compared to WT mice after HFD consumption (~35 %; ~50 %), but the difference was not significant. Analysis of hexosylceramide species revealed a decrease in C20:0 (~30 %) in KO compared to WT mice fed HFD (Figure 4.26 E). Consumption of HFD led to an increase in C16:0 and C18:0 SM species in WT mice compared to WT mice fed LFD (~40-50 %), but the difference was not significant for C16:0 SM (Figure 4.26 F). However, a similar, but significant increase in C16:0 SM (~40 %) was observed for KO mice fed HFD compared to KO mice fed LFD. Taken together, the data show that CerS4 is responsible for the generation of C18:0 and C20:0, but not C22:0 ceramide species in iBAT, as these species were rather increased in KO mice.

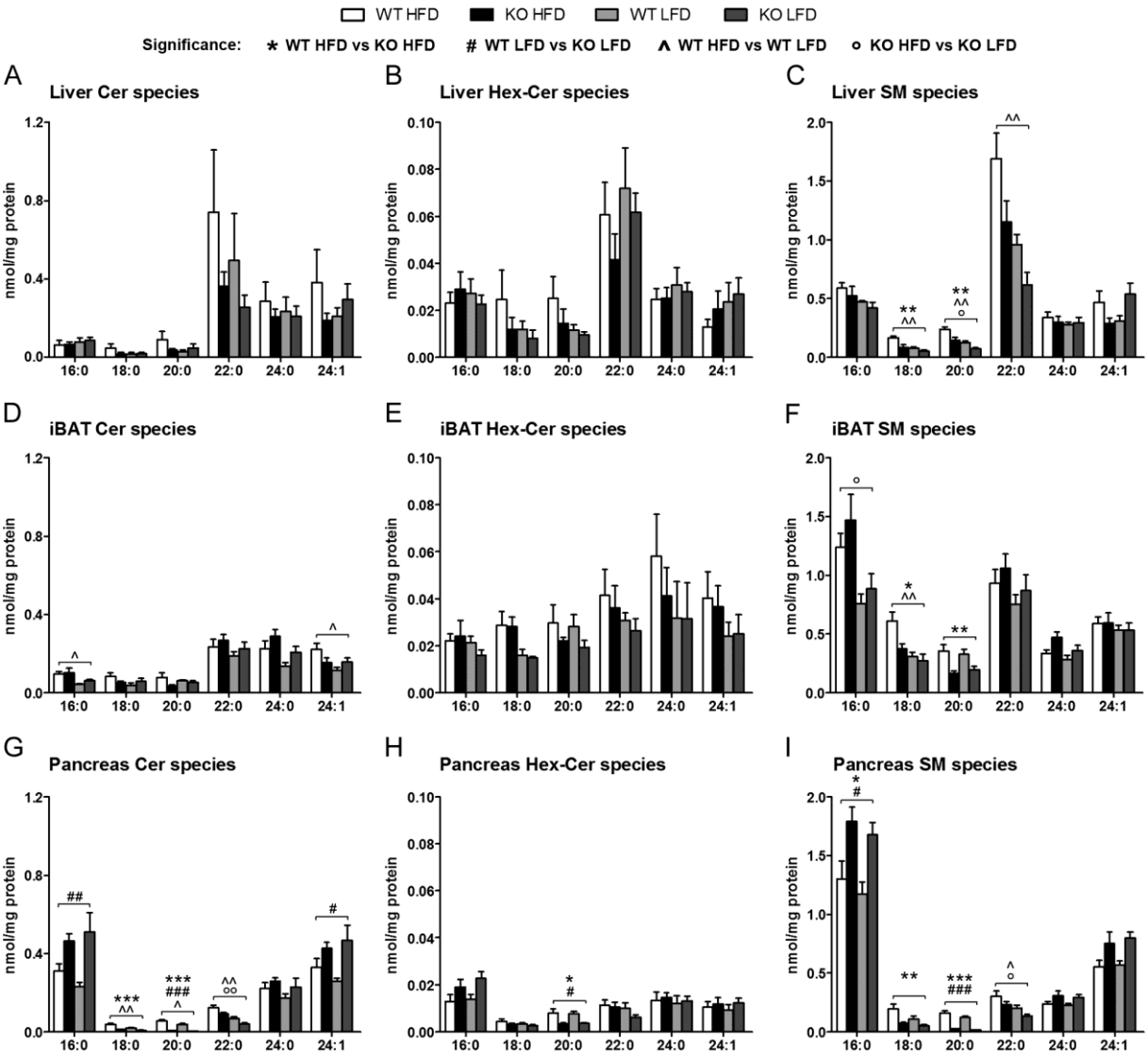

Figure 4.26 – MS analysis of sphingolipid content in liver, brown adipose tissue and pancreas after 16 week feeding. Quantification of main ceramide (Cer), hexosylceramide (Hex-Cer) and sphingomyelin (SM) species with incorporated sphingosine (d18:1) in wild type (WT) and CerS4 deficient (KO) mice after 16 week consumption of HFD or LFD. Investigation of the less abundant species with incorporated sphinganine (d18:0) and sphingadiene (d18:2) revealed similar tendencies. (A-C) Analysis of liver. (D-F) Analysis of interscapular brown adipose tissue (iBAT). (G-I) Analysis of pancreas (G-I). n=4-5; Data are means ± SEM; significance indicators: *1x, p<0.05; 2x, p<0.01; 3x, p<0.001*.

In the pancreas, exposure of WT mice to HFD led to a significant increase (~40-50%) in C18:0, C20:0 and C22:0 ceramide species compared to WT mice fed LFD (Figure 4.26 G). In KO compared to WT mice C18:0 and C20:0 ceramide species were highly significantly decreased (~70 %; ~90 %) and C22:0 species were slightly, but not significantly decreased (~20 %). Interestingly, C16:0 and C24:1 ceramide levels were increased in KO compared to WT mice on HFD (~50 %; ~30 %) and LFD (~55 %; ~45 %), but the differences were only significant for mice fed LFD. Analysis of hexosylceramide levels revealed slight increases in C16:0 and C24:1 species (~15-20 %) and a significant increase in C20:0 hexosylceramide (~40 %) in KO compared to WT mice on both diets (Figure 4.26 H). HFD consumption increased the levels of

C18:0, C20:0 and C22:0 SM levels in WT mice fed HFD compared to WT mice fed LFD (~40 %; ~20 %; ~35 %; Figure 4.26 I). In KO mice C18:0, C20:0 and C22:0 SM species were decreased compared to WT mice (HFD: ~65 %; ~85 %; ~20 %; LFD: ~50 %; ~90 %; ~30 %). The decrease was highly significant for C18:0 and C20:0 SM after HFD consumption, but after LFD consumption only the decrease in C20:0 SM was highly significant. Notably, C16:0 SM species were significantly increased in KO compared to WT mice after consumption of HFD and LFD (~30 %), and also C24:0 and C24:1 ceramide levels were increased (~20-30 %). These data show that C18:0 and C20:0, but also C22:0 sphingolipid levels in the pancreas strongly depend on CerS4 and that depletion of CerS4 leads to an increase in C16:0 ceramide production.

4.2.5 Hair loss in CerS4 deficient mice

It was expected that CerS4 deficient mice would progressively loose hair during the feeding experiment. Nevertheless, according to the findings of Ebel et al. 2014, it was assumed that heat loss up to the age of 23-24 weeks would be negligible at ambient temperatures of about 22°C. However, the thermoneutral temperature of mice is at about 30°C and it was suggested that even minor alterations in fur composition might lead to heat loss and hence compensatory increases in metabolic activity at lower ambient temperatures (Cannon & Nedergaard, 2011). Figure 4.27 presents an overview of the extent of hair loss in CerS4 deficient mice of different age. CerS4 deficient mice are indistinguishable from WT mice till the age of 6-7 weeks, when hair loss becomes visible in the neck and the fur appears tousled. With increasing age, hair loss extends to the back and the decreased density is clearly visible in the back of 22-24 week old animals.

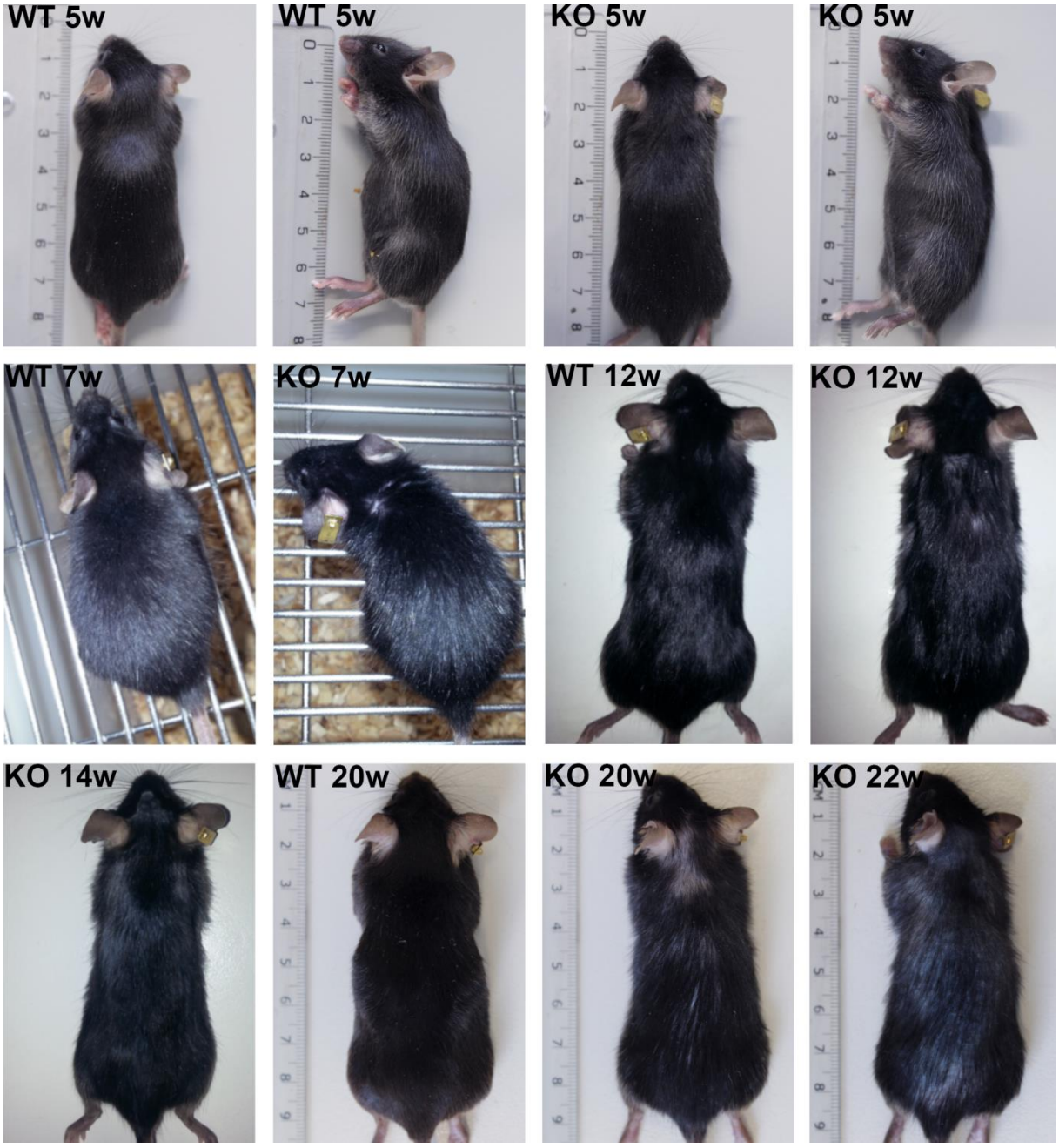

Figure 4.27 - Hair loss in CerS4 deficient mice. 5 week old CerS4 deficient (KO) mice show no obvious signs of hair loss compared to wild type (WT) mice. Hair loss becomes obvious in 6-7 week old animals, starting in the neck. In 12-14 week old animals hair loss starts to extend through the back. 20-22 week old animals show obvious hair loss, characterized by decreased density throughout the back.

It was not possible to clearly distinguish between protective effects resulting from hair loss or from improved function of metabolically active tissues due to lack of CerS4. Therefore, the analysis was continued in 5 week old animals, which as previously discussed show no obvious signs of hair loss (Figure 4.27).

4.3 Energy expenditure and adipose tissue function in CerS4 deficient mice

Protection from diet-induced obesity is often accompanied by increased energy expenditure. Increased energy expenditure can have different reasons. For instance, it can be a consequence of increased muscular activity or result from increased thermogenesis in BAT. To investigate energy expenditure and adipose tissue function in CerS4 deficient mice, a collaboration with Dr. Thorsten Gnad and Prof. Alexander Pfeifer from the Institute of Pharmacology and Toxicology (University of Bonn), who are experts on non-shivering thermogenesis, was initiated.

4.3.1 Oxygen consumption in CerS4 deficient mice

Energy expenditure is usually associated with oxygen consumption. Oxygen consumption of wild type (WT) and CerS4 deficient (KO) mice was determined at different ambient temperatures. Oxygen consumption at 23°C (housing temperature), was measured for 24 h. The analysis revealed significantly increased oxygen consumption in KO compared to WT mice (Figure 4.28 A and B). Mouse motility was not altered at this temperature (Figure 4.28 C). Measurement of food intake during the experiment revealed no differences between WT and KO mice (Figure 4.28 D). Cold exposure, the physiological stimulus for BAT activation, at 4°C for 1 h did also increase oxygen consumption in KO compared to WT mice, but the difference did not reach statistical significance (Figure 4.28 E and F). Oxygen consumption at 4°C was also not affected by increased motility (Figure 4.28 G). In contrast, analysis of mice exposed to 30°C (thermoneutral temperature) for 5 h suggested increased oxygen consumption in KO compared to WT mice, but the difference was only modest and not significant (Figure 4.28 H and I).

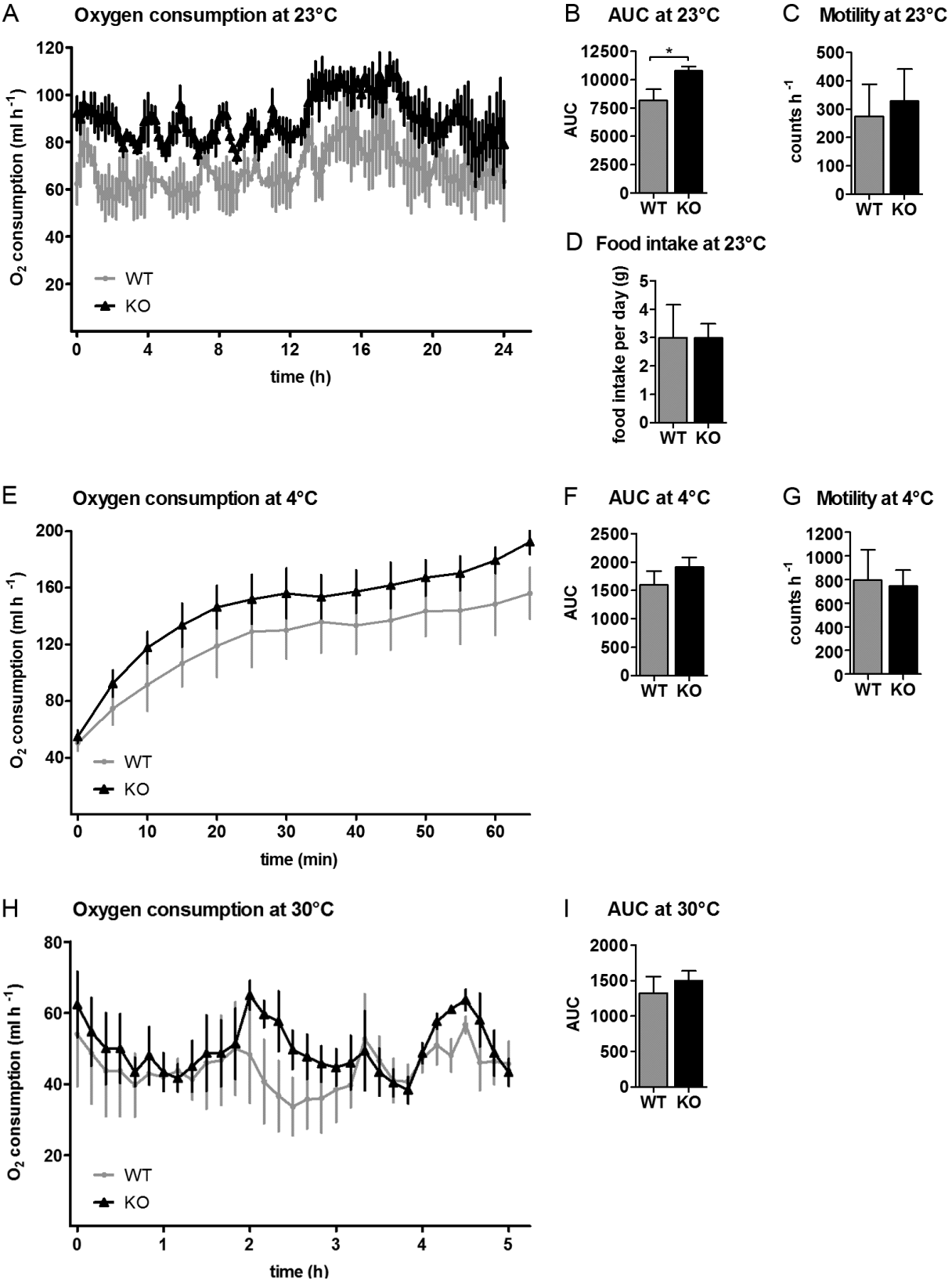

Figure 4.28 – Oxygen consumption in 5 week old mice. Wild type (WT) and CerS4 deficient (KO) mice were subjected to oxygen consumption measurements at different ambient temperatures. (A and B) Oxygen consumption measured for 24 h at 23°C (measurement started at 6 am) and motility (C) and food intake (D) during this time (n=3 for WT; 4 for KO). (E and F) Oxygen consumption measured for 1 h at 4°C and motility (G) during this time (n=3 for WT; 5 for KO). (H and I) Oxygen consumption measured for 5 h at 30°C (n=3). Data are means ± SEM; *, $p<0.05$.

4.3.2 CerS expression in adipose tissue

As a basis for further analyses, different adipose tissue depots of 5 week old WT mice were investigated by immunoblot analysis to determine the protein expression of CerS4 and other CerS (Figure 4.29). The analysis revealed that CerS4 is only weakly expressed in interscapular BAT (iBAT). Expression in white adipose tissue was much stronger, with high levels in inguinal WAT (igWAT; subcutaneous WAT depot) and especially high levels in gonadal WAT (gWAT; visceral WAT depot). CerS2 was highly expressed in all investigated adipose tissue depots with comparable levels in iBAT, igWAT and gWAT. CerS5 showed a similar expression pattern to CerS4. It was virtually absent in iBAT, strongly expressed in igWAT and even stronger in gWAT. In contrast, CerS6 was virtually absent in gWAT and expressed to similar extents in iBAT and igWAT.

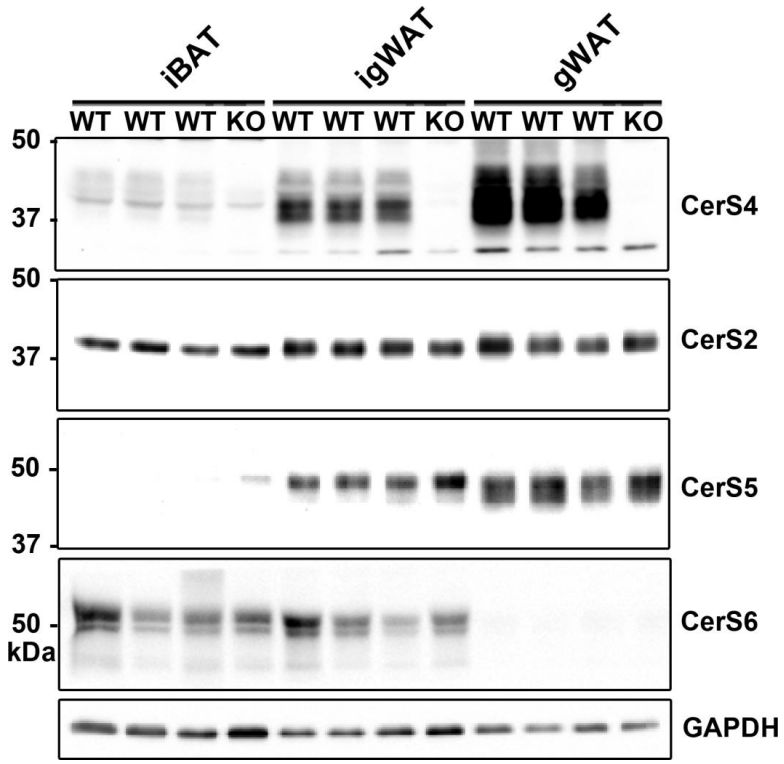

Figure 4.29 – Protein expression of ceramide synthases in adipose tissue of 5 week old mice. Immunoblot analysis of CerS4, CerS2, CerS5 and CerS6 expression in interscapular BAT (iBAT), inguinal WAT (igWAT) and gonadal WAT (gWAT) of wild type (WT) mice (n=3). Tissues from CerS4 deficient (KO) mice served as control for the anti-CerS4 antibodies; GAPDH served as loading control.

4.3.3 Adipose tissue in CerS4 deficient mice

Analysis of 5-6 week old KO mice revealed no differences in body size and body weight compared to WT mice (Figure 4.30 A and B). Similar to that, no differences were observed for iBAT, igWAT and gWAT weight (Figure 4.30 C). H&E (hematoxylin and eosin)-staining of paraffin sections from iBAT revealed slightly increased adipocyte size in KO compared to WT mice (Figure 4.30 D; upper panels). In igWAT, H&E-staining revealed a strong decrease in adipocyte size in KO compared to WT

mice (Figure 4.30 D; lower panels). Moreover, multiple, smaller multilocular adipocytes were interspersed in KO tissue, but absent in WT mice.

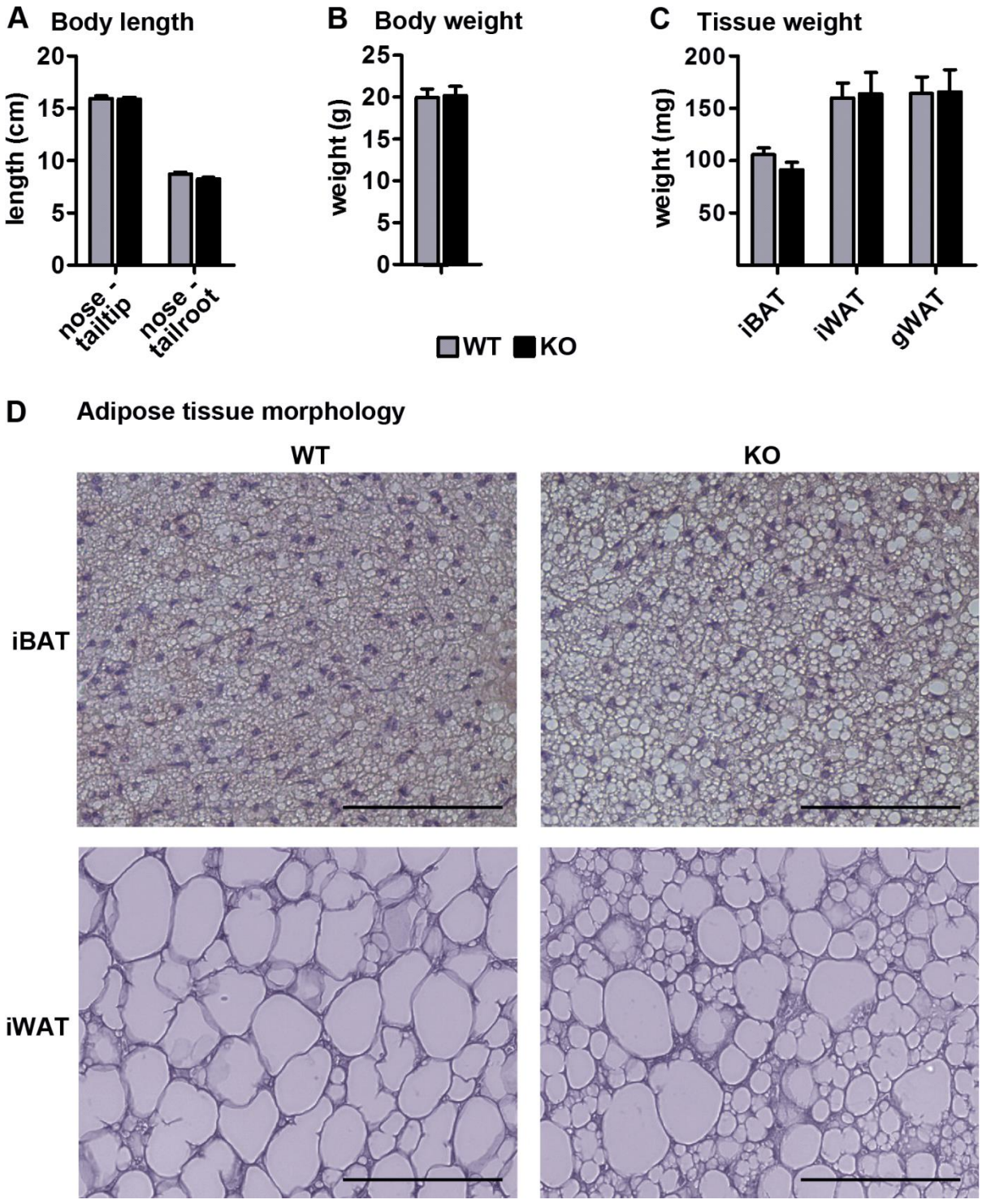

Figure 4.30 – Adipose tissue weight and morphology in 5-6 week old mice. (A) Body length (measured from nose to tailtip and from nose to tailroot) and (B) body weight of wild type (WT) and CerS4 deficient (KO) mice (n=8). (C) Tissue weight of interscapular BAT (iBAT), inguinal WAT (igWAT) and gonadal WAT (gWAT) (n=11-12). (D) Representative H&E-stainings of iBAT and igWAT paraffin sections (5 µm); scale bar 100 µm.

4.3.4 Cultured brown and white adipocytes of CerS4 deficient mice

The increased oxygen consumption and the altered adipose tissue morphology in CerS4 deficient mice point to increased browning of WAT. The fact that 5 week old mice show no signs of hair loss or altered food intake, indicates that these mice do not suffer from heat loss. Nevertheless, to completely exclude possible effects resulting from alterations of skin or fur, brown and white preadipocytes were isolated from new born and 5 week old mice, respectively, and differentiated *in vitro*. These cells were investigated by Real Time (RT)-PCR analysis of adipogenic and thermogenic markers.

In cultured brown adipocytes from WT and KO mice, no differences were observed in the mRNA levels of the adipogenic marker PPARγ (peroxisome proliferator-activated receptor γ), the major transcription factor regulating adipocyte differentiation (Kajimura *et al.*, 2010) (Figure 4.31 A). In the same line, the mRNA levels of aP2 (adipocyte Protein 2, also known as FABP4, fatty acid binding protein 4), a target gene of PPARγ and a marker for differentiated adipocytes (Shan *et al.*, 2012) were unaltered. No significant difference was also observed for the mRNA of UCP1, the characteristic marker of BAT. Stimulation of brown adipocytes with cGMP (cyclic guanosine monophosphate), which induces adipogenesis and activates BAT cells (Mitschke *et al.*, 2013), increased mRNA levels of PPARγ, aP2 and UCP1 by about 100 % compared to untreated cells. The mRNA levels of PPARγ and aP2 in cGMP-treated WT and KO cells were not altered, but UCP1 levels were slightly, but significantly increased (~10 %) in treated KO compared to WT cells.

In cultured white adipocytes, the mRNA level of PPARγ was significantly elevated by about 65 % in KO compared to WT cells (Figure 4.31 B). In contrast, aP2 levels were unaltered. Stimulation of cultured white adipocytes with cGMP increased mRNA levels of PPARγ and aP2 by about 100 % compared to untreated cells. Notably, cGMP treatment abrogated the increase in PPARγ mRNA levels observed for untreated KO cells and also aP2 levels were not altered between cGMP-treated WT and KO cells.

Analysis of thermogenic markers in cultured white adipocytes revealed a substantial increase (~500 %) in UCP1 mRNA in KO compared to WT cells (Figure 4.31 C). In addition, mRNA levels of the BAT markers PGC1α (PPARγ coactivator 1α), PRDM16 (PR domain containing 16) and CIDEA (cell death-inducing DFFA-like effector A) were determined. PGC1α regulates mitochondrial biogenesis and oxidative metabolism in BAT (Kajimura & Saito, 2014). PRDM16 (PR domain containing 16) is a major determining factor for BAT development (Lo & Sun, 2013). And CIDEA (cell death-inducing DFFA-like effector A) is a BAT specific marker involved in lipid droplet fusion and lipid storage in brown adipocytes (Wu *et al.*, 2014). All of these

thermogenic markers were increased (PGC1α ~50 %; PRDM16 ~170 %; CIDEA ~100 %) in KO compared to WT cells, but the differences did not reach statistical significance (Figure 4.31 C). Treatment with NE (norepinephrine), a well-known inducer of browning (Chen *et al.*, 2013b), substantially increased the expression levels of all thermogenic markers compared to untreated cells (UCP1 ~500 %; PGC1α ~150 %; PRDM16 ~180 %; CIDEA ~200 %). The increase was even stronger in NE-treated KO compared to WT cells. The difference was highly significant for UCP1 mRNA levels (~30 %) and also significant for CIDEA mRNA (~40 %), but not for PGC1α (~20 %) and PRDM16 (~30 %).

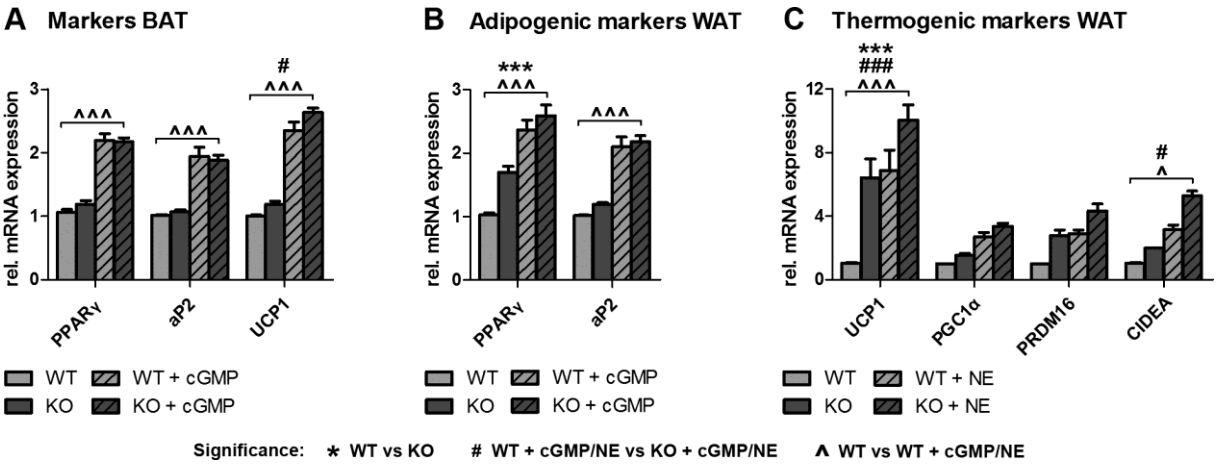

Figure 4.31 – RT-PCR analysis of adipogenic and thermogenic markers in brown and white adipocytes. (A) Relative mRNA levels of BAT markers in untreated or cGMP (cyclic guanosine monophosphate)-treated brown adipocytes isolated from iBAT of new born wild type (WT) and CerS4 deficient (KO) mice. (B) Relative mRNA levels of adipogenic markers in untreated or cGMP-treated white adipocytes isolated from igWAT of 5 week old WT and KO mice. (B) Relative mRNA levels of thermogenic markers in untreated or NE (norepinephrine)-treated white adipocytes. Data are means ± SEM, n=4; significance indicators: *1x, p<0.05; 3x, p<0.001*.

5 Discussion

5.1 SMSr

SMSr is the best-conserved member of the SMS family and together with a second member, SMS2, catalyzes production of the SM analogue CPE. Previously it was shown that in cultured cells, SMSr function is critical for ceramide homeostasis and suppression of ceramide-induced mitochondrial apoptosis (Vacaru *et al.*, 2009; Tafesse *et al.*, 2014). These studies revealed that the regulatory function of SMSr is strongly dependent on its catalytic activity and it was shown that the point mutation D348E leads to catalytic inactivity of the human SMSr protein. To investigate the *in vivo* function of SMSr, we aimed to deplete SMSr catalytic activity in mice. Therefore, the transgenic mouse lines SMSrD348E and SMSrdelEx6 were established. As a prerequisite for this study it was shown that the point mutation D348E and depletion of exon 6, both lead to catalytic inactivity of SMSr in SMSrD348E and SMSrdelEx6 mice, respectively. However, ubiquitous catalytic inactivation of SMSr in both mouse lines did not affect embryonic development, survival, healthiness or fertility. Notably, a simultaneous study from the collaborating group of Prof. Xian-Cheng Jiang (New York) reported the same for SMSr null mice (Ding *et al.*, 2015), pointing also to a discrepancy between the *in vitro* and *in vivo* function of SMSr.

5.1.1 SMSr expression

In this Ph. D thesis it was shown that the newly generated antibodies raised against SMSr specifically recognize the mouse and human protein in immunoblot analyses. In contrast, the antibodies did not recognize mouse SMSr in immunofluorescence analyses of liver and brain. Therefore, recognition of the epitope in the native protein might be prevented by protein folding.

Northern Blot analyses of human and mouse tissues suggested ubiquitous expression of SMS1 and SMS2 in mammals (Huitema *et al.*, 2004; Yang *et al.*, 2005). To investigate SMSr expression in mice, the newly generated, specific antibodies against SMSr and ß-galactosidase stainings in SMSrD348E mice were used. SMSr expression was found in every investigated mouse tissue, as well as in mouse embryonic fibroblasts and bone marrow derived macrophages, but not in embryonic stem cells, as was reported before (Ginkel, 2013). The positive signals in the original study probably resulted from staining of early differentiating cells such as embryonic fibroblasts, in which SMSr was found to be expressed in this Ph. D thesis. The strongest expression of SMSr was observed in brain and testis, which might indicate a fundamental role of the protein in these tissues. However, loss of catalytic activity in SMSr mutant mice did not obviously affect integrity of these tissues. Independent analyses of SMSr transcript levels also revealed a broad tissue

distribution and especially high levels in testis and bone marrow derived macrophages (Ding *et al.*, 2015). Although immunoblot analyses showed that SMSr is widely expressed in mice, ß-galactosidase stainings e.g. of brain, liver or testis indicated that it is not expressed in every cell type.

Interestingly, in immunoblot analyses the newly generated antibodies recognized two different protein isoforms, which according to their appearance were termed, SMSr and SMSr-2. Database analysis revealed two protein coding transcripts for the murine *smsr* (http://www.ensembl.org; Gene ID: ENSMUSG00000021770), indicating that mouse *smsr* is subject to alternative splicing. Alternative splicing was already described for mouse *sms1*, another homologue of the SMS family, with multiple transcripts in a variety of tissues e.g. brain, liver, kidney or testis (Yang *et al.*, 2005). Nevertheless, alternative splicing of the murine *smsr* seems to be more specific, since the SMSr-2 protein isoform was not found in all investigated tissues and it was the main isoform only in testis, where alternative splicing is very frequent (Elliott & Grellscheid, 2006).

5.1.2 Protein degradation in SMSrD348E and SMSrdelEx6 mice

The analysis of SMSrD348E protein levels in microsomal fractions and total tissue lysates suggests that the protein gets degraded. The point-mutated protein is translated from a bicistronic transcript, which additionally harbors the sequence for the ß-galactosidase reporter protein. Since ß-galactosidase expression was readily detected in several mouse tissues and residual SMSrD348E protein was found in microsomal fractions of brain and liver, transcription of the bicistronic mRNA is probably not compromised. The substantial decrease in SMSrD348E protein levels rather implies that due to the D348E point mutation the protein gets misfolded and at least partially degraded. As low amounts of SMSrD348E protein were detectable in ER membrane-enriched microsomal fractions of brain and liver, it is probably not completely absent. Rather the amount in total tissue lysates is below detection level. The original intention when establishing the SMSrD348E mouse line was to generate mice with catalytically inactive SMSr. Since SMSrD348E mice do not exhibit CPE synthase activity, degradation of the point-mutated protein was negligible for the phenotypic analyses of these mice.

The SMSrdelEx6 mice used in this thesis exclusively served as negative controls to verify the specificity of the newly generated antibodies against SMSr. A possible degradation of the truncated protein did not influence this, because loss of the protein due to degradation serves the same function as lack of the endogenous *C*-terminus in the $SMSr^{NT}$-eGFP fusion protein, in both cases the anti-SMSr antibodies should not detect any signal for SMSr. Even if the analyses in this thesis were not influenced by the fact that the mutated proteins in SMSrD348E and SMSrdelEx6 mice are

probably degraded, these circumstances have to be taken into account in future investigations.

5.1.3 SMSr catalytic activity

The results from the CPE synthase activity assay indicate that due to the point mutation D348E, or respectively deletion of exon 6, catalytic activity is lost in SMSrD348E and SMSrdelEx6 mice. However, the observed decrease in SMSrD348E protein levels in microsomal fractions would lead to a per se decrease in CPE synthase activity, even if catalytic activity is not affected by the D348E point mutation. Nevertheless, NBD-CPE production was completely abolished in brain and liver microsomal fractions of SMSrD348E mice, despite residual protein. Therefore, it can be concluded that the D348E point mutation and hence also deletion of exon 6, indeed lead to catalytic inactivity of SMSr.

The enzyme assay data on SMSr single and SMSr *X* SMS2 double mutant mice revealed that SMSr is the predominant CPE synthase in brain. In contrast, contribution of SMS2 to brain CPE synthase activity was only minor, although SMS2 deficiency markedly reduced SMS activity. However, SMS activity was found to be rather low, indicating that both SMSs exhibit only weak activity in brain. Contrary to this, SMS activity was very high in liver and the results indicated that SMS2 is the predominant contributor to this activity. The results are in line with previous measurements, where SMS activity was reduced by 80 % in the liver of SMS2gt animals and only by 15 % in the liver of SMS1 KO mice (Li *et al.*, 2012). The total CPE synthase activity in liver was shown to result from equal contributions of SMSr and SMS2, as NBD-CPE production was similarly decreased in all single mutants and only completely abolished in double mutants. This is in line with the observed CPE synthase activity in the liver of SMSr null mice, which was decreased by approximately 50 % (Ding *et al.*, 2015). The study further reported that CPE synthase activity in kidney and bone marrow derived macrophages from SMSr null mice is decreased to about 20-30 %. The analyses of enzyme activities in brain and liver of SMS mutant mice performed in the course of this Ph. D thesis complemented previous heterologous expression studies (Ternes *et al.*, 2009; Vacaru *et al.*, 2009), confirming that SMSr acts as monofunctional CPE synthase and that SMS2 acts as a bifunctional enzyme with both SM and CPE synthase activity. The data on CPE- and SM synthase activity in liver and brain correlate well with the protein expression of SMSr, as well as with the microarray analysis of SMS expression from BioGPS (Lattin *et al.*, 2008). Taken together, SMSr in contrast to SMS1 and SMS2 is strongly expressed in brain, whereas in liver SMSr and SMS2 are moderately expressed and SMS1 seems to be nearly absent.

5.1.4 Masspectrometric analyses of CPE and SM content

In line with previous findings in cultured mammalian cells (Vacaru *et al.*, 2009), it was shown that SMSr and SMS2 produce only trace amounts of CPE in mouse tissues. Steady-state levels of CPE, determined by mass spectrometry, were exceedingly low in all investigated tissues, i.e. ~300 to 1,500-fold below those of SM. The influence of SMSr on CPE levels was clearly pronounced only in brain. The decrease in SMSrD348E mice was in line the high expression level of SMSr and the significant contribution to total CPE synthase activity in this tissue. Decreased CPE levels in kidney were also in correlation with high expression levels of SMSr. In contrast, despite low expression of SMSr, CPE levels were also slightly decreased in spleen and lung of SMSrD348E mice, indicating that independent of protein expression other mechanisms might come into play to adjust SMSr catalytic activity. In conjunction with the expression levels of *sms2* a significant decrease in kidney CPE levels was also observed for SMS2gt mice. Since SMSrD348E mice displayed a similar decrease, it is surprising that kidney CPE levels were not further decreased in double mutants. This indicates that cells might be able to maintain CPE levels by adjusting the activity of enzymes involved in CPE synthesis or degradation. This question should be addressed by extended analyses of tissues in which the expression of SMSr and SMS2 cannot exclusively explain changes in CPE levels. In small intestine only combinatorial depletion of SMSr and SMS2 activity led to a significant decrease in CPE levels. This indicates that both enzymes equally contribute to CPE synthesis, in conjunction with comparable expression levels in this tissue. The MS analysis of liver suggests that CPE levels primarily depend on SMS2. This is in contrast to the low expression of *sms2* and the high expression of SMSr in this tissue. Surprisingly, CPE levels were particularly low in liver and no decrease was detectable in single and double mutant mice, although CPE synthase activity was completely abolished in double mutants. Metabolic labeling experiments in cultured HeLa cells indicated that CPE is not a short-lived metabolic intermediate (Vacaru *et al.*, 2009), which is supported by the fact that CPE was readily detectable in all tissues apart from liver. The present data suggest that in liver cells the liver-specific methyl-transferase PEMT (Ridgway & Vance, 1992) may use CPE as precursor in a methylation-dependent pathway of SM production. Despite expression of SMSr and SMS2, this could explain the particularly low steady-state levels of CPE in liver compared to other tissues. The results indicate that the contribution of the PEMT-dependent pathway to total SM levels in the liver is very small and the physiological relevance is unclear. To further verify that PEMT-catalyzed methylation of CPE occurs in the liver, enzyme activity assays are necessary.

An interesting finding is that primarily the shorter chain CPE species C18:0 and C20:0 (and to a lower extent C16:0) were affected in SMSrD348E mice. The preference for specific molecular species is well-established in sphingolipid

biosynthetic pathways, for instance the use of specific acyl-CoA species by CerS (see chapter 1.3.2.1). Notably, SMS2 depletion did also not affect C22:0, C24:0 and C24:1 CPE species, but all major SM species. This raises the question, whether molecular remodeling by a yet unknown mechanism could be responsible for production of longer chain CPE species. Remodeling of shorter chain CPE species could involve a mechanism analog to the elongation of fatty acids by the ELOVL (elongation of very long chain fatty acids) family (Jakobsson *et al.*, 2006). Alternatively, longer CPE species could originate from corresponding SM species via an unidentified mechanism of SM demethylation or produced by a yet unknown CPE synthase with different or broader substrate specificity.

Analysis of SM levels revealed remarkable decreases in forebrain, cerebellum and kidney of SMS2gt and double mutant mice. In case of kidney this clearly correlated with the expression of *sms2*. Interestingly, despite the decrease in SM levels, CPE levels were not affected in forebrain and cerebellum of SMS2gt mice. CPE levels are most likely not maintained by SMSr in this case, as the levels were similarly decreased in double mutant and SMSrD348E mice. The data on CPE and SM content in liver are comparable with findings from SMSr null and SMS2gt *X* SMSr null mice (Ding *et al.*, 2015). Additionally, this study reported a similar discrepancy for bone marrow derived macrophages (BMDMs) from SMS2gt *X* SMSr null mice. These BMDMs displayed no decrease in CPE levels, although SM levels were significantly decreased, and CPE synthase activity in macrophages of SMSr null mice was reduced by approximately 70 % (Ding *et al.*, 2015).

SM production by SMS2 is obviously predominant over CPE production, but the question remains why SMSr and SMS2 are intrinsically unable to produce bulk amounts of CPE. The lipid phosphate phosphatase-type reaction mechanism utilized by members of the SMS enzyme family involves a single lipid binding site and includes transfer of the headgroup from PC or PE to a conserved histidine residue in the active site of the enzymes (Tafesse *et al.*, 2006). Subsequently DAG is replaced by ceramide and the headgroup gets transferred onto ceramide generating SM or CPE, respectively. The ability of SMS2 to produce bulk amounts of SM suggests a higher affinity towards the head group donor PC in comparison to PE. The analysis of glycerophospholipid content suggests that the preferred use of PC instead of PE cannot be explained by the general PC/PE ratio, but it could be that the PC/PE ratio is especially high in the exoplasmic leaflet of the plasma membrane where the active site of SMS2 resides (Huitema *et al.*, 2004; Tafesse *et al.*, 2007). Moreover, as already suggested before, catalytic activity of SMSr and SMS2 may be under negative control by their product, CPE (see chapter 1.3.4.2). In any case, the fact that bulk production of CPE in insects is catalyzed by an unrelated enzyme from an insect-specific branch of the CDP-alcohol transferase superfamily (Vacaru *et al.*,

2013) implies that the reaction mechanism used by enzymes of the SMS family is unsuited for efficient production of CPE.

5.1.5 Determinants of CPE content

The inability of SMSr and SMS2 to produce large amounts of CPE might explain the generally low levels in tissue CPE, but unexpectedly even in double mutant mice substantial amounts of residual CPE were still detectable in any of the investigated tissues. This suggests alternative sources of CPE and probably includes enzymes different from SMSr and SMS2. A virtually inexhaustible source for CPE production would be SM, similar to its synthesis by head group transfer from PC to ceramide, SM could be converted to CPE by head group exchange with PE. However, nothing is known about the identity of proteins that catalyze such a reaction. An alternative pathway for SM synthesis involves methylation of CPE (Muehlenberg *et al.*, 1972). While on the one hand this pathway could contribute to the low CPE levels in mice, the reverse reaction i.e. demethylation of SM, could be an efficient way to keep CPE levels constant. However, the actual contribution and physiological relevance of this pathway is poorly understood.

Since SMS2 exhibits CPE synthase activity and SMS1 and SMS2 show high sequence similarity (Huitema *et al.*, 2004), it seems plausible that SMS1 might also be capable of catalyzing CPE production. Experiments with yeast cells overexpressing human SMS1 indicated that the enzyme is indeed capable of producing trace amounts of CPE and specific substitutions adjacent to the active site convert the enzyme into a monofunctional CPE synthase (Kol *et al.*, 2016). The ability of SMS1 to produce CPE was also suggested based on observations in SMS1 deficient mice, in which plasma CPE levels were significantly reduced (Ding *et al.*, 2015). Moreover, overexpression of SMS1 in SF9 insect cells increased CPE production (Ding *et al.*, 2015). In consequence depending on the tissue and the respective expression levels of *sms1*, remaining CPE levels could at least partially be explained by SMS1-mediated production. By upregulation of *sms1* expression cells could adapt to depleted CPE levels to alleviate deleterious effects resulting from that depletion. However, *sms1* mRNA levels were not altered in the liver of SMSr null and SMSr null *X* SMS2gt mice (Ding *et al.*, 2015). Nevertheless, no protein expression data is available and it could be that even in tissues where *sms1* wild type levels are relatively low e. g. forebrain and cerebellum, a slight increase in SMS1 protein levels or activity might be sufficient to adjust steady-state CPE levels according to cellular needs. On the other hand SMS1-driven CPE synthesis could explain why CPE levels, despite high expression levels of SMSr, are not decreased in some tissues of SMSrD348E mice. This may occur in testis, where combinatorial loss of SMSr and SMS2 had no impact on CPE levels, since expression levels of *sms1* are particularly

high and depletion in mice led to a substantial decrease in SMS activity (Li *et al.*, 2012).

Another important factor for determination of CPE levels might be the largely unexplored degradation of CPE. Conversion of CPE to SM (for instance by methylation, as was shown for PEMT in the liver) might be sufficient with respect to the exceedingly low levels, but the existence of a specific enzyme cannot be excluded. A possibility could be a dual activity of SMases in analogy to dual activity of SMS1 and SMS2 in the production of CPE. However, it was shown that a bacterial SMase is not capable of degrading CPE (Sergelius *et al.*, 2012). Nevertheless, the situation could be different in mammals, which express different isoforms of SMase. Alternatively, in line with the fact that usually every anabolic enzyme in the sphingolipid metabolic pathway has a catabolic counterpart (see chapter 1.3.1.4), mammals might express a specific CPEase. However, the identity of such a protein remains to be established.

Furthermore, it cannot be excluded that tissue CPE at least partially originates from dietary intake. The liver as a central metabolic organ could play a decisive role in distributing CPE (as well as SM) or precursors originating from food, but also from *de novo* synthesis. In addition to the presence of PEMT, the latter could explain why CPE levels are exceedingly low in the liver. In line with this assumption a study focusing on regulation of plasma ceramide levels reported that the liver detects and secretes *de novo* synthesized ceramides (Watt *et al.*, 2012). Such a release could be a general mechanism to ensure sphingolipid supply in various tissues or alternatively a way to protect the liver from accumulating intermediates of the sphingolipid metabolism.

5.1.6 CPE function

In insects, which lack SM synthases, CPE is a major plasma membrane constituent and produced in bulk amounts by a unique CPE synthase independent of SMSr (Vacaru *et al.*, 2013). In *Drosophila* it was shown that CPE fulfills an essential function in glial ensheathment of axons (Ghosh *et al.*, 2013). However, the role in mammals appears to be different as CPE levels are exceedingly low. This is supported by the fact that no morphological abnormalities were found in the brain and other tissues of SMSrD348E mice and even depletion of two different CPE synthases in mice did not compromise viability and healthiness. A recent study reported decreased expression of the drug transporter protein Pgp (Mdr1/P-Glycoprotein) in the brain of SMS2 deficient mice (Zhang *et al.*, 2011). The fact that CPE levels are not altered in forebrain and cerebellum of SMS2gt animals suggests that these effects are most likely not due to missing CPE production and rather are a consequence of missing SM synthesis. This is supported by the fact that despite a

significant decrease in CPE levels, integrity of brain cells was not affected in SMSrD348E mice. As CPE levels were not even completely wiped out in mice lacking two CPE synthases, the function of CPE in mice remains uncertain.

As discussed for sphingolipids in general, CPE might affect biophysical properties of mammalian membranes. The head group of CPE, in contrast to that of SM, requires less space and should allow denser packing. However, it was shown that in contrast to SM, which preferentially interacts with cholesterol to form highly-ordered membrane lipid microdomains, CPE did not interact with cholesterol in artificial membranes (Térová *et al.*, 2005). Moreover, as CPE levels in mammalian cells are exceedingly low it appears unlikely that CPE dramatically affects overall membrane properties. In contrast, CPE could exhibit specific functions e.g. in disturbing establishment or maintenance of lipid microdomains. Alternatively, as was suggested for the ganglioside GM3 (Kabayama *et al.*, 2007), it could act as a co-factor that either modulates function or complex formation of membrane proteins. It was already speculated that CPE may inhibit SMSr function by blocking the active site after its production (see chapter 1.3.4.2), which could also be valid for SMS2. CPE liberated from the active site of SMSr (or SMS2) could also act as inhibitor of other enzymes with comparable substrate binding sites.

5.1.7 SMSr is dispensable for ceramide homeostasis and cellular integrity in mice

Previously it was reported that acute disruption of SMSr catalytic activity in cultured human HeLa and *Drosophila* S2 cells results in accumulation of ceramides in the ER, a structural collapse of ER exit sites, fragmentation of the Golgi and induction of a mitochondrial pathway of apoptosis (Vacaru *et al.*, 2009; Tafesse *et al.*, 2014). Contrary to these findings, no alterations in ceramide and hexosylceramide levels were observed in ten different tissues of SMSrD348E mice in this Ph. D thesis. Moreover, histological analysis (β-galactosidase stainings) revealed no morphological abnormalities in brain, liver, kidney, heart, pancreas or testis, and ultra-structural analysis of brain, liver and kidney showed no alterations in the morphology of ER, Golgi or other organelles. The analysis of serum activities of liver transaminases and creatine phosphokinase further confirmed that liver integrity is not affected after disruption of SMSr catalytic activity. In line with the unaffected vitality of SMSrD348E mice this indicates that cellular integrity is not compromised when SMSr catalytic activity is lost *in vivo*.

While siRNA experiments in contrast to genetic approaches represent a convenient and less time consuming way to disturb gene expression, the observed consequences often result from off-target effects. However, the studies focusing on SMSr function in cultured cells reported similar effects for different siRNAs targeting

SMSr (Vacaru *et al.*, 2009; Tafesse *et al.*, 2014). Moreover, phenotypes could be rescued by transfection with an siRNA-resistant construct for wild type SMSr and in contrast, transfection with an siRNA-resistant construct for catalytically inactive SMSrD348E failed to rescue the phenotype. Therefore, it appears unlikely that the severely compromised cellular integrity in these studies resulted from off-target effects.

An independent study reported that the elevation in ceramide levels after siRNA-mediated knock-down of *smsr* in HeLa cells is not due to an increase in ceramide *de novo* synthesis (Siow & Wattenberg, 2012). Nevertheless, a block in *de novo* ceramide synthesis, a stimulated export of ceramides from the ER or consumption of excess ceramides by targeting SMS1 to the ER suppressed the compromised structural integrity and viability of cultured cells after acute depletion of SMSr (Vacaru *et al.*, 2009; Tafesse *et al.*, 2014). This indicates that the deregulation of ER ceramides is primarily responsible for these phenotypes. Therefore, it is surprising that catalytic inactivation of SMSr in mice did not alter ceramide levels, cell survival or integrity in any of the investigated tissues. The comparable findings in SMSr null mice (Ding *et al.*, 2015) further emphasize the discrepancy between the *in vitro* and the *in vivo* system and the question how these contradictory results can be explained remains unanswered.

The experiments with cultured HeLa and *Drosophila* S2 cells focused on the short-term effects after siRNA-mediated depletion of endogenous SMSr and subsequent transfection with an siRNA-resistant, catalytically inactive SMSrD348E protein (Vacaru *et al.*, 2009; Tafesse *et al.*, 2014). In these studies, the consequences of SMSr inactivation were investigated within 3 days. For some cells this time span might be too short to adapt sphingolipid metabolism and prevent ceramide accumulation and subsequent perturbation of cellular integrity and viability. Since the study in this Ph. D thesis focused on adult mice, it cannot be excluded that depletion of SMSr catalytic activity leads to a transient deregulation of ER ceramides already during early embryonic development, which individual embryonic cells may be able to overcome. In order to ensure proper development and function, these and descendant cells might permanently adjust sphingolipid metabolism to compensate jeopardizing effects resulting from missing SMSr function.

Similar to downregulation of *smsr*, acute depletion of *sms1* or *sms2* in HeLa cells led to a substantial increase in ceramide levels and was accompanied by a block in cell growth (Tafesse *et al.*, 2007). Since SMS1 and SMS2 are capable of producing bulk amounts of SM, ceramide accumulation is likely in this case. While no alterations in SM levels were observed in SMSrD348E compared to wild type mice, SM levels were reduced by about 15-25 % in forebrain, cerebellum, kidney and liver of SMS2gt mice.

Notably, no significant increase in ceramide or hexosylceramide levels was observed in forebrain and cerebellum and the increases in ceramide levels in kidney and in hexosylceramide levels in liver were rather small with respect to the high SM/(hexosyl)ceramide ratio in these tissues (~10:1 for SM/ceramide in kidney and for SM/hexosylceramide in liver). The data are in line with previous findings in SMS2gt mice (Liu *et al.*, 2009b), and also genetic ablation of SMS1 did not dramatically increase ceramide levels in different tissues (Yano *et al.*, 2011; Li *et al.*, 2012). This raises the question, whether mammals have evolved compensatory mechanisms to prevent ceramide accumulation. One possibility to prevent ceramide accumulation in SMSrD348E mice could be a reduction in ceramide synthesis. However, this should be accompanied by accumulation of the corresponding substrates (i.e. LCBs and acyl-CoAs) and the levels of LCBs were not altered in SMSrD348E mice. The unaltered LCB levels also exclude inhibited sphingolipid *de novo* synthesis. In the same line it is unlikely that steady-state ceramide levels in these mice are adjusted by an increased conversion to hexosylceramide or SM, as the levels of these sphingolipids were also unaffected. Moreover, the fact that sphingosine levels are not increased in SMSrD348E mice also argues against increased ceramide degradation by the action of ceramidases. Actually, sphingosine resulting from this degradation could be immediately converted to S1P, but substantially increased levels of S1P would probably severely affect cellular integrity (Mendelson *et al.*, 2014), and S1P levels were unaltered in the plasma of SMSr null mice (Ding *et al.*, 2015). To avoid toxic accumulation of ceramides mammals may have co-evolved different proteins with redundant function. In case of SMSr depletion such a protein could cope with missing function. The loss of such a protein in a genetically unstable cancer cell line such as HeLa might explain the inability to prevent ceramide accumulation after siRNA-mediated knock-down of *smsr*.

In the follow-up publication on SMSr function in cultured HeLa cells it was reported that the observed ceramide accumulation after acute knock-down of SMSr results in mislocalisation of ceramide to mitochondria and thereby induces a mitochondrial pathway of apoptosis (Tafesse *et al.*, 2014). Interestingly, similar to the SMSrD348E point mutation, a SAM domain deletion construct was not able to rescue this phenotype after transfection into these HeLa cells, although catalytic activity was restored (Vacaru *et al.*, 2009; Tafesse *et al.*, 2014). Since SMSrD348E and SMSrdelEx6 mice are supposed to express mutated proteins with functional SAM domain, a protective function of the SAM domain in these mice cannot be excluded. However, similar to SMSrD348E mice the previously mentioned SMSr Null mice, which completely lack SMSr, did not show any obvious phenotypic alterations (Ding *et al.*, 2015). This indicates that presence of the SAM domain does not prevent negative effects in SMSrD348E mice.

In conclusion, the study in this Ph. D thesis implies that SMSr is not a critical regulator of ceramide levels and that SMSr-mediated CPE production is dispensable for development, survival, healthiness and fertility in mice kept under standardized conditions. Nevertheless, as SMSr is highly conserved in the animal kingdom (Vacaru *et al.*, 2013) and ubiquitously expressed in mice, it cannot be excluded that it fulfills a role different from the ceramide regulatory function or only under stressed metabolic conditions.

5.1.8 Future perspectives for investigation of SMSr function

Analysis of SMSr and CPE function in mice is complicated by the fact that residual CPE was found in all investigated tissues even after depletion of two known CPE synthases. Therefore, knowing the origin of the SMSr/SMS2-independent CPE pool would facilitate future studies on the biological function of SMSr and CPE in mammals. In line with the idea that all members of the SMS family are capable of producing CPE, combinatorial depletion of these members in mice might shed further light on the origin of residual CPE in mammals, generation of these mice is already in progress in the group of Prof. Xian-Cheng Jiang (New York) (Ding *et al.*, 2015).

To investigate possible compensatory mechanisms and short-term consequences of SMSr inactivation *in vivo*, conditional SMSrdelEx6 mice could be crossbred with mice expressing an inducible Cre recombinase (Feil *et al.*, 2009). Such acute depletion of SMSr catalytic activity could help understanding the contradictory results of the *in vitro* and the *in vivo* system.

Ceramide accumulation, disruption of the early secretory pathway and induction of mitochondrial apoptosis so far were only described for depletion of SMSr catalytic activity in cultured HeLa and *Drosophila* S2 cell lines. Acute depletion of SMSr in different primary cells and further cell lines could help to identify particular cell types or specialized metabolic conditions that require proper function of SMSr. One of these approaches could focus on embryonic fibroblasts isolated from SMSr mutant mice, in which the already mentioned compensatory mechanisms could be evaluated. However, the earliest time point to isolate such cells is embryonic day 9.5 to 10.5 and a possible compensation might already occur at earlier developmental stages.

In line with the original findings in HeLa cells, SMSr might specifically influence cancer cell metabolism. By preventing ceramide accumulation and subsequent apoptosis in cancer cells, SMSr could significantly promote cancer growth. Therefore, depletion of SMSr in additional cancer cell lines and especially induced tumorigenesis in SMSr mutant mice could help unraveling SMSr function in mice. SMSr could also be involved in radiation-induced apoptosis, which in HeLa cells was

shown to be associated with an increase in ceramide *de novo* synthesis (Mesicek *et al.*, 2010). Following preliminary studies in different cell lines, SMSr mutant mice could be exposed to radiation to see whether loss of SMSr catalytic activity affects the resulting consequences.

SMS1 and SMS2, besides several other enzymes of the sphingolipid metabolic pathway have been shown to be involved in the development of diet-induced obesity and obesity-associated comorbidities e.g. atherosclerosis (see chapters 1.3.3.4 and 1.3.4). Therefore, it might be interesting to challenge SMSr mutant mice by exposure to high fat diet. A more drastical way to investigate SMSr function in mice would be drug-induced interference with ceramide metabolism. As ceramide accumulation was shown to be the cause of the severely compromised integrity of acutely SMSr-depleted HeLa cells, it would be interesting to see whether an increase in ceramide production differentially affects SMSr mutant compared to wild type mice. For this purpose several drugs are available that have been shown to increase ceramide generation via different pathways (Senchenkov *et al.*, 2001). Ceramide accumulation in SMSr mutant mice could also be induced by retroviral transduction with functional SMase. Another approach would be a block in CERT function. CERT deficient mice display dramatic increases in ER ceramide levels and would represent a promising system to investigate SMSr function (Wang *et al.*, 2009). Unfortunately, these mice die due to developmental heart defects already at embryonic day 11.5 and no conditional mice are available so far. However, a recent study identified several CERT ligands that could be used to acutely interfere with CERT function in SMSr mutant mice (Santos *et al.*, 2014). In contrast, it might also be revealing to investigate whether a block in sphingolipid *de novo* synthesis by myriocin or inhibition of ceramide synthesis by fumonisin B1 differentially affect vitality in SMSr mutant compared to wild type mice.

It was shown that SMSr is highly expressed in bone marrow derived macrophages, but genetic ablation of SMSr in mice did not alter CPE levels in these cells, although CPE synthase activity was decreased to 30 % compared to wild type controls (Ding *et al.*, 2015). According to a broad microarray analysis, SMSr expression in bone marrow derived macrophages was substantially increased following LPS treatment (Lattin *et al.*, 2008). This implies that SMSr might have a function in or after activation of macrophages. In the same line it was shown that depletion of SMS1 and SMS2 attenuated activation of macrophages after LPS treatment (Gowda *et al.*, 2011; Li *et al.*, 2012). Moreover, LPS treatment of RAW264.7 macrophages and mouse peritoneal macrophages moderately increased sphingolipid *de novo* synthesis (Chang *et al.*, 2011) and substantial increases in this case may be prevented by SMSr. Therefore, challenging SMSr mutant mice with LPS or other inflammatory stimuli could be a promising approach.

5.1.9 Regulation of ceramide homeostasis

The involvement of ceramides in essential cellular processes including proliferation or apoptosis necessitates tight regulation of ceramide homeostasis and mammals have probably evolved mechanisms to circumvent problems resulting from an imbalance in ceramide generation. While it was shown that the activity of CerS and other enzymes of the sphingolipid metabolic pathway can be modulated by post-transcriptional modification (see chapter 1.3.2.5), the intrinsic mechanisms underlying these modifications are largely unexplored. Similar to what was observed for other metabolic pathways, particular sphingolipid species could be monitored by proteins that are able to adjust synthesis and/or degradation in response to deviations from a specific threshold. The sensing of sterols is a well-understood mechanism of that type (Goldstein *et al.*, 2006). In case of high cholesterol levels in the ER, cholesterol specifically binds to a Scap/SREBP complex, leading to retention of SREBP in the ER. When cholesterol levels are low, the sequestration of SREBP is abrogated, allowing export and subsequent transcriptional activation of cholesterol synthesis. It was postulated that SMSr is the elusive protein that monitors ceramide levels and regulates ceramide homeostasis (Vacaru *et al.*, 2009; Tafesse *et al.*, 2014). However, the data presented in this thesis clearly demonstrate that SMSr is dispensable for ceramide homeostasis and cellular integrity in mice and the question how mammalian cells regulate ceramide levels to avoid jeopardizing overall integrity remains unanswered.

Aside from proteins that monitor concentrations of ceramide or possibly other intermediate or terminal products of the sphingolipid metabolic pathway, additional mechanisms might exist to ensure proper sphingolipid metabolism. These mechanisms could involve regulation of enzyme expression, activity or localization, as well as adjustment of substrate availability through altered uptake, export, synthesis or subcellular localization.

An interesting mechanism was shown in yeast, in which TORC2 (target of rapamycin kinase complex 2) is responsible for the adjustment of ceramide synthesis to regulate the levels of LCBs, LCB-phosphates and ceramides (Aronova *et al.*, 2008). Activation of ceramide synthesis was shown to be mediated by yeast protein kinase 2 (Ypk2) and counteracted by calcineurin phosphatase. Strikingly, the activation involves a feedback mechanism, which is characterized by direct activation of Ypk2 by increased levels of LCBs (Liu *et al.*, 2005). However, the mechanism is not completely understood and it is not yet established whether this mode of regulation is conserved in higher organisms (Breslow & Weissman, 2010).

Another mechanism that was discovered in yeast depends on the action of the ER-resident transmembrane proteins ORM1 and ORM2. These proteins negatively

regulate the first and rate-limiting step in the *de novo* ceramide synthesis by associating with SPT (Gururaj *et al.*, 2013). While overexpression of ORM1 and ORM2 in yeast cells decreased sphingolipid levels, the opposite effect was observed after depletion of ORMs (Breslow *et al.*, 2010). Interestingly, the inhibitory action of the yeast ORM proteins was relieved by phosphorylation of an *N*-terminal serine motif in response to disruption of sphingolipid *de novo* synthesis by myriocin, pointing to a feedback mechanism (Breslow & Weissman, 2010). Phosphorylation of ORM1 was shown to be dependent on TORC1 and mediated by Npr1 kinase in response to decreased nitrogen supply and sphingolipid content (Gururaj *et al.*, 2013). In contrast, ORM2 phosphorylation is mediated by the previously mentioned TORC2 complex through the action of Ypk1 in response to altered plasma membrane status and decreased sphingolipid content (Gururaj *et al.*, 2013). In cultured HeLa cells it was shown that the mammalian homologs ORMDL1-3 negatively regulate SPT activity (Siow & Wattenberg, 2012). However, the mammalian proteins lack the *N*-terminal phosphorylation motif and regulation of SPT activity rather depends on the coordinated expression of the individual ORMDLs (Kiefer *et al.*, 2015). In human embryonic kidney (HEK) cells exposed to palmitate, only overexpression of all ORMDLs completely inhibited SPT (Kiefer *et al.*, 2015). It was shown that this depends on the formation of oligomeric ORMDL complexes which associate with SPT and change conformation in response to alterations in sphingolipid content (Kiefer *et al.*, 2015). Currently, the identity of the sphingolipid species that regulate ORMDL expression is not known. However, inhibition of ceramide synthesis with fumonisin B1 increased SPT activity in HeLa cells, pointing to a role of ceramides or higher order sphingolipids (Siow & Wattenberg, 2012) and it was also reported that SK1-mediated production of S1P negatively regulates sphingolipid synthesis (Siow *et al.*, 2015). While ORMDL-dependent regulation of SPT activity was already investigated in several mammalian cell lines, the *in vivo* situation is largely unexplored due to the lack of appropriate systems, including ORMDL deficient mice (Paulenda & Draber, 2016).

As indicated by the above mentioned studies, it appears likely that regulation of ceramide metabolism is strongly dependent on feedback mechanisms similar to what was observed for the sterol and glycerophospholipid metabolism (Breslow & Weissman, 2010). A good example is the regulation of CERT-mediated ceramide transport. As part of a negative feedback loop, the directed transport from the ER to the trans-Golgi depends on the activation of protein kinase D (PKD) in acceptor membranes (Olayioye & Hausser, 2012). By providing ceramide for SM production, CERT indirectly contributes to the production of diacylglycerol (DAG), a side product of SM synthesis at the trans-Golgi. In a concentration dependent manner, DAG recruits and activates PKD, which in turn leads to phosphorylation of CERT. Subsequent hyperphosphorylation of a serine repeat motif leads to dissociation from

the trans-Golgi and inactivation of the ceramide transfer activity due to conformational changes. Binding to the ER allows dephosphorylation by the action of phosphatase PP2Cε, which reactivates ceramide transfer activity. In HeLa cells such regulation was observed after depletion of SM levels by SMase treatment, which led to phosphorylation of CERT, and in turn increased ceramide delivery for SM synthesis at the Golgi (Kumagai *et al.*, 2014).

Data on the identity and function of regulatory mechanisms in mammalian cells are scarce and further investigations are necessary to understand how ceramide homeostasis is controlled. In the context of this study it is especially interesting how mammalian cells might overcome harmful increases in ceramides or higher order sphingolipids.

One possibility would be adjustment of sphingolipid synthesis and/or degradation via feedback mechanisms, depending on the concentration of specific sphingolipid species. For instance, monitoring of ceramide levels in the ER would allow an immediate adjustment of *de novo* synthesis, as SPT is also located here. Alternatively, ceramide or SM levels could be sensed in the Golgi or the plasma membrane. A hypothetical model could include a protein with low affinity to ceramide or SM that binds only at particularly high concentrations. Binding could induce a conformational change and subsequent recruitment of co-factors for retrograde trafficking. Via a yet unidentified pathway this could signal abundance of ceramide or SM and therefore inhibit SPT or CerS activity, or alternatively activate SMases and ceramidases. In line with that notion it was reported that the p24 protein, a component of the COPI (coat protein complex I)-retrograde trafficking machinery, has a binding pocket that specifically binds to C18 SM (Contreras *et al.*, 2012). A bioinformatic analysis in this study identified another 50 proteins with putative sphingolipid binding domain and most of the identified proteins locate to the plasma membrane. Whether one of these proteins qualifies for a sphingolipid sensor and how such sensors adjust sphingolipid metabolic pathways remains to be established.

5.2 Diet-induced obesity in CerS4 deficient mice

Prior to starting this study, different groups already investigated CerS function in the development of diet-induced obesity in mice. CerS5 and CerS6 deficient mice were shown to be protected from diet-induced obesity. In CerS5 deficient mice this was probably a result of decreased lipid accumulation in WAT, which was accompanied by reduced adipose tissue inflammation and improved glucose tolerance (Gosejacob *et al.*, 2016). Protection of CerS6 deficient mice was characterized by improved glucose tolerance and higher energy expenditure associated with increased β-oxidation in BAT and liver (Turpin *et al.*, 2014). In contrast, mice heterozygous for CerS2 were more prone to diet-induced obesity, with increased susceptibility to steatohepatitis and insulin resistance probably due to impaired β-oxidation in liver (Raichur *et al.*, 2014). Interestingly, these studies consistently suggested that C16:0 ceramide is a major player in the development of obesity, as the levels were decreased in the respective tissues of CerS5 and CerS6 deficient mice and increased in the liver of heterozygous CerS2 mice (Raichur *et al.*, 2014; Turpin *et al.*, 2014; Gosejacob *et al.*, 2016).

5.2.1 CerS4 deficient mice are protected from diet-induced obesity

To investigate the function of CerS4 and corresponding ceramide species in the development of diet-induced obesity, wild type and CerS4 deficient mice were fed a high fat diet (HFD) for 16 weeks. Interestingly, CerS4 deficient mice were protected from diet-induced obesity, characterized by strongly decreased weight gain, reduced adipose tissue weight and improved glucose and insulin tolerance. The feces analysis revealed no alterations in the levels of triacylglycerols, diacylglycerols or free fatty acids between wild type and CerS4 deficient mice. This indicates that the reduced weight gain, despite increased food intake did most likely not result from altered intestinal lipid resorption. It cannot be excluded that some of the protective effects are a consequence of the observed hair loss in older mice (Cannon & Nedergaard, 2011), which starts to become obvious in 6-7 week old animals. Nevertheless, glucose and insulin tolerance were already significantly improved in 7-8 week old animals, when hair loss was not especially pronounced, indicating that CerS4 might affect these parameters independent of hair loss.

As discussed in chapter 1.3.3.2, overall glucose tolerance and insulin sensitivity is dependent on glucose and insulin homeostasis in different peripheral tissues. For instance, ubiquitous depletion of CerS6 in mice, significantly improved overall glucose tolerance and insulin sensitivity, whereas the effect was weaker after conditional depletion in either liver or BAT (Turpin *et al.*, 2014). In the same line, overall glucose tolerance and insulin sensitivity might be improved through independent CerS4 action in peripheral tissues.

A central organ in this context is the pancreas. The pancreas is responsible for insulin production and release in response to food intake to facilitate glucose uptake and energy storage in peripheral tissues. It could be shown that CerS4 is highly expressed in pancreas. In line with that finding, C18:0 and C20:0 (and to a minor extent C22:0) sphingolipid levels were decreased in pancreas of CerS4 deficient mice. Interestingly, C16:0 ceramide levels in pancreas of CerS4 deficient mice were increased, which could be explained by the concomitant increase in CerS6 protein levels. Given the strong impact of CerS4 deficiency on sphingolipid levels in pancreas, protection from diet-induced obesity and insulin resistance in CerS4 deficient mice might at least partially result from improved pancreas function. In line with that notion, a previous study reported increased rates of glucolipotoxicity-induced apoptosis in the pancreatic β-cell line INS-1 after overexpression of CerS4 and the concomitant increase in C18:0 and C22:0 ceramides (C20:0 ceramide levels were not determined)(Véret *et al.*, 2011). Glucolipotoxicity might also compromise pancreatic β-cell function in mice following exposure to HFD. Depletion of CerS4 in this context could result in decreased rates of β-cell apoptosis and hence maintain insulin secretion from the pancreas, leading to an overall improvement in glucose tolerance. The increase in C16:0 sphingolipid species in the pancreas of CerS4 deficient mice, might argue against improved pancreas function, since C16:0 ceramide was suggested to be a negative regulator of iBAT, liver and WAT function (Raichur *et al.*, 2014; Turpin *et al.*, 2014; Gosejacob *et al.*, 2016). However, the increase in C16:0 ceramide, as well as the decrease in C18:0 and C20:0 ceramides was comparable in CerS4 deficient mice fed either HFD or LFD. And both groups showed significantly improved glucose tolerance and insulin sensitivity compared to the corresponding wild type groups. Therefore, despite the increase in C16:0 ceramide, it appears unlikely that pancreas function is impaired in CerS4 deficient mice. A possible explanation might be that the increase in C16:0 ceramide is rather negligible due to the high levels in pancreas (3-4 fold higher compared to iBAT or liver). This could be the case, if C16:0 ceramides exert their negative actions by altering membrane biophysical properties and thereby affect membrane-associated cellular signaling, as was discussed for ceramides in general (Grösch *et al.*, 2012; Silva *et al.*, 2012). A detailed discussion of the influence of altered ceramide levels on membrane biophysical properties and cellular signaling is presented in chapter 5.2.6.

The mass spectrometric analyses of liver revealed that despite low expression levels of CerS4, liver C18:0 and C20:0 sphingolipid levels were decreased in CerS4 deficient compared to wild type mice fed HFD. The increased levels of these species in wild type mice following HFD feeding could be due to increased protein expression of CerS4, as indicated by the immunoblot analysis. Moreover, the data indicate that the levels of C22:0 sphingolipids in liver do not solely depend on CerS2, but also on CerS4, since C22:0 sphingolipid levels were lower in CerS4 deficient mice, despite a

slight increase in CerS2 protein expression. The data suggest that aside from pancreas, the overall improvement in glucose and insulin tolerance in CerS4 deficient mice could partially originate from liver. Interestingly, C18:0 and C20:0 ceramide levels in CerS4 deficient mice fed HFD were similar to those observed in wild type mice fed LFD and glucose tolerance in these groups was comparable. Protection of CerS4 deficient mice from insulin resistance could be due to the increased expression of the IRβ subchain in CerS4 deficient compared to wild type mice, which was especially pronounced after exposure to HFD. It was suggested that hepatic insulin resistance in CerS2 deficient mice is a consequence of impaired IR clustering in the plasma membrane (Park *et al.*, 2013a). This was concluded from the finding that IRs did not localize to detergent-resistant membranes, probably due to depletion of C22 and C24 ceramides. Interestingly, CerS2 protein levels were increased in CerS4 deficient compared to wild type mice. However, the increase was rather small and not accompanied by an increase in the corresponding sphingolipid species. In contrast to C22 and C24 ceramides, C18 and C20 ceramides generated by CerS4 might have a destabilizing effect on IRs and depletion in CerS4 deficient mice could contribute to the establishment of a membrane environment that stabilizes IRs, for instance by increasing the ratio of ceramides generated by CerS2. Improved cluster formation could in turn protect IRs from degradation, which might explain the increased levels of IRβ-subchain in CerS4 deficient mice.

The fact that HFD-induced weight gain and white adipose tissue weight were significantly reduced in CerS4 deficient compared to wild type mice, despite increased food intake, points to increased energy expenditure. A tissue specialized in energy expenditure is BAT. The mass spectrometric analysis of iBAT revealed that C18:0 and C20:0 sphingolipid species were decreased, despite low expression of CerS4 in this tissue. In contrast to liver and pancreas, depletion of CerS4 did not affect C22 sphingolipid levels. These levels were rather increased, probably resulting from alternative use of the accumulating substrates by CerS2. Whether protein expression of CerS2 is increased in 22-24 week old CerS4 deficient mice remains to be established. The immunoblot analysis of 5 week old mice revealed high expression of CerS2 in iBAT, but expression was not altered in the CerS4 deficient control. It remains to be established why CerS4 does not affect C22:0 sphingolipid levels in iBAT. A possible explanation could be specific modifications or interactions that affect substrate specificity of CerS4 in iBAT or alternative sources for C22:0 ceramides that cover the effect of CerS4 depletion. Notably, C16:0 (and C18:0) sphingolipid levels were increased in mice fed HFD and probably due to the before mentioned alternative use of substrates the increase in C16:0 species was even stronger in CerS4 deficient mice. It was suggested that increased levels of C16:0 ceramide compromise iBAT function and promote development of diet-induced obesity (Turpin *et al.*, 2014). This might indicate that protection from diet-induced

obesity in CerS4 deficient mice is not a result of improved iBAT function. However, as was already discussed for pancreas, iBAT function could also depend on the biophysical constitution of cellular membranes. In this context it could also be that the altered sphingolipid content in iBAT of CerS4 deficient mice allows the establishment of a membrane environment that improves iBAT function.

5.2.2 Hair loss and protection from diet-induced obesity

The hair loss in 23-24 week old CerS4 deficient mice is very obvious and with respect to the fact that the thermoneutral temperature for mice is 30°C, it is likely that heat loss occurs in these mice (Cannon & Nedergaard, 2011). Moreover, as CerS4 deficient mice can be distinguished according to fur appearance at the age of 6-7 weeks, it cannot be excluded that heat loss already occurs in these mice. The increased food intake indicates that insulation is already affected in these mice (Cannon & Nedergaard, 2011). However, in contrast to the hair loss, the food intake did not progressively increase and remained similar starting from week 7 of the 16 week experiment.

Extensive review of present literature revealed several examples for mouse mutants that are protected from diet-induced obesity due to alterations of skin or fur composition. For instance, ELOVL3 (elongation of very long chain fatty acids 3)(Zadravec *et al.*, 2010) or DGAT1 (diacylglycerol acyltransferase 1)(Smith *et al.*, 2000) deficient mice. DGAT1 deficient mice, display a hair loss phenotype even more severe than that observed in CerS4 deficient mice (Chen *et al.*, 2002). These mice also showed increased food intake at normal housing temperature (23°C) and the food intake was even higher at 4°C, but approximately the same at thermoneutral temperature (Chen *et al.*, 2003). Notably, at thermoneutral temperature HFD-induced adiposity was still less pronounced compared to wild type animals, probably as a result of increased thermogenesis in adipose tissue (Chen *et al.*, 2003). Therefore, it is possible that also protection from diet-induced obesity in CerS4 deficient mice not solely depends on hair loss.

To circumvent possible effects resulting from hair loss and to investigate the putatively beneficial effects of CerS4 deficiency, energy expenditure and adipose tissue function were investigated in 5 week old mice. 5 week old CerS4 deficient mice show no obvious alterations in fur appearance. This is supported by the finding that hair follicles of CerS4 deficient mice regularly enter anagen at postnatal day 33 (P33) and catagen at P47 (Peters *et al.*, 2015). The hair follicles remain in an anagen-like state and do not enter telogen only at P51. Together this suggests that 5 week old animals do not suffer from heat loss due to impaired insulation.

5.2.3 Energy expenditure in 5 week old mice

The reduced weight gain of CerS4 deficient compared to wild type mice after 16 week exposure to HFD clearly indicates increased energy expenditure in these mice. However, analysis of energy expenditure in these mice could be misleading due to the progressive hair loss. Therefore, oxygen consumption was investigated in 5 week old wild type and CerS4 deficient mice. Despite similar body size, body weight and adipose tissue weights (iBAT, igWAT and gWAT) compared to wild type mice, CerS4 deficient mice exhibited significantly increased oxygen consumption compared to wild type mice at 23°C. The same effect was observed at 4°C and to a lower extent at thermoneutral temperature (30° C), but the differences did not reach statistical significance. However, energy expenditure appeared to be increased due to loss of CerS4 independent of hair loss. This is supported by the finding that food intake was not altered at 23°C, which further indicated that 5 week old CerS4 deficient mice do not suffer from heat loss. As motility was unaltered in CerS4 deficient compared to wild type mice at 23°C and 4°C, it is likely that the increased energy expenditure is independent of muscular activity.

5.2.4 CerS expression in 5 week old mice

As increased energy expenditure can be the result of stimulated development and activity of BAT, further analyses focused on adipose tissue. Interestingly, CerS4 expression in iBAT was only weak, arguing against activation of iBAT due to loss of CerS4 in CerS4 deficient mice. In contrast, CerS4 was strongly expressed in igWAT and the levels were even higher in gWAT, pointing to a specific role in these tissues. The expression pattern of CerS5 was similar to that of CerS4, with low levels in iBAT, high levels in igWAT and even higher levels in gWAT, consistent with the previous expression analysis and the observed WAT phenotype in CerS5 deficient mice after HFD feeding (Gosejacob *et al.*, 2016). In a similar fashion, the high levels of CerS6 in iBAT are in line with the improved BAT function in CerS6 deficient mice after HFD feeding (Turpin *et al.*, 2014). The low expression levels of CerS6 in gWAT and of CerS5 in iBAT could explain why altered gWAT function in CerS5 deficient mice and altered iBAT function in CerS6 deficient mice cannot be compensated after exposure to HFD (Turpin *et al.*, 2014; Gosejacob *et al.*, 2016). Whether CerS5 and CerS6, consistent with their preference for C16 acyl-CoAs, can compensate each other's loss is not known. None of the previously mentioned studies focused on igWAT, in which both are expressed to a similar extent. Therefore, it would be interesting to see whether depletion of one or both of these CerS affects igWAT function after HFD feeding.

5.2.5 Browning in CerS4 deficient mice

Surprisingly, analysis of iBAT morphology revealed slightly increased adipocyte size in KO compared to wild type mice, despite low expression levels of CerS4. Usually,

brown adipocytes accumulate lipid droplets to store energy, which can be used for non-shivering thermogenesis e.g. in response to adrenergic stimulation following cold exposure (Westerberg *et al.*, 2006). Therefore, the increased adipocyte size might point to enhanced thermogenic capacity of iBAT in CerS4 deficient mice. Contrary to this assumption, mRNA levels of the adipogenic markers PPARγ and aP2 were not altered in *in vitro* differentiated brown adipocytes from iBAT of new born mice. This could indicate that CerS4 affects iBAT thermogenic capacity only at later developmental stages. The finding that mRNA levels of UCP1 were also unaffected is in line with that notion. Despite this, UCP1 mRNA levels were increased in CerS4 deficient cells after stimulation of adipogenesis and BAT function by cGMP, but the difference was rather small and probably without physiological consequences. Therefore, consistent with the low expression levels of CerS4, it appears unlikely that CerS4 deficiency affects adipocyte differentiation in iBAT or increases oxygen consumption by stimulating iBAT activity.

The morphology of igWAT, in which CerS4 is highly expressed, was severely affected in CerS4 deficient mice. The reduced adipocyte size in CerS4 deficient compared to wild type mice could be a direct consequence of the observed increase in energy expenditure. The numerous smaller, multilocular adipocytes interspersed in CerS4 deficient tissue might represent thermogenic beige adipocytes, indicating increased browning (Chen *et al.*, 2013b; Gnad *et al.*, 2014). The RT-PCR analysis of *in vitro* differentiated white adipocytes from igWAT of 5 week old mice revealed a slight increase in PPARγ mRNA levels in CerS4 deficient compared to wild type cells. Since the mRNA levels of aP2, an adipogenic target gene of PPARγ were unaltered, this could indicate increased differentiation of adipocyte precursor cells to thermogenic beige adipocytes. This is in line with the finding that ectopic expression of PPARγ in fibroblasts and mesenchymal cells induces white adipocyte differentiation, but together with other transcriptional regulators is also required for brown adipocyte differentiation (Kajimura *et al.*, 2010). Genetic ablation of PPARγ completely disrupts adipocyte differentiation in WAT and BAT (Kajimura & Saito, 2014). Interestingly, it was shown that PPARγ in adipose tissue is also an essential regulator of whole body insulin sensitivity, as it regulates production and secretion of the adipokines adiponectin and leptin, important mediators of insulin action in peripheral tissues (Kintscher & Law, 2005). Therefore, the improved insulin sensitivity in CerS4 deficient mice could also be a consequence of increased PPARγ levels in WAT. However, it remains to be investigated if PPARγ levels are also elevated in WAT of CerS4 deficient mice.

Notably, the levels of PPARγ mRNA in cultured white adipocytes were not increased in CerS4 deficient compared to wild type cells after stimulation of adipogenesis and browning by cGMP. In contrast, mRNA levels of thermogenic markers were

increased in CerS4 deficient compared to wild type cells and comparable increases were observed after stimulation with the browning inducer norepinephrine (NE). Especially the levels of UCP1, which uncouples the electron transport chain from ATP production to dissipate energy as heat, were significantly elevated in CerS4 deficient cells. In addition, the mRNA levels of PRDM16 and PGC1α were increased. Both are involved in the regulation of mitochondrial biogenesis, oxidative metabolism and expression of BAT-selective genes (Lo & Sun, 2013; Kajimura & Saito, 2014). The mRNA levels of CIDEA were especially increased in CerS4 deficient compared to wild type cells following NE treatment. CIDEA is involved in lipid droplet fusion and lipid storage in brown adipocytes (Wu *et al.*, 2014). Taken together, these results indicate that thermogenic capacity in CerS4 deficient mice is increased due to increased browning of igWAT.

A study focusing on the farnesoid X receptor (FXR) reported protection from diet-induced obesity and insulin resistance due to increased browning of igWAT following treatment of mice with glycine-β-muricholic acid (Gly-MCA), a specific inhibitor of FXR signaling in intestine (Jiang *et al.*, 2015). This was characterized by decreased expression of several genes involved in ceramide synthesis in ileum, the distal part of the small intestine. For instance, expression of genes for subunits of serine palmitoyltransferase, for dihydroceramide desaturase or for CerS2 (decreased by ~25 %) and CerS4 (decreased by ~50 %) was decreased. Notably, expression of ceramide synthesis-related genes was unaltered in WAT and liver. The altered expression in ileum resulted in a decrease in all major ceramide species (C16 to C24) and the decrease in C18 to C22 ceramides was especially pronounced. The mass spectrometric analysis of serum ceramides revealed a similar pattern and the authors conclude that the increase in thermogenic beige fat was likely a result of decreased ceramide generation in ileum (Jiang *et al.*, 2015). Strikingly, administration of C16 ceramide restored the levels of all major ceramide species and reversed the beneficial effects of Gly-MCA in mice. Moreover, C16 ceramide treatment of cultured beige adipocytes markedly reduced expression of thermogenic markers. Taken together, these data support the assumption that depletion of CerS4 and the associated decrease in C18 to C22 ceramides promotes browning of igWAT. Notably, Gly-MCA treatment did not affect expression of thermogenic markers in iBAT (Jiang *et al.*, 2015). In the same line, thermogenic markers were not affected in cultured brown adipocytes from iBAT of CerS4 deficient mice, further indicating that CerS4 and the corresponding ceramides affect development of beige adipocytes, rather than thermogenic activity in general.

5.2.6 CerS4-mediated attenuation of browning

The morphological analysis of adipose tissue and the RT-PCR analysis of cultured white adipocytes from CerS4 deficient mice suggest that CerS4 is a negative

regulator of browning in WAT. This raises the question, how this could be accomplished and which signaling pathways may be involved?

PPARγ mRNA levels were increased in cultured white adipocytes from CerS4 deficient compared to wild type mice, but the difference was abrogated after cGMP treatment. Endogenous cGMP is produced by the action of guanylyl cyclases in response to stimulation by nitric oxide (NO) or natriuretic peptides and the cGMP-dependent effects on brown fat cell differentiation and thermogenesis are mediated by PKGI (Protein kinase G I)(Haas *et al.*, 2009). The finding that no difference in the expression of adipogenic markers was observed in CerS4 deficient compared to wild type cells after cGMP treatment might argue against an involvement of CerS4 in this signaling pathway. In contrast, expression of thermogenic markers in CerS4 deficient compared to wild type cells was also increased after NE treatment. NE, which is endogenously released from the sympathetic nervous system, induces a thermogenic program in WAT by activating β-adrenoceptors (β-ARs)(Mottillo & Granneman, 2011). The subsequent signaling cascade is characterized by activation of adenylyl cyclases, and the resulting increase in cAMP activates PKA (Protein kinase A), which mediates for instance, increased lipolysis, lipid oxidation or transcription of PPARγ, PGC1α and UCP1 (Mottillo & Granneman, 2011). It could be that CerS4 attenuates browning by affecting β-adrenergic signaling. Pharmacological activation of β_3-ARs in mice reduced body fat and improved insulin sensitivity at least partially by increasing lipid oxidation in adipose tissue (Grujic *et al.*, 1997). In line with that, CerS4 deficient mice fed with a HFD also displayed reduced body fat and higher insulin sensitivity and the latter was already higher in 7-8 week old animals prior to starting the experiment. Due to hair loss, browning and increased lipid oxidation is likely to occur in these mice (Cannon & Nedergaard, 2011). However, as indicated by the investigation of younger mice and cultured cells, CerS4 deficiency might contribute to these phenotypes independent of hair loss.

Identification of the signaling pathways modulated by CerS4 is a prerequisite to determine the mechanism by which CerS4 affects browning. With respect to the analysis of ELOVL3 deficient mice, CerS4 deficiency might affect adipose tissue development by altering intracellular fatty acid levels. ELOVL3 is a fatty acid elongase responsible for production of fatty acids ranging from C20 to C24 and ELOVL3 deficient mice suffer from a hair phenotype characterized by tousled fur, similar to that observed in 6-7 week old CerS4 deficient mice (Westerberg *et al.*, 2004). It was shown that ELOVL3 deficient mice are unable to hyperrecruit BAT following cold exposure and at thermoneutral temperature, number and size of lipid droplets, and metabolic capacity within BAT cells was reduced (Westerberg *et al.*, 2006). These effects were accompanied by a decrease in C20:0 and C22:0 fatty acids and it could be that the impaired BAT function is a consequence of this

decrease. In a similar fashion, differentiation or function of thermogenic cells could be affected by lower levels of these fatty acids due to consumption of the corresponding fatty acyl-CoAs by CerS4. Notably, it was shown that a diet enriched in C20:1 and C22:1 fatty acids ameliorates metabolic dysfunction by increasing PPARγ expression in WAT (Yang *et al.*, 2013). In line with this finding the increase in PPARγ mRNA levels observed in cultured white adipocytes of CerS4 deficient mice may be a result of increased C20 and C22 fatty acids. This is especially interesting with respect to the fact that fatty acids can act as ligands for PPARs, which are major transcriptional regulators of adipocyte differentiation and function (Georgiadi & Kersten, 2012). However, so far only interactions of PPARs with polyunsaturated fatty acids have been shown, and the question remains open whether mono-unsaturated or saturated fatty acids (especially C18 to C22 species) can bind to PPARs and affect their transcriptional activity.

As previously discussed, increased browning in response to inhibition of FXR signaling is probably a consequence of decreased ceramide levels (Jiang *et al.*, 2015). Since CerS4 expression and the levels of the corresponding ceramide species were markedly reduced in this study, it is more likely that increased browning in CerS4 deficient mice is a direct consequence of altered ceramide levels. As already mentioned before, it has been suggested that altered ceramide levels can affect cellular signaling by altering membrane biophysical properties (Grösch *et al.*, 2012; Silva *et al.*, 2012). For instance, in giant unilamellar vesicles (GUVs) prepared from liver and brain microsomal fractions of CerS2 deficient mice, it was shown that the decrease in C22 to C24 ceramides increases membrane fluidity and order (Silva *et al.*, 2012). This was accompanied by an overall alteration of membrane morphology. Such alterations have been shown to influence activation or inhibition of specific signaling molecules, for instance through curvature-dependent conformational changes (Reynwar *et al.*, 2007). Especially interesting in this context are sphingolipid and cholesterol-enriched membrane lipid microdomains (Lingwood & Simons, 2010). It is assumed that such highly-ordered domains are rather small (10-200 nm), heterogeneous and highly dynamic, and that they can be stabilized to larger platforms (Pike, 2009). The temporary establishment of such microdomains probably facilitates local clustering of proteins involved in the execution and control of cellular signaling (Pike, 2009; van Meer & Hoetzl, 2010). Interestingly, C16 ceramide preferentially interacts with cholesterol, whereas C24 ceramide does not (ten Grotenhuis *et al.*, 1996). Moreover, the existence of highly-ordered C16 ceramide/cholesterol domains was already demonstrated in membranes of cultured cells (Goldschmidt-Arzi *et al.*, 2011). With biophysical properties ranging between those of C16 and C24 ceramides, ceramides generated by CerS4 (C18, C20 and depending on the tissue maybe C22) could facilitate establishment of microdomains in which C16 and C24 ceramides exist together. A decrease in CerS4-generated

ceramides might in contrast favor the establishment of C16 ceramide-enriched platforms. The favored establishment of C16 ceramide-enriched microdomains and the possible consequences for cellular signaling could also explain the positive correlation between increased levels of C16 ceramide and the development of obesity and comorbidities observed after HFD feeding of CerS2, CerS5 and CerS6 deficient mice (Raichur *et al.*, 2014; Turpin *et al.*, 2014; Gosejacob *et al.*, 2016).

It was already suggested that ceramides with different acyl-chain length differentially affect membrane biophysical properties and establishment of membrane lipid microdomains (Pinto *et al.*, 2014). Together with the distinct expression pattern this could explain why depletion of different CerS leads to completely different phenotypes in mice. However, despite high expression levels and significantly altered sphingolipid content, CerS depletion does not necessarily alter the function of a given tissue. For instance, in the heart of CerS4 deficient mice C18 to C22-containing sphingolipids were strongly decreased and shorter (C16) and longer (C24) chain species were elevated, without affecting heart function (Ebel, 2014). This implies that a change in membrane biophysical properties due to altered sphingolipid content does not inevitably affect cellular signaling. Instead it presumably depends on cell type-specific components. For instance, it was shown that due to altered membrane biophysical properties in the liver of CerS2 deficient mice, TNFR1 (tumor necrosis factor α receptor 1) internalization in response to LPS (lipopolysaccharide) treatment is disrupted (Ali *et al.*, 2013). The altered membrane biophysical properties in hepatocytes of CerS2 deficient mice are probably also responsible for mislocalisation of connexin 32 (Cx32), a major constituent of gap junction channels in the liver (Park *et al.*, 2013b).

Assuming that CerS4 attenuates browning of WAT by affecting β-adrenergic signaling, the depletion of C18 and C20-containing sphingolipids in CerS4 deficient mice may allow to establish a membrane environment that attracts or stabilizes β_3-adrenoceptors, which are specifically expressed in adipose tissue (Mottillo & Granneman, 2011). The finding that iBAT function was not significantly affected in CerS4 deficient mice could then be explained by the low expression levels of CerS4. Changes in membrane biophysical properties in CerS4 deficient mice could also affect ligand attraction or stabilization of other receptors and membrane-bound components of specific signaling pathways.

While the above mentioned mechanisms would affect the membrane constitution in general, it cannot be excluded that ceramides act as specific co-factors for proteins involved in cellular signaling. As discussed in chapter 5.1.9, several proteins with putative sphingolipid binding domain were already identified and most of them localize to the plasma membrane (Contreras *et al.*, 2012). Specific ceramide/protein

interactions have already been suggested (Grösch *et al.*, 2012). For instance, the activity of protein phosphatase 2 A (PP2A), a major phosphatase involved in insulin-dependent signaling pathways, was stimulated in a stereospecific manner by the naturally occurring D-erythro-C18-ceramide, but not by the enantiomeric L-erythro-C18-ceramide or diastereoisomeres (Chalfant *et al.*, 1999). Hyperactivation of PP2A following treatment with free fatty acids decreased hepatic insulin sensitivity (Galbo *et al.*, 2011). This suggests that the increased insulin sensitivity in CerS4 deficient mice could be a consequence of decreased PP2A activity due to the decrease in activating C18 ceramides. While data on specific interactions between ceramides and proteins are rather scarce, several interactions have been shown for gangliosides. For instance, the ganglioside GM3 modulates activity of the insulin receptor (IR) (Kabayama *et al.*, 2007) and inhibits the epidermal growth factor (EGF) receptor in absence of the appropriate ligand (Coskun *et al.*, 2011). However, these interactions probably depend on the head group, rather than the chain length of the ceramide backbone. Whether endogenous ceramides generated by CerS4 specifically interact with proteins involved in cellular signaling remains to be established. A prerequisite for such investigations is the already mentioned identification of signaling pathways that are affected by CerS4 function.

Taken together, the study in this Ph. D thesis revealed that CerS4 deficient mice are protected from diet-induced obesity and insulin resistance. As indicated by the increased food intake in these mice, it cannot be excluded that the beneficial effects are caused by the progressive hair loss. However, glucose and insulin tolerance were already significantly improved in 7-8 week old animals, which exhibit only modest alterations in their fur appearance. The hair loss-independent analyses of younger mice and cultured adipocytes suggested increased browning in igWAT of CerS4 deficient mice. Therefore, independent of hair loss, increased browning may lead to higher energy expenditure and alleviate diet-induced obesity in CerS4 deficient mice. Stimulation of browning is a potential strategy for the treatment of obesity and type 2 diabetes in humans. Given the fact that CerS4 deficiency, apart from the hair loss phenotype, does not severely impact survival, vitality or fertility of mice (Ebel *et al.*, 2014; Peters *et al.*, 2015), CerS4 could be a potential therapeutical target for the treatment of obesity and associated diseases.

5.2.7 Future perspectives for investigation of CerS4 function in the development of obesity

Further analyses of 5 week old animals and cultured adipocytes are necessary to verify the hypothesis that CerS4 is a negative regulator of browning in WAT. For instance, it needs to be verified whether the smaller cells interspersed in igWAT of CerS4 deficient mice actually represent thermogenic beige adipocytes. This could be verified by immunohistochemistry using antibodies against UCP1. Stainings with Oil

Red O, which stains neutral triacylglycerols (TAGs) and lipids, could be used to determine the general lipid storage capacity of igWAT adipocytes and to distinguish between white adipocytes (usually containing one large lipid droplet) and brown adipocytes (usually containing multiple small lipid droplets). Expression of adipogenic and thermogenic markers in adipose tissue depots needs to be investigated by RT-PCR and immunoblot analyses. Determination of cAMP or cGMP levels could help to identify the involved signaling pathways. RT-PCR analyses could also include genes involved in lipogenesis, lipolysis or β-oxidation, as well as transcriptional regulators of these processes. Lipolysis (TAG hydrolysis) is usually increased following activation of thermogenic adipose tissue (Mottillo & Granneman, 2011) and β-oxidation of the provided fatty acids is indispensable for thermogenesis in mitochondria of brown and beige adipocytes (Lee *et al.*, 2015). Increased β-oxidation in iBAT (and liver) of CerS6 deficient mice probably contributed to protection from diet-induced obesity (Turpin *et al.*, 2014). In contrast, β-oxidation was decreased in the liver of heterozygous CerS2gt mice and these mice were more susceptible to diet-induced obesity (Raichur *et al.*, 2014). These studies suggested that high levels of C16 ceramide positively correlate with the development of diet-induced obesity and impaired mitochondrial β-oxidation. As a basis for further investigations, it is necessary to determine the sphingolipid profile in iBAT, igWAT and gWAT of CerS4 deficient mice by mass spectrometry.

In addition to the analyses of igWAT, further analyses could also focus on gWAT, in which CerS4 expression is even stronger. In contrast to the subcutaneous igWAT, gWAT represents a visceral adipose tissue depot. Subcutaneous and visceral adipose tissue depots strongly differ in their metabolic profile and it was suggested that visceral adipose tissue depots have a more negative impact on health (Sackmann-Sala *et al.*, 2012). Therefore, it would be interesting to see whether depletion of CerS4 also affects browning in gWAT.

The browning of WAT depots and the general capacity for non-shivering thermogenesis in CerS4 deficient mice could be further investigated by injecting mice with the β_3-adrenoceptor agonist CL 316,243, which induces browning and stimulates thermogenesis (Gnad *et al.*, 2014). Increased browning in CerS4 deficient mice could also be the result of altered release of catecholamines (e.g. NE) from the sympathetic nervous system. Therefore, it could be revealing to determine serum levels of NE in CerS4 deficient mice. The function of the sympathetic nervous system is controlled by the hypothalamus. It was shown that the hypothalamus is an important regulator of cold- and diet-induced thermogenesis and browning (Zhang & Bi, 2015). This may be relevant, since CerS4 is widely expressed in the brain (Brach, 2012). Morphological and mass spectrometric analyses of the hypothalamus in CerS4 deficient mice could provide a basis for the investigation of CerS4 function in this

tissue. Further analyses could then focus on the signaling pathways involved in hypothalamic regulation of adipose tissue function (Zhang & Bi, 2015).

The thermogenic potential of *in vitro* differentiated brown and white adipocytes from CerS4 deficient mice could be assessed by determining the *in vitro* oxygen consumption rate following NE treatment. To identify the signaling pathways that mediate increased browning in CerS4 deficient mice, cAMP and cGMP levels could be determined. In addition, further RT-PCR and immunoblot analyses of potentially involved receptors, protein kinases or target genes are necessary. Another interesting target of investigation are phosphodiesterases (PDEs), which mediate conversion of cAMP or cGMP to AMP or GMP, respectively (Mitschke *et al.*, 2013). Decreased expression or activity of these enzymes in WAT of CerS4 deficient mice could increase intracellular cAMP or cGMP levels and thereby promote browning.

In order to identify the mechanism by which CerS4 affects browning in WAT it is necessary to determine the sphingolipid profile of cultured brown and white adipocytes from CerS4 deficient mice by mass spectrometry. Cultured adipocytes could be treated with ceramides of different chain length (C16-C24) to assess the influence on adipogenic and thermogenic marker expression. In addition, CerS4 could be overexpressed in CerS4 deficient cells in order to restore C18 to C22 ceramide levels. If ceramides generated by CerS4 actually compromise browning of WAT, elevated levels of C18 to C22 ceramides should affect the browning capacity of CerS4 deficient cells.

Due to the progressive hair loss it is difficult to pinpoint beneficial effects in the development of diet-induced obesity that actually result from CerS4 deficiency in peripheral tissues. A suitable system to circumvent possible effects resulting from hair loss would be mice which allow conditional depletion of CerS4 in a specific tissue. As previously described, such mice were already generated and used for the investigation of the hair loss phenotype (Peters *et al.*, 2015). Based on the assumption that CerS4 might attenuate browning in WAT, a promising approach would be crossbreeding of conditional mice with mice expressing the Cre recombinase under control of an adipose tissue specific promoter (Lee *et al.*, 2013). The mass spectrometric and immunoblot analyses of pancreas and liver suggest that these tissues might also contribute to protection from diet-induced obesity and insulin resistance in CerS4 deficient mice. Therefore, CerS4 could also be conditionally depleted in these tissues. Adipose tissue-, pancreas- and liver-specific CerS4 mutants should be subjected to repeated feeding experiments to unequivocally determine the contribution of these tissues to protection from diet-induced obesity. Alternatively, CerS4 deficient mice could be exposed to HFD at thermoneutral temperature (30°C) to minimize effects resulting from heat loss. The identification of

the involved tissues is a prerequisite to unravel the mechanisms by which CerS4 might affect the development of obesity.

Aside from the investigation of adipose tissue depots, further analyses could also focus on pancreas function. CerS4 is strongly expressed in this tissue and depletion significantly affected the sphingolipid profile. It was suggested that CerS4 mediates glucolipotoxicity-induced apoptosis of INS1 β-cells (Véret *et al.*, 2011). Therefore, the improved glucose and insulin tolerance observed in CerS4 deficient mice could be a consequence of improved pancreas function. Pancreas function could be investigated in pancreas-specific CerS4 mutants after HFD feeding. Such analyses could focus on apoptosis in pancreas or isolated β-cells, to see if insulin release is improved in CerS4 mutants due to decreased β-cell apoptosis.

6 Summary

The first project of this Ph. D thesis focused on the biological function of the sphingomyelin synthase related protein (SMSr). Previously, it was reported that SMSr catalytic activity is essential to prevent ceramide accumulation and disruption of the early secretory pathway in cultured HeLa cells. The enzymatic product of SMSr is the sphingomyelin analog ceramide phosphoethanolamine (CPE), which can also be generated by the bifunctional sphingomyelin synthase 2 (SMS2). In this Ph. D thesis SMSr function was investigated in two mouse lines lacking SMSr catalytic activity. Conditional SMSrflox mice were generated during my diploma thesis and crossbred with pgk-Cre expressing mice for ubiquitous depletion of SMSr catalytic activity in the resulting SMSrdelEx6 mice. Point-mutated SMSrD348E mice were generated in our group already before. Mice from both mouse lines were born according to Mendelian ratio with no obvious phenotypic abnormalities. CPE synthase activity assays confirmed that SMSr catalytic activity is lost in both mouse lines and revealed that CPE synthase activity in brain primarily depends on SMSr and in liver to similar extent each on SMSr and SMS2. Immunoblot analyses with newly generated antibodies against SMSr revealed ubiquitous expression of SMSr with high levels in testis, brain and pancreas, but stainings of the ß-galactosidase reporter protein in tissues from SMSrD348E mice indicated that SMSr is not expressed in every cell type. Ultra-structural analysis of brain and liver cells from SMSrD348E mice showed no morphological abnormalities and analysis of serum activities of liver transaminases indicated that liver integrity is not affected. Mass spectrometric analysis revealed no alterations in ceramide levels in ten different tissues of SMSrD348E mice. Wild type levels of CPE were exceedingly low in all investigated tissues. In SMSrD348E mice CPE levels were largely decreased in brain and to a minor extent in testis, kidney, spleen and lung. Surprisingly, combined inactivation of SMSr and SMS2 reduced, but did not eliminate tissue-specific CPE pools. Besides providing a comprehensive inventory of CPE and metabolizing enzymes, the study in this Ph. D thesis shows that SMSr is not a critical regulator of ceramide homeostasis in mice, as was suggested for cultured HeLa cells. SMSr-mediated CPE biosynthesis is dispensable for mouse development, vitality, fertility and survival.

The second project was directed on the function of ceramide synthase 4 (CerS4) in the development of diet-induced obesity. Previously, it was shown that loss of CerS5 or CerS6 protects mice from high fat diet-induced obesity due to a decrease in C16 ceramide in WAT, liver or BAT, and mice heterozygous for CerS2 were more susceptible to high fat diet-induced hepatosteatosis and insulin resistance due to an increase in C16 ceramide. The study in this Ph. D thesis showed that CerS4 deficient mice are protected from diet-induced obesity after 16 week exposure to high fat diet. This was characterized by reduced weight gain and adipose tissue weight compared

to wild type mice. In addition, glucose and insulin tolerance were improved, which was already observed in 7-8 week old animals prior to starting the feeding experiment. Mass spectrometric analysis revealed decreased levels of C18 to C22 sphingolipid species in pancreas, liver and interscapular brown adipose tissue (iBAT) of CerS4 deficient mice, indicating that these tissues could contribute to the protection from diet-induced obesity. Since CerS4 deficient mice suffer from a progressive hair loss, which starts at the age of 6-7 weeks, it cannot be excluded that beneficial effects result from increased energy expenditure initiated to compensate heat loss. This is likely to occur, as these mice showed increased food intake. However, 5 week old CerS4 deficient mice, showed no obvious signs of hair loss and unaltered food intake, but exhibited already increased oxygen consumption and hence energy expenditure. Analysis of adipose tissue morphology in these mice suggested increased browning of inguinal white adipose tissue (igWAT), i.e. increased development of brown-like adipocytes, which similar to classical brown adipocytes are specialized in energy combustion for thermogenesis. In line with that, expression of PPARγ, a major transcriptional regulator of adipogenesis, and of thermogenic markers was increased in *in vitro* differentiated adipocytes from igWAT of CerS4 deficient mice. The results indicate that CerS4 might be an attenuator of browning in WAT. Increased browning independent of hair loss could contribute to the beneficial effects of CerS4 deficiency in the development of diet-induced obesity in mice.

7 References

Adams, J.M., Pratipanawatr, T., Berria, R., Wang, E., DeFronzo, R.A., Sullards, M.C., & Mandarino, L.J. (2004) Ceramide content is increased in skeletal muscle from obese insulin-resistant humans. *Diabetes*, **53**, 25–31.

Alessi, D.R. & Cohen, P. (1998) Mechanism of activation and function of protein kinase B. *Curr. Opin. Genet. Dev.*, **8**, 55–62.

Ali, M., Fritsch, J., Zigdon, H., Pewzner-Jung, Y., Schütze, S., & Futerman, A.H. (2013) Altering the sphingolipid acyl chain composition prevents LPS/GLN-mediated hepatic failure in mice by disrupting TNFR1 internalization. *Cell Death Dis.*, **4**, e929.

Aronova, S., Wedaman, K., Aronov, P.A., Fontes, K., Ramos, K., Hammock, B.D., & Powers, T. (2008) Regulation of ceramide biosynthesis by TOR complex 2. *Cell Metab.*, **7**, 148–158.

Attal, J., Théron, M.C., & Houdebine, L.M. (1999) The optimal use of IRES (internal ribosome entry site) in expression vectors. *Genet. Anal.*, **15**, 161–165.

Aviv, T., Lin, Z., Lau, S., Rendl, L.M., Sicheri, F., & Smibert, C.A. (2003) The RNA-binding SAM domain of Smaug defines a new family of post-transcriptional regulators. *Nat. Struct. Biol.*, **10**, 614–621.

Balla, T. (2013) Phosphoinositides: tiny lipids with giant impact on cell regulation. *Physiol. Rev.*, **93**, 1019–1137.

Bartlett, E.M. & Lewis, D.H. (1970) Spectrophotometric determination of phosphate esters in the presence and absence of orthophosphate. *Anal. Biochem.*, **36**, 159–167.

Bauer, R., Voelzmann, A., Breiden, B., Schepers, U., Farwanah, H., Hahn, I., Eckardt, F., Sandhoff, K., & Hoch, M. (2009) Schlank, a member of the ceramide synthase family controls growth and body fat in Drosophila. *EMBO J.*, **28**, 3706–3716.

Bickert, A. (2011) Vorarbeiten zur Erzeugung einer Mauslinie in der die katalytische Aktivität des Sphingomyelinsynthase verwandten Proteins (SMSr) konditional deaktiviert werden kann.

Bickert, A., Ginkel, C., Kol, M., vom Dorp, K., Jastrow, H., Degen, J., Jacobs, R.L., Vance, D.E., Winterhager, E., Jiang, X.-C., Dörmann, P., Somerharju, P., Holthuis, J.C.M., & Willecke, K. (2015) Functional characterization of enzymes catalyzing ceramide phosphoethanolamine biosynthesis in mice. *J. Lipid Res.*, **56**, 821–835.

Bijl, N., Sokolović, M., Vrins, C., Langeveld, M., Moerland, P.D., Ottenhoff, R., van Roomen, C.P.A.A., Claessen, N., Boot, R.G., Aten, J., Groen, A.K., Aerts, J.M.F.G., & van Eijk, M. (2009) Modulation of glycosphingolipid metabolism significantly improves hepatic insulin sensitivity and reverses hepatic steatosis in mice. *Hepatology*, **50**, 1431–1441.

Bionda, C., Portoukalian, J., Schmitt, D., Rodriguez-Lafrasse, C., & Ardail, D. (2004) Subcellular compartmentalization of ceramide metabolism: MAM (mitochondria-associated membrane) and/or mitochondria? *Biochem. J.*, **382**, 527–533.

Bligh, E.G. & Dyer, W.J. (1959) A RAPID METHOD OF TOTAL LIPID EXTRACTION AND PURIFICATION. *Can. J. Biochem. Physiol.*, **37**, 911–917.

Bonet, M.L., Oliver, P., & Palou, A. (2013) Pharmacological and nutritional agents promoting browning of white adipose tissue. *Biochim. Biophys. Acta*, **1831**, 969–985.

Booth, A., Magnuson, A., & Foster, M. (2014) Detrimental and protective fat: body fat distribution and its relation to metabolic disease. *Horm. Mol. Biol. Clin. Investig.*, **17**, 13–27.

Bourbon, N.A., Yun, J., & Kester, M. (2000) Ceramide directly activates protein kinase C zeta to regulate a stress-activated protein kinase signaling complex. *J. Biol. Chem.*, **275**, 35617–35623.

Brach, T. (2012) Erste Charakterisierung von transgenen Mäusen die keine Ceramid Synthase 4 exprimieren.

Bradley, A., Evans, M., Kaufman, M.H., & Robertson, E. (1984) Formation of germ-line chimaeras from embryo-derived teratocarcinoma cell lines. *Nature*, **309**, 255–256.

Brady, R.O., Kanfer, J.N., Mock, M.B., & Fredrickson, D.S. (1966) The metabolism of sphingomyelin. II. Evidence of an enzymatic deficiency in Niemann-Pick diseae. *Proc.*

Natl. Acad. Sci. U. S. A., **55**, 366–369.
Breslow, D.K., Collins, S.R., Bodenmiller, B., Aebersold, R., Simons, K., Shevchenko, A., Ejsing, C.S., & Weissman, J.S. (2010) Orm family proteins mediate sphingolipid homeostasis. *Nature*, **463**, 1048–1053.
Breslow, D.K. & Weissman, J.S. (2010) Membranes in balance: mechanisms of sphingolipid homeostasis. *Mol. Cell*, **40**, 267–279.
Brodesser, S. (2007) Der Stoffwechsel der Sphingolipide Einfluss von Substratanaloga der Dihydroceramid-Desaturase auf den Sphingolipidstoffwechsel humaner Keratinozyten und Untersuchungen zum Lipidstoffwechsel bei Spinocerebellärer Ataxie Typ 2.
Brown, D.A. & London, E. (1997) Structure of detergent-resistant membrane domains: does phase separation occur in biological membranes? *Biochem. Biophys. Res. Commun.*, **240**, 1–7.
Bruce, C.R., Hoy, A.J., Turner, N., Watt, M.J., Allen, T.L., Carpenter, K., Cooney, G.J., Febbraio, M.A., & Kraegen, E.W. (2009) Overexpression of carnitine palmitoyltransferase-1 in skeletal muscle is sufficient to enhance fatty acid oxidation and improve high-fat diet-induced insulin resistance. *Diabetes*, **58**, 550–558.
Brüggen, B., Kremser, C., Bickert, A., Ebel, P., Vom Dorp, K., Schultz, K., Dörmann, P., Willecke, K., & Dedek, K. (2016) Defective ceramide synthases in mice cause reduced amplitudes in electroretinograms and altered sphingolipid composition in retina and cornea. *Eur. J. Neurosci.*,.
Cannon, B. & Nedergaard, J. (2011) Nonshivering thermogenesis and its adequate measurement in metabolic studies. *J. Exp. Biol.*, **214**, 242–253.
Cavaghan, M.K., Ehrmann, D.A., & Polonsky, K.S. (2000) Interactions between insulin resistance and insulin secretion in the development of glucose intolerance. *J. Clin. Invest.*, **106**, 329–333.
Cerantola, V., Vionnet, C., Aebischer, O.F., Jenny, T., Knudsen, J., & Conzelmann, A. (2007) Yeast sphingolipids do not need to contain very long chain fatty acids. *Biochem. J.*, **401**, 205–216.
Chalfant, C.E., Kishikawa, K., Mumby, M.C., Kamibayashi, C., Bielawska, A., & Hannun, Y.A. (1999) Long chain ceramides activate protein phosphatase-1 and protein phosphatase-2A. Activation is stereospecific and regulated by phosphatidic acid. *J. Biol. Chem.*, **274**, 20313–20317.
Chang, Z.-Q., Lee, S.-Y., Kim, H.-J., Kim, J.R., Kim, S.-J., Hong, I.-K., Oh, B.-C., Choi, C.-S., Goldberg, I.J., & Park, T.-S. (2011) Endotoxin activates de novo sphingolipid biosynthesis via nuclear factor kappa B-mediated upregulation of Sptlc2. *Prostaglandins Other Lipid Mediat.*, **94**, 44–52.
Chavez, J. a & Summers, S. a (2012) A ceramide-centric view of insulin resistance. *Cell Metab.*, **15**, 585–594.
Chavez, J.A., Knotts, T.A., Wang, L.-P., Li, G., Dobrowsky, R.T., Florant, G.L., & Summers, S.A. (2003) A role for ceramide, but not diacylglycerol, in the antagonism of insulin signal transduction by saturated fatty acids. *J. Biol. Chem.*, **278**, 10297–10303.
Chen, H., Tran, J.-T.A., Eckerd, A., Huynh, T.-P., Elliott, M.H., Brush, R.S., & Mandal, N.A. (2013) Inhibition of de novo ceramide biosynthesis by FTY720 protects rat retina from light-induced degeneration. *J. Lipid Res.*, **54**, 1616–1629.
Chen, H.C., Ladha, Z., Smith, S.J., & Farese, R. V (2003) Analysis of energy expenditure at different ambient temperatures in mice lacking DGAT1. *Am. J. Physiol. Endocrinol. Metab.*, **284**, E213–E218.
Chen, H.C., Smith, S.J., Tow, B., Elias, P.M., & Farese, R. V (2002) Leptin modulates the effects of acyl CoA:diacylglycerol acyltransferase deficiency on murine fur and sebaceous glands. *J. Clin. Invest.*, **109**, 175–181.
Chen, Y., Siegel, F., Kipschull, S., Haas, B., Fröhlich, H., Meister, G., & Pfeifer, A. (2013) miR-155 regulates differentiation of brown and beige adipocytes via a bistable circuit. *Nat. Commun.*, **4**, 1769.
Choi, S. & Snider, A.J. (2015) Sphingolipids in High Fat Diet and Obesity-Related Diseases. *Mediators Inflamm.*, **2015**, 520618.

Cinti, S. (2009) Transdifferentiation properties of adipocytes in the adipose organ. *Am. J. Physiol. Endocrinol. Metab.*, **297**, E977–E986.

Cinti, S. (2012) The adipose organ at a glance. *Dis. Model. Mech.*, **5**, 588–594.

Collins, S., Sarzani, R., & Bordicchia, M. (2014) Coordinate control of adipose "browning" and energy expenditure by β-adrenergic and natriuretic peptide signalling. *Int. J. Obes. Suppl.*, **4**, S17–S20.

Contreras, F.-X., Ernst, A.M., Haberkant, P., Björkholm, P., Lindahl, E., Gönen, B., Tischer, C., Elofsson, A., von Heijne, G., Thiele, C., Pepperkok, R., Wieland, F., & Brügger, B. (2012) Molecular recognition of a single sphingolipid species by a protein's transmembrane domain. *Nature*, **481**, 525–529.

Coskun, Ü., Grzybek, M., Drechsel, D., & Simons, K. (2011) Regulation of human EGF receptor by lipids. *Proc. Natl. Acad. Sci. U. S. A.*, **108**, 9044–9048.

Cuvillier, O., Pirianov, G., Kleuser, B., Vanek, P.G., Coso, O.A., Gutkind, S., & Spiegel, S. (1996) Suppression of ceramide-mediated programmed cell death by sphingosine-1-phosphate. *Nature*, **381**, 800–803.

Cvetkovic, B. & Sigmund, C.D. (2000) Understanding hypertension through genetic manipulation in mice. *Kidney Int.*, **57**, 863–874.

D'Angelo, G., Capasso, S., Sticco, L., & Russo, D. (2013) Glycosphingolipids: synthesis and functions. *FEBS J.*, **280**, 6338–6353.

D'Angelo, G., Polishchuk, E., Di Tullio, G., Santoro, M., Di Campli, A., Godi, A., West, G., Bielawski, J., Chuang, C.-C., van der Spoel, A.C., Platt, F.M., Hannun, Y.A., Polishchuk, R., Mattjus, P., & De Matteis, M.A. (2007) Glycosphingolipid synthesis requires FAPP2 transfer of glucosylceramide. *Nature*, **449**, 62–67.

D'mello, N.P., Childress, A.M., Franklin, D.S., Kale, S.P., Pinswasdi, C., & Jazwinski, S.M. (1994) Cloning and characterization of LAG1, a longevity-assurance gene in yeast. *J. Biol. Chem.*, **269**, 15451–15459.

Daleke, D.L. (2007) Phospholipid flippases. *J. Biol. Chem.*, **282**, 821–825.

Deevska, G.M., Rozenova, K.A., Giltiay, N. V, Chambers, M.A., White, J., Boyanovsky, B.B., Wei, J., Daugherty, A., Smart, E.J., Reid, M.B., Merrill, A.H., & Nikolova-Karakashian, M. (2009) Acid Sphingomyelinase Deficiency Prevents Diet-induced Hepatic Triacylglycerol Accumulation and Hyperglycemia in Mice. *J. Biol. Chem.*, **284**, 8359–8368.

Degen, J. (2003) Erzeugung und Charakterisierung von konditionalen Knock-in-Reportergen-Mäusen des Connexin36.

Ding, T., Kabir, I., Li, Y., Lou, C., Yazdanyar, A., Xu, J., Dong, J., Zhou, H., Park, T., Boutjdir, M., Li, Z., & Jiang, X.-C. (2015) All members in the sphingomyelin synthase gene family have ceramide phosphoethanolamine synthase activity. *J. Lipid Res.*, **56**, 537–545.

Ebel, P. (2014) Characterization of two transgenic mouse lines deficient in Ceramide Synthase 6 and Ceramide Synthase 4.

Ebel, P., Imgrund, S., Vom Dorp, K., Hofmann, K., Maier, H., Drake, H., Degen, J., Dörmann, P., Eckhardt, M., Franz, T., & Willecke, K. (2014) Ceramide synthase 4 deficiency in mice causes lipid alterations in sebum and results in alopecia. *Biochem. J.*, **461**, 147–158.

Ebel, P., Vom Dorp, K., Petrasch-Parwez, E., Zlomuzica, A., Kinugawa, K., Mariani, J., Minich, D., Ginkel, C., Welcker, J., Degen, J., Eckhardt, M., Dere, E., Dörmann, P., & Willecke, K. (2013) Inactivation of ceramide synthase 6 in mice results in an altered sphingolipid metabolism and behavioral abnormalities. *J. Biol. Chem.*, **288**, 21433–21447.

Eggeling, C., Ringemann, C., Medda, R., Schwarzmann, G., Sandhoff, K., Polyakova, S., Belov, V.N., Hein, B., von Middendorff, C., Schönle, A., & Hell, S.W. (2009) Direct observation of the nanoscale dynamics of membrane lipids in a living cell. *Nature*, **457**, 1159–1162.

Elliott, D.J. & Grellscheid, S.N. (2006) Alternative RNA splicing regulation in the testis. *Reproduction*, **132**, 811–819.

Eto, M., Bennouna, J., Hunter, O.C., Hershberger, P.A., Kanto, T., Johnson, C.S., Lotze,

M.T., & Amoscato, A.A. (2003) C16 ceramide accumulates following androgen ablation in LNCaP prostate cancer cells. *Prostate*, **57**, 66–79.

Fabrias, G., Muñoz-Olaya, J., Cingolani, F., Signorelli, P., Casas, J., Gagliostro, V., & Ghidoni, R. (2012) Dihydroceramide desaturase and dihydrosphingolipids: debutant players in the sphingolipid arena. *Prog. Lipid Res.*, **51**, 82–94.

Fahy, E., Subramaniam, S., Brown, H.A., Glass, C.K., Merrill, A.H., Murphy, R.C., Raetz, C.R.H., Russell, D.W., Seyama, Y., Shaw, W., Shimizu, T., Spener, F., van Meer, G., VanNieuwenhze, M.S., White, S.H., Witztum, J.L., & Dennis, E.A. (2005) A comprehensive classification system for lipids. *J. Lipid Res.*, **46**, 839–861.

Fahy, E., Subramaniam, S., Murphy, R.C., Nishijima, M., Raetz, C.R.H., Shimizu, T., Spener, F., van Meer, G., Wakelam, M.J.O., & Dennis, E.A. (2009) Update of the LIPID MAPS comprehensive classification system for lipids. *J. Lipid Res.*, **50 Suppl**, S9–S14.

Fan, J., Sammalkorpi, M., & Haataja, M. (2010) Formation and regulation of lipid microdomains in cell membranes: theory, modeling, and speculation. *FEBS Lett.*, **584**, 1678–1684.

Feil, S., Valtcheva, N., & Feil, R. (2009) Inducible Cre mice. *Methods Mol. Biol.*, **530**, 343–363.

Folch, J., Lees, M., & Stanley Sloane, G.H. (1957) A simple method for the isolation and purification of total lipides from animal tissues. *J. Biol. Chem.*, **226**, 497–509.

Fox, T.E., Houck, K.L., O'Neill, S.M., Nagarajan, M., Stover, T.C., Pomianowski, P.T., Unal, O., Yun, J.K., Naides, S.J., & Kester, M. (2007) Ceramide recruits and activates protein kinase C zeta (PKC zeta) within structured membrane microdomains. *J. Biol. Chem.*, **282**, 12450–12457.

Frangioudakis, G., Garrard, J., Raddatz, K., Nadler, J.L., Mitchell, T.W., & Schmitz-Peiffer, C. (2010) Saturated- and n-6 polyunsaturated-fat diets each induce ceramide accumulation in mouse skeletal muscle: reversal and improvement of glucose tolerance by lipid metabolism inhibitors. *Endocrinology*, **151**, 4187–4196.

Freitas Lima, L.C., Braga, V. de A., do Socorro de França Silva, M., Cruz, J. de C., Sousa Santos, S.H., de Oliveira Monteiro, M.M., & Balarini, C. de M. (2015) Adipokines, diabetes and atherosclerosis: an inflammatory association. *Front. Physiol.*, **6**, 304.

Galbo, T., Olsen, G.S., Quistorff, B., & Nishimura, E. (2011) Free fatty acid-induced PP2A hyperactivity selectively impairs hepatic insulin action on glucose metabolism. *PLoS One*, **6**, e27424.

Gao, S., Zhu, G., Gao, X., Wu, D., Carrasco, P., Casals, N., Hegardt, F.G., Moran, T.H., & Lopaschuk, G.D. (2011) Important roles of brain-specific carnitine palmitoyltransferase and ceramide metabolism in leptin hypothalamic control of feeding. *Proc. Natl. Acad. Sci. U. S. A.*, **108**, 9691–9696.

Gault, C.R., Obeid, L.M., & Hannun, Y.A. (2010) An overview of sphingolipid metabolism: from synthesis to breakdown. *Adv. Exp. Med. Biol.*, **688**, 1–23.

Gehring, W.J., Affolter, M., & Bürglin, T. (1994) Homeodomain proteins. *Annu. Rev. Biochem.*, **63**, 487–526.

Georgiadi, A. & Kersten, S. (2012) Mechanisms of gene regulation by fatty acids. *Adv. Nutr.*, **3**, 127–134.

Gesta, S., Tseng, Y.-H., & Kahn, C.R. (2007) Developmental origin of fat: tracking obesity to its source. *Cell*, **131**, 242–256.

Ghosh, A., Kling, T., Snaidero, N., Sampaio, J.L., Shevchenko, A., Gras, H., Geurten, B., Göpfert, M.C., Schulz, J.B., Voigt, A., & Simons, M. (2013) A global in vivo Drosophila RNAi screen identifies a key role of ceramide phosphoethanolamine for glial ensheathment of axons. *PLoS Genet.*, **9**, e1003980.

Gibellini, F. & Smith, T.K. (2010) The Kennedy pathway--De novo synthesis of phosphatidylethanolamine and phosphatidylcholine. *IUBMB Life*, **62**, 414–428.

Ginkel, C. (2013) Herstellung und Charakterisierung von zwei Mauslinien mit Mutationen im Ceramidsynthase1 Protein und Sphingomyelin Synthase related Protein.

Ginkel, C., Hartmann, D., vom Dorp, K., Zlomuzica, A., Farwanah, H., Eckhardt, M., Sandhoff, R., Degen, J., Rabionet, M., Dere, E., Dörmann, P., Sandhoff, K., & Willecke,

K. (2012) Ablation of neuronal ceramide synthase 1 in mice decreases ganglioside levels and expression of myelin-associated glycoprotein in oligodendrocytes. *J. Biol. Chem.*, **287**, 41888–41902.

Glaros, E.N., Kim, W.S., Quinn, C.M., Jessup, W., Rye, K.-A., & Garner, B. (2008) Myriocin slows the progression of established atherosclerotic lesions in apolipoprotein E gene knockout mice. *J. Lipid Res.*, **49**, 324–331.

Gnad, T., Scheibler, S., von Kügelgen, I., Scheele, C., Kilić, A., Glöde, A., Hoffmann, L.S., Reverte-Salisa, L., Horn, P., Mutlu, S., El-Tayeb, A., Kranz, M., Deuther-Conrad, W., Brust, P., Lidell, M.E., Betz, M.J., Enerbäck, S., Schrader, J., Yegutkin, G.G., Müller, C.E., & Pfeifer, A. (2014) Adenosine activates brown adipose tissue and recruits beige adipocytes via A2A receptors. *Nature*, **516**, 395–399.

Goldschmidt-Arzi, M., Shimoni, E., Sabanay, H., Futerman, A.H., & Addadi, L. (2011) Intracellular localization of organized lipid domains of C16-ceramide/cholesterol. *J. Struct. Biol.*, **175**, 21–30.

Goldstein, J.L., DeBose-Boyd, R.A., & Brown, M.S. (2006) Protein sensors for membrane sterols. *Cell*, **124**, 35–46.

Górski, J., Dobrzyn, A., & Zendzian-Piotrowska, M. (2002) The sphingomyelin-signaling pathway in skeletal muscles and its role in regulation of glucose uptake. *Ann. N. Y. Acad. Sci.*, **967**, 236–248.

Gosejacob, D., Jäger, P.S., Vom Dorp, K., Frejno, M., Carstensen, A.C., Köhnke, M., Degen, J., Dörmann, P., & Hoch, M. (2016) Ceramide synthase 5 is essential to maintain C16:0 ceramide pools and contributes to the development of diet induced obesity. *J. Biol. Chem.*,.

Gowda, S., Yeang, C., Wadgaonkar, S., Anjum, F., Grinkina, N., Cutaia, M., Jiang, X.-C., & Wadgaonkar, R. (2011) Sphingomyelin synthase 2 (SMS2) deficiency attenuates LPS-induced lung injury. *Am. J. Physiol. Lung Cell. Mol. Physiol.*, **300**, L430–L440.

Green, J.B., Gardner, C.D., Wharton, R.P., & Aggarwal, A.K. (2003) RNA recognition via the SAM domain of Smaug. *Mol. Cell*, **11**, 1537–1548.

Grösch, S., Schiffmann, S., & Geisslinger, G. (2012) Chain length-specific properties of ceramides. *Prog. Lipid Res.*, **51**, 50–62.

Grujic, D., Susulic, V.S., Harper, M.E., Himms-Hagen, J., Cunningham, B.A., Corkey, B.E., & Lowell, B.B. (1997) Beta3-adrenergic receptors on white and brown adipocytes mediate beta3-selective agonist-induced effects on energy expenditure, insulin secretion, and food intake. A study using transgenic and gene knockout mice. *J. Biol. Chem.*, **272**, 17686–17693.

Guillas, I., Kirchman, P.A., Chuard, R., Pfefferli, M., Jiang, J.C., Jazwinski, S.M., & Conzelmann, A. (2001) C26-CoA-dependent ceramide synthesis of Saccharomyces cerevisiae is operated by Lag1p and Lac1p. *EMBO J.*, **20**, 2655–2665.

Gururaj, C., Federman, R.S., Federman, R., & Chang, A. (2013) Orm proteins integrate multiple signals to maintain sphingolipid homeostasis. *J. Biol. Chem.*, **288**, 20453–20463.

Haas, B., Mayer, P., Jennissen, K., Scholz, D., Berriel Diaz, M., Bloch, W., Herzig, S., Fässler, R., & Pfeifer, A. (2009) Protein kinase G controls brown fat cell differentiation and mitochondrial biogenesis. *Sci. Signal.*, **2**, ra78.

Hadjantonakis, A.K., Pirity, M., & Nagy, A. (1999) Cre recombinase mediated alterations of the mouse genome using embryonic stem cells. *Methods Mol. Biol.*, **97**, 101–122.

Haimi, P., Uphoff, A., Hermansson, M., & Somerharju, P. (2006) Software tools for analysis of mass spectrometric lipidome data. *Anal. Chem.*, **78**, 8324–8331.

Hajduch, E., Balendran, A., Batty, I.H., Litherland, G.J., Blair, A.S., Downes, C.P., & Hundal, H.S. (2001) Ceramide impairs the insulin-dependent membrane recruitment of protein kinase B leading to a loss in downstream signalling in L6 skeletal muscle cells. *Diabetologia*, **44**, 173–183.

Hajduch, E., Turban, S., Le Liepvre, X., Le Lay, S., Lipina, C., Dimopoulos, N., Dugail, I., & Hundal, H.S. (2008) Targeting of PKCzeta and PKB to caveolin-enriched microdomains represents a crucial step underpinning the disruption in PKB-directed signalling by

ceramide. *Biochem. J.*, **410**, 369–379.
Hajer, G.R., van Haeften, T.W., & Visseren, F.L.J. (2008) Adipose tissue dysfunction in obesity, diabetes, and vascular diseases. *Eur. Heart J.*, **29**, 2959–2971.
Hanada, K. (2003) Serine palmitoyltransferase, a key enzyme of sphingolipid metabolism. *Biochim. Biophys. Acta*, **1632**, 16–30.
Hanada, K., Kumagai, K., Yasuda, S., Miura, Y., Kawano, M., Fukasawa, M., & Nishijima, M. (2003) Molecular machinery for non-vesicular trafficking of ceramide. *Nature*, **426**, 803–809.
Hannun, Y. a & Obeid, L.M. (2008) Principles of bioactive lipid signalling: lessons from sphingolipids. *Nat. Rev. Mol. Cell Biol.*, **9**, 139–150.
Hartmann, D., Wegner, M.-S., Wanger, R.A., Ferreirós, N., Schreiber, Y., Lucks, J., Schiffmann, S., Geisslinger, G., & Grösch, S. (2013) The equilibrium between long and very long chain ceramides is important for the fate of the cell and can be influenced by co-expression of CerS. *Int. J. Biochem. Cell Biol.*, **45**, 1195–1203.
Hirose, H., Lee, Y.H., Inman, L.R., Nagasawa, Y., Johnson, J.H., & Unger, R.H. (1996) Defective fatty acid-mediated beta-cell compensation in Zucker diabetic fatty rats. Pathogenic implications for obesity-dependent diabetes. *J. Biol. Chem.*, **271**, 5633–5637.
Hla, T. & Dannenberg, A.J. (2012) Sphingolipid signaling in metabolic disorders. *Cell Metab.*, **16**, 420–434.
Holland, W.L., Miller, R.A., Wang, Z. V, Sun, K., Barth, B.M., Bui, H.H., Davis, K.E., Bikman, B.T., Halberg, N., Rutkowski, J.M., Wade, M.R., Tenorio, V.M., Kuo, M.-S., Brozinick, J.T., Zhang, B.B., Birnbaum, M.J., Summers, S.A., & Scherer, P.E. (2011) Receptor-mediated activation of ceramidase activity initiates the pleiotropic actions of adiponectin. *Nat. Med.*, **17**, 55–63.
Holthuis, J.C., Pomorski, T., Raggers, R.J., Sprong, H., & Van Meer, G. (2001) The organizing potential of sphingolipids in intracellular membrane transport. *Physiol. Rev.*, **81**, 1689–1723.
Holthuis, J.C.M. & Luberto, C. (2010) Tales and mysteries of the enigmatic sphingomyelin synthase family. *Adv. Exp. Med. Biol.*, **688**, 72–85.
Huitema, K., van den Dikkenberg, J., Brouwers, J.F.H.M., & Holthuis, J.C.M. (2004) Identification of a family of animal sphingomyelin synthases. *EMBO J.*, **23**, 33–44.
Ikeda, M., Kihara, A., & Igarashi, Y. (2004) Sphingosine-1-phosphate lyase SPL is an endoplasmic reticulum-resident, integral membrane protein with the pyridoxal 5'-phosphate binding domain exposed to the cytosol. *Biochem. Biophys. Res. Commun.*, **325**, 338–343.
Imgrund, S. (2011) Erzeugung und erste Charakterisierungen zweier Mausmutanten mit Defekten in der Ceramidsynthase 2 und 4.
Imgrund, S., Hartmann, D., Farwanah, H., Eckhardt, M., Sandhoff, R., Degen, J., Gieselmann, V., Sandhoff, K., & Willecke, K. (2009) Adult ceramide synthase 2 (CERS2)-deficient mice exhibit myelin sheath defects, cerebellar degeneration, and hepatocarcinomas. *J. Biol. Chem.*, **284**, 33549–33560.
Inokuchi, J. (2006) Insulin resistance as a membrane microdomain disorder. *Biol. Pharm. Bull.*, **29**, 1532–1537.
Jacobs, R.L., Zhao, Y., Koonen, D.P.Y., Sletten, T., Su, B., Lingrell, S., Cao, G., Peake, D.A., Kuo, M.-S., Proctor, S.D., Kennedy, B.P., Dyck, J.R.B., & Vance, D.E. (2010) Impaired de novo choline synthesis explains why phosphatidylethanolamine N-methyltransferase-deficient mice are protected from diet-induced obesity. *J. Biol. Chem.*, **285**, 22403–22413.
Jakobsson, A., Westerberg, R., & Jacobsson, A. (2006) Fatty acid elongases in mammals: their regulation and roles in metabolism. *Prog. Lipid Res.*, **45**, 237–249.
Jennemann, R., Rabionet, M., Gorgas, K., Epstein, S., Dalpke, A., Rothermel, U., Bayerle, A., van der Hoeven, F., Imgrund, S., Kirsch, J., Nickel, W., Willecke, K., Riezman, H., Gröne, H.-J., & Sandhoff, R. (2012) Loss of ceramide synthase 3 causes lethal skin barrier disruption. *Hum. Mol. Genet.*, **21**, 586–608.

Jiang, C., Xie, C., Lv, Y., Li, J., Krausz, K.W., Shi, J., Brocker, C.N., Desai, D., Amin, S.G., Bisson, W.H., Liu, Y., Gavrilova, O., Patterson, A.D., & Gonzalez, F.J. (2015) Intestine-selective farnesoid X receptor inhibition improves obesity-related metabolic dysfunction. *Nat. Commun.*, **6**, 10166.

Johnson, K.R., Becker, K.P., Facchinetti, M.M., Hannun, Y.A., & Obeid, L.M. (2002) PKC-dependent activation of sphingosine kinase 1 and translocation to the plasma membrane. Extracellular release of sphingosine-1-phosphate induced by phorbol 12-myristate 13-acetate (PMA). *J. Biol. Chem.*, **277**, 35257–35262.

Kabayama, K., Sato, T., Saito, K., Loberto, N., Prinetti, A., Sonnino, S., Kinjo, M., Igarashi, Y., & Inokuchi, J. (2007) Dissociation of the insulin receptor and caveolin-1 complex by ganglioside GM3 in the state of insulin resistance. *Proc. Natl. Acad. Sci. U. S. A.*, **104**, 13678–13683.

Kainu, V., Hermansson, M., & Somerharju, P. (2010) Introduction of phospholipids to cultured cells with cyclodextrin. *J. Lipid Res.*, **51**, 3533–3541.

Kajimura, S. & Saito, M. (2014) A new era in brown adipose tissue biology: molecular control of brown fat development and energy homeostasis. *Annu. Rev. Physiol.*, **76**, 225–249.

Kajimura, S., Seale, P., & Spiegelman, B.M. (2010) Transcriptional control of brown fat development. *Cell Metab.*, **11**, 257–262.

Karahatay, S., Thomas, K., Koybasi, S., Senkal, C.E., Elojeimy, S., Liu, X., Bielawski, J., Day, T.A., Gillespie, M.B., Sinha, D., Norris, J.S., Hannun, Y.A., & Ogretmen, B. (2007) Clinical relevance of ceramide metabolism in the pathogenesis of human head and neck squamous cell carcinoma (HNSCC): attenuation of C(18)-ceramide in HNSCC tumors correlates with lymphovascular invasion and nodal metastasis. *Cancer Lett.*, **256**, 101–111.

Kiefer, K., Carreras-Sureda, A., García-López, R., Rubio-Moscardó, F., Casas, J., Fabriàs, G., & Vicente, R. (2015) Coordinated regulation of the orosomucoid-like gene family expression controls de novo ceramide synthesis in mammalian cells. *J. Biol. Chem.*, **290**, 2822–2830.

Kihara, A. & Igarashi, Y. (2004) FVT-1 is a mammalian 3-ketodihydrosphingosine reductase with an active site that faces the cytosolic side of the endoplasmic reticulum membrane. *J. Biol. Chem.*, **279**, 49243–49250.

Kim, C. a & Bowie, J.U. (2003) SAM domains: uniform structure, diversity of function. *Trends Biochem. Sci.*, **28**, 625–628.

Kim, S.H. & Plutzky, J. (2016) Brown Fat and Browning for the Treatment of Obesity and Related Metabolic Disorders. *Diabetes Metab. J.*, **40**, 12–21.

Kintscher, U. & Law, R.E. (2005) PPARgamma-mediated insulin sensitization: the importance of fat versus muscle. *Am. J. Physiol. Endocrinol. Metab.*, **288**, E287–E291.

Kitatani, K., Idkowiak-Baldys, J., & Hannun, Y. a (2008) The sphingolipid salvage pathway in ceramide metabolism and signaling. *Cell. Signal.*, **20**, 1010–1018.

Klahre, M. (2012) The effect of the Hox- domain on the activity of mouse ceramide synthase 2 in transfected cells.

Knight, M.J., Leettola, C., Gingery, M., Li, H., & Bowie, J.U. (2011) A human sterile alpha motif domain polymerizome. *Protein Sci.*, **20**, 1697–1706.

Kol, M., Panatala, R., Nordmann, M., Swart, L., van Suijlekom, L., Cabukusta, B., Hilderink, A., Gabrietz, T., Mina, J.G.M., Somerharju, P., Korneev, S., Tafesse, F.G., & Holthuis, J.C.M. (2016) Switching Head Group Selectivity in Mammalian Sphingolipid Biosynthesis by Active-site-engineering of Sphingomyelin Synthases. *J. Lipid Res.*,.

Kotronen, A., Seppänen-Laakso, T., Westerbacka, J., Kiviluoto, T., Arola, J., Ruskeepää, A.-L., Yki-Järvinen, H., & Oresic, M. (2010) Comparison of lipid and fatty acid composition of the liver, subcutaneous and intra-abdominal adipose tissue, and serum. *Obesity (Silver Spring).*, **18**, 937–944.

Koves, T.R., Ussher, J.R., Noland, R.C., Slentz, D., Mosedale, M., Ilkayeva, O., Bain, J., Stevens, R., Dyck, J.R.B., Newgard, C.B., Lopaschuk, G.D., & Muoio, D.M. (2008) Mitochondrial overload and incomplete fatty acid oxidation contribute to skeletal muscle insulin resistance. *Cell Metab.*, **7**, 45–56.

Kremser, C., Klemm, A.-L., van Uelft, M., Imgrund, S., Ginkel, C., Hartmann, D., & Willecke, K. (2013) Cell-type-specific expression pattern of ceramide synthase 2 protein in mouse tissues. *Histochem. Cell Biol.*,.

Kumagai, K., Kawano-Kawada, M., & Hanada, K. (2014) Phosphoregulation of the Ceramide Transport Protein CERT at Serine 315 in the Interaction with VAMP-associated Protein (VAP) for Inter-organelle Trafficking of Ceramide in Mammalian Cells. *J. Biol. Chem.*,.

Kumagai, K., Yasuda, S., Okemoto, K., Nishijima, M., Kobayashi, S., & Hanada, K. (2005) CERT mediates intermembrane transfer of various molecular species of ceramides. *J. Biol. Chem.*, **280**, 6488–6495.

Kumagai, T., Sato, T., Natsuka, S., Kobayashi, Y., Zhou, D., Shinkai, T., Hayakawa, S., & Furukawa, K. (2010) Involvement of murine β-1,4-galactosyltransferase V in lactosylceramide biosynthesis. *Glycoconj. J.*, **27**, 685–695.

Lahiri, S., Lee, H., Mesicek, J., Fuks, Z., Haimovitz-Friedman, A., Kolesnick, R.N., & Futerman, A.H. (2007) Kinetic characterization of mammalian ceramide synthases: determination of K(m) values towards sphinganine. *FEBS Lett.*, **581**, 5289–5294.

Lallemand, Y., Luria, V., Haffner-Krausz, R., & Lonai, P. (1998) Maternally expressed PGK-Cre transgene as a tool for early and uniform activation of the Cre site-specific recombinase. *Transgenic Res.*, **7**, 105–112.

Lamour, N.F., Stahelin, R. V, Wijesinghe, D.S., Maceyka, M., Wang, E., Allegood, J.C., Merrill, A.H., Cho, W., & Chalfant, C.E. (2007) Ceramide kinase uses ceramide provided by ceramide transport protein: localization to organelles of eicosanoid synthesis. *J. Lipid Res.*, **48**, 1293–1304.

Lattin, J.E., Schroder, K., Su, A.I., Walker, J.R., Zhang, J., Wiltshire, T., Saijo, K., Glass, C.K., Hume, D.A., Kellie, S., & Sweet, M.J. (2008) Expression analysis of G Protein-Coupled Receptors in mouse macrophages. *Immunome Res.*, **4**, 5.

Laviad, E.L., Albee, L., Pankova-Kholmyansky, I., Epstein, S., Park, H., Merrill, A.H., & Futerman, A.H. (2008) Characterization of ceramide synthase 2: tissue distribution, substrate specificity, and inhibition by sphingosine 1-phosphate. *J. Biol. Chem.*, **283**, 5677–5684.

Laviad, E.L., Kelly, S., Merrill, A.H., & Futerman, A.H. (2012) Modulation of ceramide synthase activity via dimerization. *J. Biol. Chem.*, **287**, 21025–21033.

Le Stunff, H., Galve-Roperh, I., Peterson, C., Milstien, S., & Spiegel, S. (2002) Sphingosine-1-phosphate phosphohydrolase in regulation of sphingolipid metabolism and apoptosis. *J. Cell Biol.*, **158**, 1039–1049.

Lee, J., Ellis, J.M., & Wolfgang, M.J. (2015) Adipose fatty acid oxidation is required for thermogenesis and potentiates oxidative stress-induced inflammation. *Cell Rep.*, **10**, 266–279.

Lee, K.Y., Russell, S.J., Ussar, S., Boucher, J., Vernochet, C., Mori, M.A., Smyth, G., Rourk, M., Cederquist, C., Rosen, E.D., Kahn, B.B., & Kahn, C.R. (2013) Lessons on conditional gene targeting in mouse adipose tissue. *Diabetes*, **62**, 864–874.

Levine, T.P. & Munro, S. (2002) Targeting of Golgi-specific pleckstrin homology domains involves both PtdIns 4-kinase-dependent and -independent components. *Curr. Biol.*, **12**, 695–704.

Levy, M. & Futerman, A.H. (2010) Mammalian ceramide synthases. *IUBMB Life*, **62**, 347–356.

Li, Z., Fan, Y., Liu, J., Li, Y., Huan, C., Bui, H.H., Kuo, M.-S., Park, T.-S., Cao, G., & Jiang, X.-C. (2012) Impact of sphingomyelin synthase 1 deficiency on sphingolipid metabolism and atherosclerosis in mice. *Arterioscler. Thromb. Vasc. Biol.*, **32**, 1577–1584.

Li, Z., Zhang, H., Liu, J., Liang, C.-P., Li, Y., Li, Y., Teitelman, G., Beyer, T., Bui, H.H., Peake, D. a, Zhang, Y., Sanders, P.E., Kuo, M.-S., Park, T.-S., Cao, G., & Jiang, X.-C. (2011) Reducing plasma membrane sphingomyelin increases insulin sensitivity. *Mol. Cell. Biol.*, **31**, 4205–4218.

Lingwood, D. & Simons, K. (2010) Lipid rafts as a membrane-organizing principle. *Science*, **327**, 46–50.

Liu, J., Huan, C., Chakraborty, M., Zhang, H., Lu, D., Kuo, M.-S., Cao, G., & Jiang, X.-C.

(2009) Macrophage sphingomyelin synthase 2 deficiency decreases atherosclerosis in mice. *Circ. Res.*, **105**, 295–303.

Liu, J., Zhang, H., Li, Z., Hailemariam, T.K., Chakraborty, M., Jiang, K., Qiu, D., Bui, H.H., Peake, D. a, Kuo, M.-S., Wadgaonkar, R., Cao, G., & Jiang, X.-C. (2009) Sphingomyelin synthase 2 is one of the determinants for plasma and liver sphingomyelin levels in mice. *Arterioscler. Thromb. Vasc. Biol.*, **29**, 850–856.

Liu, K., Zhang, X., Lester, R.L., & Dickson, R.C. (2005) The sphingoid long chain base phytosphingosine activates AGC-type protein kinases in Saccharomyces cerevisiae including Ypk1, Ypk2, and Sch9. *J. Biol. Chem.*, **280**, 22679–22687.

Lo, K.A. & Sun, L. (2013) Turning WAT into BAT: a review on regulators controlling the browning of white adipocytes. *Biosci. Rep.*, **33**.

Loewen, C.J.R., Roy, A., & Levine, T.P. (2003) A conserved ER targeting motif in three families of lipid binding proteins and in Opi1p binds VAP. *EMBO J.*, **22**, 2025–2035.

Lopez, P.H.H. & Schnaar, R.L. (2009) Gangliosides in cell recognition and membrane protein regulation. *Curr. Opin. Struct. Biol.*, **19**, 549–557.

Lyn-Cook, L.E., Lawton, M., Tong, M., Silbermann, E., Longato, L., Jiao, P., Mark, P., Wands, J.R., Xu, H., & de la Monte, S.M. (2009) Hepatic ceramide may mediate brain insulin resistance and neurodegeneration in type 2 diabetes and non-alcoholic steatohepatitis. *J. Alzheimers. Dis.*, **16**, 715–729.

Maedler, K., Oberholzer, J., Bucher, P., Spinas, G.A., & Donath, M.Y. (2003) Monounsaturated fatty acids prevent the deleterious effects of palmitate and high glucose on human pancreatic beta-cell turnover and function. *Diabetes*, **52**, 726–733.

Magin, T.M., McWhir, J., & Melton, D.W. (1992) A new mouse embryonic stem cell line with good germ line contribution and gene targeting frequency. *Nucleic Acids Res.*, **20**, 3795–3796.

Malgat, M., Maurice, A., & Baraud, J. (1986) Sphingomyelin and ceramide-phosphoethanolamine synthesis by microsomes and plasma membranes from rat liver and brain. *J. Lipid Res.*, **27**, 251–260.

Malgat, M., Maurice, A., & Baraud, J. (1987) Sidedness of ceramide-phosphoethanolamine synthesis on rat liver and brain microsomal membranes. *J. Lipid Res.*, **28**, 138–143.

Marion-Letellier, R., Savoye, G., & Ghosh, S. (2015) Polyunsaturated fatty acids and inflammation. *IUBMB Life*, **67**, 659–667.

Mendelson, K., Evans, T., & Hla, T. (2014) Sphingosine 1-phosphate signalling. *Development*, **141**, 5–9.

Merrill, A.H. (2002) De novo sphingolipid biosynthesis: a necessary, but dangerous, pathway. *J. Biol. Chem.*, **277**, 25843–25846.

Mesicek, J., Lee, H., Feldman, T., Jiang, X., Skobeleva, A., Berdyshev, E. V, Haimovitz-Friedman, A., Fuks, Z., & Kolesnick, R. (2010) Ceramide synthases 2, 5, and 6 confer distinct roles in radiation-induced apoptosis in HeLa cells. *Cell. Signal.*, **22**, 1300–1307.

Mesika, A., Ben-Dor, S., Laviad, E.L., & Futerman, A.H. (2007) A new functional motif in Hox domain-containing ceramide synthases: identification of a novel region flanking the Hox and TLC domains essential for activity. *J. Biol. Chem.*, **282**, 27366–27373.

Mitschke, M.M., Hoffmann, L.S., Gnad, T., Scholz, D., Kruithoff, K., Mayer, P., Haas, B., Sassmann, A., Pfeifer, A., & Kilic, A. (2013) Increased cGMP promotes healthy expansion and browning of white adipose tissue. *FASEB J.*, **27**, 1621–1630.

Mitsutake, S., Zama, K., Yokota, H., Yoshida, T., Tanaka, M., Mitsui, M., Ikawa, M., Okabe, M., Tanaka, Y., Yamashita, T., Takemoto, H., Okazaki, T., Watanabe, K., & Igarashi, Y. (2011) Dynamic modification of sphingomyelin in lipid microdomains controls development of obesity, fatty liver, and type 2 diabetes. *J. Biol. Chem.*, **286**, 28544–28555.

Miyaji, M., Jin, Z.-X., Yamaoka, S., Amakawa, R., Fukuhara, S., Sato, S.B., Kobayashi, T., Domae, N., Mimori, T., Bloom, E.T., Okazaki, T., & Umehara, H. (2005) Role of membrane sphingomyelin and ceramide in platform formation for Fas-mediated apoptosis. *J. Exp. Med.*, **202**, 249–259.

Mizutani, Y., Kihara, A., & Igarashi, Y. (2004) Identification of the human sphingolipid C4-

hydroxylase, hDES2, and its up-regulation during keratinocyte differentiation. *FEBS Lett.*, **563**, 93–97.
Mizutani, Y., Kihara, A., & Igarashi, Y. (2005) Mammalian Lass6 and its related family members regulate synthesis of specific ceramides. *Biochem. J.*, **390**, 263–271.
Mizutani, Y., Kihara, A., & Igarashi, Y. (2006) LASS3 (longevity assurance homologue 3) is a mainly testis-specific (dihydro)ceramide synthase with relatively broad substrate specificity. *Biochem. J.*, **398**, 531–538.
Mojakgomo, R., Mbita, Z., & Dlamini, Z. (2015) Linking the ceramide synthases (CerSs) 4 and 5 with apoptosis, endometrial and colon cancers. *Exp. Mol. Pathol.*, **98**, 585–592.
Morad, S.A.F. & Cabot, M.C. (2013) Ceramide-orchestrated signalling in cancer cells. *Nat. Rev. Cancer*, **13**, 51–65.
Mottillo, E.P. & Granneman, J.G. (2011) Intracellular fatty acids suppress β-adrenergic induction of PKA-targeted gene expression in white adipocytes. *Am. J. Physiol. Endocrinol. Metab.*, **301**, E122–E131.
Mouritsen, O.G. & Zuckermann, M.J. (2004) What's so special about cholesterol? *Lipids*, **39**, 1101–1113.
Muehlenberg, B.A., Sribney, M., & Duffe, M.K. (1972) Occurrence and biosynthesis of ceramide phosphorylethanolamine in chicken and rat liver. *Can. J. Biochem.*, **50**, 166–173.
Nedergaard, J., Bengtsson, T., & Cannon, B. (2007) Unexpected evidence for active brown adipose tissue in adult humans. *Am. J. Physiol. Endocrinol. Metab.*, **293**, E444–E452.
Newton, J., Lima, S., Maceyka, M., & Spiegel, S. (2015) Revisiting the sphingolipid rheostat: Evolving concepts in cancer therapy. *Exp. Cell Res.*, **333**, 195–200.
Nilsson, O. & Svennerholm, L. (1982) Accumulation of Glucosylceramide and Glucosylsphingosine (Psychosine) in Cerebrum and Cerebellum in Infantile and Juvenile Gaucher Disease. *J. Neurochem.*, **39**, 709–718.
Nishimura, S., Manabe, I., & Nagai, R. (2009) Adipose tissue inflammation in obesity and metabolic syndrome. *Discov. Med.*, **8**, 55–60.
Novgorodov, S.A., Riley, C.L., Keffler, J.A., Yu, J., Kindy, M.S., Macklin, W.B., Lombard, D.B., & Gudz, T.I. (2015) SIRT3 Deacetylates Ceramide Synthases: Implications for Mitochondrial Dysfunction and Brain Injury. *J. Biol. Chem.*,.
Ohvo-Rekilä, H., Ramstedt, B., Leppimäki, P., & Slotte, J.P. (2002) Cholesterol interactions with phospholipids in membranes. *Prog. Lipid Res.*, **41**, 66–97.
Olayioye, M.A. & Hausser, A. (2012) Integration of non-vesicular and vesicular transport processes at the Golgi complex by the PKD-CERT network. *Biochim. Biophys. Acta*, **1821**, 1096–1103.
Osawa, Y., Uchinami, H., Bielawski, J., Schwabe, R.F., Hannun, Y.A., & Brenner, D.A. (2005) Roles for C16-ceramide and sphingosine 1-phosphate in regulating hepatocyte apoptosis in response to tumor necrosis factor-alpha. *J. Biol. Chem.*, **280**, 27879–27887.
Ouchi, N., Parker, J.L., Lugus, J.J., & Walsh, K. (2011) Adipokines in inflammation and metabolic disease. *Nat. Rev. Immunol.*, **11**, 85–97.
Parasuraman, S., Raveendran, R., & Kesavan, R. (2010) Blood sample collection in small laboratory animals. *J. Pharmacol. Pharmacother.*, **1**, 87–93.
Park, J.-H. & Schuchman, E.H. (2006) Acid ceramidase and human disease. *Biochim. Biophys. Acta*, **1758**, 2133–2138.
Park, J.-W., Park, W.-J., Kuperman, Y., Boura-Halfon, S., Pewzner-Jung, Y., & Futerman, A.H. (2013) *Ablation of Very Long Acyl Chain Sphingolipids Causes Hepatic Insulin Resistance in Mice due to Altered Detergent-Resistant Membranes.*, Hepatology (Baltimore, Md.).
Park, T.-S., Rosebury, W., Kindt, E.K., Kowala, M.C., & Panek, R.L. (2008) Serine palmitoyltransferase inhibitor myriocin induces the regression of atherosclerotic plaques in hyperlipidemic ApoE-deficient mice. *Pharmacol. Res.*, **58**, 45–51.
Park, W.-J., Park, J.-W., Erez-Roman, R., Kogot-Levin, A., Bame, J.R., Tirosh, B., Saada, A., Merrill, A.H., Pewzner-Jung, Y., & Futerman, A.H. (2013) Protection of a ceramide

synthase 2 null mouse from drug-induced liver injury: role of gap junction dysfunction and connexin 32 mislocalization. *J. Biol. Chem.*, **288**, 30904–30916.

Paulenda, T. & Draber, P. (2016) The Role of ORMDL Proteins, Guardians of Cellular Sphingolipids, in Asthma. *Allergy*,.

Peters, F., Vorhagen, S., Brodesser, S., Jakobshagen, K., Brüning, J.C., Niessen, C.M., & Krönke, M. (2015) Ceramide synthase 4 regulates stem cell homeostasis and hair follicle cycling. *J. Invest. Dermatol.*, **135**, 1501–1509.

Pewzner-Jung, Y., Brenner, O., Braun, S., Laviad, E.L., Ben-Dor, S., Feldmesser, E., Horn-Saban, S., Amann-Zalcenstein, D., Raanan, C., Berkutzki, T., Erez-Roman, R., Ben-David, O., Levy, M., Holzman, D., Park, H., Nyska, A., Merrill, A.H., & Futerman, A.H. (2010) A critical role for ceramide synthase 2 in liver homeostasis: II. insights into molecular changes leading to hepatopathy. *J. Biol. Chem.*, **285**, 10911–10923.

Pewzner-Jung, Y., Park, H., Laviad, E.L., Silva, L.C., Lahiri, S., Stiban, J., Erez-Roman, R., Brügger, B., Sachsenheimer, T., Wieland, F., Prieto, M., Merrill, A.H., & Futerman, A.H. (2010) A critical role for ceramide synthase 2 in liver homeostasis: I. alterations in lipid metabolic pathways. *J. Biol. Chem.*, **285**, 10902–10910.

Pick, A., Clark, J., Kubstrup, C., Levisetti, M., Pugh, W., Bonner-Weir, S., & Polonsky, K.S. (1998) Role of apoptosis in failure of beta-cell mass compensation for insulin resistance and beta-cell defects in the male Zucker diabetic fatty rat. *Diabetes*, **47**, 358–364.

Pike, L.J. (2009) The challenge of lipid rafts. *J. Lipid Res.*, **50 Suppl**, S323–S328.

Pinto, S.N., Laviad, E.L., Stiban, J., Kelly, S.L., Merrill, A.H., Prieto, M., Futerman, A.H., & Silva, L.C. (2014) Changes in membrane biophysical properties induced by sphingomyelinase depend on the sphingolipid N-acyl chain. *J. Lipid Res.*, **55**, 53–61.

Plück, A. (1996) Conditional mutagenesis in mice: the Cre/loxP recombination system. *Int. J. Exp. Pathol.*, **77**, 269–278.

Powell, D.J., Hajduch, E., Kular, G., & Hundal, H.S. (2003) Ceramide disables 3-phosphoinositide binding to the pleckstrin homology domain of protein kinase B (PKB)/Akt by a PKCzeta-dependent mechanism. *Mol. Cell. Biol.*, **23**, 7794–7808.

Raichur, S., Wang, S.T., Chan, P.W., Li, Y., Ching, J., Chaurasia, B., Chaurasia, B., Dogra, S., Öhman, M.K., Takeda, K., Sugii, S., Pewzner-Jung, Y., Futerman, A.H., & Summers, S.A. (2014) CerS2 haploinsufficiency inhibits β-oxidation and confers susceptibility to diet-induced steatohepatitis and insulin resistance. *Cell Metab.*, **20**, 687–695.

Requardt, R.P., Kaczmarczyk, L., Dublin, P., Wallraff-Beck, A., Mikeska, T., Degen, J., Waha, A., Steinhäuser, C., Willecke, K., & Theis, M. (2009) Quality control of astrocyte-directed Cre transgenic mice: the benefits of a direct link between loss of gene expression and reporter activation. *Glia*, **57**, 680–692.

Reynwar, B.J., Illya, G., Harmandaris, V.A., Müller, M.M., Kremer, K., & Deserno, M. (2007) Aggregation and vesiculation of membrane proteins by curvature-mediated interactions. *Nature*, **447**, 461–464.

Ridgway, N.D. & Vance, D.E. (1992) Phosphatidylethanolamine N-methyltransferase from rat liver. *Methods Enzymol.*, **209**, 366–374.

Riebeling, C., Allegood, J.C., Wang, E., Merrill, A.H., & Futerman, A.H. (2003) Two mammalian longevity assurance gene (LAG1) family members, trh1 and trh4, regulate dihydroceramide synthesis using different fatty acyl-CoA donors. *J. Biol. Chem.*, **278**, 43452–43459.

Rodgers, W., Farris, D., & Mishra, S. (2005) Merging complexes: properties of membrane raft assembly during lymphocyte signaling. *Trends Immunol.*, **26**, 97–103.

Rodríguez, C.I., Buchholz, F., Galloway, J., Sequerra, R., Kasper, J., Ayala, R., Stewart, A.F., & Dymecki, S.M. (2000) High-efficiency deleter mice show that FLPe is an alternative to Cre-loxP. *Nat. Genet.*, **25**, 139–140.

Russo, S.B., Ross, J.S., & Cowart, L.A. (2013) Sphingolipids in obesity, type 2 diabetes, and metabolic disease. *Handb. Exp. Pharmacol.*, 373–401.

Sackmann-Sala, L., Berryman, D.E., Munn, R.D., Lubbers, E.R., & Kopchick, J.J. (2012) Heterogeneity among white adipose tissue depots in male C57BL/6J mice. *Obesity (Silver Spring).*, **20**, 101–111.

Saely, C.H., Geiger, K., & Drexel, H. (2012) Brown versus White Adipose Tissue: A Mini-Review. *Gerontology*, **58**, 15–23.

Samad, F., Badeanlou, L., Shah, C., & Yang, G. (2011) Adipose tissue and ceramide biosynthesis in the pathogenesis of obesity. *Adv. Exp. Med. Biol.*, **721**, 67–86.

Santos, C., Rogriguez, F., Garcia, V., Moravčíková, D., Berkeš, D., Daïch, A., Levade, T., Baudoin-Dehoux, C., Ballereau, S., & Génisson, Y. (2014) Identification of novel CERT ligands as potential ceramide trafficking inhibitors. *Chembiochem*, **15**, 2522–2528.

Sassa, T., Hirayama, T., & Kihara, A. (2016) Enzyme Activities of the Ceramide Synthases CERS2-6 Are Regulated by Phosphorylation in the C-terminal Region. *J. Biol. Chem.*,.

Schissel, S.L., Schuchman, E.H., Williams, K.J., & Tabas, I. (1996) Zn2+-stimulated sphingomyelinase is secreted by many cell types and is a product of the acid sphingomyelinase gene. *J. Biol. Chem.*, **271**, 18431–18436.

Schmitz-Peiffer, C. (2010) Targeting ceramide synthesis to reverse insulin resistance. *Diabetes*, **59**, 2351–2353.

Schulze, H. & Sandhoff, K. (2014) Sphingolipids and lysosomal pathologies. *Biochim. Biophys. Acta*, **1841**, 799–810.

Schütz, M. (2011) Charakterisierung von Cx30 und Cx26 Punktmutationen in der Maus, die im Menschen zu syndromischer und nicht-syndromischer Taubheit führen.

Seale, P., Bjork, B., Yang, W., Kajimura, S., Chin, S., Kuang, S., Scimè, A., Devarakonda, S., Conroe, H.M., Erdjument-Bromage, H., Tempst, P., Rudnicki, M.A., Beier, D.R., & Spiegelman, B.M. (2008) PRDM16 controls a brown fat/skeletal muscle switch. *Nature*, **454**, 961–967.

Senchenkov, A., Litvak, D.A., & Cabot, M.C. (2001) Targeting ceramide metabolism--a strategy for overcoming drug resistance. *J. Natl. Cancer Inst.*, **93**, 347–357.

Senkal, C.E., Ponnusamy, S., Bielawski, J., Hannun, Y. a, & Ogretmen, B. (2010) Antiapoptotic roles of ceramide-synthase-6-generated C16-ceramide via selective regulation of the ATF6/CHOP arm of ER-stress-response pathways. *FASEB J.*, **24**, 296–308.

Separovic, D., Semaan, L., Tarca, A.L., Awad Maitah, M.Y., Hanada, K., Bielawski, J., Villani, M., & Luberto, C. (2008) Suppression of sphingomyelin synthase 1 by small interference RNA is associated with enhanced ceramide production and apoptosis after photodamage. *Exp. Cell Res.*, **314**, 1860–1868.

Serebriiskii, I.G. & Golemis, E.A. (2000) Uses of lacZ to study gene function: evaluation of beta-galactosidase assays employed in the yeast two-hybrid system. *Anal. Biochem.*, **285**, 1–15.

Sergelius, C., Niinivehmas, S., Maula, T., Kurita, M., Yamaguchi, S., Yamamoto, T., Katsumura, S., Pentikäinen, O.T., & Slotte, J.P. (2012) Structure-activity relationship of sphingomyelin analogs with sphingomyelinase from Bacillus cereus. *Biochim. Biophys. Acta*, **1818**, 474–480.

Seumois, G., Fillet, M., Gillet, L., Faccinetto, C., Desmet, C., François, C., Dewals, B., Oury, C., Vanderplasschen, A., Lekeux, P., & Bureau, F. (2007) De novo C16- and C24-ceramide generation contributes to spontaneous neutrophil apoptosis. *J. Leukoc. Biol.*, **81**, 1477–1486.

Shan, T., Liu, W., & Kuang, S. (2012) Fatty acid binding protein 4 expression marks a population of adipocyte progenitors in white and brown adipose tissues. *FASEB J.*, **27**, 277–287.

Shepherd, P.R., Withers, D.J., & Siddle, K. (1998) Phosphoinositide 3-kinase: the key switch mechanism in insulin signalling. *Biochem. J.*, **333 (Pt 3**, 471–490.

Sidossis, L. & Kajimura, S. (2015) Brown and beige fat in humans: thermogenic adipocytes that control energy and glucose homeostasis. *J. Clin. Invest.*, **125**, 478–486.

Silva, L.C., Ben David, O., Pewzner-Jung, Y., Laviad, E.L., Stiban, J., Bandyopadhyay, S., Merrill, A.H., Prieto, M., & Futerman, A.H. (2012) Ablation of ceramide synthase 2 strongly affects biophysical properties of membranes. *J. Lipid Res.*, **53**, 430–436.

Simons, K. & Sampaio, J.L. (2011) Membrane organization and lipid rafts. *Cold Spring Harb. Perspect. Biol.*, **3**, a004697.

Singer, S.J. & Nicolson, G.L. (1972) The fluid mosaic model of the structure of cell membranes. *Science*, **175**, 720–731.

Siow, D., Sunkara, M., Morris, A., & Wattenberg, B. (2015) Regulation of de novo sphingolipid biosynthesis by the ORMDL proteins and sphingosine kinase-1. *Adv. Biol. Regul.*, **57**, 42–54.

Siow, D.L. & Wattenberg, B.W. (2012) Mammalian ORMDL proteins mediate the feedback response in ceramide biosynthesis. *J. Biol. Chem.*, **287**, 40198–40204.

Siskind, L.J. (2005) Mitochondrial ceramide and the induction of apoptosis. *J. Bioenerg. Biomembr.*, **37**, 143–153.

Siskind, L.J., Kolesnick, R.N., & Colombini, M. (2002) Ceramide channels increase the permeability of the mitochondrial outer membrane to small proteins. *J. Biol. Chem.*, **277**, 26796–26803.

Siskind, L.J., Mullen, T.D., Romero Rosales, K., Clarke, C.J., Hernandez-Corbacho, M.J., Edinger, A.L., & Obeid, L.M. (2010) The BCL-2 protein BAK is required for long-chain ceramide generation during apoptosis. *J. Biol. Chem.*, **285**, 11818–11826.

Smith, S.J., Cases, S., Jensen, D.R., Chen, H.C., Sande, E., Tow, B., Sanan, D.A., Raber, J., Eckel, R.H., & Farese, R. V (2000) Obesity resistance and multiple mechanisms of triglyceride synthesis in mice lacking Dgat. *Nat. Genet.*, **25**, 87–90.

Spassieva, S., Seo, J.-G., Jiang, J.C., Bielawski, J., Alvarez-Vasquez, F., Jazwinski, S.M., Hannun, Y. a, & Obeid, L.M. (2006) Necessary role for the Lag1p motif in (dihydro)ceramide synthase activity. *J. Biol. Chem.*, **281**, 33931–33938.

Sud, M., Fahy, E., Cotter, D., Brown, A., Dennis, E.A., Glass, C.K., Merrill, A.H., Murphy, R.C., Raetz, C.R.H., Russell, D.W., & Subramaniam, S. (2007) LMSD: LIPID MAPS structure database. *Nucleic Acids Res.*, **35**, D527–D532.

Tafesse, F.G., Huitema, K., Hermansson, M., van der Poel, S., van den Dikkenberg, J., Uphoff, A., Somerharju, P., & Holthuis, J.C.M. (2007) Both sphingomyelin synthases SMS1 and SMS2 are required for sphingomyelin homeostasis and growth in human HeLa cells. *J. Biol. Chem.*, **282**, 17537–17547.

Tafesse, F.G., Ternes, P., & Holthuis, J.C.M. (2006) The multigenic sphingomyelin synthase family. *J. Biol. Chem.*, **281**, 29421–29425.

Tafesse, F.G., Vacaru, A.M., Bosma, E.F., Hermansson, M., Jain, A., Hilderink, A., Somerharju, P., & Holthuis, J.C.M. (2014) Sphingomyelin synthase-related protein SMSr is a suppressor of ceramide-induced mitochondrial apoptosis. *J. Cell Sci.*, **127**, 445–454.

ten Grotenhuis, E., Demel, R.A., Ponec, M., Boer, D.R., van Miltenburg, J.C., & Bouwstra, J.A. (1996) Phase behavior of stratum corneum lipids in mixed Langmuir-Blodgett monolayers. *Biophys. J.*, **71**, 1389–1399.

Ternes, P., Brouwers, J.F.H.M., van den Dikkenberg, J., & Holthuis, J.C.M. (2009) Sphingomyelin synthase SMS2 displays dual activity as ceramide phosphoethanolamine synthase. *J. Lipid Res.*, **50**, 2270–2277.

Térová, B., Heczko, R., & Slotte, J.P. (2005) On the importance of the phosphocholine methyl groups for sphingomyelin/cholesterol interactions in membranes: a study with ceramide phosphoethanolamine. *Biophys. J.*, **88**, 2661–2669.

Tidhar, R., Ben-Dor, S., Wang, E., Kelly, S., Merrill, A.H., & Futerman, A.H. (2012) Acyl chain specificity of ceramide synthases is determined within a region of 150 residues in the Tram-Lag-CLN8 (TLC) domain. *J. Biol. Chem.*, **287**, 3197–3206.

Tidhar, R. & Futerman, A.H. (2013) The complexity of sphingolipid biosynthesis in the endoplasmic reticulum. *Biochim. Biophys. Acta*, **1833**, 2511–2518.

Turpin, S.M., Nicholls, H.T., Willmes, D.M., Mourier, A., Brodesser, S., Wunderlich, C.M., Mauer, J., Xu, E., Hammerschmidt, P., Brönneke, H.S., Trifunovic, A., LoSasso, G., Wunderlich, F.T., Kornfeld, J.-W., Blüher, M., Krönke, M., & Brüning, J.C. (2014) Obesity-induced CerS6-dependent C16:0 ceramide production promotes weight gain and glucose intolerance. *Cell Metab.*, **20**, 678–686.

Turpin, S.M., Ryall, J.G., Southgate, R., Darby, I., Hevener, A.L., Febbraio, M.A., Kemp, B.E., Lynch, G.S., & Watt, M.J. (2009) Examination of “lipotoxicity” in skeletal muscle of

high-fat fed and ob/ob mice. *J. Physiol.*, **587**, 1593–1605.

Ussher, J.R., Koves, T.R., Cadete, V.J.J., Zhang, L., Jaswal, J.S., Swyrd, S.J., Lopaschuk, D.G., Proctor, S.D., Keung, W., Muoio, D.M., & Lopaschuk, G.D. (2010) Inhibition of de novo ceramide synthesis reverses diet-induced insulin resistance and enhances whole-body oxygen consumption. *Diabetes*, **59**, 2453–2464.

Vacaru, A.M., Tafesse, F.G., Ternes, P., Kondylis, V., Hermansson, M., Brouwers, J.F.H.M., Somerharju, P., Rabouille, C., & Holthuis, J.C.M. (2009) Sphingomyelin synthase-related protein SMSr controls ceramide homeostasis in the ER. *J. Cell Biol.*, **185**, 1013–1027.

Vacaru, A.M., van den Dikkenberg, J., Ternes, P., & Holthuis, J.C.M. (2013) Ceramide phosphoethanolamine biosynthesis in Drosophila is mediated by a unique ethanolamine phosphotransferase in the Golgi lumen. *J. Biol. Chem.*, **288**, 11520–11530.

van Eijk, M., Aten, J., Bijl, N., Ottenhoff, R., van Roomen, C.P.A.A., Dubbelhuis, P.F., Seeman, I., Ghauharali-van der Vlugt, K., Overkleeft, H.S., Arbeeny, C., Groen, A.K., & Aerts, J.M.F.G. (2009) Reducing glycosphingolipid content in adipose tissue of obese mice restores insulin sensitivity, adipogenesis and reduces inflammation. *PLoS One*, **4**, e4723.

van Marken Lichtenbelt, W.D., Vanhommerig, J.W., Smulders, N.M., Drossaerts, J.M.A.F.L., Kemerink, G.J., Bouvy, N.D., Schrauwen, P., & Teule, G.J.J. (2009) Cold-activated brown adipose tissue in healthy men. *N. Engl. J. Med.*, **360**, 1500–1508.

van Meer, G. & Hoetzl, S. (2010) Sphingolipid topology and the dynamic organization and function of membrane proteins. *FEBS Lett.*, **584**, 1800–1805.

van Meer, G. & Holthuis, J.C. (2000) Sphingolipid transport in eukaryotic cells. *Biochim. Biophys. Acta*, **1486**, 145–170.

Vance, J.E. & Tasseva, G. (2013) Formation and function of phosphatidylserine and phosphatidylethanolamine in mammalian cells. *Biochim. Biophys. Acta*, **1831**, 543–554.

Venkataraman, K. & Futerman, A.H. (2002) Do longevity assurance genes containing Hox domains regulate cell development via ceramide synthesis? *FEBS Lett.*, **528**, 3–4.

Venkataraman, K., Riebeling, C., Bodennec, J., Riezman, H., Allegood, J.C., Sullards, M.C., Merrill, A.H., & Futerman, A.H. (2002) Upstream of growth and differentiation factor 1 (uog1), a mammalian homolog of the yeast longevity assurance gene 1 (LAG1), regulates N-stearoyl-sphinganine (C18-(dihydro)ceramide) synthesis in a fumonisin B1-independent manner in mammalian cells. *J. Biol. Chem.*, **277**, 35642–35649.

Véret, J., Coant, N., Berdyshev, E. V, Skobeleva, A., Therville, N., Bailbé, D., Gorshkova, I., Natarajan, V., Portha, B., & Le Stunff, H. (2011) Ceramide synthase 4 and de novo production of ceramides with specific N-acyl chain lengths are involved in glucolipotoxicity-induced apoptosis of INS-1 β-cells. *Biochem. J.*, **438**, 177–189.

Villani, M., Subathra, M., Im, Y.-B., Choi, Y., Signorelli, P., Del Poeta, M., & Luberto, C. (2008) Sphingomyelin synthases regulate production of diacylglycerol at the Golgi. *Biochem. J.*, **414**, 31–41.

Virtanen, K.A., Lidell, M.E., Orava, J., Heglind, M., Westergren, R., Niemi, T., Taittonen, M., Laine, J., Savisto, N.-J., Enerbäck, S., & Nuutila, P. (2009) Functional Brown Adipose Tissue in Healthy Adults. *N. Engl. J. Med.*, **360**, 1518–1525.

Voelzmann, A. & Bauer, R. (2010) Ceramide synthases in mammalians, worms, and insects: emerging schemes. *Biomol. Concepts*, **1**, 411–422.

Voelzmann, A., Wulf, A.-L., Eckardt, F., Thielisch, M., Brondolin, M., Pesch, Y.-Y., Sociale, M., Bauer, R., & Hoch, M. (2016) Nuclear Drosophila CerS Schlank regulates lipid homeostasis via the homeodomain, independent of the lag1p motif. *FEBS Lett.*,.

Walker, G.E., Marzullo, P., Ricotti, R., Bona, G., & Prodam, F. (2014) The pathophysiology of abdominal adipose tissue depots in health and disease. *Horm. Mol. Biol. Clin. Investig.*, **19**, 57–74.

Walkey, C.J., Donohue, L.R., Bronson, R., Agellon, L.B., & Vance, D.E. (1997) Disruption of the murine gene encoding phosphatidylethanolamine N-methyltransferase. *Proc. Natl. Acad. Sci. U. S. A.*, **94**, 12880–12885.

Wang, X., Rao, R.P., Kosakowska-Cholody, T., Masood, M.A., Southon, E., Zhang, H.,

Berthet, C., Nagashim, K., Veenstra, T.K., Tessarollo, L., Acharya, U., & Acharya, J.K. (2009) Mitochondrial degeneration and not apoptosis is the primary cause of embryonic lethality in ceramide transfer protein mutant mice. *J. Cell Biol.*, **184**, 143–158.

Warner, A. & Mittag, J. (2015) Breaking BAT: can browning create a better white? *J. Endocrinol.*, **228**, R19–R29.

Watt, M.J., Barnett, A.C., Bruce, C.R., Schenk, S., Horowitz, J.F., & Hoy, A.J. (2012) Regulation of plasma ceramide levels with fatty acid oversupply: evidence that the liver detects and secretes de novo synthesised ceramide. *Diabetologia*, **55**, 2741–2746.

Wattenberg, B.W. (2010) Role of sphingosine kinase localization in sphingolipid signaling. *World J. Biol. Chem.*, **1**, 362–368.

Wegner, M.-S., Wanger, R.A., Oertel, S., Brachtendorf, S., Hartmann, D., Schiffmann, S., Marschalek, R., Schreiber, Y., Ferreirós, N., Geisslinger, G., & Grösch, S. (2014) Ceramide synthases CerS4 and CerS5 are upregulated by 17β-estradiol and GPER1 via AP-1 in human breast cancer cells. *Biochem. Pharmacol.*, **92**, 577–589.

Wei, N., Pan, J., Pop-Busui, R., Othman, A., Alecu, I., Hornemann, T., & Eichler, F.S. (2014) Altered sphingoid base profiles in type 1 compared to type 2 diabetes. *Lipids Health Dis.*, **13**, 161.

Welti, R., Li, W., Li, M., Sang, Y., Biesiada, H., Zhou, H.-E., Rajashekar, C.B., Williams, T.D., & Wang, X. (2002) Profiling membrane lipids in plant stress responses. Role of phospholipase D alpha in freezing-induced lipid changes in Arabidopsis. *J. Biol. Chem.*, **277**, 31994–32002.

Westerberg, R., Månsson, J.-E., Golozoubova, V., Shabalina, I.G., Backlund, E.C., Tvrdik, P., Retterstøl, K., Capecchi, M.R., & Jacobsson, A. (2006) ELOVL3 is an important component for early onset of lipid recruitment in brown adipose tissue. *J. Biol. Chem.*, **281**, 4958–4968.

Westerberg, R., Tvrdik, P., Undén, A.-B., Månsson, J.-E., Norlén, L., Jakobsson, A., Holleran, W.H., Elias, P.M., Asadi, A., Flodby, P., Toftgård, R., Capecchi, M.R., & Jacobsson, A. (2004) Role for ELOVL3 and fatty acid chain length in development of hair and skin function. *J. Biol. Chem.*, **279**, 5621–5629.

Wewer, V., Dombrink, I., vom Dorp, K., & Dörmann, P. (2011) Quantification of sterol lipids in plants by quadrupole time-of-flight mass spectrometry. *J. Lipid Res.*, **52**, 1039–1054.

White, M.F. (1998) The IRS-signalling system: a network of docking proteins that mediate insulin action. *Mol. Cell. Biochem.*, **182**, 3–11.

White-Gilbertson, S., Mullen, T., Senkal, C., Lu, P., Ogretmen, B., Obeid, L., & Voelkel-Johnson, C. (2009) Ceramide synthase 6 modulates TRAIL sensitivity and nuclear translocation of active caspase-3 in colon cancer cells. *Oncogene*, **28**, 1132–1141.

Winter, E. & Ponting, C.P. (2002) TRAM, LAG1 and CLN8: members of a novel family of lipid-sensing domains? *Trends Biochem. Sci.*, **27**, 381–383.

Wu, C., Macleod, I., & Su, A.I. (2013) BioGPS and MyGene.info: organizing online, gene-centric information. *Nucleic Acids Res.*, **41**, D561–D565.

Wu, L., Zhou, L., Chen, C., Gong, J., Xu, L., Ye, J., Li, D., & Li, P. (2014) Cidea controls lipid droplet fusion and lipid storage in brown and white adipose tissue. *Sci. China. Life Sci.*, **57**, 107–116.

Yamaoka, S., Miyaji, M., Kitano, T., Umehara, H., & Okazaki, T. (2004) Expression cloning of a human cDNA restoring sphingomyelin synthesis and cell growth in sphingomyelin synthase-defective lymphoid cells. *J. Biol. Chem.*, **279**, 18688–18693.

Yamashita, T., Hashiramoto, A., Haluzik, M., Mizukami, H., Beck, S., Norton, A., Kono, M., Tsuji, S., Daniotti, J.L., Werth, N., Sandhoff, R., Sandhoff, K., & Proia, R.L. (2003) Enhanced insulin sensitivity in mice lacking ganglioside GM3. *Proc. Natl. Acad. Sci. U. S. A.*, **100**, 3445–3449.

Yang, Z., Jean-Baptiste, G., Khoury, C., & Greenwood, M.T. (2005) The mouse sphingomyelin synthase 1 (SMS1) gene is alternatively spliced to yield multiple transcripts and proteins. *Gene*, **363**, 123–132.

Yang, Z.-H., Miyahara, H., Iwasaki, Y., Takeo, J., & Katayama, M. (2013) Dietary supplementation with long-chain monounsaturated fatty acids attenuates obesity-related

metabolic dysfunction and increases expression of PPAR gamma in adipose tissue in type 2 diabetic KK-Ay mice. *Nutr. Metab. (Lond).*, **10**, 16.

Yano, M., Watanabe, K., Yamamoto, T., Ikeda, K., Senokuchi, T., Lu, M., Kadomatsu, T., Tsukano, H., Ikawa, M., Okabe, M., Yamaoka, S., Okazaki, T., Umehara, H., Gotoh, T., Song, W.-J., Node, K., Taguchi, R., Yamagata, K., & Oike, Y. (2011) Mitochondrial dysfunction and increased reactive oxygen species impair insulin secretion in sphingomyelin synthase 1-null mice. *J. Biol. Chem.*, **286**, 3992–4002.

Yano, M., Yamamoto, T., Nishimura, N., Gotoh, T., Watanabe, K., Ikeda, K., Garan, Y., Taguchi, R., Node, K., Okazaki, T., & Oike, Y. (2013) Increased oxidative stress impairs adipose tissue function in sphingomyelin synthase 1 null mice. *PLoS One*, **8**, e61380.

Yao, J.K. & Rastetter, G.M. (1985) Microanalysis of complex tissue lipids by high-performance thin-layer chromatography. *Anal. Biochem.*, **150**, 111–116.

Yeang, C., Varshney, S., Wang, R., Zhang, Y., Ye, D., & Jiang, X.-C. (2008) The domain responsible for sphingomyelin synthase (SMS) activity. *Biochim. Biophys. Acta*, **1781**, 610–617.

Zadravec, D., Brolinson, A., Fisher, R.M., Carneheim, C., Csikasz, R.I., Bertrand-Michel, J., Borén, J., Guillou, H., Rudling, M., & Jacobsson, A. (2010) Ablation of the very-long-chain fatty acid elongase ELOVL3 in mice leads to constrained lipid storage and resistance to diet-induced obesity. *FASEB J.*, **24**, 4366–4377.

Zarringhalam, K., Zhang, L., Kiebish, M.A., Yang, K., Han, X., Gross, R.W., & Chuang, J. (2012) Statistical analysis of the processes controlling choline and ethanolamine glycerophospholipid molecular species composition. *PLoS One*, **7**, e37293.

Zhang, H., Cui, J., & Zhang, C. (2010) Emerging role of adipokines as mediators in atherosclerosis. *World J. Cardiol.*, **2**, 370–376.

Zhang, T., Barclay, L., Walensky, L.D., & Saghatelian, A. (2015) Regulation of mitochondrial ceramide distribution by members of the BCL-2 family. *J. Lipid Res.*, **56**, 1501–1510.

Zhang, W. & Bi, S. (2015) Hypothalamic Regulation of Brown Adipose Tissue Thermogenesis and Energy Homeostasis. *Front. Endocrinol. (Lausanne).*, **6**, 136.

Zhang, Y., Dong, J., Zhu, X., Wang, W., & Yang, Q. (2011) The effect of sphingomyelin synthase 2 (SMS2) deficiency on the expression of drug transporters in mouse brain. *Biochem. Pharmacol.*, **82**, 287–294.

Zhao, L., Spassieva, S.D., Jucius, T.J., Shultz, L.D., Shick, H.E., Macklin, W.B., Hannun, Y. a, Obeid, L.M., & Ackerman, S.L. (2011) A deficiency of ceramide biosynthesis causes cerebellar purkinje cell neurodegeneration and lipofuscin accumulation. *PLoS Genet.*, **7**, e1002063.

Zinda, M.J., Vlahos, C.J., & Lai, M.T. (2001) Ceramide induces the dephosphorylation and inhibition of constitutively activated Akt in PTEN negative U87mg cells. *Biochem. Biophys. Res. Commun.*, **280**, 1107–1115.

8 List of abbreviations

AC	Acid ceramidase
ALT	Alanine transaminase
ANOVA	Analysis of variance
aP2	Adipocyte Protein 2
AR	Adrenoceptor
aSMase	Acid Sphingomyelinase
AST	Aspartate transaminase
ATP	Adenosine triphosphate
AUC	Area under the curve
BAC	Bacterial artificial chromosome
BAT	Brown adipose tissue
BCA	Bicinchoninic acid
BMDM	Bone marrow derived macrophages
bp	base pairs
BSA	Bovine serum albumin
C1P	Ceramide-1-phosphate
cAMP	cyclic adenosine monophosphate
cDNA	complementary DNA
CDP	Cytidine diphosphate
Cer	Ceramide
CERK	Ceramide kinase
CerS	Ceramide synthase
CERT	Ceramide transfer protein
cGMP	cyclic guanosine monophosphate
CIDEA	Cell death-inducing DFFA-like effector A
CoA	Coenzyme A
CPE	Ceramide phosphoethanolamine
CPK	Creatine phosphokinase
Cre	Causes recombination
CT	Carboxy terminus
CTP	Cytidine triphosphate
DAG	Diacylglycerol
dCTP	Deoxycytidine triphosphate
DGAT	Diacylglycerol acyltransferase
DMEM	Dulbecco's modified Eagle medium
DMSO	Dimethyl sulfoxide
DNA	Deoxyribonucleic acid
dNTP	Deoxynucleotide triphosphate
e.g.	exempli gratia
ECL	Enhanced chemiluminiscence
EDTA	Ethylenediaminetetraacetic acid
eGFP	enhanced green fluorescent protein
ELOVL	Elongation of very long chain fatty acids
ER	Endoplasmic reticulum
ES cells	Embryonic stem cells
FCS	Fetal calf serum
FFA	Free fatty acid
Flp	Flippase
frt	Flippase recognition target
FXR	Farnesoid X receptor
GalNAc	*N*-acetylgalactosamine
GAPDH	Glyceraldehyde-3-phosphate dehydrogenase
GCS	Glucosylceramide synthase
GFP	Green fluorescent protein
GluCer	Glucosylceramide
Gly-MCA	Glycine-β-muricholic acid
GPI	Glycosylphosphatidylinositol
GSL	Glycosphingolipid
gt	Gene trap
GTT	Glucose tolerance test
gWAT	gonadal WAT
H&E	Hematoxylin and eosin staining
HEK	Human embryonic kidney cells
HexCer	Hexosylceramide
HF	Hair follicle
HFD	High fat diet
His	Histidine
HNSCC	Human head and neck squamous cell carcinomas
Hox	Homeobox
HRP	Horse radish peroxidase
hSMSr	human SMSr
i.e.	id est
iBAT	interscapular BAT
IR	Insulin receptor
IRES	Internal ribosomal entry site
ITT	Insulin tolerance test
igWAT	inguinal WAT
kbp	kilo base pairs
kDa	kilo Dalton
KO	Knock out
LacZ	β-galactosidase
Lag	Longevity assurance gene
LCB	Long chain base

LC-MS	Liquid chromatography-MS
LDL	Low density lipoprotein
LFD	Low fat diet
loxP	locus of crossing over in P1
LPS	Lipopolysaccharide
MEF	Mouse embryonic fibroblasts
min	Minute
mRNA	messenger RNA
MS	Mass spectrometry
mSMSr	mouse SMSr
Myf5	Myogenic factor 5
NBD	Nitrobenz-2-Oxa-1,3-Diazol-4-yl
NE	Norepinephrine
NLS	Nuclear localisation signal
nSMase	Neutral Sphingomyelinase
NT	Amino terminus
ORM	Orosomucoid
P	Postnatal day
P/S	Penicillin/Streptomycin
PARP	Poly ADP ribose polymerase
PBS	Phosphate buffered saline
PC	Phosphatidylcholine
PCR	Polymerase chain reaction
PE	Phosphatidylethanolamine
PEMT	Phosphatidylethanolamine N-methyltransferase
PGC1α	PPARγ coactivator 1α
PGK	Phosphoglycerate kinase
PH	Pleckstrin homology
PI	Phosphatidylinositol
PIC	Proteinase inhibitor cocktail
PKA	Protein kinase A (B, C, D, G)
PMSF	Phenylmethanesulfonylfluoride
PP2A	Protein phosphatase 2 A
PPAR	peroxisome proliferator-activated receptor
PRDM16	PR domain containing 16
PS	Phosphatidylserine
Q-TOF	Quantitative Time of Flight-MS
RNA	Ribonucleic acid
RT	Room temperature
RT-PCR	Real Time-PCR
rWAT	renal WAT
S1P	Sphingosin-1-phosphate
SAM	Sterile alpha motif
Samd8	SAM domain-containing protein 8
SAP	Sphingolipid activator protein
SDS	Sodium dodecyl sulfate
SEM	Standard error of the mean
Ser	Serine
siRNA	small interfering RNA
SK1/2	Sphingosine kinase 1/2
SM	Sphingomyelin
SMase	Sphingomyelinase
SMS	Sphingomyelin synthase
SMSr	Sphingomyelin synthase related protein
Sph	Sphingosine
SPT	Serine palmitoyltransferase
SREBP	Sterol-responsive element binding protein
SRM	Selective reaction monitoring
SV40	Simian Virus 40
SVF	Stromal vascular fraction
sWAT	subcutaneous WAT
T3	Triiodothyronine
TAG	Triacylglycerol
TBST	Tris-buffered saline-Tween
Thr	Threonine
TLC	Thin layer chromatography
TNFα	Tumor necrosis factor α
TORC2	Target of rapamycin kinase complex 2
Tyr	Tyrosine
UCP1	Uncoupling protein 1
UV	Ultraviolet light
WAT	White adipose tissue
WT	Wild type
Ypk2	Yeast protein kinase 2